TUM School of Engineering and Design
Technical University of Munich

Design of Thermal Management Systems for Future Aircraft

Hagen Kellermann

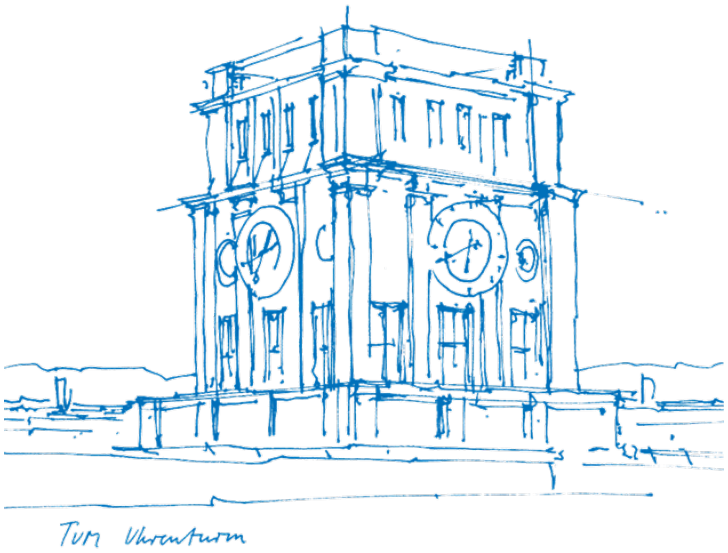

TUM School of Engineering and Design
Technische Universität München

Design of Thermal Management Systems for Future Aircraft

Hagen Kellermann

Vollständiger Abdruck der von der TUM School of Engineering and Design der Technischen Universität München zur Erlangung eines

Doktors der Ingenieurwissenschaften (Dr.-Ing.)

genehmigten Dissertation.

Vorsitz:
Prof. Dr.-Ing. Volker Gümmer

Prüfende der Dissertation:
1. Prof. Dr.-Ing. Mirko Hornung
2. Prof. Dr.-Ing. Andreas Strohmayer

Die Dissertation wurde am 02.05.2023 bei der Technischen Universität München eingereicht und durch die TUM School of Engineering and Design am 12.02.2024 angenommen.

Abstract

Advanced Thermal Management Systems (TMSs) are required for future aircraft powertrains due to the expected increase in emitted waste heat, e.g., by large electric components. Additionally, the expected waste heat is of low quality. The main objective of this thesis is the development of TMS models for future aircraft to assess different TMS options already at an early stage of the aircraft conceptual design process. In each TMS assessment the first priority is the removal of all waste heat in all operating points to ensure the safe operation of the aircraft at all times. The second priority is the minimization of the TMS's negative impact on the aircraft through its mass, drag, and required power. For the assessment, physical models of all relevant TMS components are developed and connected in computational simulations. The thesis consists of four papers and a final discussion. In each paper, a different TMS model is developed, discussed, and applied to an individual application case. The final discussion links the different TMS options. It compares their performance for one shared application case to demonstrate the ability to incorporate the TMS assessment at the early stages of the aircraft conceptual design process.

In the first paper, the most conventional TMS using a Ram-Air Heat Exchanger (R-HEX) as a heat sink is investigated. Design and off-design studies are conducted for a hybrid-electric aircraft leading to an optimized TMS for the application case. The additional required fuel burn is quantified at 0.19% if the TMS is sized for top-of-climb conditions and an additional fan is used during take-off or 0.29% if the system is oversized in top-of-climb to meet the take-off requirement without a fan.

In the second publication, the heat removal potential of the existing aircraft surfaces is quantified with simple and fast methods to allow an estimation prior to a more detailed TMS design. The potential assessment is conducted for a large range of aircraft. Depending on the operating conditions and assumed surface temperatures, the existing aircraft surfaces are capable of removing multiple megawatts of heat.

In the third paper, two detailed TMSs utilizing surface heat exchangers (S-HEX) are designed for a hybrid-electric application case. The S-HEX uses fuel as the coolant and similarly to the R-HEX study, a partial dependence analysis is conducted prior to the final design to identify the most important design variables. One concept that circulates hot fuel underneath the wing surfaces is capable of removing all required heat in most operating points except for taxi where the low aircraft velocity limits convective heat transfer. The other concept, which places a heat exchanger directly into the tank and relies on natural convection for the heat removal is less effective and only able to provide the required heat removal rate in take-off.

In the fourth paper, the specific challenge of TMSs for low-temperature heat sinks is addressed by the design of a TMS for a battery of an aircraft with an all-electric design mission. A large number of potential heat-pump technologies is discussed and a TMS using thermoelectric modules is designed. The final results are very sensitive towards battery operating temperature and ambient temperature ranging between 2% to 16% additional aircraft mass caused by the TMS.

Finally, the previous TMS assessments are combined to design a TMS for a hybrid-electric aircraft with a similar size as the ATR42-600. The surface heat removal potential is quantified and detailed R-HEX and S-HEX TMSs are designed. Afterward, the simplification of the design and off-design results into data tables enables the implementation of the computationally expensive TMS results in the conceptual aircraft design loop. The use of the data is demonstrated with an exemplary scenario leading to two different optimal TMS for heat sources at a temperature level of 370 K and 328 K respectively.

Contents

List of abbreviations

(H)EP	(Hybrid) Electric Propulsion
ACARE	Advisory Council for Aviation Research and Innovation in Europe
AOC	Air-Oil Cooler
Bat	Battery
Brg	Bearing
CFD	Computational Fluid Dynamics
CL	Climb
CR	Cruise
CS	Certification Specification
DEP	Distributed Electric Propulsion
DES	Design
DS	Drive System
EASA	European Union Aviation Safety Agency
ECS	Environmental Control System
EPR	Engine Pressure Ratio
ESAero	Empirical Systems Aerospace
FOC	Fuel-Oil Cooler
FP	Fuel Pump
Gbx	Gearbox
GT-HEAT	Georgia Tech Hybrid Electric Analysis Tool
GTF	Geared Turbo Fan
HAS	Heat Acquisition System
HDTO	Hot-Day Take-Off
HEX	Heat Exchanger
HRS	Heat Rejection System
HS	High Spool
HTS	Heat Transport System
IDG	Integrated Drive Generator
ISA	International Standard Atmosphere
LHV	Lower Heating Value
LS	Low Spool
MD	Motor Drive
MEA	More Electric Aircraft
MF	Modeling Framework
MG	Motor/Generator
MTOM	Maximum Take-off Mass
NASA	National Aeronautics and Space Administration
NM	Nautical Miles
NPSS	Numerical Propulsion System Simulation
NTU	Number of Transfer Units
OD	Off-Design
PAO	Polyalphaolefin
PCM	Phase Change Material
PMAD	Power Management and Distribution System
R-HEX	Ram-Air Heat Exchanger
RCC	Ram-Cooled Cooler
RTRC	Raytheon Technologies Research Center
S-HEX	Surface Heat Exchanger
SCEPTOR	Scalable Convergent Electric Propulsion Technology and Operations Research
SG	Starter Generator
SLS	Sea Level Static
SRIA	Strategic Research & Innovation Agenda
STARC-ABL	Single-Aisle Turboelectric Aircraft with an Aft Boundary Layer propulsor

SUGAR	Subsonic Ultra-Green Aircraft
TEM	Thermoelectric Module
TLAR	Top Level Aircraft Requirement
TMS	Thermal Management System
TO	Take-Off
ToC	Top of Climb
TRL	Technology Readiness Level
TWIH	Tank with Internal Heating
TX	Taxi
UNFCCC	United Nations Framework Convention on Climate Change
UTRC	United Technologies Research Center
VTOL	Vertical Take-Off and Landing
WIFHE	Wing Integrated Fuel Heat Exchanger
WISH	Wing Integrated Surface Heat Exchanger

List of symbols

A	area	m^2	T	temperature	K
α	heat transfer coefficient	$W\,m^{-2}\,K^{-1}$	F_N	thrust	N
β	material absorption coefficient	–	u	velocity	$m\,s^{-1}$
C	absolute heat capacity	$W\,K^{-1}$	w	mass flow rate	$kg\,s^{-1}$
c	chord length	m			
C_R	ratio of heat capacities of two sides of a heat exchanger	–			
$CIPR$	pump displacement	in^3/rev			
D	drag	N			
d	diameter	m			
δA	relative area	–			
δc	relative chord length	–			
δFB	relative fuel burn increase	‰			
δp	relative pressure drop	–			
δS	relative semi-span	–			
ΔT	temperature difference	K			
δw	relative mass flow change	–			
ϵ	effectiveness	–			
η	efficiency	–			
Γ	area ratio	–			
L	length	m			
m	mass	kg			
Ma	Mach number	–			
P	power	W			
Π	pressure ratio defined as outlet/inlet pressure	–			
Q	heat flow rate	W			
Re	Reynolds number	–			
ρ	density	$kg\,m^{-3}$			
S	semi-span	m			

List of subscripts

∞	free-stream
air	air
amb	ambient
av	average
c	cold side
cts	control surface
diff	diffuser
exp	exposed
face	face of one side of the heat exchanger
fan	fan
flap	wing flap
fslg	fuselage
H	hydraulic
h	hot side
inst	installed
kink	wing kink position
max	maximum
mot	motor and PMAD
nozz	nozzle
out	outlet
prop	propeller
pump	pump
R	ratio of design to off-design value unless otherwise defined in the list of symbols
root	wing root position
shaft	shaft
slat	wing slat
slip	slipstream
solar	solar
surf	surface
tip	wing tip position
tot	total
uh	unheated
wet	wetted
wing	wing

1 Introduction

This thesis is a publication-based dissertation. Sources [1–4] are the main body of the thesis and are included in their original format. Prior to the publications, an introduction provides the motivation for the topic, the current state of the art in the field, the overall objective of the thesis as well as an overall methodology. The thesis concludes with a discussion, which connects the individual papers to the higher-level objectives.

1.1 Motivation

Humanity-induced climate change is widely recognized as one of the major worldwide challenges today. The United Nations Framework Convention on Climate Change (UNFCCC) agreed to "Holding the increase in the global average temperature to well below 2°C above pre-industrial levels and pursuing efforts to limit the temperature increase to 1.5°C above pre-industrial levels, recognizing that this would significantly reduce the risks and impacts of climate change" [5] in Article 2(a) of their Paris Agreement. [5]

The Advisory Council for Aviation Research and Innovation in Europe (ACARE) developed a Strategic Research & Innovation Agenda (SRIA) [6], which defines research and development goals for the aviation sector. Under "Challenge 3: Protecting the environment and the energy supply" [6], the emission targets of the Paris Agreement are directly addressed: Despite the current share of global CO_2 emissions of the aviation industry of only 2%, research measures leading to emission reductions have to be taken to prevent it from increasing. Additional aircraft emissions are nitrogen oxide (NOx), condensation trails, and noise. Specific emission reduction goals for the year 2050 are defined in the so-called "Flightpath 2050" [6, 7]:

- A reduction of CO_2 emissions per passenger kilometer of 75% compared to the year 2000
- A reduction of NOx emissions per passenger kilometer of 90% compared to the year 2000
- A reduction of perceived noise by 65% compared to the year 2000
- Emission-free aircraft movements when taxiing

The SRIA defines "Action Areas" to aid in the achievement of the Flightpath 2050 goals. Action Areas number 3.1 and 3.2 call for the development of future air vehicles in evolutionary and revolutionary steps respectively. [6, 7]

The Flightpath 2050 goals were recently replaced by a new vision called "Fly the Green Deal: Europe's vision for sustainable aviation" [8]. This new vision of the ACARE is more ambitious as it aims for net-zero CO_2 emissions for all intra-EU flights as well as the flights departing the EU by the year 2050. Also, other emissions such as non-volatile particulate matter are now addressed in addition to the previously defined CO_2, NOx, and noise emissions. The new vision expects hybrid- and all-electric aircraft to be part of the path to achieving its goals. [8]

A higher level of electrification of the aircraft is one of the major research areas in the development of future air vehicles. As part of the trend towards More Electric Aircraft (MEA), the installed electric power on commercial aircraft has drastically increased from less than 100 kW to more than 1 MW over the last decades [9] with the Boeing 787 currently having the most installed electric power of 1 MW of all commercial aircraft [10]. Generally, the MEA aims to successively replace conventional aircraft systems, e.g., pneumatic, mechanical, and hydraulic systems, with electric systems [11].

A more radical approach, which has been heavily investigated over the last decade, is the partial or full electrification of the aircraft propulsion system [12]. Research on electrified propulsion systems covers the entire range of aircraft. Small vehicles with only a few passengers have the most advanced Technology Readiness

Level (TRL) currently. Some companies already have full-scale prototypes which successfully completed one or multiple unmanned or manned test flights, e.g., [13–17] with some of them having started the certification process and one product with a completed type certification [18]. Slightly larger (hybrid) electric aircraft are under development and close to their first flight, e.g., [19–21]. The electrification of small commuter aircraft will only play a minor role in the achievement of the Flightpath 2050 goals as the majority of aircraft CO_2 emissions today originates from Narrowbody (43%) and Widebody (33%) passenger aircraft [22].

Electrification of larger aircraft, i.e., aircraft that are covered by the European Union Aviation Safety Agency (EASA) Certification Specification (CS)-25, is only present in conceptual studies. For example, Boeing developed a concept aircraft called Subsonic Ultra-Green Aircraft (SUGAR) Volt as part of their SUGAR program. The design specifications for all aircraft concepts of the SUGAR series were 900 Nautical Miles(NM) and 154 passengers. For the SUGAR Volt, a fully electric drive train with batteries, a hybrid electric drive train with fuel cells, and a hybrid electric drive train with batteries were considered. [23]

The final hybrid electric study on the SUGAR VOLT configuration revealed fuel burn benefits due to the electrification of the powertrain of 10.9% for a "Balanced" configuration with moderate electric power and up to 21.7% for a configuration with an all-electric cruise segment [24]. Other conceptual studies on large electrified aircraft have also shown promising results with regard to the partial fulfillment of the SRIA goals such as the National Aeronautics and Space Administration (NASA) STARC-ABL concept. It is an aircraft concept with a size similar to a Boeing 737-800 and has an electrically driven tailcone thruster. The aircraft does not use alternative energy sources but harvests the necessary electric power to drive the tailcone thruster from large generators inside the main engines - a so-called turboelectric concept. The results show a 7% reduction in fuel burn for the economic mission and 12% for the design mission. [25]

A similar concept was investigated at Bauhaus Luftfahrt for a slightly larger aircraft concept with a size similar to an Airbus A330-300 [26]. The final fuel burn reduction results are slightly lower: between 3.2% and 4.7% depending on whether a preliminary assessment of 3D aero effects for the tailcone thruster is considered [27].

Another turboelectric aircraft concept for a Boeing 737-800 sized aircraft is the latest iteration of the ECO-150 by EASAero, which is labeled ECO-150-300. It uses distributed electric propulsion to increase propulsive efficiency and thereby lower its fuel burn by 9.2% for the economic mission and 11.5% for the design mission compared to a conventional reference aircraft with similar technology assumptions. [28]

These examples share an increase of electrification of the aircraft's systems, in particular the propulsion system, which poses a challenge for the Thermal Management System (TMS) of the aircraft. The main challenge is the absence of a natural heat sink for electric components. In contrast, hydraulic systems, for example, have a working fluid that can act as a heat sink for the waste heat from hydraulic pumps and conveniently transport it to a heat exchanger. The propulsion system of modern transport aircraft typically consists of gas turbines, which reject the majority of their waste heat directly via the exhaust gas. Electric components on the other hand need an external cooling system that can be a simple housing with possibly external cooling fins, but also a complex liquid system with embedded cooling channels. Despite the comparatively high efficiencies of electric components, their integration into the aircraft propulsion system will lead to unprecedented heat loads for transport aircraft, e.g., the ECO-150-R was expected to generate 1.491 MW of waste heat [29]. The second major difficulty regarding TMSs of electric powertrains is the low quality of the waste heat. Electric components generally have low operating temperatures compared to gas turbines, resulting in a need for high mass flows of cooling fluid or high heat transfer coefficients to achieve high heat fluxes. While these challenges are acknowledged in the research community already, e.g., [30], there is a research gap regarding the optimal design and integration of TMSs into the aircraft to minimize parasitic effects such as increased mass, drag, and power off-take. These parasitic effects largely impact the final benefit for the SRIA targets of any new aircraft concept and, therefore, their quantification is necessary for a fair assessment of future aircraft. Reliable and robust TMS models are not only necessary for more electric, hybrid-electric, and all-electric aircraft, but also for other future aircraft with thermal management challenges such as advanced engine concepts, e.g., [31]. This thesis seeks to fill the gap and provide numerical models and methods for the design and optimization of TMSs for future aircraft.

1.2 Objectives

The objectives of the thesis are presented in the form of research questions to be answered. They are directly derived from the identified research gap. The state-of-the-art chapter highlights the need to answer the following research questions:

1. **Which impact can be expected from the TMS on overall aircraft level?**
   While the addition of a TMS is non-negotiable for the above-mentioned cases of novel propulsion systems, it may be optimized to least negatively impact the aircraft. The impact of the TMS on the overall aircraft consists of multiple parasitic effects. Primarily, additional mass, drag, and required power are added. The development of methods to quantify these effects to a precision satisfactory for aircraft conceptual design is the first objective of this thesis. A computer program combining different suitable methods to component and system models will provide a tool to answer this and the following research questions.

2. **Which parameters are most influential for the optimization of the TMS on overall aircraft level?**
   With an analysis tool at hand from the previous research question, the next step is understanding the physical properties of the TMS. With the goal of a TMS optimized towards an overall aircraft level in mind, the understanding of sensitivities on the component and system level is the second objective of this thesis. It will provide insights that are useful for any future TMS design optimization.

3. **Which are the best heat sinks for a TMS on an aircraft?**
   For a TMS on-board of an aircraft, multiple heat sink options exist. A quantitative comparison of the different options with regard to the aforementioned parasitic effects is the third objective of this thesis.

4. **What is the optimized TMS for a given application case?**
   The last objective is the application of the developed methods and models from objective one, the knowledge about the system sensitivities from objective two, and the impact of the heat sink choice from objective three for one exemplary aircraft concept. The overall goal is to design an optimized TMS for the application case.

In the process of finding answers to these research questions, two priorities regarding any TMS on board an aircraft will be considered in the given order:

1. The TMS must ensure the safe operation of all heat sources within their defined temperature limits at all times in all operating conditions.

2. The TMS's negative impact on the aircraft should be as small as possible.

The first priority is non-negotiable. Any TMS not fulfilling this requirement has to be disregarded even if it offers superior results in the second priority. The first priority is usually expressed by a set heat load at a maximum temperature for each heat source.

1.3 State of the art

A simple search on SCOPUS highlights the recent developments in the field of electrified propulsion as shown in Figure 1.1 [32]. When searching for the combination "Aircraft Electric Propulsion", which is chosen as a representative term for similar search terms, an exponential increase in publications can be observed especially from 2015 onward. The number of publications with the search term "Aircraft Thermal Management" (again chosen as the best representative term for similar combinations) lags significantly behind. Only three years later, in 2018, a sudden increase reflects the new interest in the topic. The shown graph is only an illustrative example and not a detailed statistical analysis.

For this thesis, due to its publication-based nature, the literature until the year 2018, when the work on the first publication commenced, was most relevant for the identification of the research gap and thus the choice of the aforementioned objectives. However, the following section includes more recent sources to present an updated

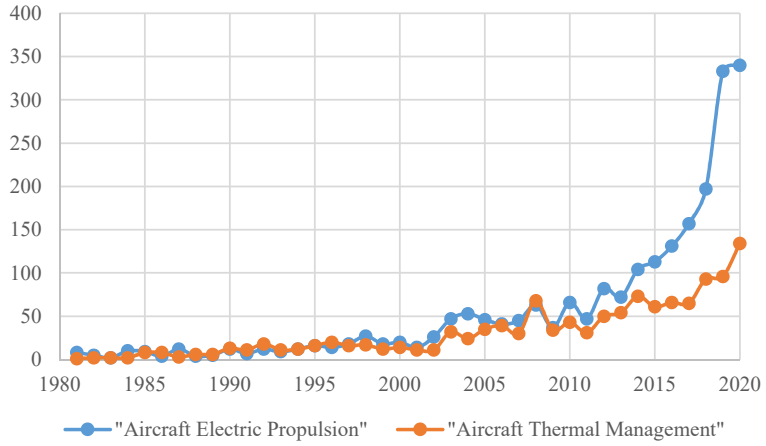

Figure 1.1 SCOPUS literature search in title, abstract, and keywords [32]

state-of-the-art. The section is split into three major parts. First, a historical overview with the earliest TMSs on aircraft is given. Next, the specific TMS challenges of current aircraft are discussed. The last part summarizes the current research activities on future TMSs, which are mainly motivated by research on electrified aircraft. The section closes with a small summary that relates the described state of the art to the thesis objectives.

1.3.1 Early development of aircraft thermal management systems

TMS are required on aircraft ever since the first successful attempts at motorized flight in the early 20th century. The early piston engines used for aircraft produced large quantities of waste heat due to the losses of the thermodynamic cycle. The development of a large number of piston engines with rapid development cycles and, therefore, quickly evolving cooling systems, was accelerated by two world wars up to the year 1945. The main reason to cool piston engines is the thermal limit of the wall material, especially in hot zones such as the piston head. Additionally, higher pressure ratios are possible without engine knocking if the piston is well-cooled and thereby the performance of the engine is enhanced. Sufficient cooling also prevents the coking of lubricants and thus ensures a smooth operation and a long life cycle of the engine. The historical development of TMS for piston engines in Germany is well described in [33]. The following section summarizes the most relevant challenges and the corresponding development steps. One possibility to categorize cooling options for early piston engines is presented in Figure 1.2. [33]

The cooling methods applied to early piston engines are generally divided into external and internal cooling. External cooling is used to cool the piston walls from the outside. Two main methods were developed in parallel and coexisted for high-power piston engines: direct air cooling and indirect liquid cooling. With direct air cooling, ambient air directly passes over the outer walls of the pistons. Advantages are simplicity, robustness, comparatively light systems, simple maintenance, low costs, and a cooling fluid without technical limits such as freezing or boiling. On the other hand, the thermodynamic properties of air are inferior to other cooling fluids, e.g., water. Air has a relatively low thermal conductivity, density, and specific heat capacity, resulting in a high required air volume passing the piston walls at high velocities. The poor cooling properties of air resulted in higher piston temperatures and the need for constructive measures to extend the surface area of the pistons with fins. The higher piston temperature has the positive effect of lower thermal losses due to the lower temperature difference between the wall and the combustion gas, which increases the thermodynamic efficiency of the cycle. Contrarily, the higher mean temperature inside the piston limits the maximum compression ratio and thus power. Therefore, engines, which were designed for maximum power outputs, such as the ones used in the late stages of the second world war, e.g., Daimler-Benz DB 603 and Jumo 213, did not employ an air cooling system, but a liquid one. The air cooling systems are further differentiated into ram air and forced

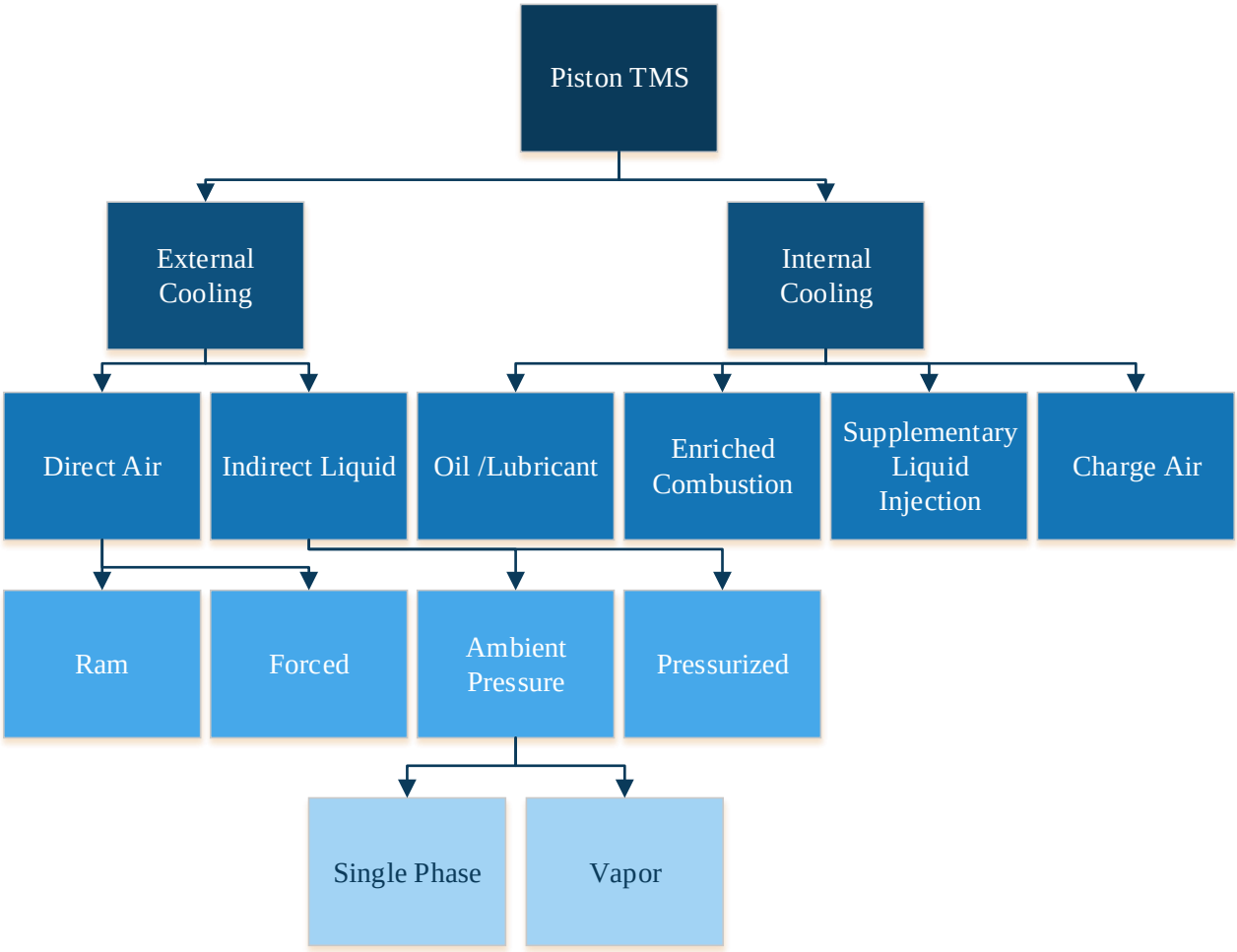

Figure 1.2 Scheme of early piston engine thermal management options derived from [33]

flow systems. Ram systems use the aircraft's velocity to provide adequate airflow around the cooling surfaces. They are the simplest cooling form possible, however, they have two major disadvantages. During low-speed operation, they offer poor cooling performance and during high-speed operation, their drag contribution is high. Engine manufacturers developed technological enhancements to partially solve these problems. Advancements in the heat flow structure of the piston walls as well as more sophisticated cooling ribs increased the heat transfer rates in all operating points. Cowlings and ducts guided the airflow to the most relevant hot spots on the engine, increasing the effectiveness of the TMS. Cowlings also were able to decrease the air velocity around the pistons and inside the cooling ribs, especially in high-speed operations, which greatly reduced the drag of the TMS. Control surfaces, such as split flaps or throttle rings were added to the outlet of the cooling duct to control the airflow within it, which further optimized the cooling performance and drag contribution at different operating points. For some engines, none of these measures could provide adequate cooling air flows. In those cases, an additional cooling fan was installed to force the air to flow over the pistons. [33]

Indirect liquid systems were competing with direct air cooling systems from the beginning of the TMS developments. Water circulation systems were already used for the earliest aircraft engines in the 1910s. Water is guided through or along the piston walls to absorb heat and transport it to a Heat Exchanger (HEX), where the heat is transferred to the ambient air. Other cooling fluids are possible, but in the early developments, only water and water-glycol mixtures were used. Adding glycol in concentrations of up to 50% offers frost protection in cold operating conditions. These indirect liquid cooling systems are employed mainly due to the preferential thermodynamic properties of the cooling fluid compared to air. Water, for example, has a roughly four times higher specific heat capacity and thermal conductivity than air. A liquid cooling system can remove more heat from the limited cooling space available around a piston allowing an overall more aggressive thermodynamic

cycle design and thus, higher specific engine powers. Also, the decoupling of the heat source location from the heat removal location enables better integration of the HEX for aerodynamic benefits. The first liquid cooling systems were open systems, i.e., they worked at ambient pressure. To avoid cavitation on the pump's suction side and possible local overheating, the temperature in an open system has to stay below the boiling temperature at all times. For water, the boiling temperature decreases with altitude. Therefore, starting in 1917, when engines were designed for increasingly large altitudes, liquid cooling systems were mostly designed as closed pressurized systems reaching up to 2 bar for the most sophisticated engines of the second world war. The HEX for liquid cooling systems were already developed towards aircraft-specific optimization targets that are still relevant today: the HEX was supposed to be lightweight and compact with high heat transfer rates and low flow resistances on both sides. In the 1930ies the flat-tubed ribbed HEX became the preferred overall HEX design option and in the 1940ies aluminum replaced heavier metals to reduce the HEX weight by 30%. Besides the HEX-technology, the integration of the HEX was intensively researched. Criteria were aerodynamic and thermodynamic performance, vision obstruction, the complexity of the HEX-shape, and susceptibility to failure. Nearly every location was tried: above, below, behind, and in front of the engine, in the upper and lower wing, and below the fuselage or on its sides. With increasing aircraft speeds, the reduction of the aerodynamic resistance of the HEX became more important. A patent by Junkers in 1915 suggested the integration of the HEX inside a duct with a diffuser at the front and a nozzle at the rear. The ram air was slowed by the diffuser to decrease the pressure loss of the air over the HEX and the nozzle allowed the recovery of momentum, which overall reduced the cooling drag of the system and in some cases led to additional thrust. These ducted coolers were mounted either below the fuselage or below the wings. [33]

Prime examples of aerodynamically optimized cooling systems were the pressurized water-glycol cooler of the DB 601A engine on the Me 109E aircraft in Germany [33] and the cooler of the P51D Mustang in the U.S.A. [34]. Similar to air cooling systems, control surfaces enabled the aircraft to adapt the cooler's performance to the operating point. In contrast to the pressurized system, which was motivated by the temperature limitation of the liquid's boiling point, vapor systems exploited the latent heat of the liquid's phase change. Vapor systems operated at ambient pressure and thus had a lower complexity than pressurized systems, e.g., no pressure control valves were required, and sealing the system was less difficult. The largest difficulty in the design of a vapor cooling system was the integration of the voluminous condenser. To reduce the aerodynamic resistance, experiments with skin surface coolers were conducted, but the strong distortion of the metal surface as well as a general trend in aircraft design towards less wing area prevented further development of the vapor systems with surface coolers. [33]

Besides the external cooling options, there were many options for internal cooling in early piston engines. Any oil used for lubrication had to be cooled since it either received waste heat directly from the heated walls or through friction. With increasing engine performance towards the most powerful engines of the fighter aircraft, the oil heat load increased so that dedicated oil coolers were required. These were either air coolers integrated in addition to the main HEX or, in some cases, the oil heat was transferred to the main cooling loop through a liquid-liquid HEX. While oil cooling was necessary for any engine, most other internal cooling methods were employed specifically to increase engine power. Enriching the combustion by increasing the fuel flow above the stoichiometric fuel-air ratio is possibly the simplest form of internal cooling. The additional fuel was vaporized and the required latent heat resulted in an overall cooling of the combustion gas. In more complex engines, additional liquids were injected for a temporary power increase. For cooling, water is preferable due to its very high heat of evaporation, however, susceptibility to corrosion or freezing was a strong argument against the use of water. Instead, methanol-water or ethanol-water mixtures were used. In addition to the cooling effect through evaporation, the increased mass flow rate also increased the engine's power. With increasing altitude, the pressure ratio of the engine's charge air also had to increase to provide sufficient oxygen levels inside the pistons, which also resulted in increased compressor outlet temperatures of the air. To avoid engine knocking, the charge air had to be cooled either at the outlet of the compressor or between two compressor stages. The HEX for the pre-cooling of the charge air were either air-air HEX or the heat was transferred to the main cooling loop. [33]

After the second world war, piston engines became less significant both on military and civil aircraft.

1.3.2 Thermal management systems on today's aircraft

Engine cooling

In modern aircraft, the propulsion system still is one of the most challenging systems concerning thermal management. CS-25 type aircraft sometimes have turboprop engines for the smaller types while larger aircraft always use turbofan engines. Regardless, the engine core is a gas turbine, which faces different cooling challenges than the earlier piston engines. From a cooling perspective, the major difference is the strict flow direction of the hot gas in the gas turbine as well as the almost isobaric combustion, which enables new cooling concepts such as film cooling. Therefore, TMS of modern aircraft engines differ significantly from their historic counterparts for piston engines.

Generally the cooling efforts for a modern gas turbine can be divided into two main categories:

1. Primary cooling of the components in the hot section of the engine
2. Cooling of secondary engine systems

The air already heats up significantly through the compression before the combustion chamber, however, the compressor blade materials can withstand these temperatures without active cooling. With the increasing trend in Engine Pressure Ratio (EPR) in aircraft engines, the temperature in the later compressor stages also increases. In some engines, the compressor drum of the high-pressure compressor is cooled internally with air taken from the low-pressure compressor stages. Still, the combustion chamber and the turbine are the main components requiring active cooling, which is provided by air taken from different stages of the compressor. [35]

Active cooling is necessary since even the most advanced materials and thermal coatings used for the components are not able to withstand the temperatures of the hot gas, especially with the ongoing trend towards higher EPRs and turbine inlet temperatures. In the combustion chamber, variations of the film cooling concept are employed. The main idea is to protect the wall material with a film of cold air. In modern combustion chambers, up to 40% of the airflow is guided around the flame zone and enters the combustion chamber through small tangential holes in the walls at different locations downstream of the flame. It then flows parallel to the hot main stream and thereby provides isolation. The cooling air heats up downstream so that fresh air is required in regular intervals. [35]

The main principle of combustion chamber film cooling has remained the same, but the implementation has evolved. Examples are Wiggle-Strips, Stacked Rings, Machined Rings, and Z-Rings. Details can be found in modern textbooks such as [35]. Transpiration cooling additionally uses the effect of convection inside the walls. The outer surface of the combustion chamber wall consists of multiple layers with internal cooling channels. The cooling air moving through these channels cools the wall from the inside and then exits through multiple holes. These holes are typically much smaller and in a more dense arrangement than in classic film cooling concepts and the special term effusion cooling is used . Transpiration cooling is one of the most effective methods of cooling walls exposed to hot gas flows due to the combined effects of protecting the surface through a film and removing heat from the material through the internal cooling flow. It is investigated for other high heat flux applications in aerospace such as hypersonic vehicles [36]. [35, 37]

The high-pressure turbine is located right behind the combustion chamber and, therefore, the first stage is exposed to the highest gas temperatures inside the entire engine. A combination of internal and external cooling is applied to withstand extreme temperatures. Typically, the internal cooling has a multi-channel air flow guided through the blade with impingement cooling on the inside of the leading edge. The cooling air exits at the blade tips which offers an additional sealing effect. Another part of the cooling air is directed through small holes distributed over the blade to provide film cooling. Subsequent stages require less cooling effort due to the expansion and corresponding reduction in the temperature of the hot gas. Localized film cooling and internal cooling methods are sufficient and the later stages of the low-pressure turbine do not require active cooling at all. The complex design of the current high-pressure turbine blades is the result of decades of research and optimization. It is necessary to further increase cooling effectiveness since, with the increasing EPR trend, both cooling air and hot gas have increased temperatures. The next technological improvement with transpiration cooling for turbine blades could not yet be realized due to material and manufacturing constraints. An increase

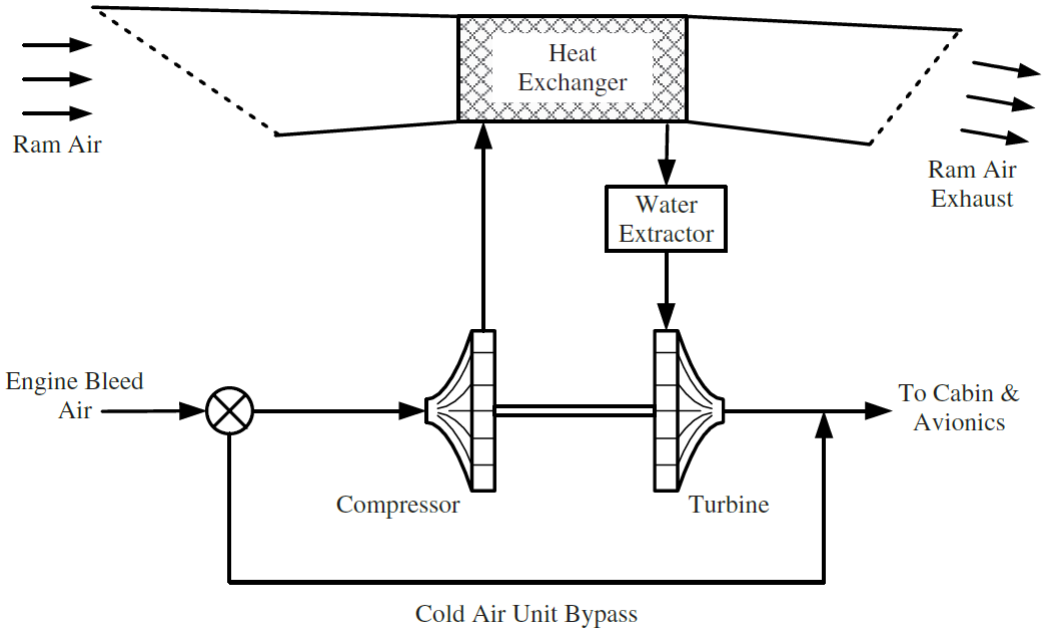

Figure 1.3 Bootstrap Cooling System [40]

in cooling air mass flow is also not possible because the air used for the cooling of a stage is not available for work extraction for that same stage and the previous stages. [35]

Besides the air cooling of the primary engine components in the hot section of the engine, multiple other heat sources exist in a modern aircraft engine. The main heat sources are bearings, gears, and the Integrated Drive Generator (IDG). Typically, there are two oil loops in an engine: the main loop and the IDG loop. The oil serves multiple purposes including lubrication, corrosion protection, and cooling. Since the oil systems are closed, the absorbed heat has to be rejected. Two heat sinks are available and used: the fuel and air from the bypass duct. The fuel is used primarily since preheating the fuel before entering the combustion chamber is thermodynamically desirable. However, in some operating points with low fuel flow to the combustion chamber, the thermal capacity of the fuel is not sufficient to absorb the entire heat load. In these cases, more fuel than required by the combustion chamber is pumped and recirculated either within the fuel supply system or for some aircraft back to the tanks. If even fuel circulation does not provide enough cooling capacity an additional air-oil-cooler is used to pre-cool the oil. [35]

Recently, large reduction gearboxes have been added to aircraft engines to reduce the fan rotational speed while keeping the low-pressure turbine speed high. While these gearboxes operate at very high efficiencies between 97.7% and 99.7%, they have to translate the majority of the engine's power and thus add a significant amount of heat to the oil system. Additionally, the trend towards MEA results in larger IDGs in the engines also adding to the oil heat load. To resolve the corresponding thermal management challenges, improved or enlarged air oil coolers at different locations in the engine are investigated. [38]

Environmental control system and avionics

Another system on modern aircraft requiring thermal management effort is the Environmental Control System (ECS). It is required to provide comfortable conditions for the crew and passengers. In cruising altitudes that often exceed 10 000 m, compressed air is required for the fresh air supply of the cabin. Typically, this air is "bled" from one of the engine's compressor stages, but alternatives exist such as onboard the Boeing 787 where a dedicated electrically driven compressor is installed with a ram-air intake [39]. After compression, the air has temperatures levels above human comfort. Therefore, cooling is required before the air enters the cabin. Multiple technical concepts exist and are well explained in [39, 40]. Most commonly, open reversed Brayton cycles are used. Figure 1.3 shows a common scheme of an ECS for large civil aircraft from [40]. The engine bleed-air (engine bleed-air is replaced by compressed ram air in MEAs) is compressed before it enters a HEX

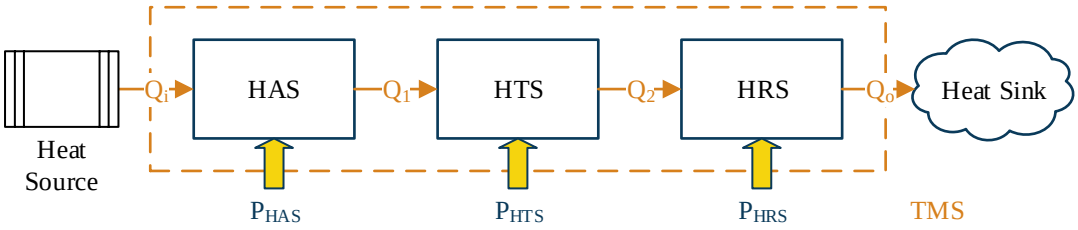

Figure 1.4 Sketch of a general TMS adapted from [4]

with uncompressed ram air on the other side. Behind the HEX, a water extractor removes any excessive water. The turbine expands the air and drives the compressor. For flight state-dependent temperature regulation, the cold air unit bypass can be used. The temperature control valve varies the air bypassing the pack. Mixing the turbine outlet flow with the bypass flow results in the final air temperature and pressure which is fed to the cabin. [40]

Another heat source on today's aircraft is the electric avionics equipment. It is typically stored in a separate ventilated compartment. On civil aircraft, the avionic heat loads tend to be low and cabin exhaust air is sufficient as a coolant since the electrical equipment can safely operate at temperatures above human comfort level. [40]

1.3.3 Modeling of future aircraft thermal management systems

The previous section summarized the TMS efforts on currently available civil aircraft. Future aircraft are constantly investigated and some of the concepts, especially the ones employing some form of (Hybrid) Electric Propulsion ((H)EP), are predicted to have substantially larger cooling challenges. Research addressing these challenges will be presented in the following section. A TMS can generally be split into three parts as shown in Figure 1.4 [4]. It consists of a Heat Acquisition System (HAS) to directly capture the heat from the source, a Heat Transport System (HTS) to move the heat from the source location to the sink location, and a Heat Rejection System (HRS) to reject the heat from the system to the terminal heat sink. Each of these systems may require some power (P). The following sections will provide insight into specific aircraft configurations or research activities concerning the TMS of future aircraft.

ECO150

Empirical Systems Aerospace (ESAero) conducted a series of studies investigating turbo-electric distributed-propulsion aircraft configurations for regional aircraft with 150 passengers [41]. A turbo-electric propulsion system does not use an alternative energy source in addition to the gas turbine but converts at least a part of the gas turbine's mechanical power to electric power to drive electric motors. Distributed-propulsion systems utilize the flexibility gained from using multiple electric motors by, e.g., distributing propellers along the wing in the spanwise direction [42]. One of the earliest configurations was the ECO-150-16 featuring a cryogenically cooled turbo-electric distributed-propulsion system and a split wing. It targeted the NASA N+3 (year 2035+) timeframe. Another version of the aircraft used a conventional (non-cryogenic) cooling system for the N+2 (year 2025+) timeframe. The TMS was already considered at that early development stage on a basic level. For the motors, a liquid cooling technology was assumed. The cooling system weight was estimated at 30% of the motor weight and a fixed coolant flow rate similar to a car engine was assumed. Some qualitative considerations regarding an optimal airframe integration, e.g., placing the components in high-speed airflow to reduce component sizes, were made. [41]

In a later study, the concept was redesigned and named ECO-150R [29]. The split wing as well as the conventionally cooled turbo-electric distributed-propulsion system were kept. Improved models were used for the simulation of the aircraft to achieve a higher level of detail. The TMS was investigated more thoroughly

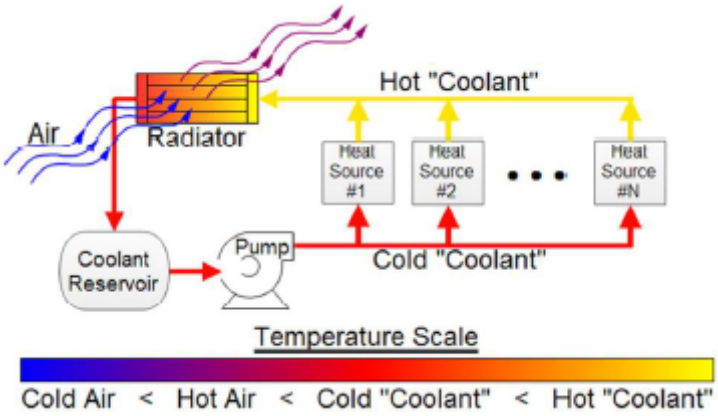

Figure 1.5 Thermal Management System Diagram [29]

and the concept is shown in Figure 1.5. A liquid cooling system in a parallel arrangement, i.e., each heat source is cooled by a portion of the cool coolant flow, was used to cool a turbo-electric propulsion system with a maximum heat load of 1 491 kW. While no specification of the HAS is provided, the HTS consisted of pipes and pumps and the HRS was a ducted Ram-Air Heat Exchanger (R-HEX) including a diffuser and a nozzle. As shown in Figure 1.5, the hot coolant streams are combined into one stream fed to the hot side of the HEX. The HEX had a tube and fin configuration with flat tubes. A design space exploration of the TMS with two parameters was performed in Top of Climb (ToC) conditions. The face Mach number of the HEX as well as the diffuser area ratio were varied to assess the impact on TMS weight, drag, and power consumption. The results show that a higher face Mach number (Ma_{face}) is beneficial for weight and pump power, however, there is a contrary trend for the drag. The diffuser area ratio (Γ_{diff}) should be chosen according to the selected Ma_{face}. For an off-design evaluation, a TMS from the design space was chosen at Ma_{face}= 0.1 and Γ_{diff} = 0.29, which presents a good compromise between weight and power on the one side and drag on the other side. In off-design, altitudes and Mach numbers for the entire flight envelope were considered and the TMS maximum heat rejection rate combined with its drag were calculated. The study showed that there is a possibility to tune the TMS performance towards higher heat rejection or lower drag with a variable nozzle outlet area. [29]

The presented work is one of the most detailed analyses of an aircraft TMS to date with some attempts at optimization as well as the consideration of multiple mission points. However, the authors already identified some key improvement possibilities such as optimizing the HEX geometry instead of arbitrarily choosing a fixed one [29].

In another update of the ECO-150 concept resulting in the ECO-150-300, the TMS simulation detail was increased [28]. The study emphasized failure cases and the requirement that TMS failure should only be as impactful as a single-component failure of the electric components. Therefore, the TMS of the generators had to be decoupled from the TMS of the motors. The motor and inverter TMS consisted of cooling fins inside the fan duct that were sized to the maximum throttle conditions during Take-Off (TO). To cope with the peak heat loads during TO, a fuel-based TMS was introduced for the generators and rectifiers, cf. Figure 1.6. Fuel from the aircraft tanks is stored in a feeder tank and used as a coolant for the generator and rectifiers of the turbo-electric propulsion system. The heated fuel is split into two streams: one feeds the gas turbine and the second one is returned to the feeder tank after a temperature reduction through an air-fuel HEX. The advantage of using the fuel is the addition of a heat reservoir with high thermal capacitance to the TMS without a weight penalty. A mission simulation (cf. Figure 1.7) showed that the system operated at a thermal deficit, i.e., more heat entered the system than the air-fuel HEX rejected until approximately 20 min into the mission, which leads to a continuous increase in fuel temperature up to a peak temperature of about 45°C. Also, the peak coolant outlet temperature of the electric components stayed below the set limit of 90°C. It was assumed that the starting temperature of the fuel was 20°C, which is a good assumption for a standard day, however, may be difficult to keep in hot-day conditions. [28]

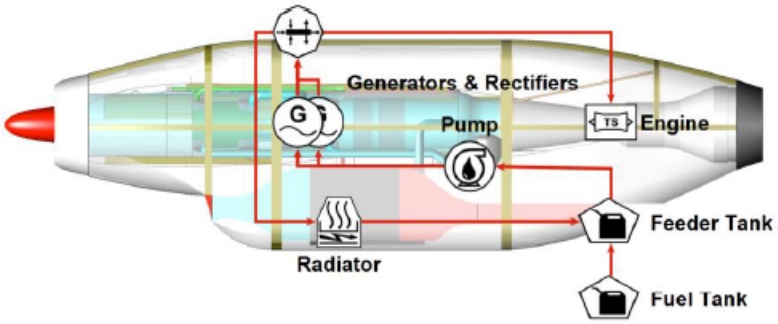

Figure 1.6 Fuel thermal management system architecture [28]

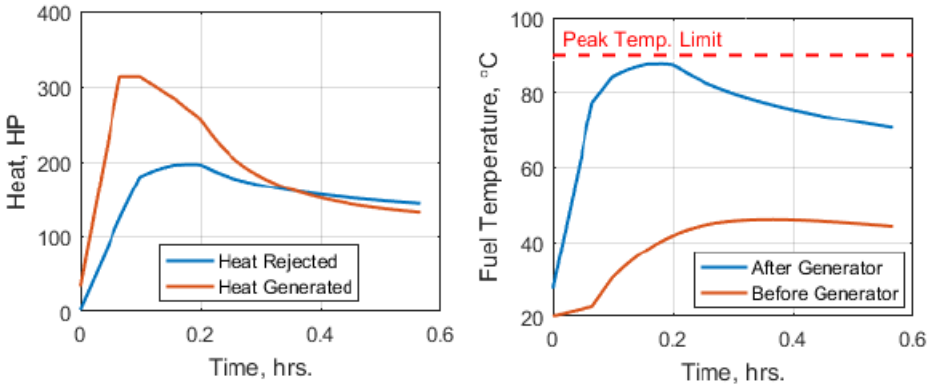

Figure 1.7 Mission simulation of FTMS performance through takeoff and climbout [28]

SUGAR

The Raytheon Technologies Research Center (RTRC) (former United Technologies Research Center (UTRC)) carried out a series of studies developing an aircraft based on the Boeing-defined N+4 2035 Refined SUGAR. The reference aircraft for the Refined SUGAR was the Boeing 737-800. It can carry 154 passengers in a dual-class layout and has a Maximum Take-off Mass (MTOM) of 61 875 kg [43]. In a parallel-hybrid electric architecture, an electric energy source drives an electric motor, which provides part of the mechanical power required by the propulsors. The other part of the required propulsive power is provided by a gas turbine. The parallel-hybrid architecture differs from the series-hybrid architecture through its form of power coupling, which is mechanical, whereas in a series-hybrid architecture, the coupling is done electrically [42]. The investigated propulsion system used electric power to boost a Geared Turbo Fan (GTF) that was sized for Cruise (CR) conditions. [43]

The first study at RTRC considered all heat, power, and volume flows of the entire propulsion system at Hot-Day Take-Off (HDTO) conditions, which were identified as the most critical conditions for the TMS due to the highest system heat loads combined with the highest ambient temperatures. A schematic representation of the system including all volume, power, and heat flows at HDTO is shown in Figure 1.8a. [43]

High Spool (HS)-Starter Generator (SG), Gearbox (Gbx), Fan-Drive System (DS), Bearing (Brg) and Low Spool (LS)-Motor/Generator (MG) are cooled in parallel by an oil loop. The hot oil is first cooled by a Fuel-Oil Cooler (FOC), which is placed after the Fuel Pump (FP), and later by an Air-Oil Cooler (AOC), which uses engine-bypass air as coolant. Battery (Bat) and Motor Drive (MD) are cooled in series in a separate cooling loop with a Ram-Cooled Cooler (RCC) as HRS. The shown heat loads result from the shown component power loads in combination with component efficiencies that are described in [43]. The volume flows are a result of the temperature differences between the components and the heat loads. The study presented weights for the three components of the HRS, namely FOC, AOC, and RCC, for three time horizons: current, 10 years, and 20 years into the future based on the time of publication, without providing details on the modeling methodology. For the current technology assumption, the RCC with a mass of 140.16 kg had a share of 80% in the total TMS mass of

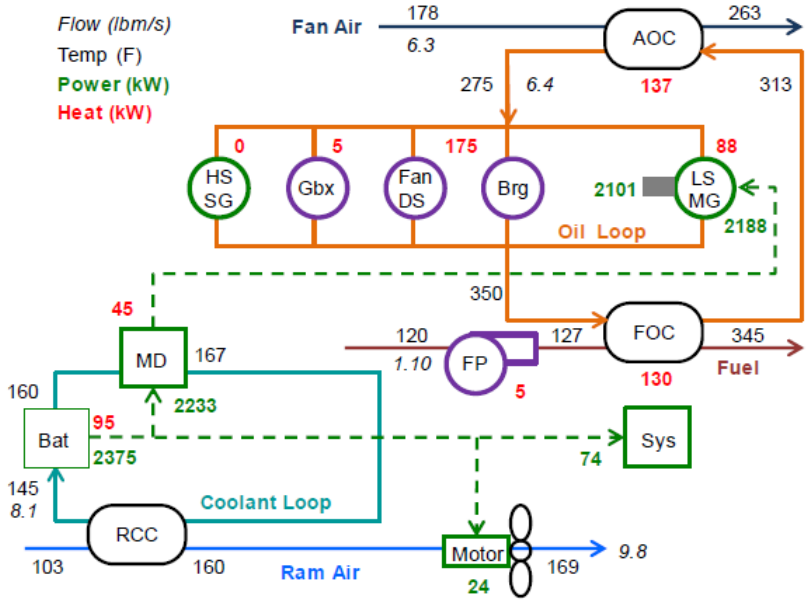

(a) Design Condition State Points for 10 year Horizon Component Efficiencies with High Temperature Fuel Capability and Electric Fuel Pump Technology and High 160°F Battery Coolant Capability [43]

AOC	Air Oil Cooler
Bat	Battery
Brg	Bearing
Fan DS	Fan Drive System
FOC	Fuel Oil Cooler
FP	Fuel Pump
Gbx	Gearbox
HS SG	High Spool Starter Generator
LS MG	Low Spool Motor/Generator
MD	Motor Drive
RCC	Ram-Cooled Cooler

(b) List of abbreviations for Figure 1.8a adapted from [43]

Figure 1.8 Thermal management system scheme at design condition adapted with a list of abbreviations from [43]

177.36 kg. The relatively low temperature difference between the battery coolant and the ambient heat sink was identified as a reason and a sensitivity study of RCC mass over battery coolant temperature was performed. The RCC mass could be lowered by 50% through an increase in battery coolant temperature from 60°C to 82.2°C. The TMS for a 20-year technology horizon had a mass close to one-fourth of the TMS of the current technology assumption. The study identified high-temperature fuels and electric fuel pumps as additional technologies to further decrease the TMS mass. [43]

In a later study, the TMS of the propulsion system was reevaluated in a different simulation environment called "REHEATS" at RTRC [44]. The TMS architecture kept the basic concept shown in Figure 1.8a with an oil circuit for the high-temperature heat sources and a 50% water-glycole mixture circuit for the Bat and MD. The entire mission including all power and thus heat loads for the propulsion system was predefined. TMS performance was evaluated at seven operating points all in International Standard Atmosphere (ISA)+15 conditions (Sea Level Static (SLS), TO, TO-climb, initial-climb, mid-climb, ToC, and CR) while others such as descent and taxi were neglected. The overall mission fuel consumption was the target function of the optimization and several constraints regarding fuel, oil, and coolant temperature as well as oil flow rates were imposed. Detailed results including the TMS component masses, inlet and outlet temperatures as well as mass flow rates and pressures are presented. All components were sized at the operating point at which their largest heat transfer duty was required. TO was the most critical point for the RCC and FOC whereas the AOC was sized in SLS. Similar to the previous study ([43]), the RCC has the largest mass of all TMS components with 162.3 kg. At low altitudes and low velocities, more power for the ram-air fan was required to provide the necessary cooling air mass flow to the RCC. Overall it was estimated that the TMS added an additional 3.4% of total mission fuel burn compared to an aircraft that neglects TMS design. With a projected mission fuel burn decrease between 4% and 7% for the parallel-hybrid aircraft without TMS compared to the baseline aircraft, the expected benefit after regarding the TMS shrunk to a value between 0.6% and 3.6%. [44]

In a further update of the study, an effort was made to reduce the RCC weight [45]. Two major modifications were implemented to improve the TMS. First, the MD and Bat were placed on separate cooling loops, and second, it was assumed that the thermal capacity of the battery mass was sufficient to absorb all heat generated by it until the aircraft reached its mid-climb altitude of 6 096 m. Figure 1.9 shows the updated system as well as the temperatures, pressures, mass-flows, powers, and efficiencies at the various stations. The Bat-RCC is placed before the MD-RCC on the same ram-air-flow since the Bat has the lower operating temperature. The

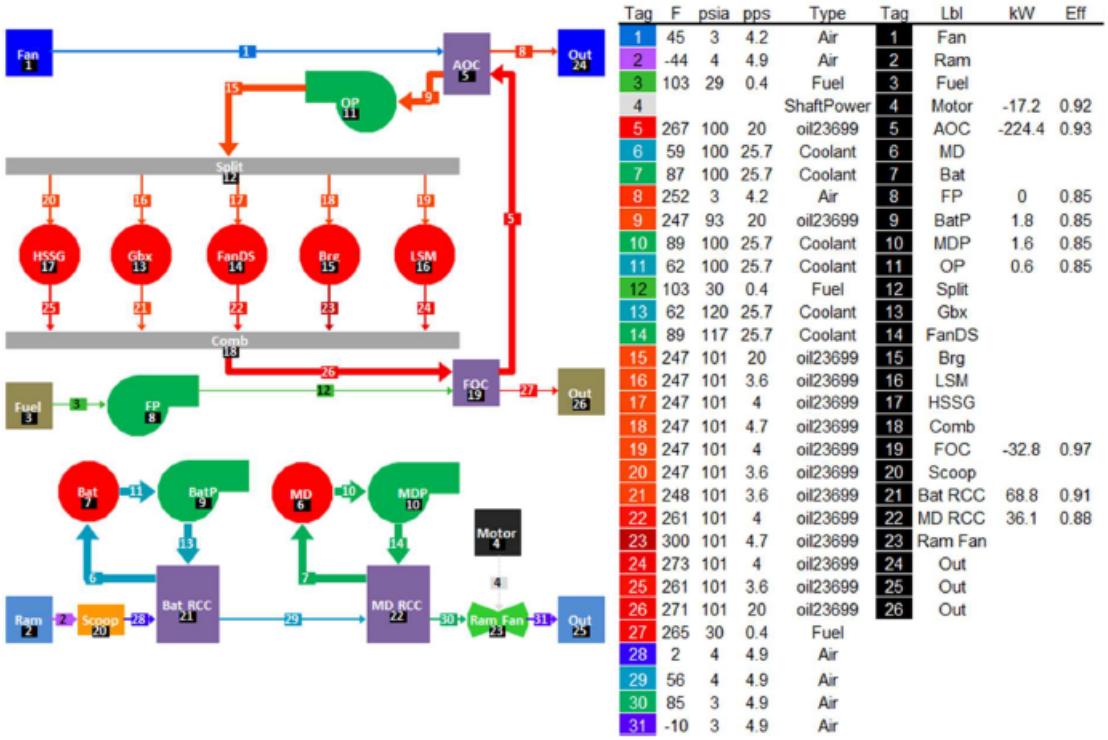

Tag	F	psia	pps	Type	Tag	Lbl	kW	Eff
1	45	3	4.2	Air	1	Fan		
2	-44	4	4.9	Air	2	Ram		
3	103	29	0.4	Fuel	3	Fuel		
4				ShaftPower	4	Motor	-17.2	0.92
5	267	100	20	oil23699	5	AOC	-224.4	0.93
6	59	100	25.7	Coolant	6	MD		
7	87	100	25.7	Coolant	7	Bat		
8	252	3	4.2	Air	8	FP	0	0.85
9	247	93	20	oil23699	9	BatP	1.8	0.85
10	89	100	25.7	Coolant	10	MDP	1.6	0.85
11	62	100	25.7	Coolant	11	OP	0.6	0.85
12	103	30	0.4	Fuel	12	Split		
13	62	120	25.7	Coolant	13	Gbx		
14	89	117	25.7	Coolant	14	FanDS		
15	247	101	20	oil23699	15	Brg		
16	247	101	3.6	oil23699	16	LSM		
17	247	101	4	oil23699	17	HSSG		
18	247	101	4.7	oil23699	18	Comb		
19	247	101	4	oil23699	19	FOC	-32.8	0.97
20	247	101	3.6	oil23699	20	Scoop		
21	248	101	3.6	oil23699	21	Bat RCC	68.8	0.91
22	261	101	4	oil23699	22	MD RCC	36.1	0.88
23	300	101	4.7	oil23699	23	Ram Fan		
24	273	101	4	oil23699	24	Out		
25	261	101	3.6	oil23699	25	Out		
26	271	101	20	oil23699	26	Out		
27	265	30	0.4	Fuel				
28	2	4	4.9	Air				
29	56	4	4.9	Air				
30	85	3	4.9	Air				
31	-10	3	4.9	Air				

Figure 1.9 TMS at End Climb (37,000 ft) [45]

Bat-RCC is sized for mid-climb conditions and shut off prior to reaching the mid-climb altitude. A simple analysis assuming a bulk heat capacity for the battery pack and the integrated HAS showed that a battery pack with a specific energy of 500 W h kg^{-1} would experience a 14 °C temperature rise from the start of the mission until mid-climb. Assuming a maximum battery temperature of 40 °C the pack would have to be pre-cooled to 26 °C before the start of the mission. The updated study also included several small modifications to the mission definition as well as technology assumptions and optimization constraints. Overall, the TMS mass was reduced to 97.1 kg, which is roughly one-third of the baseline value in [44]. The main contribution to this reduction came from the total RCC mass, which decreased to 30.8 kg corresponding to about one-fifth of the baseline mass. The additional mission fuel burn caused by the TMS was reduced to 0.74%. Another observation was the share of the parasitic effects in the total fuel burn penalty: 37% were due to fan-drag by the AOC, 36% were caused by the ram-drag from the RCCs, 26% stemmed from the TMS-mass and 2% could be attributed to the additional shaft power for the pumps and the cooling-fan-motor. [45]

In [46], the Bat-HAS was modeled in detail resulting in a 3D thermal model. A transient analysis of the Bat temperature over the entire mission was performed on a hot day with 40°C ambient temperature. The Bat was able to absorb the heat generated during Taxi (TX) and TO up to an altitude of 6 096 m while not exceeding 40°C cell temperature. The initial cell temperature had been set to 26°C, which would require some form of pre-cooling on a hot day. [46]

The most recent addition to the TMS studies performed at RTRC [47] are sensitivity studies regarding the impact of hybridization on AOC and FOC size and electric component efficiencies as well as the design altitude for the RCCs on RCC size. The previous studies had always assumed an electrified propulsion system as a baseline. This study quantified the effect of electrification on the AOC and FOC by calculating a non-electrified propulsion system with a conventional GTF as reference. The addition of the LSMG caused a 32% increase in mass for the AOC due to increased oil heat loads and a 10.5% decrease in FOC mass due to a decreased maximum fuel flow and thus maximum heat capacity of the fuel. Increasing the assumed Bat efficiency from 0.95 to 0.96 lead to a reduction in Bat-RCC mass of 26%. Similarly increasing the assumed MD efficiency from 0.96 to 0.98 resulted in a MD-RCC mass reduction of 38%. The Bat efficiency increase corresponds to a reduction of the Bat heat load of 20%. The corresponding mass change of the Bat-RCC of 26% indicates a

correlation between HEX mass and battery heat load stronger than linear. Contrarily, the MD-RCC showed a 38% mass decrease for a 50% heat load reduction and thus a less than linear correlation. The paper does not explain this contrary trend nor do the published modeling methods allow a deduction. [47]

Additionally, the effect of changing the design altitude for the Bat-RCC was studied. Increasing it from 2 438.4 m to 6 096 m resulted in a 49.5% reduction in Bat-RCC mass due to the lower ambient temperature and a 47.7% reduction in fan mass due to the lower required air mass flow. It was suggested that the battery's thermal capacity is used to absorb the heat prior to reaching the design altitude. An approximation of the adiabatic temperature increase for batteries with different specific energies was conducted for both design altitudes. The results ranged from a temperature increase of 2°C for a battery with low specific energy ($125\,\mathrm{W\,h\,kg^{-1}}$) at 2 438.4 m to 20.9°C for a battery with high specific energy ($750\,\mathrm{W\,h\,kg^{-1}}$) at 6 096 m. Installing a chiller for both, cooling the battery during charging as well as pre-cooling the battery prior to TO was offered as a solution. [47]

GT-HEAT

The Georgia Tech Hybrid Electric Analysis Tool (GT-HEAT) was developed at Georgia Tech University and is a toolset with extensions of the Numerical Propulsion System Simulation (NPSS) propulsion modeling core. It was initially developed for fast assessment of (H)EP-aircraft and is constantly extended. Its generally modular approach allows separation into three main sections: mission assembly, vehicle analysis, and engine assembly. Both, vehicle analysis and engine assembly allow the assessment of the thermal state of any thermal system, e.g., the fuel's temperature. [48]

Among other studies, GT-HEAT was used to assess the performance of an aircraft with a parallel-hybrid propulsion system. In [49], parametric trade studies were conducted to understand the interaction of aircraft, gas turbines, and the electric system. The number of passengers, and thus the aircraft size, varied considerably between 50 and 210. In [50], a truss-braced wing aircraft carrying 150 passengers with a parallel-hybrid propulsion system is sized and optimized. Both studies [49, 50] present overall aircraft level results with little detail on the specific TMS results, e.g., 13.6 kg TMS-HEX mass in [50].

The details and assumptions of the TMS modeling procedure are described in [51]. Four major components required cooling: the battery, the inverter, the motor, and the gearbox connecting the motor with the low-pressure spool of the gas turbine. The inverter, motor, and gearbox were liquid-cooled on separate cooling loops. Oil was used as the coolant for the motor and the gearbox due to the high assumed maximum temperatures of 176°C. For the inverter, the lower maximum temperature of 80°C resulted in the choice of a water-glycol mixture as the coolant. Each coolant loop had a dedicated HEX with air on the cold side. The cold-side air flow was controlled to keep a constant hot-side outlet temperature. For the battery, direct air cooling was assumed. The battery was placed in a ram-air duct with a variable outlet nozzle to control the air mass flow. [51]

In a more recent study [52], a 78-passenger regional aircraft with a serial-hybrid propulsion system was investigated with GT-HEAT. The concept had two energy supplies: gas turbines placed at the wing tips driving generators and a large battery placed under the cabin inside the pressurized fuselage. Eight pods with electrically driven fans were distributed along the wing span. The TMS was split into two major parts as shown in Figure 1.10. Each electric motor and the corresponding inverter were cooled via a Polyalphaolefin (PAO) loop with an AOC utilizing fan air as the heat sink. The AOC was designed using the well-known effectiveness (ϵ)-Number of Transfer Units (NTU) method and it had a one-pass tube and fin configuration. The power electronics with the lowest assumed maximum temperature were placed before the electric motor on the cooling loop. The battery was cooled with the existing ECS and it was found that the battery could be kept below the target temperature of 45°C if the ECS operated at maximum power throughout the entire mission. The additional engine bleed-air and ram air resulted in a block fuel burn increase of 1.4%. Also, the battery was assumed to have a temperature of 24°C at the beginning of the mission. [52]

The TMS of the above concept was further investigated with regards to critical peak heat loads in the motor-inverter cooling loop [53, 54]. The sizing methodology of the HEX allowed the variation of the relative pressure drop (δp) on the cold side [55] up to a constraint value [54]. Also, the study imposed a limit to the fraction of the air mass flow inside the pod that could be used for cooling. The initially selected δp of 1% combined with a bleed limit of 5% lead to a HEX-design capable of providing enough cooling throughout the majority

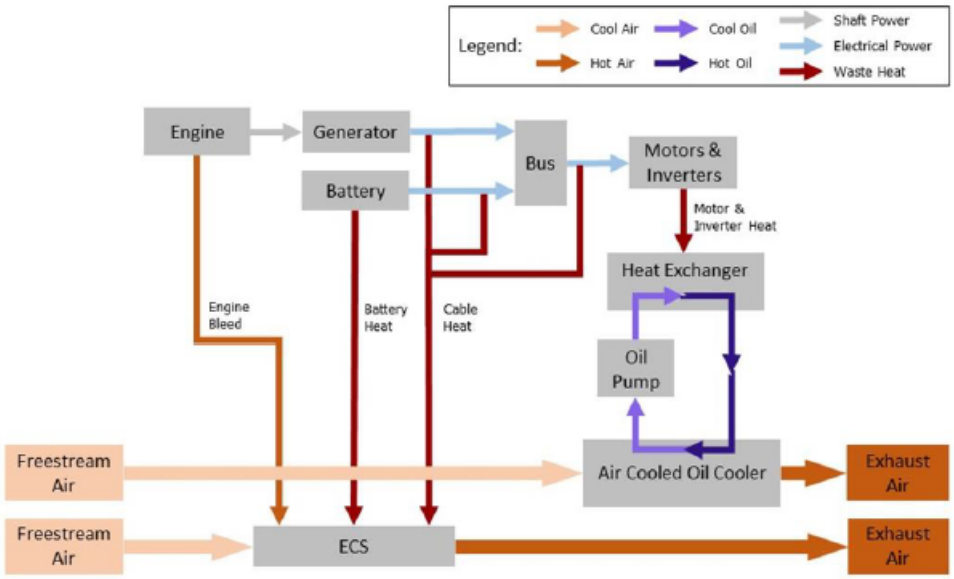

Figure 1.10 Architecture of the overall TMS [53]

of the mission, however, there was a gap between the generated waste heat and the heat removal capability in early mission segments such as TO and climb. Sensitivity studies for δp and the bleed air fraction were carried out. Increasing δp to 4% increased the heat removal capability in the critical early flight stages. The improvement rate degraded with increasing δp and an increased δp has a fuel burn penalty. Varying the bleed air limit showed that there was an optimum near 5% since while increasing the bleed limit increases the heat capacity on the cold side, the HEX performance degrades [54]. Therefore, two other measures to cope with the peak heat loads were studied: using additional PAO to store heat in a reservoir and using Phase Change Materials (PCMs) to temporarily absorb the peak heat loads. Two different PCMs were investigated. The base TMS increased the MTOM by 1.64%. The additional PAO to absorb peak heat loads added another 7.53% while the two different PCM solutions only contributed another 2.42% or 2.12% respectively. Depending on the flown range, the overall fuel burn penalty of the PAO-based solution was between 6.5% and 9.0% while the best PCM-based solution ranged between 2.8% and 3.8% [54]. Despite these results, the additional PAO solution was selected in the most recent update of the overall concept [53]. [53, 54]

NASA SCEPTOR (X-57)

NASA is one of the most active research facilities in the field of (H)EP. The Scalable Convergent Electric Propulsion Technology and Operations Research (SCEPTOR) aircraft is a 9-passenger, all-electric demonstrator, which uses Distributed Electric Propulsion (DEP) and thus has multiple electric motors with propellers distributed along the wingspan. [56]

Early TMS assessments included the assumption of a fixed specific heat rejection of $0.68\,\mathrm{kW\,kg^{-1}}$. Additionally, a small sensitivity study was conducted relating the specific heat rejection among other parameters to the overall propulsion system weight. [57]

Further studies on the cooling of the SCEPTOR were conducted. In [58], the cooling of the electric motors for the SCEPTOR aircraft was investigated. The TMS for the permanent magnet electric motors was a direct air cooling system. In the first step, different inlet configurations were analyzed including nose inlets, annular inlets, and in some configurations small compressors to increase the air mass flow rate during ground operations. Another study using Computational Fluid Dynamics (CFD) assessed the heat transfer increase on a surface in wake of a propeller through the added turbulence of the propeller downwash. It resulted in an average heat transfer coefficient of $185\,\mathrm{W\,m^{-2}\,K^{-1}}$ for a heated surface fraction of the nacelle compared to the $136\,\mathrm{W\,m^{-2}\,K^{-1}}$ resulting from turbulent flat-plate empirical correlations for the same area. [58]

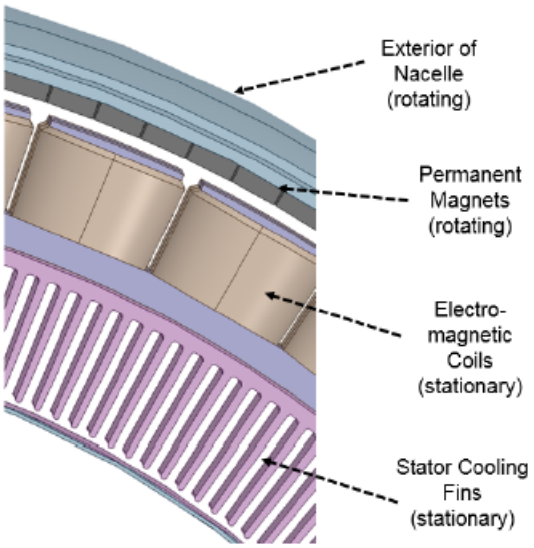

Figure 1.11 Out-runner motor [58]

In [59], different motor configurations including in-runners, out-runners and double-runners were studied with regard to the expected cooling drag among other properties. For all three concepts, a cooling architecture is presented including technical measures such as additional cooling fins attached to the motor. The cooling system was sized for Climb (CL) conditions, due to the high ambient temperatures and the large heat losses of the motor, however, the CR drag was constrained to 2%. Full CFD studies were performed to assess the cooling drag of all motor concepts, which played a major role in selecting the first motor candidate. The final concept was able to keep the motor temperature below 120°C during CL with outside temperatures up to 60°C. [59]

A lumped parameter model to quickly assess the motor cooling system was also developed [58] and validated against the CFD results from [59]. The simplified heat transfer model was used to quickly assess different measures to improve the motor cooling system. A sketch of a part of the motor including the main cooling sources is shown in Figure 1.11. The main heat sinks are the additional stator cooling fins, the annular gap between the coils and the permanent magnets, and the tangential gap between the coils and the exterior of the nacelle. It was concluded that increasing the cooling area was the most effective measure to increase motor cooling. [58]

Following these studies, a different approach was considered to further minimize the negative effects of the motor cooling systems. An aircraft trajectory optimization was conducted with thermal constraints on the motor temperature [60]. The results are displayed in Figure 1.12. A maximum range trajectory was optimized for the current motor design (black line) and a motor with a HEX area reduced by 30% (dashed red line). The reduction of the HEX-area does not result in a significant reduction of the maximum range (<0.5%), however, the maximum motor power and, as a direct result, the maximum rate of climb during the majority of the climb is reduced. The study also included a minimum time trajectory and a maximum efficiency trajectory. [60]

For any heat source without an active cooling system on the SCEPTOR, transient models were used to track the temperature throughout the mission, in particular the battery, wires, high lift motors as well as the outer wing surface. Most models were simple lumped parameter models, which were validated with experimental data. Interestingly, it was shown that the motor nacelles, as well as the wing surfaces, could be accurately modeled by flat-plate approximations. [61]

Since the NASA Maxwell X-57 is a demonstrator aircraft, a lot of research went beyond the conceptual level to actual component development. A motor controller was developed and the motor nacelle served as a sufficient heat sink. [62]

While the previous studies were concerned with the main motors mounted to the wingtips of the X-57, the smaller motors for the distributed high-lift propellers also need adequate cooling. In [63], the nacelles of the high-lift propellers were aerodynamically optimized. The optimization considered sufficient heat transfer as a constraint. For the assumed motor efficiency of 96.6% no deviation from the baseline shape was present due to

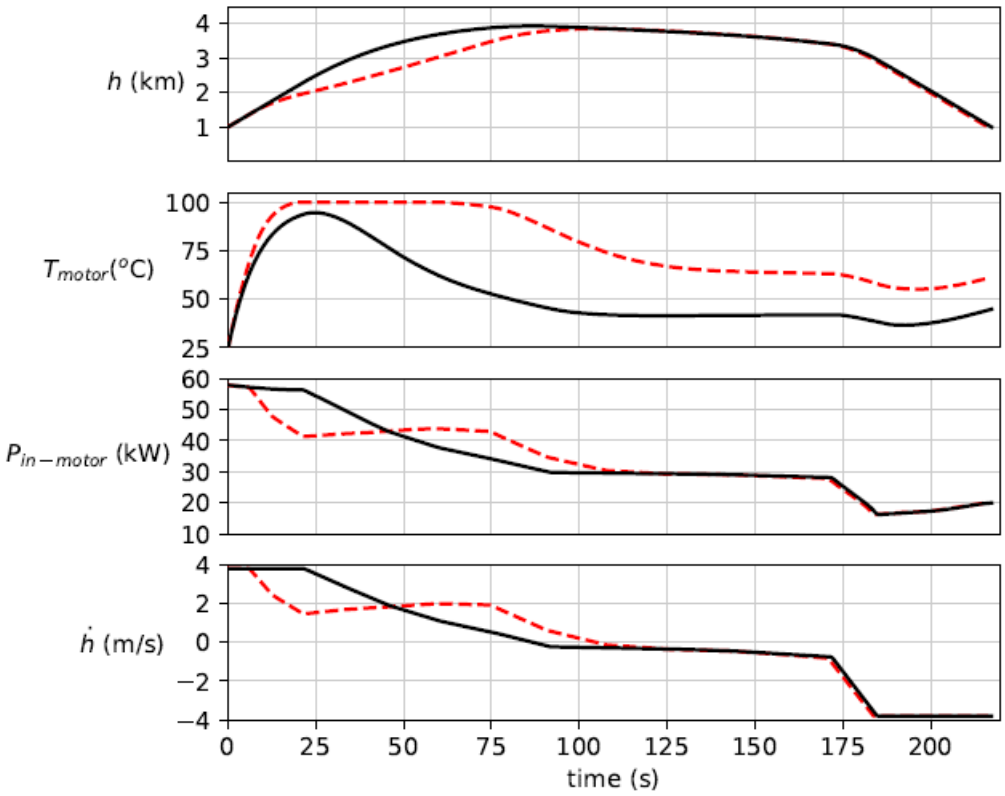

Figure 1.12 Reducing the motor heat exchanger area by 30% has little impact on the maximum range. The trajectory addresses the motor temperature limit by reducing rate of climb ($\dot{h}$) [The black line represents the current motor design and the red dashed line represents a motor with 30% reduced motor heat exchanger area; authors note] [60]

the thermal constraint. However, when increasing the motor heat load corresponding to an efficiency of 96.0%, the nacelle thickened to increase heat transfer area. [63]

Another study showed that the X-57 wingtip motors could also be cooled by the propeller wake on the outer mold line of the nacelles. This solution omits the need for a dedicated TMS for the electric machines, however, whether it is the best solution on the overall aircraft level depends on the application case. [64]

Other NASA concepts

Recently, dedicated activities towards the design of TMS for various (H)EP aircraft concepts were performed [65, 66]. First, a TMS was developed for a 15-passenger tilt-wing Vertical Take-Off and Landing (VTOL) aircraft with a turbo-electric propulsion system [65]. The TMS consisted of a R-HEX placed in front of a fan inside a duct. The study considered all parasitic effects namely mass, drag, and power to optimize the TMS towards an objective function of the aircraft. The ϵ-NTU method was used for the HEX performance modeling, i.e., heat transfer and pressure drop calculations, and simple geometric models were employed to estimate the HEX-mass. The overall HEX design was a single-pass cross-flow configuration. The air inlet and all coolant lines were simply assumed to have a constant pressure loss of 1% and their mass was neglected. An empirical mass calculation based on manufacturer data sheets was used to estimate the mass of the fan. Isentropic relations were used to model the fan performance and the nozzle was assumed as ideal throat. The OpenMDAO framework was used to perform numerical calculations such as optimization of the TMS. [65]

In a first study, the TMS was designed at steady-state conditions with varying input parameters and the sensitivities of some important HEX parameters, e.g., NTU and ϵ, towards the hot- and cold side mass flows and temperatures were shown. The study contains additional interesting sensitivities, e.g., the replacement of some parts of the higher fidelity calculations of the HEX with simpler performance maps, a correction factor to avoid iterative pressure loss calculations, and the use of different hot side fluids. Next, a transient analysis of the system was performed by adding lump masses to the heat sources and a coolant reservoir. Both masses

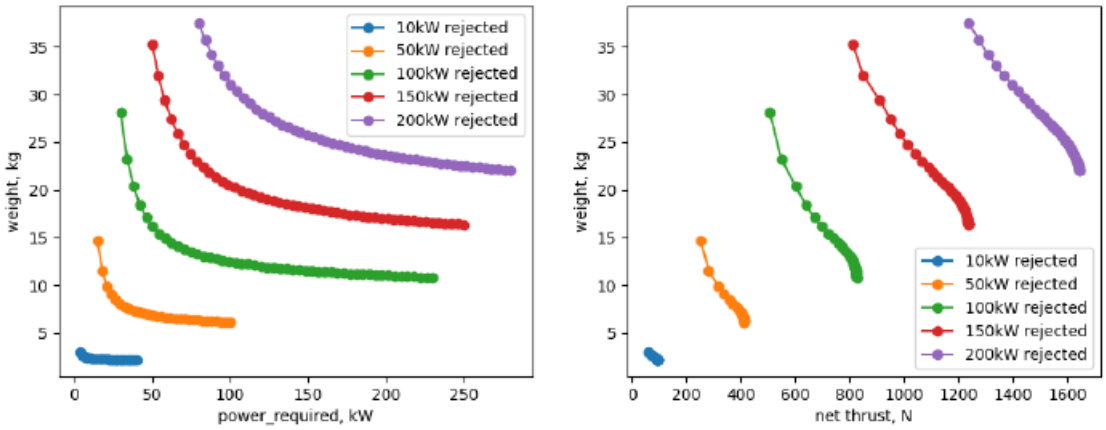

Figure 1.13 Pareto fronts of heat exchanger system optimized to different power rejection levels for weight and required power for rectifier cooling (sea level static) [65]

were varied and the step response of the system towards a 7 000 s long 50 kW heat flow followed by a 7 000 s long 25 kW heat flow was tested. The results showed increasing thermal inertia of the system with increasing masses. To gain further understanding of the TMS, the system was optimized towards a mixed target function of mass and required power. Drag was neglected because it was assumed that a fan was required to pull air through the heat exchanger and therefore the thrust would be directly linked to the required power. A set of Pareto fronts resulted from the different weighting of the target function and the variation of some input parameters, e.g., heat load and air input temperature as shown in Figure 1.13. The L-shaped fronts indicate a linear dependency of the TMS parasitic effects on the input heat load. In the last step, a discrete optimization target function from the tilt-wing aircraft was used to specifically design an optimized TMS for the application case. [65]

The work was expanded to two additional aircraft configurations [66], namely the Single-Aisle Turboelectric Aircraft with an Aft Boundary Layer propulsor (STARC-ABL) [25] and the PEGASUS concept [67]. The former is a 154-passenger aircraft with an electrically driven tail cone thruster and the latter is an all-electric 48-passenger regional aircraft [66]. For the STARC-ABL, a previous study simply assumed a specific heat rejection of 0.68 $\mathrm{kW\,kg^{-1}}$ [57]. First, a sensitivity analysis of the TMS mass, thrust, required power, and air mass flow was carried out over various heat loads and hot-side temperatures in HDTO conditions. The TMS was optimized towards a set target function that considered all parasitic effects. The sensitivity quantified the TMS improvement with increasing hot-side temperature and decreasing heat load. Next, the effect of varying the TMS design point was considered. Representative altitudes and Mach numbers for TO, CL, and CR were set in combination with a fixed heat load and hot-side temperature. Also, the impact of varying the weighting of the different parasitic effects in the optimization target function was investigated. In the second part of the study, a TMS was designed for each of the three different aircraft configurations. Fuel-burn sensitivity functions concerning the three parasitic effects served as target functions for the optimization. The detailed results are well described and visualized in [66]. An interesting final assessment compared the results of all three configurations for all three parasitic effects. The results for the TMS mass are displayed in Figure 1.14. The lines result from scaling the converter + motor cooling loop of each configuration to different heat loads. The baseline values (solid lines) consider state-of-the-art electric equipment, whereas the advanced values (dashed lines) use projected future electric component technologies. The assumptions for future electric component technologies include higher maximum temperatures, which result in the requirement of a different coolant compared to the baseline technology. Therefore, the TMSs of the future electric components have a higher specific mass, i.e., their lines are above their baseline counterparts. However, the individual markers show the actual masses of the different components of the TMS. The resulting actual TMSs of the advanced configurations are still lighter than their baseline counterparts due to the reduced heat loads of the electric components, i.e., they are positioned further to the left in Figure 1.14. Another observation is the large offset between some discrete TMS designs and the corresponding average line, e.g., baseline battery. The average lines were calculated using the

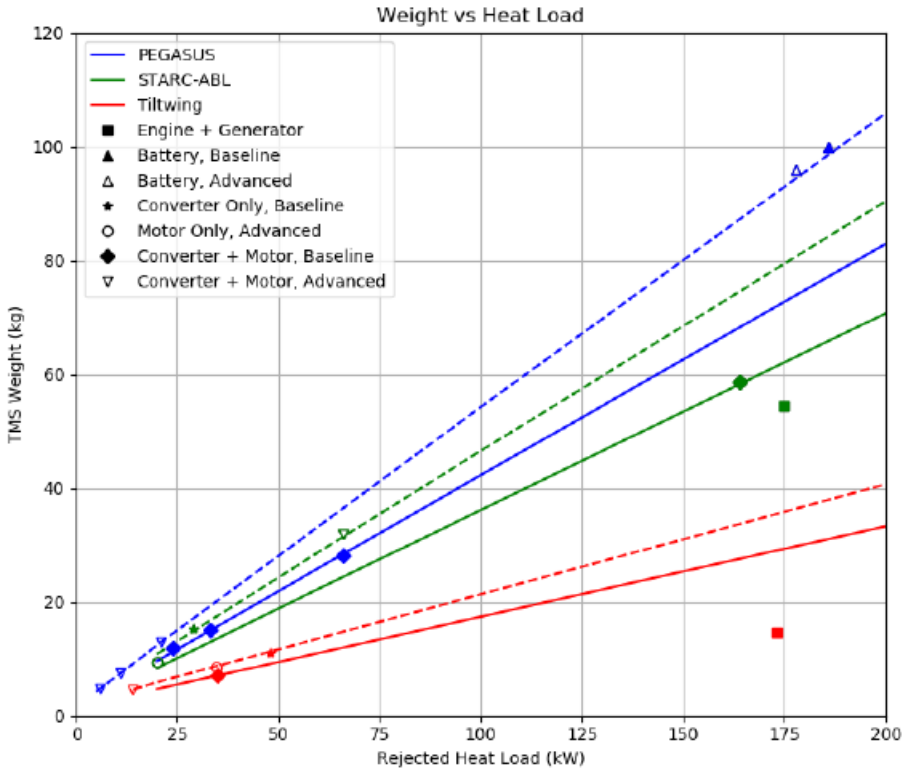

Figure 1.14 TMS loop weight values and rejected power sensitivity comparison, where markers and lines that are blue show PEGASUS, green show STARC-ABL, and red tiltwing. Additionally, solid lines denote baseline and dotted lines denote advanced electrical system technology levels [66]

design conditions of the motor + converter TMS. Since the battery has stricter temperature limits it deviates significantly from the averaged results. [66]

The results showcase the difficulty in deriving general heuristics for TMS in aircraft conceptual design.

1.3.4 Reflection on the objectives

With the current state of the art evaluated, the need for the suggested analysis in the thesis at hand is highlighted. The relevance of the TMS for any aircraft with a (partly) electrified powertrain is clear since the aircraft could not operate without an adequate cooling system. The various assessments in Section 1.3.3 showed that the impact of the TMS on the aircraft is non-negligible since it adds significant mass, drag, and required power to the overall system. The small number of sources in Section 1.3.3 with an even smaller number of authors or research groups behind them, indicates the possibility of a research gap. It confirms the initial assumption drawn from Figure 1.1.

The studies described in Section 1.3.3 mostly follow the same pattern: An idea for an electrified aircraft exists at first and later a TMS is designed for the already specified concept. This concept-specific view leads to detailed solutions that fit one application case. Some of the studies already performed various optimizations, which could eventually lead to general trends in aircraft-TMS design. However, most studies lack an open design space for the TMS at the start. Often, the heat sink is already pre-set as an R-HEX, and even in studies with a more in-depth heat sink analysis (e.g. [29]), the heat sink has few degrees of freedom. In the particular example, the internal HEX surface was pre-defined [29].

The proposed objectives of this thesis aim to change the point of view by moving the TMS to the center of the analysis. Especially with objectives two and three, the design space for a TMS is opened. Rather than starting the analysis with a pre-set heat sink, different heat sinks will be evaluated and compared. For a specific heat sink, e.g., an R-HEX, a broad variety of parameters will be subject to sensitivity analyses to identify the most relevant optimization parameters. The expected findings will enable any future researcher to start the TMS design

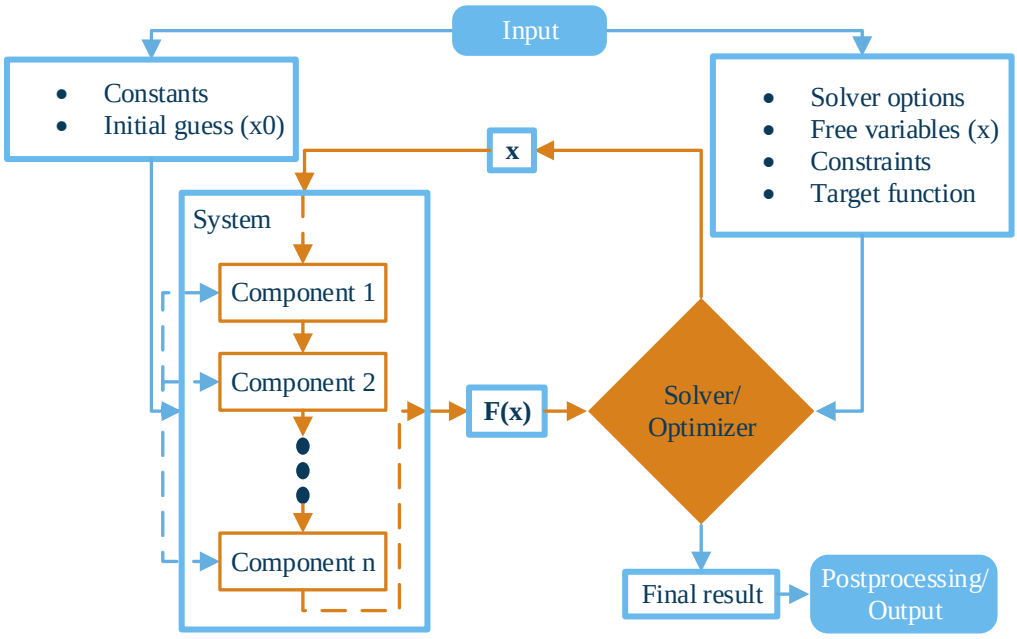

Figure 1.15 Concept scheme of the TMS modeling framework

and optimization process for their specific application case more efficiently. The design and optimization of a TMS always depend on the application case. Therefore, besides the general sensitivity analysis, the developed methods will be applied to design and optimize TMSs for different application cases.

1.4 Methodology

Each of the papers of this thesis already contains a methods or methodology section presenting the most important methods required for the individual content. To avoid duplication, this section focuses on the overall modeling framework and on updates performed after the publications.

1.4.1 Thermal management system modeling framework

All publications of this thesis used the same TMS-Modeling Framework (MF), which was developed specifically for that purpose. The working principle of the python-based TMS-MF is sketched in Figure 1.15. The physical models described hereafter and in the publications are sorted in components, e.g., a compact HEX or a component as simple as a pipe. These components are arranged in systems, which have a serial order of execution. After the completion of a component's calculation, its fluid properties are passed on to one or multiple subsequent components. Each component also needs a set of input variables apart from the input fluid properties that have to be defined prior to the calculations. There are three general calculation forms available:

1. Execution: This simplest form of calculation does not require any additional numerical methods. The orange loop in Figure 1.15 is not active here, and each component is calculated exactly once. This mode was used primarily in [2, 3].

2. Solving: In this mode, the numeric root finding algorithm "scipy.optimize.root" of the "SciPy" package with algorithms from [68] was used to find the roots of a system of non-linear equations. To define said equation system, the input has to contain equal numbers of free variables and target functions. This mode uses an iterative procedure to match the system output with the target functions to a pre-defined precision.

3. Optimization: This mode is similar to the solving one, but rather than root finding methods, minimization methods are employed from "scipy.optimize.minimize" with algorithms from [69]. Only one target function is possible, but the number of free variables is unlimited. Additional constraints and bounds can be enforced. Again, an iterative procedure is used to minimize the target function while respecting the constraints and bounds.

The chosen setup of an arbitrary definition of free variables and target functions has the advantage of allowing flexibility in the choice of pre-defined (input) parameters versus the calculated output parameters. On the other hand, each change of free variables or target functions entails a change in the system of non-linear equations. Therefore, it is difficult to choose a suitable numeric algorithm for all combinations of free variables and target functions as the underlying system of equations is prone to changes.

1.4.2 Enhancements of component models

The component models that were implemented in the TMS analysis framework are described in detail in the publications and should allow replication of the simulation. Some additions to the models were implemented after the publication of the papers, but are used in the final discussion (cf. Section 3) of this thesis. These enhancements are described hereafter.

Propeller slipstream model

In [2] and [3], the Surface Heat Exchanger (S-HEX) components were operated with the ambient airflow resulting from the flight speed alone. However, for open-rotor configurations or on the interior surface of nacelles, forced air flow with speeds exceeding the flight speed may be present. To account for this effect, a simple propeller slipstream model is implemented. It is based on [70].
P_{shaft} is calculated from free-stream velocity $(u)_\infty$, thrust (F_N) and propeller efficiency $(\eta)_{\text{prop}}$:

$$P_{\text{shaft}} = F_N \, u_\infty / \eta_{\text{prop}} \tag{1.1}$$

For a moving propeller, i.e., $u_\infty \neq 0$ the slip stream velocity is calculated via the propeller disc area $(A)_{\text{prop}}$ and the free-stream density $(\rho)_\infty$:

$$u_{\text{slip}} = \sqrt{\frac{2 \, \eta_{\text{prop}} P_{\text{shaft}}}{u_\infty \, A_{\text{prop}} \, \rho_\infty} + u_\infty^2} \tag{1.2}$$

This model was added to the calculations of the external heat transfer coefficient (α) calculation for the wing-shaped S-HEXs. [70]

Pump and fan empirical mass estimation

In [1] and [4] some component masses were not yet considered. For a more complete assessment of the system's mass, additional empirical correlations are implemented to estimate the mass of the pump and the fan. They are found in [65]. The fan mass (m_{fan}) is calculated via the air mass flow rate (w_{air}) with:

$$m_{\text{fan}} = 0.4386 \, w_{\text{air}} + 0.1104 \tag{1.3}$$

and the pump mass via the pump displacement $(CIPR)$:

$$CIPR = 0.0092 \, (w \, \rho)^{1.3857} \tag{1.4}$$

$$m_{\text{pump}} = 8.5942 \, CIPR + 2.4229 \tag{1.5}$$

These equations use inputs and outputs in anglo-American units, thus the inputs and outputs were transformed into SI units. [65]

Surface heat exchanger hot side

Both publications on S-HEXs ([2, 3]) have simple hot side models. In [2] the hot side is assumed as constant surface temperature, i.e., no hot side convection model is implemented, and in [3] the hot side is assumed to be a simple rectangular duct. The investigations in [1, 4] especially showed that the variation of the hydraulic diameter (d_{H}) can have a large influence on α, i.e., a smaller d_{H} increases α and thus the overall heat transferred. The simplified rectangular duct model from [3] has a large d_{H} compared to a hot side with small channels. These small channels would require additional straight fins to be implemented internally in the flow direction, which is a constructive measure that would be required for structural stability in any case. The thermo- and fluid-dynamic models for straight rectangular fins were readily available from [1], where they are described in detail in the appendix. In Section 3.5, the Wing Integrated Fuel Heat Exchanger (WIFHE) model from [3] is used with the modified hot side calculations. Since fuel is not necessarily the coolant used for the component the more general term Wing Integrated Surface Heat Exchanger (WISH) is used in section 3.

2 Publications

2.1 Design and Optimization of Ram Air-Based Thermal Management Systems for Hybrid Electric Aircraft

The paper [1] presents methods and results for the sizing of an R-HEX for a hybrid-electric aircraft with 180 passengers. It is structured into five sections.

The first section "introduction" motivates the topic by illustrating the thermal management challenge for future aircraft with electric components in the powertrain. Unprecedented heat loads combined with low operating temperatures result in a difficult design scenario for TMSs. The current state of the art is summarized and the objective and procedure are outlined. Section 1 was conceptualized and written by Hagen Kellermann.

The second section "Models and Methods" describes all developed component models in detail including coldplates, a compact HEX, a diffuser, a fan, a nozzle, pipes, and a pump. The overall TMS scheme is also presented with the different heat sources connected thermally in parallel. The coldplate model uses analytical and semi-empirical equations to calculate heat transfer rate and pressure loss inside the channels. For off-design calculations, an analytical procedure is presented with some constraints. The off-design model is validated against existing coldplate data. The compact HEX model is developed using existing procedures from various textbooks combining analytical and semi-empirical equations. The model is capable of predicting the thermal performance of the HEX as well as the dimensions of the core matrix and the mass. The diffuser is modeled as rectangular with an expansion in one dimension. Besides the internal pressure losses, the spillage drag is also accounted for. In Section 2.5, the fuel burn sensitivity of the aircraft towards small mass and drag increments is investigated. The resulting function is later utilized as an optimization target function for the TMS design. Subsection 2.5 was conceptualized and written by Michael Lüdemann. The remainder of Section 2 was conceptualized and written by Hagen Kellermann.

The third section "System Sensitivity Analysis" analyzes the system's responses to changes in the values of the input variables. At first, one variable is varied at a time and the effect on the TMS's mass and drag is studied. In a second study, multiple variables are varied at the same time to show interdependencies in the model inputs. Lastly, the effect of the geometry of the hot and cold side channels of the HEX on the core matrix dimensions is investigated. The sensitivity analysis provides a better understanding of the physical system behavior. Section 3 was written and conceptualized by Hagen Kellermann. Markus Pohl provided the design and off-design heat loads that are displayed in Figure 6.

The fourth section "Design and Off-Design Optimization for the Application Case" presents the optimization of the R-HEX-TMS for the given application case. The first part of the study considers only the TMS design point at different power splits, and thus heat loads, and hot side temperatures. Overall mass and drag of the TMS are calculated and converted to fuel burn via the aircraft sensitivity function. In the second part, the off-design performance is assessed for one of the TMS from the design space. Power and drag are calculated in TO for different ambient temperatures and different hot side temperature increases. In a third study, the previous studies are combined and the off-design performance is used as a constraint for the design point. The fan power is varied and for low fan pressure ratios, oversizing of the TMS in its design point is required to provide sufficient off-design cooling. Section 4 was conceptualized and written by Hagen Kellermann.

The fifth section is a combined conclusion and outlook. The main findings are summarized and a few recommendations for future work are presented. Mainly, a more in-depth analysis is recommended, e.g., answering safety and redundancy questions. Section 5 was written by Hagen Kellermann. The entire paper was reviewed by Mirko Hornung.

Author contributions in short: The author's contributions are declared at the end of the publication.

aerospace

MDPI

Article

Design and Optimization of Ram Air-Based Thermal Management Systems for Hybrid-Electric Aircraft

Hagen Kellermann [1,*], Michael Lüdemann [1], Markus Pohl [2] and Mirko Hornung [1]

[1] Bauhaus Luftfahrt e. V., Willy-Messerschmitt Straße 1, 82024 Taufkirchen, Germany
[2] Institute of Jet Propulsion and Turbomachinery, RWTH Aachen University, 52062 Aachen, Germany
* Correspondence: hagen.kellermann@bauhaus-luftfahrt.net

Abstract: Ram air-based thermal management systems (TMS) are investigated herein for the cooling of future hybrid-electric aircraft. The developed TMS model consists of all components required to estimate the impacts of mass, drag, and fuel burn on the aircraft, including the heat exchangers, coldplates, ducts, pumps, and fans. To gain a better understanding of the TMS, one- and multi-dimensional system sensitivity analyses were conducted. The observations were used to aid with the numerical optimization of a ram air-based TMS towards the minimum fuel burn of a 180-passenger short-range turboelectric aircraft with a power split of up to 30% electric power. The TMS was designed for the conditions at the top of the climb. For an aircraft with the maximum power split, the additional fuel burn caused by the TMS is 0.19%. Conditions occurring at a hot-day takeoff represent the most challenging off-design conditions for TMS. Steady-state cooling of all electric components with the designed TMS is possible during a hot-day takeoff if a small puller fan is utilized. Omitting the puller fan and instead oversizing the TMS is an alternative, but the fuel burn increase on the aircraft level grows to 0.29%.

Keywords: thermal management; hybrid-electric aircraft; ram air-based cooling; compact heat exchangers; meredith effect

Citation: Kellermann, H.; Lüdemann, M.; Pohl, M.; Hornung, M. Design and Optimization of Ram Air-Based Thermal Management Systems for Hybrid-Electric Aircraft. *Aerospace* **2020**, *8*, 3. https://doi.org/10.3390/aerospace8010003

Received: 27 November 2020
Accepted: 15 December 2020
Published: 23 December 2020

1. Introduction

The introduction of (hybrid-)electric powertrains to future aircraft is one of the innovations that could help to achieve the ambitious target of a 75% reduction in CO_2 emissions by the year 2050 set by the European Commission's Strategic Research and Innovation Agenda (SRIA) [1]. Thermal management is one of the key challenges for the successful realization of such powertrains [2].

Thermal management systems (TMS) were already part of early motorized aircraft, especially for the cooling of piston engines. When the engine power density increased, air cooling became insufficient and additional radiators were installed to reject heat from the oil system to ambiance. The Mustang P-51D and Messerschmitt Bf 109 are examples of aircraft which had these radiators installed inside a duct with a diffuser and a nozzle to reduce cooling air drag utilizing the so-called Meridith effect [3]. This principal architecture of a ram air-based cooling system is still present in modern aircraft systems, e.g., in the environmental control system [4].

With the introduction of gas turbines, and for turbofan engines especially, engine thermal management became a less critical issue for commercial aircraft because of the large, steady airflow that carries most of the engine's waste heat to ambiance. However, the continuous increase in turbine entry temperature, and the introduction and further development of new technologies—for example, a gearbox for geared turbofan (GTF) engines—have led to increasing heat loads in modern aircraft engines. A summary of the development of engine waste heat and corresponding TMS developments can be found in [5].

Over the last two decades, research in (hybrid-)electric powertrains as an alternative to gas turbines has significantly increased. One of the key challenges for both realizing a theoretical benefit on the aircraft level and successfully implementing first demonstrations, is the thermal management of up to multi-megawatt electric powertrains [6,7]. Besides the high efficiency of electric components compared to gas turbines, they have no natural large heat rejection system such as the engine exhaust, so only small amounts of heat can be dissipated naturally via conduction through the structure. Therefore, the TMS has to manage their entire heat load. Additionally, electric components typically have low operating temperatures compared to combustion engines, which result in only small available temperature differences from ambient conditions for the TMS.

In recent research on hybrid-electric aircraft (HEA), the TMS is addressed more frequently and with increasing levels of detail. For the NASA STARC-ABL concept, a specific power of 0.68 kW/kg of the TMS was assumed [8]. A hybrid version of the NASA N+4 "Refined Sugar" research platform was designed with a dynamic model of a TMS for both the electric system and the engine oil system. The system was designed for conditions during a hot-day takeoff (HDTO), which together with a low allowable battery temperature resulted in a ram air cooler of about 150 kg. However, a 50% mass reduction was shown for an increase in battery temperature of 20 °F [9]. Further analysis of the concept, including various off-design points, showed an increase in design mission fuel burn (FB) of 3.4% due to TMS mass, power, and drag [10]. With additional optimization, such as decoupling the battery cooling loop, the additional fuel burn was reduced to 0.75% [11]. In [12] a ram air-based TMS was designed for a vertical takeoff and landing (VTOL) vehicle with both steady-state and transient methods. Sensitivities of key parameters of the developed compact heat exchanger (HEX) model were shown, as were Pareto fronts for a system optimization towards minimum system mass and power required by a puller fan. The final TMS of the VTOL had a mass of 171.63 kg and required 257.6 kW of power.

For HEA, the potential of using existing aircraft surfaces as alternative heat sinks was investigated, resulting in an indication that smaller aircraft can reject large parts of their heat load via the skin [13]. In a more detailed investigation, a TMS utilizing recirculating fuel underneath the wing surfaces for cooling of a 180-passenger short-range HEA was designed [14]. Despite the promising results, these surface cooling concepts have major disadvantages, such as the low available cooling power at low flight velocities and the low amount of coolant in case of fuel cooling towards the end of the mission. Therefore, a ram air-based TMS was considered for this study.

The research on ram air-based TMS has already developed some sensitivities and optimization for the compact HEX rather than solely solving the thermal management issue of one specific HEA. In this study, an even broader approach was chosen. The objective was threefold: Firstly, a static model of all necessary components for a ram air-based TMS was developed. Secondly, the overall system sensitivities were studied rather than just those of the compact HEX. Thirdly, different TMS architectures were optimized towards a weighted objective function derived from a 180-passenger short-range turboelectric aircraft. The study will further improve knowledge of ram air-based TMS and their impacts on HEA. It will thereby enable future studies on HEA to assess their performances in more detail.

2. Models and Methods

The following section describes all required component models of the ram air-based TMS. Figure 1 shows an exemplary centralized TMS architecture with all electric components being cooled in parallel. It requires the following components:

1. Coldplates to receive heat from the electric components and transfer it to the coolant.
2. A compact HEX to reject the collected heat to ambiance.
3. A diffuser to reduce cooling air speed and thereby the cold-side pressure loss of the compact HEX.
4. Optionally, a puller fan to increase cooling air flow.

5. A nozzle to recover some of the momentum of the cooling air and thereby reduce drag.
6. Pipes to transfer the coolant.
7. A pump to recover the pressure loss of the coolant.

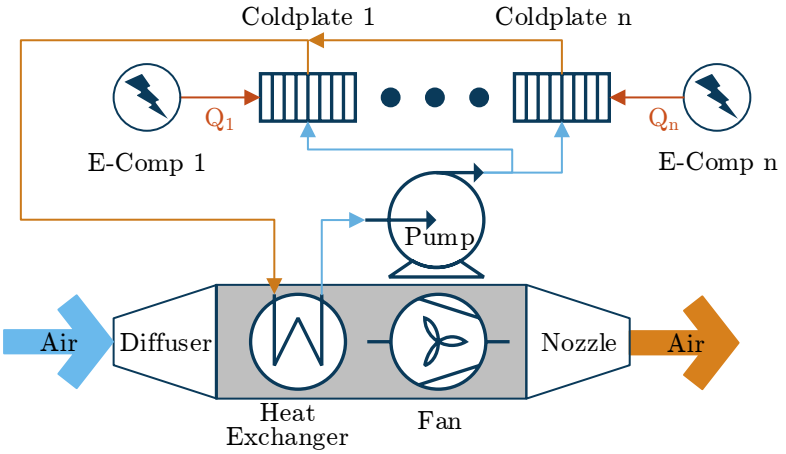

Figure 1. Centralized parallel thermal management system (TMS).

2.1. Coldplates

Coldplates are flat components with internal liquid flow to cool electronic devices, such as chips. Research trends towards lower thermal resistances (R_{th}) of future coldplates—for example, by decreasing the hydraulic diameters (d_H) of microchannels or by integrating the cooling channels closer to the working parts of the electronics [15]. Here, a simplified model of a coldplate is used not only for the cooling of the power electronics but also as a substitute for a model of the internal cooling of electrical machines. Despite the inlet properties (pressure (p), temperature (T), and heat load (Q)), the model only requires thermal insulance (r_{th}), maximum junction temperature (T_{cp}), area density (ρ_A), and design pressure loss (Δp_{des}) as inputs. These can be estimated from existing manufacturer data or research articles for future coldplate technology. The off-design performance is analytically derived assuming straight parallel microchannels with laminar flow. A detailed explanation of the implemented coldplate model is provided in Appendix A.1. To validate the model, data from a numerical study of a microchannel coldplate is used [16]. The design point of the model was set to the highest Reynolds number (Re), and for the off-design performance, the mass flow rate (w) was subsequently decreased. All inputs to the design model are listed in Table A3 in Appendix A.2. The results of the validation are shown in Figure 2.

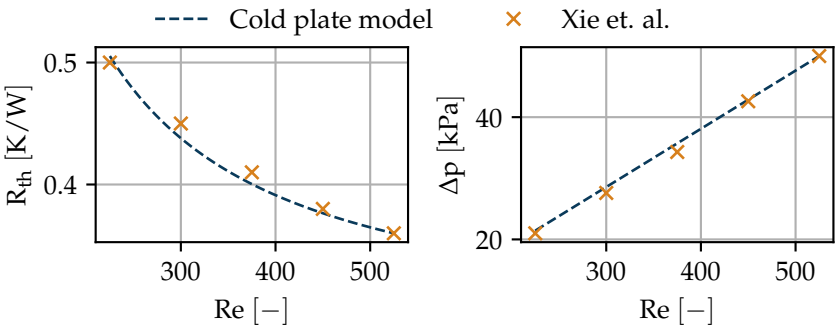

Figure 2. Coldplate model validation for thermal resistance (**left**) and pressure loss (**right**) with data from [16].

The predicted performances for both parameters (R_{th} and Δp) are within 2% of the validation data. The slight inaccuracy stems from the errors made in the visual acquisition

of the data and the simplifications of the model. For the use in preliminary aircraft design, the accuracy is acceptable.

2.2. Compact Heat Exchanger

Heat exchangers can be built in many different architectures that have been described and categorized by different authors, e.g., [17,18]. Models attempting to cover all the different HEX types are therefore limited to a very low level of detail, which is not sufficient for the aim of this study to predict mass, dimensions, power, and drag of the TMS. However, due to the specific requirements of aircraft, only light, compact HEXs are considered. In [19] the most promising types of HEXs for aircraft applications are summarized as plate-fin heat exchangers (PFHE), printed circuit heat exchangers (PCHE), and in the future, microchannel heat exchangers.

There is no hard distinction between these three, as PFHE is a description of the overall architecture (plates and fins), PCHE is a description of the manufacturing technique (additive), and microchannel is a description of the layout on the microscopic level. Therefore, a HEX could match all three categories if it is an additively manufactured PFHE with very small channels. Thus, from a modeling perspective, it is only one type, which can be described as a single-phase, multi-pass, cross-flow HEX in overall counterflow arrangement. Both design and performance calculations were derived from the detailed procedures described in [17] for PFHE. Adaptions for the number of transfer units (NTU), the effectiveness (ϵ), and the dimensions of the HEX for multipass arrangements were implemented from [18]. The key equation for core mass velocity (cmv) from [17] then becomes:

$$cmv_{des} = \sqrt{2\Delta p_{des}} \cdot \left[\frac{f_{corr}}{j} \frac{ntu}{\eta_o} \cdot Pr^{\frac{2}{3}} \cdot \frac{1}{\rho_m} + 2 \cdot \left(\frac{1}{\rho_o} - \frac{1}{\rho_i} \right) + (1 - \sigma^2 + K_c) \cdot \frac{n_p}{\rho_i} - (1 - \sigma^2 - K_e) \cdot \frac{n_p}{\rho_o} + (n_p - 1) \cdot K_{bt} \cdot \frac{\sigma^2}{\rho_m} \right]^{-0.5} \quad (1)$$

with corrected friction factor (f_{corr}), number of transfer units on one side (ntu), overall fin efficiency (η_o), Prandtl number (Pr), inlet, outlet and mean density (ρ_i, ρ_o and ρ_m), ratio of free flow to frontal area (σ), inlet, outlet and bend loss coefficient (K_c, K_e and K_{bt}) and number of passes (n_p).

The described algorithm can work with any HEX core as long as the parameters in Table 1 are given. The Colburn factor (j) and the Fanning friction factor (f) depend on Re, which means a correlation rather than one value has to be given. All other parameters are geometric and do not change in off-design operation. Three options for the HEX core are considered:

1. Rectangular microchannels.
2. Offset-strip fins.
3. Louvered fins.

A detailed explanation for the calculation of all parameters in Table 1 for all three types of HEX core can be found in Appendix B.

2.3. Diffuser, Nozzle, and Pipes

In many TMS models, e.g., the model presented in [12], the diffuser pressure loss is assumed to be constant. However, at low flight speeds, this simple assumption may overestimate the actual pressure loss and lead to the necessity of a puller fan. Its installation should be carefully considered, because it usually is less efficient than the main propulsion devices. Therefore, in this study a Mach number (Ma) dependent pressure loss model is used for the diffuser.

A drawing of the two-dimensional diffuser model is shown in Figure 3. It has a rectangular cross-section, an opening angle (θ) in the z-direction, and a constant width (y-direction). Depending on the flight conditions, there is a pre-entry compression or

expansion, i.e., $A_0 \neq A_1$. The changes in fluid properties between the flow cross-sections A_0 and A_1 are calculated with the isentropic relations. Inside the diffuser, the ideal pressure recovery factor (c_p^*) can be obtained from correlations found in [20]:

$$c_p^* = g_1 \cdot g_2 \cdot \left\{ 1 - \frac{1.03 \cdot (1-B)^2}{\overline{A_R}^2 \cdot \left[1 - 0.82 \cdot \overline{A_R}^{0.07} \cdot B^{1/(2 \cdot \overline{A_R} - 1)} \right]^2} \right\} \tag{2}$$

g_1 is a term depending on Ma and diffuser area ratio ($A_R = A_2/A_1$) and g_2 is a term depending on Re and relative inlet blockage (B). $\overline{A_R}$ is a corrected A_R to account for the influence of the aspect ratio of the inlet cross section. Using c_p^* implies a diffuser with optimal θ, which for the 2-D diffusers is around 8°. The outlet pressure is:

$$p_{2,s} = c_p^* \cdot \rho_1 \cdot v_1^2 + p_{1,s} \tag{3}$$

If $A_0 < A_1$, some air is spilled around the inlet and spillage drag occurs. It can be calculated according to [21,22]:

$$D_{spill} = K_{spill} \cdot [w_1 \cdot (v_1 - v_0) + A_1 \cdot (p_1 - p_0)] \tag{4}$$

K_{spill} is an empirical coefficient accounting for the lip suction effect. D_{spill} is added to the internal drag calculated from conservation of momentum equations over the entire system, i.e., from diffuser inlet to nozzle outlet.

Table 1. Required heat exchanger core parameters.

Name	Symbol	Unit
Colburn factor	j	–
Fanning friction factor	f	–
Hydraulic diameter	d_H	m
Plate space	b	m
Area density	β	m^2/m^3
Fin thickness	δ	m
Fin thermal conductivity	λ_f	$W/(m\,K)$
Ratio finned to total heat transfer area	A_f/A	–

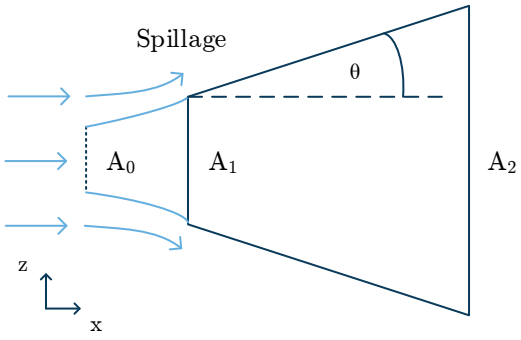

Figure 3. Diffuser model.

Since the nozzle has a negative static pressure gradient in the flow direction, its total pressure loss is less sensitive to shape and flow conditions than the diffuser. However, for the same reasons as mentioned above, it is important to have a pressure loss correlation sensitive to flow velocity rather than just a constant. It can be calculated according to [23]:

$$\Delta p_t = K_{loss} \cdot p_{1,t} \cdot \left[1 - \frac{p_{1,s}}{p_{1,t}} \right] \tag{5}$$

with shape specific loss coefficient (K_{loss}) from [23]. Otherwise, the nozzle model uses area ratios to calculate outlet velocity and isentropic relations for the outlet fluid properties.

The pipe is modeled as a straight circular channel and the well-known head loss formulas, e.g., from [24], are used to estimate pressure loss. For turbulent flow, the correlation from [25] is used to predict the friction factor.

All three models have simple geometric models to estimate their dry masses. In case of the pipe, a wet mass depending on the coolant is also available.

2.4. Pump and Fan

The puller fan is modeled as a repetition stage according to [22], i.e., the outlet velocity equals the inlet velocity. Isentropic relations are used to calculate the outlet fluid properties and compression work.

The pump model is simpler as the fluid is considered to be incompressible. Two efficiencies are implemented: The hydraulic efficiency (η_{hyd}) and the electric efficiency (η_{elec}). Mechanical power and outlet temperature are calculated as:

$$P_{mech} = \frac{\Delta p \cdot w}{\rho \cdot \eta_{hyd}} \tag{6}$$

$$T_2 = T_1 + P_{mech} \cdot \frac{1 - \eta_{hyd}}{c_v \cdot w} \tag{7}$$

2.5. Aircraft Fuel Burn Sensitivities

The HEA used for the TMS design and integration is the research platform of the so-called IVeA (Integrierte Vorauslegung elektrohybrider Antriebe) project. This section briefly presents information about the aircraft and the propulsion system investigated in this project as far as they are relevant for the scope of this study. Further details about the project in general and the design, methods and assumptions of the underlying propulsion system and aircraft are provided in [26].

The aircraft examined within the IVeA project (cf. Figure 4) is designed to carry 180 passengers over a range of 1300 NM and features a turboelectric propulsion system. The propulsion system is composed of advanced turboprop (TP) engines and electrically driven wingtip propellers (WTPs). This architecture was chosen for two reasons. Firstly, compared to GTF engines, TP engines in combination with constant-speed propellers are better suited to supply the high power demands of the WTPs relative to the engine power. Secondly, adding propellers at the tips of the wing reduces induced drag and thus leads to induced thrust [27]. Both technology bricks, combined with a flight speed adapted to the application of the chosen propulsion technology and their associated influence on the design of the aircraft, are expected to reduce FB compared to conventional aircraft in this segment. A key variable of this propulsion system architecture is the power split (S_P, cf. Equation (8)). S_P is defined as the ratio of the shaft power of the WTP (P_{WTP}) to the sum of P_{WTP} and the shaft power of the TP engine's main propeller (P_{MP}).

$$S_P = \frac{P_{WTP}}{P_{MP} + P_{WTP}} \tag{8}$$

The design power of the electric system is determined by S_P and P_{MP} at the top of climb (TOC) of the aircraft design mission. This electric power remains constant throughout the mission unless the power of the gas turbine is lower than its TOC power of the design mission. In this case, P_{WTP} is lowered accordingly to match the defined S_P. A total of three different power splits (10%, 20% and 30%) are studied in the course of the IVeA project.

To derive an optimized TMS design on aircraft level, the impact of the variation of its most important parameters on an aircraft target optimization variable is required. For this purpose, the sensitivity of the turboelectric aircraft's FB to varying mass and drag increments due to the TMS integration was analyzed. Regarding the additional mass of a TMS (m_{TMS}), the operating empty mass (OEM) was gradually increased to include an

assumed m_{TMS} of up to 1000 kg. In the same manner, the wing profile drag was increased to include an assumed TMS drag (D_{TMS}) of up to 1000 N as an integration into the wing was found to be reasonable. Consequently, every combination of m_{TMS} and D_{TMS} represents a new aircraft design including detailed cascading effects. The corresponding results for each S_P are similar in their relative FB changes. For this reason, only the FB sensitivity for $S_P = 30\%$ is shown in Figure 5 below.

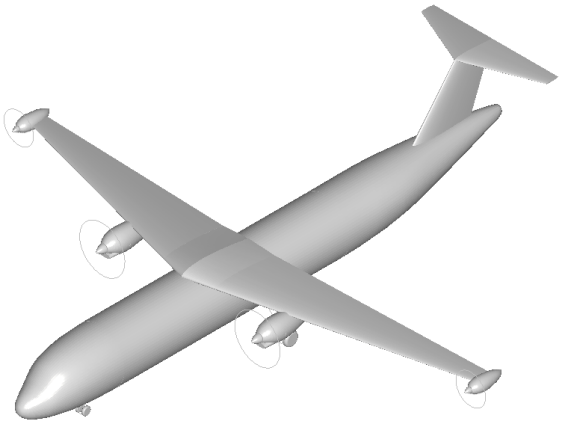

Figure 4. Visualization of the aircraft design used for the sensitivity analyses (here: $S_P = 30\%$).

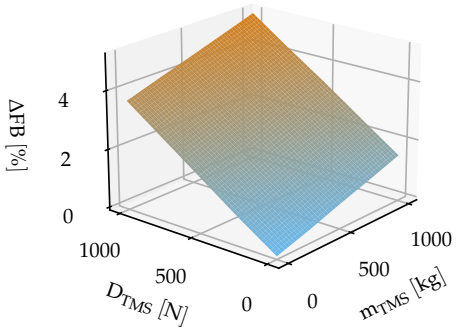

Figure 5. Example of an aircraft fuel burn sensitivity (here: $S_P = 30\%$).

3. System Sensitivity Analysis

The following section investigates the aircraft FB sensitivity to all relevant parameters of the system. It establishes a general understanding of the system and verifies the implementation of the models. Additionally, computational costs in the following optimization (cf. Section 4) are reduced when parameters with low sensitivity can be set to a constant value. The sensitivity analysis is conducted at TOC conditions. However, HDTO conditions are more challenging for the TMS and are considered later in Section 4.2. $S_P = 30\%$ is used for the sensitivity analysis. The trends shown in this section are also valid for the other S_P values. The heat loads of the design and the off-design point are shown in Figure 6.

Power electronics include inverters, rectifiers, and protection switches. The absolute values are rather close due to the aforementioned strategy of keeping the electric power near its maximum throughout the mission. In takeoff, the generator has a higher efficiency because of a better position in the operational characteristics and therefore less waste heat than in design. A 50%-water-glycol mixture is chosen as the coolant to cope with the low ambient temperatures at high altitudes.

3.1. One-Dimensional Sensitivities

The one-dimensional sensitivity analysis considers the sensitivity of each parameter isolated, i.e., only one parameter is varied at a time. In Section 3.2 some coupled or multi-dimensional sensitivities are discussed. The parameters considered for the one-dimensional analysis are summarized in Table 2 and the results are shown in Figure 7.

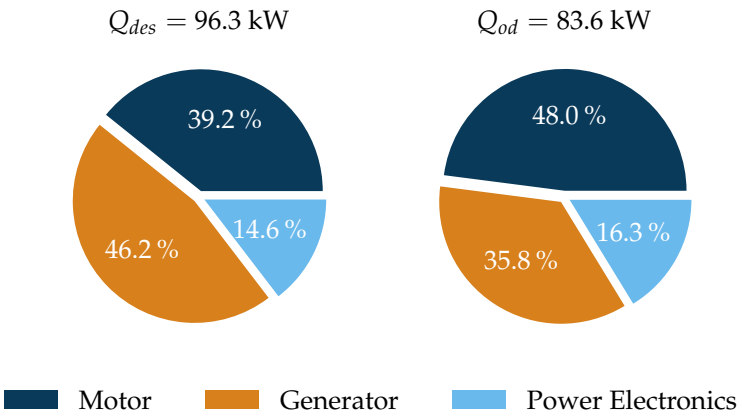

Figure 6. Design and off-design (HDTO) heat loads for $S_P = 30\%$ for one powertrain.

Table 2. Parameters considered in the one-dimensional sensitivity analysis.

Parameter	Symbol	Unit	Default Value
Coldplate surface temperature	T_{cp}	K	370
Heat capacity ratio HEX cold to hot side	C_R^*	–	1.0
Coldplate coolant inlet temperature	T_1	K	275
Pressure ratio HEX cold side	Π_c	–	0.95
Hydraulic diameter HEX cold side	$d_{H,c}$	mm	10.0
Coldplate effectiveness	ϵ_{cp}	–	0.4

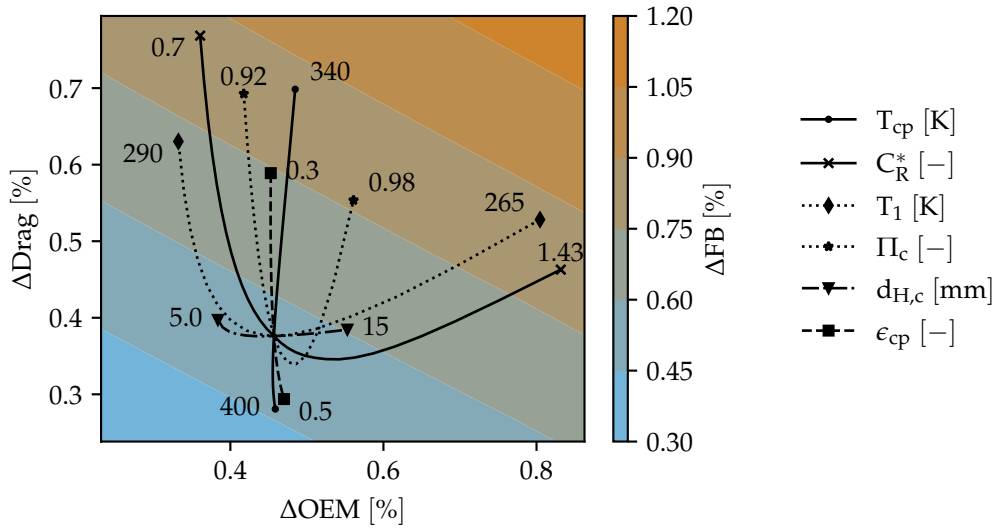

Figure 7. One-dimensional sensitivity analysis.

The default values from Table 2 are located at the intersection of all lines in Figure 7. The default values for each parameter are the median values of the respective parameter range. They are mostly not located at the middle of the resulting sensitivity line, indicating a higher sensitivity of the parameter to one end of the range. Increasing T_{cp} by 30 K from 370 K to 400 K, for example, results in roughly a 0.07% decrease in ΔFB, whereas decreasing it by 30 K to 340 K results in an about 0.3% increase in ΔFB.

T_{cp} and ϵ_{cp} have the highest proportionality with ΔFB. Increasing either one of them directly results in an increase of ΔT across the HEX, which leads to a decrease in HEX size. Both parameters cannot be freely chosen, but T_{cp} is constrained by the allowed operating temperature of the electric component and ϵ_{cp} by the possible size of the coldplate. High ϵ_{cp} values require a longer length of stay of the cooling fluid inside the coldplate, which causes an increase in the size of the coldplate for constant heat loads.

All other parameters have an optimal value with a minimum in ΔFB inside the given range. Decreasing C_R^* to values lower than 1.0 is a direct increase of w_c. This improves the cold-side heat transfer coefficient (α_c), which results in a slightly smaller and lighter HEX; however, the corresponding increase in drag leads to an overall increased ΔFB. Increasing C_R^* past 1.0 has the opposite effect. The increased w_h causes an increased hot-side length (L_h) of the HEX to achieve the same T_1. This allows a shorter cold-side length (L_c) and thereby less drag. There is a limit to this effect—it will eventually result in an increase in drag again due to an unnecessarily large HEX area.

Π_c has a higher drag than OEM sensitivity. Low Π_c values directly result in more drag, but also allow slightly lighter systems due to the increased cold-side flow velocity and thus higher α_c. The increased drag towards very high Π_c values originates in the diffuser. Very low face Ma are required for the HEX, leading to a large diffuser with larger internal losses and also larger spillage.

Decreasing T_1 further from the default value requires a more effective HEX, i.e., a larger HEX with increased L_h and L_c. Besides becoming heavier, the increased L_c also results in more drag for the system. At constant Π_c, an increased L_c requires a smaller face Ma with the above-described consequences for the diffuser. However, T_1 should not be infinitely increased either. Large T_1 values require large w_h values, a constant C_R^*, and large w_c values, resulting in a steep increase in drag.

$d_{H,c}$ is inversely proportional to mass because α_c increases with decreasing $d_{H,c}$. A very small $d_{H,c}$ leads to increased FB, since for constant Π_c a very low face Ma is required, which again causes large diffuser losses, and consequently drag, as mentioned above.

3.2. Multi-Dimensional Sensitivities

The results of Figure 7 may not be used to observe the optimal value for each parameter. This would only be possible if they were independent of each other. In reality, they are linked to each other via various interdependencies. Some of the more interesting ones are shown in Figure 8. Contrary to Figure 7, the lines in Figure 8 are lines of constant parameter values—e.g., along the dotted lines of the left image, Π_c has a constant value, which is indicated on the left side of each line.

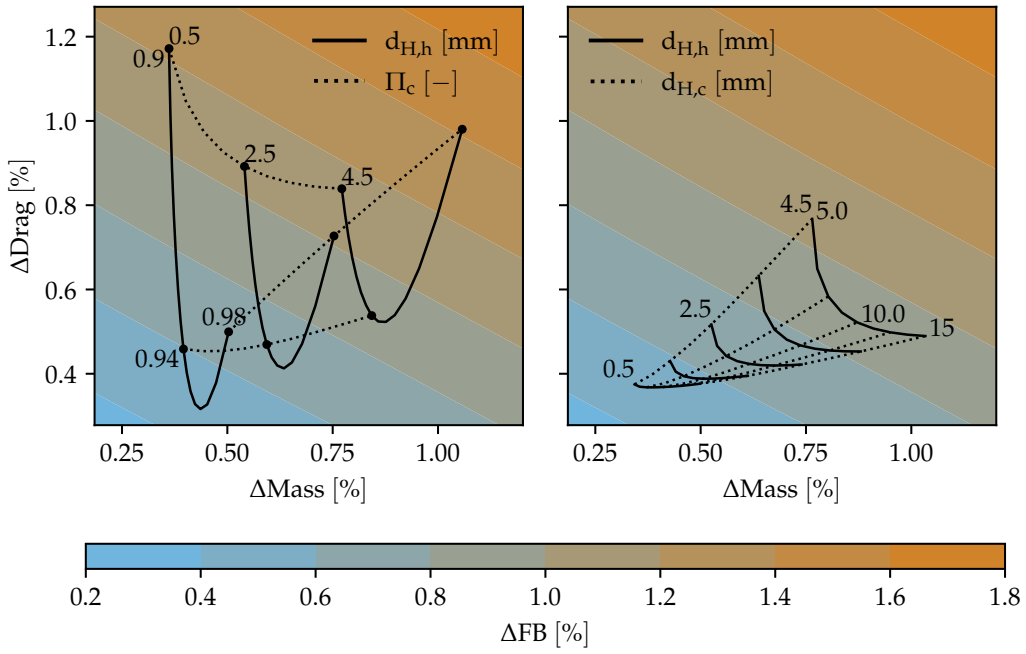

Figure 8. Two-dimensional sensitivity analysis of the hot-side hydraulic diameter with the cold-side pressure ratio (**left**), and the hot-side hydraulic diameter with the cold-side hydraulic diameter (**right**).

The study settings are the same as in Table 2 except for the indicated parameters. On the left side $d_{H,h}$ and Π_c are varied. Varying Π_c shows the same curve shapes for each $d_{H,h}$ as in Figure 7. The minimum in ΔFB shifts. For $d_{H,h} = 4.5$ mm the best Π_c would be about 0.94, whereas for smaller $d_{H,h}$, the ideal Π_c value increases slightly to about 0.96 for $d_{H,h} = 0.5$ mm. $d_{H,h}$ shows a rather clear trend indicating that lower $d_{H,h}$ values always result in less ΔFB. This statement is only valid as long as Π_c can be appropriately chosen. If, for example, Π_c is fixed at 0.9, the best $d_{H,h}$ value would be roughly 2 mm.

The main reason for the effects described above is the influence of $d_{H,h}$ on the HEX cold-side ratio of the free flow to the frontal area (σ_c). A larger $d_{H,h}$ increases the hot-side channel height (if the channel aspect ratio is not changed) and therefore decreases σ_c. If Π_c is left constant, the flow velocity in the cold-side channel is also about constant. However, due to the lower σ_c value, the face Ma must be smaller since a lower σ_c results in a higher difference between frontal and free flow velocity. Therefore, the diffuser must be larger, resulting in more drag. The system mass always decreases with decreasing $d_{H,h}$ because of an increased α_h and a more compact HEX.

On the right, the effects of varying d_H on both cold and hot sides of the HEX are shown. Again, reducing $d_{H,h}$ results in less ΔFB in every case. The reason is the same as described above. The optimal $d_{H,c}$ value depends heavily on the chosen $d_{H,h}$. For a large $d_{H,h}$, a larger $d_{H,c}$ should be chosen. A small $d_{H,c}$ with a large $d_{H,h}$ results in small σ_c values with its negative effects on drag as described above. For the lowest considered $d_{H,h}$ of 0.5 mm, the best $d_{H,c}$ value is about 5 mm. The factor between $d_{H,h}$ and the corresponding best $d_{H,c}$ value varies between 2 and 10. This large difference can be attributed to the different fluid properties, especially the large difference in thermal conductivity between water and air.

For TMS-equipped aircraft, a few interesting conclusions can be derived. The general trend in HEX design towards smaller d_H is only beneficial for the aircraft on the hot side if the drag is considered. Studies only focusing on HEX masses will still find smaller $d_{H,c}$ beneficial. For practical reasons, $d_{H,h}$ can be reduced far easier than $d_{H,c}$. The smaller the d_H, the higher the risk of congestion, and the greater the drop in performance for the HEX. The hot side is a closed loop, and therefore the fluid can be kept very pure through regular exchange and the incorporation of filter systems, thereby minimizing said risk. On the cold side, ambient air has to be used. The implementation of a filter would directly result in more drag and is therefore not a feasible option. With optimal $d_{H,c}$, values of more than 5 mm for maintenance are less of a problem than $d_{H,c}$ values of only a millimeter or less. Due to its obvious trends, $d_{H,h}$ does not need to be considered as a free variable but rather as direct input constrained mainly by manufacturing techniques for the optimization studies in Section 4 if mass, drag, and fuel burn are the only relevant metrics.

3.3. Heat Exchanger Size

While mass, drag, and fuel burn are the most relevant metrics for the aircraft performance, the system size cannot be neglected since the TMS has to be integrated into the aircraft. The influences of $d_{H,h}$ and $d_{H,c}$ on the three HEX dimensions L_h, L_c, and stack height (H_{stack}) are shown in Figure 9. The study settings are equal to those in Figure 8 except for a smaller range of considered values for both d_H.

Clearly, d_H on both sides has a direct influence on overall HEX dimensions. In any size constrained optimization problem, $d_{H,h}$ should therefore be considered as a free variable as well. Increasing $d_{H,h}$ results in an increase of L_h because Π_h is kept constant. To have the same pressure drop for a lower f_h, L_h needs to be higher. As a consequence of the increased L_h, H_{stack} is reduced because Q is also constant. Without a reduction in H_{stack}, the total heat exchange area would be larger, and therefore Q would be higher than actually required. Increasing $d_{H,c}$ shows an analogue trend.

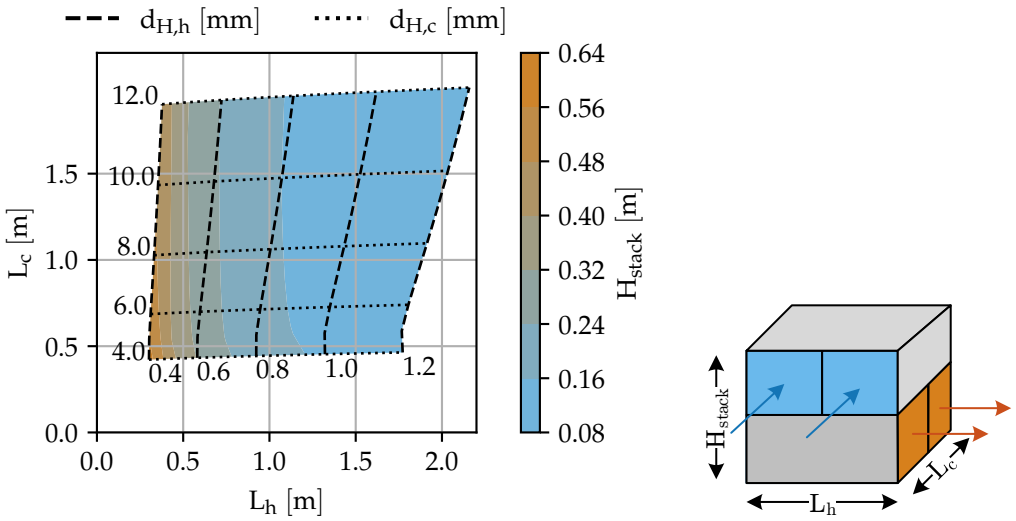

(**a**) Results (**b**) Core sketch

Figure 9. Heat exchanger size sensitivity in three dimensions: hot-side length, cold-side length, and stack height over hot and cold-side hydraulic diameter.

4. Design and Off-Design Optimization for the Application Case

This section uses the previously gathered knowledge to design and optimize TMS for the application case of a HEA described in Section 2.5. The section is divided into design, off-design, and multi-point-design.

4.1. Design Point Optimization

The settings of the study have already been described in the previous sections. The design point of choice is the TOC, which is also the design point of the gas turbine. The aircraft has been designed with three different S_P values, so a TMS was designed for each of them. Free variables for the optimization were $d_{H,h}$, $d_{H,c}$, Π_h, Π_c, C_R, $(A_0/A_1)_{diff}$, and T_1. The cumulative optimization results of two identical TMS (one for each powertrain) are shown in Figure 10.

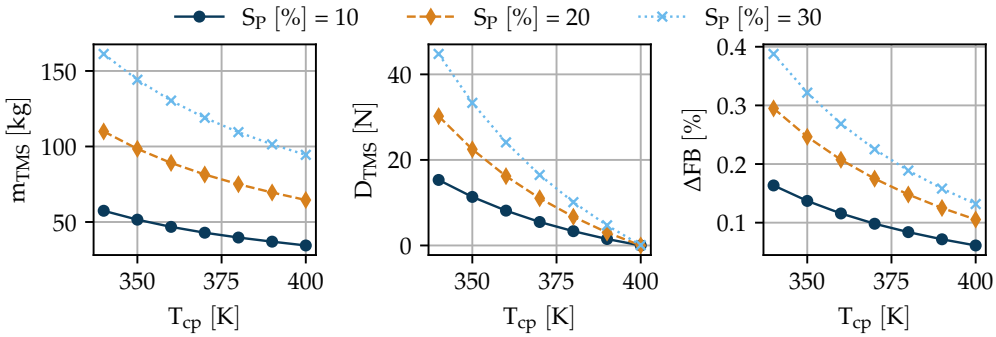

Figure 10. Design optimization results for different power splits.

For each S_P, multiple designs for different T_{cp} were made, as T_{cp} is subject to electric component technology and therefore not certainly known. S_P values were imposed by the aircraft studies [26], and the given range of T_{cp} was chosen to include current electric component technology. Results are shown for m_{TMS}, D_{TMS}, and ΔFB, which was the target function of the optimization. As expected, all three parameters grow with increasing S_P and decreasing T_{cp}. The exponential behavior towards decreasing T_{cp} was also anticipated from the results shown in Figure 7. D_{TMS} gets reduced to almost 0 N when increasing T_{cp} to 400 K, due to the Meridith effect. The heat rejected by the HEX is recovered as thrust and compensates for the pressure loss of the TMS. If even higher T_{cp} values are possible,

the aircraft's FB sensitivity has to be extended towards negative drags, i.e., thrust from the TMS.

With state-of-the-art electric components, i.e., motors, generators, and power electronics, a T_{cp} of 380 K is realistic. For the three different S_P values, ΔFB is 0.09%, 0.15%, and 0.19%, respectively. There are several reasons for these very low values. Firstly, S_P is not very large and therefore Q stays relatively low (cf. Figure 6). Secondly, the turboelectric architecture only includes electric components with comparably high maximum operating temperatures. If a large battery or fuel cell is included in the powertrain, the TMS design becomes more complex and will likely have a higher impact on ΔFB. Thirdly, the currently implemented system mass estimations have to be refined in a more detailed analysis. So far, redundancy is not considered. Additionally, the technology assumptions for the HEX have been rather optimistic with wall thicknesses for the plates assumed at 0.5 mm and for the fins at 0.1 mm.

Fourthly, integration of the TMS has not been considered in the design yet. For T_{cp} = 380 K and S_P = 30%, the HEX would measure $L_c \times L_h \times H_{stack}$ = 0.48 m × 0.73 m × 0.18 m. The diffuser and nozzle would be 2.2 m and 0.9 m long, respectively, resulting in an overall cold-side system length of 3.5 m. If needed, the diffuser could be shortened, trading efficiency. The current model (cf. Section 2.3) only allows diffusers with $\theta = 8°$. In this case, a fuselage integration seems feasible, but cargo space would be reduced. Another option could be the installation on top of the wing near the root, but it would possibly require additional cowlings, resulting in additional mass and drag.

It is worth noting that the numeric optimization resulted in ΔFB values of less than 0.2% for S_P = 30% and T_{cp} = 380 K, whereas even the best values in the sensitivity studies (cf. Figures 7 and 8) were above 0.4%. While the difference in percent points is not of large relevance to the aircraft in this case, the relative difference achieved through numeric optimization is remarkable, i.e., a reduction of more than 50%.

4.2. Off-Design Point Optimization

An exemplary off-design optimization was conducted for $T_{cp,des}$ = 380 K and S_P = 30%. The target function was the electric power required to drive the TMS (P_{TMS}), which includes the power for the hydraulic pump and the fan. The efficiencies of the pump η_{hyd} and η_{elec} were assumed to be 0.75 and 0.95 respectively, and the fan efficiency (η_{Fan}) was set to 0.50. In a more detailed study, proper maps should be implemented for pump and fan efficiency to accurately predict their behavior with changing operating conditions. Variables of the study were the international standard atmosphere temperature deviation (ΔT_{ISA}) and the differences between cooling fluid outlet and inlet temperatures of the electric components (ΔT_{cp}). The results are shown in Figure 11.

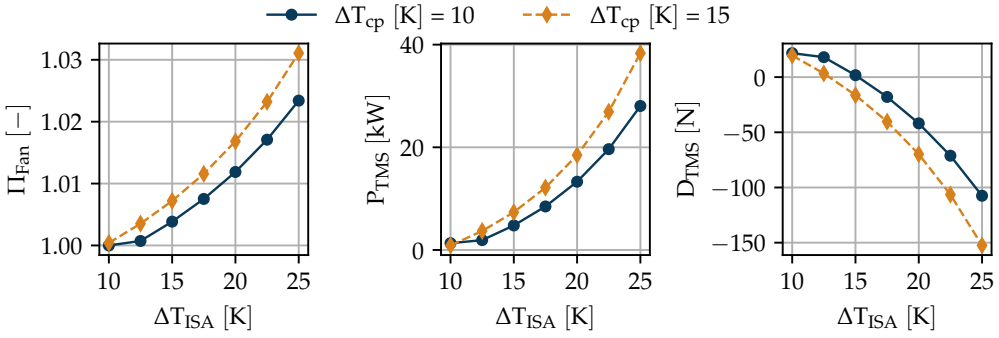

Figure 11. Off-design optimization at takeoff for a TMS designed for $T_{cp,des}$ = 380 K and S_P = 30%.

Hot days are a particular challenge for the TMS because the available ΔT between cooling fluid and ambient is smaller. Raising ΔT_{ISA} results in an exponential increase in required fan pressure ratio (Π_{Fan}). ΔT_{cp} is an operational parameter that can be controlled via P_{pump}. A lower P_{pump} results in a smaller w_h, and thereby a higher ΔT_{cp}. A higher ΔT_{cp}

value does require a larger Π_{Fan} because the ΔT between hot-side HEX inlet to outlet is larger, and therefore a higher α_c is needed. P_{TMS} follows Π_{Fan} almost directly because P_{pump} is at a different order of magnitude, i.e., only 1.1 kW and 0.5 kW for $\Delta T_{cp} = 10$ K and 15 K, respectively. The large difference between P_{pump} and P_{Fan} is due to the fact that the pump compresses an incompressible fluid, and the compressor a compressible one. About 25% P_{TMS} can be saved on a hot day by choosing the lower ΔT_{cp} value.

P_{TMS} has not been considered in the aircraft fuel burn sensitivities. During the majority of the mission, the fan is not required and could either be removed from the flow path or set to idle. The takeoff segment is rather short compared to the overall mission length, and even if the maximum load of 60 kW is required, the impact on the powertrain is negligible. The generators have a combined power of more than 2 MW, and some of the P_{TMS} is actually converted to useful thrust, as seen by the negative drag values of up to −150 N.

4.3. Multi-Point Optimization

From the previous section, the question arises of whether it is possible to design a TMS without the additional puller fan. Though its impact on ΔFB is negligible, it is still an additional component with costs and requirements for certification and maintenance. To answer the question, a multi-point study was conducted that combined the previous design point with an additional constraint to achieve the required cooling power in off-design as well. The target function was again ΔFB—the same as in Section 4.1. The results are shown in Figure 12.

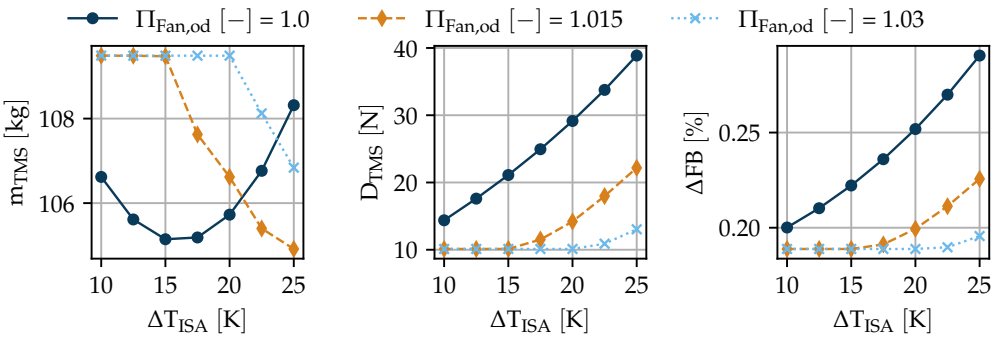

Figure 12. Multi-point optimization for a TMS for $T_{cp,des} = 380$ K and $S_P = 30\%$.

Three different off-design fan pressure ratios ($\Pi_{Fan,od}$) were investigated. If $\Pi_{Fan,od}$ is 1.0, no fan installation is required. For the larger values of $\Pi_{Fan,od}$, all results form horizontal lines for lower ΔT_{ISA}. This implies that the optimal design is only dependent on the design point, and the additional off-design constraint is met because $\Pi_{Fan,od}$ is oversized. Only when ΔT_{ISA} increases beyond a certain threshold does the off-design constraint become relevant.

If no fan is installed ($\Pi_{Fan,od} = 1.0$), the constraint is relevant even at low ΔT_{ISA}, immediately resulting in a larger TMS with increased ΔFB. ΔFB grows exponentially with ΔT_{ISA}. It is certainly possible to design the TMS without the puller fan, however, assuming a maximum ΔT_{ISA} of 25 K, ΔFB would increase from 0.19% to 0.29%. In absolute numbers this difference is negligible, but for a TMS with a larger fuel burn impact, it could be better to install the fan. Using a puller fan also has the advantage of an additional degree of freedom for the system that can help to better adapt to operational changes.

5. Conclusions and Outlook

Ram air-based thermal management systems (TMS) were investigated regarding their overall impacts on an aircraft's fuel burn. The fuel burn sensitivity was derived from a 180-passenger short-range turboelectric aircraft equipped with wingtip propellers by adding a general TMS design drag and mass to it.

A TMS model consisting of coldplates for heat acquisition, pipes and pumps for hot-side heat transfer, a two-pass cross-flow plate-fin heat exchanger for heat rejection, and a diffuser and a nozzle for cold-side flow velocity control was developed. Variations of one- and multi-dimensional parameter sensitivities were used to gain an understanding of the system. The system reacted very sensitively to seven parameters that were selected as free variables for a numeric optimization.

Alternating the hydraulic diameter of the main heat exchanger on both sides was shown to be one of the most effective ways to control the overall system dimensions and therefore manage the integration problem.

TMS optimization studies were conducted. It was found that increasing electric component junction temperature to about 400 K could eliminate parasitic drag from the TMS in cruise entirely. For a more realistic temperature of 380 K, additional fuel burn for an aircraft with 30% power split was 0.19%. The system could withstand hot-day take-off conditions with the help of a small puller fan installed behind the main heat exchanger. Alternatively, oversizing the TMS removed the need for a puller fan, but increased additional fuel burn to 0.29%.

In the future, the mass of the system should be re-investigated. Redundancy considerations are most likely going to cause an increase in system mass of up to 100%. In this study, only rectangular channels were considered for the heat exchanger core. Other options such as offset-strip fins and louvered fins should be considered in the future. Additionally, integration of the TMS, including secondary mass and drag increases, will be discussed in the future. The integration of the TMS seems to be one of the largest challenges. In concrete aircraft applications, this problem should be addressed and possibly solved in a synergistic manner—e.g., by installing the ram inlets behind an open rotor. Additionally, adaptive nozzle geometries are an idea to better adapt TMS performance in different operating conditions.

Author Contributions: Conceptualization, methodology, simulation, analysis and writing of all aspects of the research except for Section 2.5, H.K.; conceptualization, methodology, simulation, analysis and writing of all aspects of the research of Section 2.5, M.L.; conceptualization, methodology, simulation and analysis of the powertrain, M.P.; supervision, M.H. All authors have read and agreed to the published version of the manuscript.

Funding: This research was funded by the German Federal Ministry of Economics and Technology (BMWi) under the German Aviation Research Program (LuFo) call V-3.

Data Availability Statement: Not applicable.

Acknowledgments: We would like to thank everyone involved in the IVeA project for their dedication to its success. Additionally, we thank Arne Seitz for his continued support and fruitful discussions.

Conflicts of Interest: The authors declare no conflict of interest. The funders had no role in the design of the study; in the collection, analyses, or interpretation of data; in the writing of the manuscript, or in the decision to publish the results.

Abbreviations

The following abbreviations are used in this manuscript:

BMWi	Bundesministerium für Wirtschaft und Energie
GTF	Geared turbofan
HDTO	Hot-day takeoff
HEA	Hybrid-electric aircraft
HEX	Heat exchanger
ICA	Initial cruise altitude
IVeA	Integrierte Vorauslegung elektrohybrider Antriebssysteme

LuFo	Luftfahrtforschungsprogramm
MP	Main propeller
MTOM	Maximum takeoff mass
NASA	National Aeronautics and Space Administration
OEM	Operating empty mass
PCHE	Printed circuit heat exchanger
PFHE	Plate fin heat exchanger
SRIA	Strategic Research and Innovation Agenda
TMS	Thermal management system
TOC	Top of climb
TP	Turboprop
VTOL	Vertical takeoff and landing
WTP	Wingtip propeller

Roman Symbols

A	Area	m^2
A_R	Diffuser area ratio	−
$\overline{A_R}$	Corrected diffuser area ratio	−
b	Heat exchanger plate space	m
B	Diffuser inlet blockage	−
c_p	Specific heat capacity at constant pressure	J/(kgK)
c_p^*	Ideal diffuser pressure recovery factor	−
c_v	Specific heat capacity at constant volume	J/(kgK)
C	Absolute heat capacity	W/K
C_R	Heat capacity ratio (C_{min}/C_{max})	−
C_R^*	Side specific heat capacity ratio (C_h/C_c)	−
cmv	Core mass velocity	kg/(m^2s)
d_H	Hydraulic diameter	m
D	Drag	N
f	Fanning friction factor	−
FB	Fuel burn	kg
g	Diffuser pressure recovery geometry factor	−
j	Colburn factor	−
K_{bt}	Bend loss coefficient	−
K_c	Inlet loss coefficient	−
K_e	Outlet loss coefficient	−
K_{loss}	Nozzle pressure loss coefficient	−
K_{spill}	Spillage coefficient	−
L	Length	m
m	Mass	kg
Ma	Mach number	−
n_p	Number of passes	−
ntu	Number of transfer units on one side	−
NTU	Number of transfer units	−
p	Pressure	Pa
P	Power	W
Pr	Prandtl number	−
q	Area specific heat flow rate	W/m^2
Q	Heat flow rate	W
r_{th}	Thermal insulance	m^2K/W
R_{th}	Thermal resistance	K/W

Re	Reynolds number	–
S_P	Power split	%
t	Channel width	m
T	Temperature	K
U	Overall heat transfer coefficient	$W/(m^2K)$
v	Velocity	m/s
V	Volume	m^3
w	Mass flow rate	kg/s

Greek Symbols

α	Heat transfer coefficient	$W/(m^2K)$
δ	Fin thickness	m
Δ	Difference	–
ϵ	Heat exchanger effectiveness	–
η_o	Overall fin efficiency	–
Φ	Aspect ratio	–
Π	Pressure ratio	–
ρ	Density	kg/m^3
ρ_A	Area density	kg/m^2
σ	Heat exchanger ratio of free flow to frontal area	–
θ	Diffuser opening angle	deg

Subscripts

c	Cold
$cond$	Conductive
$conv$	Convective
$corr$	Corrected
cp	Coldplate
cs	Cross section
des	Design
f	Finned
h	Hot
i	Inlet
m	Mean
o	Outlet
od	Off-design
s	Static
$spill$	Spillage
tot	Total

Appendix A. Coldplate Model

Appendix A.1. Model Description

For the coldplate design model, all input and output parameters are listed in Table A1. The input parameters have to be estimated or obtained from manufacturer data.

The area specific heat load (q_{des}) is calculated from the thermal insulance ($r_{th,des}$) and the coldplate surface temperature ($T_{cp,des}$) [28,29].

$$q_{des} = (T_{cp,des} - T_{i,des})/r_{th} \tag{A1}$$

The outlet temperature ($T_{o,des}$) can be obtained from the effectiveness (ϵ_{des}). The evaluation of fluid properties inside a heat exchanging device is conducted at an average temperature (T_m):

$$T_{o,des} = (T_{cp,des} - T_{i,des}) \cdot \epsilon_{des} + T_{i,des} \tag{A2}$$

$$T_m = (T_i + T_o)/2 \tag{A3}$$

The specific heat capacity of the cooling fluid (c_v) is a function of T_m and p_i (the pressure drop is neglected here as c_v has much larger temperature than pressure sensitivity) and is evaluated from the CoolProp fluid database [30]. The required mass flow (w_{des}) can be calculated from Q_{des} and the area of the coldplate (A_{cp}) from q_{des}:

$$w_{des} = Q_{des}/(c_v \cdot (T_{o,des} - T_{i,des})) \tag{A4}$$

$$A_{cp} = Q_{des}/q_{des} \tag{A5}$$

The dry mass is then calculated from the area density (ρ_A):

$$m_{dry} = A_{cp} \cdot \rho_A \tag{A6}$$

The product of the overall heat transfer coefficient and heat exchange area ($(UA)_{des}$) is required for later off-design calculations (note: $A_{des} \neq A_{cp}$ since A_{cp} is the coldplate base area and A_{des} the inner channel surface area). It is calculated from the number of transfer units (NTU). The NTU–ϵ relation for heat exchanging devices with a heat capacity ratio of $C_r = 0$ is found in many thermodynamic textbooks, e.g., [24].

$$NTU_{des} = -\ln(1 - \epsilon_{des}) \tag{A7}$$

$$UA_{des} = NTU_{des} \cdot c_p \cdot w_{des}/A_{cp} \tag{A8}$$

Finally, the outflow pressure (p_o) is calculated:

$$p_{o,des} = p_{i,des} - \Delta p_{des} \tag{A9}$$

Table A1. Design parameters for the coldplate model.

Parameter	Symbol	Unit
Inputs		
Inlet pressure	$p_{i,des}$	Pa
Inlet temperature	$T_{i,des}$	K
Effectiveness	ϵ_{des}	–
Heat load	Q_{des}	W
Coldplate surface temperature	$T_{cp,des}$	K
Thermal insulance	$r_{th,des}$	m^2K/W
Area density	ρ_A	kg/m^2
Pressure drop	Δp_{des}	Pa
Outputs		
Design mass flow	w_{des}	kg/s
Outlet pressure	$p_{o,des}$	Pa
Outlet temperature	$T_{o,des}$	K
Area specific heat load	q_{des}	W/m^2
coldplate area	A_{cp}	m^2
Dry mass	m_{dry}	kg
Number of transfer units	NTU_{des}	–
U-A product	$(UA)_{des}$	W/K

In off-design calculations the dimensions of the coldplate are fixed. Only fluid inlet conditions (T_i, p_i, w_{od}) vary, as does the off-design heat load (Q_{od}). All input and output parameters of the off-design model are listed in Table A2.

Table A2. Off-design parameters for the coldplate model.

Parameter	Symbol	Unit
Inputs		
Inlet pressure	p_i	Pa
Inlet temperature	T_i	K
Outlet temperature	T_o	K
Heat load	Q_{od}	W
Outputs		
Off-design mass flow	w_{od}	kg/s
Outlet pressure	p_o	Pa
coldplate temperature	$T_{cp,od}$	K
Area specific thermal resistance	$r_{th,od}$	m^2K/W
Effectiveness	ϵ_{od}	−

Since (A_{cp}) has been defined in the design model, the off-design area specific heat flow (q_{od}) can be calculated:

$$q_{od} = Q_{od} / A_{cp} \tag{A10}$$

T_m is calculated from (A3) and c_p is obtained from tabulated data. The off-design mass flow (w_{od}) is determined from (A4) with off-design inputs. The off-design coldplate temperature ($T_{cp,od}$) can be determined from the off-design effectiveness (ϵ_{od}).

$$NTU_{od} = (UA)_{od} / (c_p \cdot w_{od}) \tag{A11}$$

$$\epsilon_{od} = 1 - e^{-NTU_{od}} \tag{A12}$$

$$T_{cp,od} = q_{od} / h_{od} + T_m \tag{A13}$$

With $(UA)_{od} = (UA)_{des}$. This will be proven in the following paragraph.

The area is constant as no geometries are changed. For a coldplate, U is comprised of conductive (α_{cond}) and convective (α_{conv}) heat transfer coefficients. α_{cond} does not change in off-design situations because material and thickness are constant. The change in thermal conductivity of the material (λ) is neglected because the mean material temperature is not expected to differ greatly between design and off-design. α_{conv} can be calculated from:

$$\alpha_{conv} = Nu \cdot \lambda / d_H \tag{A14}$$

with Nusselt number (Nu) and hydraulic diameter (d_H) [31]. Microchannels provide compact, light-weight coldplates with the ability to absorb very high q_{des} as required by modern chip generations. The flow in such small channels is typically laminar due to the very small d_H [32]. In laminar flow, Nu is constant regardless of the flow velocity [24]. For this model, laminar flow is assumed in all operating points. To ensure this assumption is true, the coldplate should always be designed for maximum mass flow and off-design operating points should have smaller mass flows ($w_{des} > w_{od}$). d_H is also constant as it is a fixed geometry. Neglecting the $T - p$ dependency of λ the equity of both α_{conv} follows:

$$\alpha_{conv,des} = \alpha_{conv,od} \tag{A15}$$

U_{des} is known from (A7). If the temperature differences between design and off-design are large, the λ T-p sensitivity can be accounted for by means of a ratio $\lambda_{od}/\lambda_{des}$. The off-design thermal insulance ($r_{th,od}$) is:

$$r_{th,od} = (T_{cp,od} - T_i)/q_{od} \tag{A16}$$

Since no exact geometry is known from the design model, the off-design pressure loss (Δp_{od}) has to be derived from its design counterpart and the design/ off-design w-ratio:

$$\Delta p_{od} = f(\Delta p_{des}, w_{des}/w_{od}) \tag{A17}$$

In general Δp can be calculated from [24]:

$$\Delta p = h \cdot \rho \cdot g \tag{A18}$$

with head loss (h) and gravitational constant (g). The head loss is [33]:

$$h = f \cdot L \cdot u^2/(d_H \cdot 2 \cdot g) \tag{A19}$$

with friction factor (f), flow length (L), and flow velocity (u). In laminar flow, f is a function of Re and a channel geometry depending constant (c_{geom}) [24]:

$$f = c_{geom}/Re \tag{A20}$$

$$Re = u \cdot d_H/\nu \tag{A21}$$

with kinematic viscosity (ν). Combining (A18)–(A21) results in:

$$\Delta p = c_{geom} \cdot L \cdot u \cdot \rho \cdot \nu/(2 \cdot d_H^2) \tag{A22}$$

c_{geom}, L, and d_H do not change from design to off-design conditions the difference in ρ and ν is neglected so that:

$$\Delta p_{od}/\Delta p_{des} = u_{od}/u_{des} \tag{A23}$$

$$u = w/(\rho \cdot A_{cs}) \tag{A24}$$

with flow cross section area (A_{cs}). Again, A_{cs} stays constant, and the difference in ρ is neglected, finally resulting in:

$$\Delta p_{od} = \Delta p_{des} \cdot w_{od}/w_{des} \tag{A25}$$

$p_{o,od}$ can now be calculated via (A9).

Appendix A.2. Coldplate Validation Design Inputs

Table A3. Design inputs for coldplate validation.

Parameter	Unit	Value
$T_{1,des}$	K	294
ϵ_{des}	−	0.47
Q_{des}	W	100
$T_{cp,des}$	K	330
$r_{th,des}$	m^2K/W	2.88×10^{-5}
Δp_{des}	Pa	50×10^3

Appendix B. Compact Heat Exchanger Core Model

This section describes how the core geometry parameters and Colburn factor (j) and Fanning friction factor (f) for the different core surfaces of a compact heat exchanger are calculated.

1. **Rectangular microchannels**. j and f are calculated according to the methods described for rectangular channels in [24]. Of the parameters in Table 1, d_H and δ are used as known inputs, and the other parameters are calculated. The aspect ratio of the channels is also an input and defined as:

$$\Phi = b/t \tag{A26}$$

with channel width (t). Starting from (A26) and the definition of d_H

$$d_H = \frac{4A_{cs}}{P} \tag{A27}$$

with channel cross section area A_{cs} and perimeter P, rearrangement leads to:

$$b = d_H \cdot \frac{1+\Phi}{2} \tag{A28}$$

In a similar fashion, using basic geometry and regarding the side walls of the channels as fins results in:

$$A_f/A = \frac{\Phi}{\Phi+1} \tag{A29}$$

with finned area A_f and total heat exchange area A. The area density is defined as:

$$\beta = \frac{A}{V} \tag{A30}$$

with core volume V. Combining (A26), (A27) and (A30) concludes after some rearrangements in:

$$\beta = \frac{4 \cdot (1+\Phi)}{d_H \cdot (1+\Phi) + 2 \cdot \Phi \cdot \delta} \tag{A31}$$

2. **Offset-strip fins**. The model for this core is entirely based on [34]. j and f correlations were directly adapted and used within the given limits. For offset-strip fins, the fin length (L_f) is required as an additional input parameter. The missing geometries were derived from Figure 1 in [34]. If offset-strip fins could be realized without additional material on the top or bottom b, A_f/A, and β could be calculated from (A28), (A29) and (A30) respectively. With enhanced manufacturing techniques, it may become possible. Hence, for this model, the additional material thickness on the top and bottom is neglected.
3. **Louvered fins**. The correlation for j was directly implemented from [35] and for f from [36]. b is used as direct input for this model. A_f/A and β were calculated with (8.76–8.84) from [17]. Additional input parameters to be considered here are louver angle, louver pitch, and louver cut length, which should be selected carefully within the valid ranges given in [35,36].

References

1. Advisory Council for Aviation Research and Innovation in Europe. *Strategic Research and Innovation Agenda: Volume 1: 2017 Update*; Advisory Council for Aviation Research and Innovation in Europe: Brussels, Belgium, 2017.
2. Singh, R.; Freeman, J.; Osterkamp, P.; Green, M.; Gibson, A.; Schiltgen, B. Challenges and opportunities for electric aircraft thermal management. *Aircr. Eng. Aerosp. Technol.* **2014**, *86*, 519–524.

3. Piancastelli, L.; Frizziero, L.; Donnici, G. The Meredith Ramjet: An Efficient Way To Recover The Heat Wasted in Piston Engine Cooling. *J. Eng. Appl. Sci.* **2015**, *10*, 5327–5333.
4. Pérez-Grande, I.; Leo, T.J. Optimization of a commercial aircraft environmental control system. *Appl. Therm. Eng.* **2002**, *22*, 1885–1904. [CrossRef]
5. Jafari, S.; Nikolaidis, T. Thermal Management Systems for Civil Aircraft Engines: Review, Challenges and Exploring the Future. *Appl. Sci.* **2018**, *8*, 2044. [CrossRef]
6. Brelje, B.J.; Martins, J.R. Electric, hybrid, and turboelectric fixed-wing aircraft: A review of concepts, models, and design approaches. *Prog. Aerosp. Sci.* **2018**, *104*, 1–19. [CrossRef]
7. National Acadamy of Sciences. *Commercial Aircraft Propulsion and Energy Systems Research*; National Academies Press: Washington, DC, USA, 2016.
8. Jansen, R.; Bowman, C.; Jankovsky, A. Sizing Power Components of an Electrically Driven Tail Cone Thruster and a Range Extender. In Proceedings of the 16th AIAA Aviation Technology, Integration, and Operations Conference, Washington, DC, USA, 13–17 June 2016.
9. Lents, C.E.; Hardin, L.W.; Rheaume, J.; Kohlman, L. Parallel Hybrid Gas-Electric Geared Turbofan Engine Conceptual Design and Benefits Analysis. In Proceedings of the 52nd AIAA/SAE/ASEE Joint Propulsion Conference, Salt Lake City, UT, USA, 25–27 July 2016.
10. Rheaume, J.; Lents, C.E. Design and Simulation of a Commercial Hybrid Electric Aircraft Thermal Management System. In Proceedings of the 2018 AIAA/IEEE Electric Aircraft Technologies Symposium, Cincinnati, OH, USA, 9–11 July 2018.
11. Rheaume, J.M.; MacDonald, M.; Lents, C.E. Commercial Hybrid Electric Aircraft Thermal Management System Design, Simulation, and Operation Improvements. In Proceedings of the 2019 AIAA/IEEE Electric Aircraft Technologies, Indianapolis, IN, USA, 19–22 August 2019.
12. Chapman, J.W.; Schnulo, S.L. Development of a Thermal Management System for Electrified Aircraft. In Proceedings of the AIAA Scitech 2020 Forum, Orlando, FL, USA, 6–10 January 2020; p. 2273.
13. Kellermann, H.; Habermann, A.L.; Hornung, M. Assessment of Aircraft Surface Heat Exchanger Potential. *Aerospace* **2020**, *7*, 1. [CrossRef]
14. Kellermann, H.; Habermann, A.L.; Vratny, P.C.; Hornung, M. Assessment of fuel as alternative heat sink for future aircraft. *Appl. Therm. Eng.* **2020**, *170*, 114985. [CrossRef]
15. Wei, T. All-in-one design integrates microfluidic cooling into electronic chips. *Nature* **2020**, *585*, 188–189. [CrossRef] [PubMed]
16. Xie, G.; Li, S.; Sunden, B.; Zhang, W.; Li, H. A Numerical Study of the Thermal Performance of Microchannel Heat Sinks with Multiple Length Bifurcation in Laminar Liquid Flow. *Numer. Heat Transf. A Appl.* **2014**, *65*, 107–126. [CrossRef]
17. Shah, R.K.; Sekulić, D.P. *Fundamentals of Heat Exchanger Design*; Wiley-Interscience: Hoboken, NJ, USA, 2003.
18. Kays, W.M.; London, A.L. *Compact Heat Exchangers*, 3rd ed.; Krieger: Malabar, FL, USA, 1998.
19. Sundén, B.; Fu, J. *Heat Transfer in Aerospace Applications*; Academic Press: London, UK, 2017.
20. Pittaluga, F. A set of correlations proposed for diffuser performance prediction. *Mech. Res. Commun.* **1981**, *8*, 161–168. [CrossRef]
21. Malan, P.; Brown, E.F. Inlet drag prediction for aircraft conceptual design. *J. Aircr.* **1994**, *31*, 616–622. [CrossRef]
22. Bräunling, W.J.G. *Flugzeugtriebwerke: Grundlagen, Aero-Thermodynamik, Ideale und Reale Kreisprozesse, Thermische Turbomaschinen, Komponenten, Emissionen und Systeme*, 4th ed.; VDI-Buch; Springer: Berlin, Germany, 2015.
23. Walsh, P.P.; Fletcher, P. *Gas Turbine Performance*, 2nd ed.; Blackwell Science: Oxford, UK, 2008.
24. Incropera, F.P.; DeWitt, D.P.; Bergman, T.L.; Lavine, A.S. *Principles of Heat and Mass Transfer*, 7th ed.; International Student Version ed.; Wiley: Singapore, 2013.
25. Haaland, S.E. Simple and Explicit Formulas for the Friction Factor in Turbulent Pipe Flow. *J. Fluids Eng.* **1983**, *105*, 89. [CrossRef]
26. Pohl, M.; Köhler, J.; Jeschke, P.; Kellermann, H.; Lüdemann, M.; Hornung, M.; Weintraub, D. Integrated Preliminary Design of Turboelectric Aircraft Propulsion Systems. 2020. Manuscript in preparation.
27. Loth, J.L.; Loth, F. Induced drag reduction with wing tip mounted propellers. In Proceedings of the 2nd Applied Aerodynamics Conference, Seattle, WA, USA, 21–23 August 1984.
28. Matsuda, M.; Mashiko, K.; Saito, Y.; Nguyen, T.; Nguyen, T. *Mico-Channel Cold Plate Units for Cooling Super Computer*; Fujikura: Tokyo, Japan, 2015.
29. Advanced Thermal Solutions. The Thermal Resistance of Microchannel Cold Plates. *Qpedia Therm. Emagazine* **2012**, *2012*, 6–9.
30. Bell, I.H.; Wronski, J.; Quoilin, S.; Lemort, V. Pure and Pseudo-pure Fluid Thermophysical Property Evaluation and the Open-Source Thermophysical Property Library CoolProp. *Ind. Eng. Chem. Res.* **2014**, *53*, 2498–2508. [CrossRef] [PubMed]
31. VDI-Wärmeatlas. *Mit 320 Tabellen*, 11th ed.; VDI-Buch; Springer: Berlin, Germany, 2013.
32. Denkenberger, D.C.; Brandemuehl, M.J.; Pearce, J.M.; Zhai, J. Expanded microchannel heat exchanger: Design, fabrication, and preliminary experimental test. *Proc. Inst. Mech. Eng. A J. Power Energy* **2012**, *226*, 532–544. [CrossRef]
33. Nakayama, Y.; Boucher, R.F. *Introduction to Fluid Mechanics*; Butterworth Heinemann: Oxford, UK; Boston, MA, USA, 1999.
34. Wieting, A.R. Empirical Correlations for Heat Transfer and Flow Friction Characteristics of Rectangular Offset-Fin Plate-Fin Heat Exchangers. *J. Heat Transf.* **1975**, *97*, 488–490. [CrossRef]

35. Chang, Y.J.; Wang, C.C. A generalized heat transfer correlation for Iouver fin geometry. *Int. J. Heat Mass Transf.* **1997**, *40*, 533–544. [CrossRef]
36. Chang, Y.J.; Hsu, K.C.; Lin, Y.T.; Wang, C.C. A generalized friction correlation for louver fin geometry. *Int. J. Heat Mass Transf.* **2000**, *43*, 2237–2243. [CrossRef]

2.2 Assessment of Aircraft Surface Heat Exchanger Potential

The paper [2] presents methods and results for a potential assessment of utilizing the existing aircraft wetted surfaces as a heat sink. A wide range of commercial aircraft is analyzed. The paper is structured into five sections.

The first section "Introduction" motivates the topic with the increasing waste heat for future aircraft, e.g., caused by including electric components in the powertrain and the potentially drag-free heat removal via S-HEXs. Providing fast assessment methods to estimate the possible heat flow rate (Q) via the aircraft surfaces is presented as objective and the procedure is outlined. Section 1 was conceptualized and written by Hagen Kellermann.

The second section "Aircraft Correlations" presents statistical methods to estimate various aircraft parameters required for the heat transfer calculations. For S-HEXs, the most important parameter is the wetted surface area (A_{wet}). A large data set is used with existing aircraft ranging from small regional aircraft to large wide-body jets. The dataset is strictly limited to tube and wing aircraft. Since A_{wet} is not directly available in the used aircraft data set it has to be calculated from other available geometric parameters. Geometric simplifications are introduced, e.g., assuming the fuselage as straight cylinder and the error of the simplification for each major component (fuselage, wing, nacelles, horizontal and vertical tailplane) is calculated by comparison to a model of an A320-sized aircraft. Next, the correlation of four parameters with A_{wet} is investigated and MTOM is found to have the strongest correlation. Thus, it is used for the rest of the study. Finally, the propulsive power of the aircraft is estimated via the available thrust to later compare the available Q to a potentially required Q. Section 2 was conceptualized and written by Hagen Kellermann.

The third section "Surface Heat Transfer" introduces the heat transfer models used. They are based on flat plate convection. Various sensitivities for either cylindrical or trapezoidal geometries are presented. The critical Reynolds number has a large influence on Q for low Ma since large parts of the surfaces have laminar flow regimes if high critical Reynolds numbers are assumed. A larger wing aspect ratio increases Q due to the lower chord lengths and thus thermal boundary layer thicknesses on the wings. The effects of varying taper ratios and fuselage slenderness were also studied but found to have only a minor impact on Q. In Section 3.3 the potential effect of heated surfaces on the aircraft drag is discussed. The various different physical effects, e.g. possible movement of the transition location, are explained and a recommendation to place S-HEXs in turbulent regions is given. Section 3.3 was conceptualized and written by Anais Habermann and all other parts of Section 3 were conceptualized and written by Hagen Kellermann.

The fourth section "Surface Cooling Potential" presents and discusses the final results of the assessment study. Various surface area reduction assumptions, e.g., for the windows, are presented as well as the investigated operating points TO, HDTO, CL, and CR. The available Q is calculated for the entire range of aircraft in the dataset represented by their MTOM values. Finally, the available Q is compared to a hypothetical required Q by an assumed electric drive train, which was scaled via thrust with MTOM. Smaller aircraft, i.e., with lower MTOM values were found to have an advantageous ratio of available to required Q. Two reasons were identified. First, larger aircraft have longer surfaces in flow direction and thus increased thermal boundary layer thicknesses. Second, larger aircraft have a lower A_{wet} to MTOM ratio, but the required power and thus waste heat scales linearly with MTOM. Section 4 was conceptualized and written by Hagen Kellermann.

The final section is a combined conclusion and outlook, which summarizes the key methods and results and recommends the development of more detailed S-HEX models as well as a deeper investigation of the expected drag. It was conceptualized and written by Hagen Kellermann. The entire paper was reviewed by Mirko Hornung.

The paper contains an error in Section 4.2 (page 13) in the part that describes Figure 7: "Assuming T_{surf} of 360 K an estimated Q_{av} of approximately 250 kW in HTO [...]" [2]. The calculated heat load (Q_{av}) for the described conditions is displayed in Figure 7 in [2] and the actual value is correctly shown as 2.5 MW. The error is repeated in the conclusion (page 15). The journal has been notified of the error and a correction process was initialized. The error does not affect the main conclusions of the paper nor does it entail subsequent errors.

Author contributions in short: The author's contributions are declared at the end of the publication.

aerospace

MDPI

Article

Assessment of Aircraft Surface Heat Exchanger Potential

Hagen Kellermann *, Anaïs Luisa Habermann and Mirko Hornung

Bauhaus Luftfahrt e.V., Willy-Messerschmitt Straße 1, 82024 Taufkirchen, Germany
* Correspondence: hagen.kellermann@bauhaus-luftfahrt.net

Received: 20 November 2019; Accepted: 12 December 2019; Published: 19 December 2019

Abstract: Providing sufficient cooling power for an aircraft will become increasingly challenging with the introduction of (hybrid-) electric propulsion. To avoid excessive drag from heat exchangers, the heat sink potential of the aircraft surface is evaluated in this study. Semi-empirical correlations are used to estimate aircraft surface area and heat transfer. The impact of surface heating on aircraft drag is qualitatively assessed. Locating surface heat exchangers where fully turbulent flow is present promises a decrease in aircraft drag. Surface cooling potential is investigated over a range from small regional aircraft to large wide body jets and a range of surface temperatures. Four mission points are considered: Take-off, hot day take-off, climb and cruise. The results show that surface heat exchangers can provide cooling power in the same order of magnitude as the waste heat expected from (hybrid-) electric drive trains for all sizes of considered aircraft. Also, a clear trend favouring smaller aircraft with regards to the ratio of available to required cooling power is visible.

Keywords: aircraft thermal management; hybrid electric propulsion; surface heat exchanger

1. Introduction

Research for next generation commercial aircraft is driven by ambitious goals to reduce the aircraft's environmental impact such as the European Commission's Strategic Research and Innovation Agenda (SRIA) [1] that targets a 75% reduction in CO_2 emissions by the year 2050 compared to the year 2000. A big contributor to achieve those targets is the propulsion system. Novel propulsion concepts with intercoolers [2], topping cycles [3] or bottoming cycles [4] are currently under investigation to reduce the specific fuel consumption. Another promising approach seems to be a higher electrification of the on-board systems or even the propulsion system. Examples are the more electric aircraft [5] or (hybrid-) electric propulsion systems [6]. Their electric components generate waste heat that needs to be rejected in an efficient way. Many concepts result in higher thermal loads of the systems. Conventional cooling concepts require ram air and heat exchangers, which are placed in the airflow path and thus generate drag [7]. Another option is to use existing aircraft surfaces for heat transfer from the inside of the aircraft to the ambient [8]. These structurally integrated heat exchangers may be beneficial for both weight and drag of the Thermal Management System (TMS) because no additional components such as the ram air heat exchanger are required and no components are installed in the flow path. Additionally, heat rejection to the aircraft's boundary layer may lead to drag reductions [9]. The aim of this paper is to investigate the heat sink potential of available aircraft surfaces.

Wang et al. present a good overview of the application of surface heat exchangers in aircraft up to the year 1999. In the beginning, the development of surface heat exchangers was driven by the cooling demand of piston engines with increasing power densities. In the 1920ies and 1930ies they were mainly used in racing aircraft. In some aircraft such as the "Supermarine S.6" surface heat exchangers covered surfaces of multiple components such as wings, fuselage and floats. In military aircraft, leading edge steam radiators were successfully tested. However, despite the proven thermodynamic performance

the technology was not put into practical applications due to hazards such as machine gun fire. When gas turbines started to replace piston engines in aircraft, the engine cooling problem vanished and with it surface heat exchangers. However, academic research on surface heating continued. The results indicate that heating aircraft surfaces might not only serve for heat dissipation but also as means of boundary layer control. It is commonly agreed that heat addition to a laminar boundary layer increases instabilities and therefore may lead to an earlier transition, thus increasing drag [8].

More recent studies showed a growing interest in surface heat exchangers again due to the increased cooling demand from the aforementioned technologies. Especially new engine concepts such as Ultra High Bypass Ratio Turbofans and open rotors with very compact gas generators and mechanical transmission have increased oil heat loads. Sousa et al. investigated a surface cooler with fins inside a turbo fan engine bypass as air cooled oil cooler (ACOC). Numerical calculations in combination with experiments were conducted. They showed that the surface cooler was capable of rejecting 76% of the take-off oil heat load [10]. Surface air cooled oil coolers (SACOC) are investigated by multiple EU-funded projects such as SHEFAE [11], SHEFAE 2 [12] and SACOC [13]. Sakuma et al. carried out investigations of the effects of varying SACOC geometries in the context of SHEFAE 2. They found that two 200 mm long heat exchangers could reject the same heat as one 900 mm long one while maintaining the same pressure drop allowing for area and weight optimization of the SACOC [14].

Recently, Liu et al. conducted numerical studies to describe pressure loss and heat transfer of different aircraft surface heat exchanger fin configurations including continuous, segmented and staggered fins. They found the continuous configuration to have the most advantageous heat transfer to pressure drop ratio [15]. Part of the wing surfaces were used for heat dissipation of a hybrid electric aircraft with a TMS utilizing fuel as working fluid. The results showed that steady state cooling of the electric propulsion system is possible in most operating points, however the aircraft only had 20% hybridization [16].

While there is a good amount of literature on surface coolers in aircraft applications, most investigate research questions tailored to one specific engine or aircraft or try to optimize the surface heat exchanger geometry. In contrast, this study aims to generally predict the thermodynamic potential of the aircraft surface for a range of differently sized aircraft. The goal is to quickly assess the feasibility of using a TMS with surface heat exchangers for a hybrid electric configuration.

For that purpose, a thermodynamic model of a surface heat exchanger covering existing aircraft surfaces is developed. A scalable geometric model of a tube and wing type aircraft with podded engines is derived with a semi-empirical approach. It is used to analyse the impact of aircraft size and available portions of the total surface area on the potential cooling power. Various sensitivities of the model including surface temperature, incoming radiation and component geometries are considered. In addition, drag increments resulting from non-adiabatic boundary layers are assessed.

The ambient conditions differ at each operating point. The study evaluates steady state heat transfer performance in pre-defined sets of Mach number (Ma), altitude (alt) and ISA temperature deviation (dT_{ISA}). They reflect typical operating conditions of commercial aircraft namely Take-Off (TO), Hot Day Take-Off (HTO), Climb (CL) and Cruise (CR), which are relevant sizing points for the TMS. The quantification of the potential of the aircraft's skin as heat sink can be used by future projects on advanced propulsion concepts to account for the total amount or a fraction of the system's waste heat removal.

2. Aircraft Correlations

The study aims to estimate the surface heat sink potential of a range of aircraft covering most of the commercial aviation market. Therefore, data for aircraft ranging from small regional aircraft up to large wide body jets are used as basis for the correlations. Besides correlations for the wetted surface area (A_{wet}), the data is analysed with regard to propulsive power as it will be an indicator for the size of future hybrid electric power trains and thus the expected required cooling power (Q_{rq}). Most data

are obtained from Reference [17]. They provide aircraft data up to the year 2000 for aircraft from different manufactures including Airbus, Boeing, Fokker and Bombardier. Additional data especially for newer aircraft are extracted from documents provided by the manufacturers [18,19].

2.1. Aircraft Component Geometries

A_{wet} of the aircraft consists of the surface areas of multiple components. This study is strictly limited to the tube and wing aircraft configuration and thus the components considered as possible locations for surface heat exchangers are:

- Fuselage
- Wing
- Nacelles
- Horizontal tail
- Vertical tail

For wing, horizontal and vertical tail the data at hand contains the exposed area (A_{exp}) that is, for a wing the area given is the base area outside the fuselage. In a first order approximation, A_{exp} is doubled to calculate A_{wet}. More accurate semi-empirical methods to calculate the wetted area of bodies with an airfoil cross section for example in Reference [20] exist, however, for an initial potential assessment, it seems more reasonable to choose the simplest method possible. For the fuselage and nacelles, A_{wet} is also not directly available. Instead, length and diameter (in case of the nacelle the maximum diameter) are included. A_{wet} of these components is estimated by using the geometric model of a cylinder. This approach overestimates the area for the nacelles, because a cylinder with the nacelle length and the maximum diameter as constant diameter has a larger A_{wet} than the actual nacelle with a variable diameter. For the fuselage, the overestimation of the lateral surface area is reduced by the fact that an open cylinder model is used but the fuselage is actually a closed body. For a quick estimation of the order of magnitude of the error from these geometric simplifications, a point validation is conducted using available data from an A320 sized aircraft model [21]. Table 1 shows the comparison between the simplified A_{wet} (A_{sim}) and the actual A_{wet} (A_{act}) as well as the relative deviation of A_{sim} from A_{act}:

Table 1. Comparison of simplified A_{wet} with actual A_{wet}.

Component	A_{sim} (m^2)	A_{act} (m^2)	$\Delta_{A,wet}$ (%)
Fuselage	478.0	412.9	+15.8
Wing	202.4	208.7	−3.0
Nacelles	55.8	52.4	+6.4
Horizontal tail	48.4	49.6	−2.4
Vertical tail	42.2	43.3	−2.7
Total	826.8	766.9	7.8

The deviation for the total A_{wet} is less than 10%. For each component, the expected direction of deviation is confirmed that is, for fuselage and nacelles the simplifications lead to an overestimation of A_{wet} whereas for all the other components the methods underestimate A_{wet}. The largest deviation is present for the fuselage with 15.8%. Overall, the deviations are considered acceptable for the scope of this study, because the aim is to find basic correlations among a wide range of aircraft rather than developing precise calculation methods for one specific aircraft.

2.2. Surface Area Correlations

Four possible aircraft design parameters are identified as potential variables to correlate with the total wetted surface area:

1. Maximum Take-Off Weight ($MTOW$)
2. Maximum number of seats (n_{max})
3. Maximum payload (MPL)
4. Design range (R_{des})

All four are defined in the conceptual design stage of an aircraft and affect the overall aircraft design. For all four variables, correlations with A_{wet} are found using least squares polynomial fits. To assess the quality of each fit, the coefficient of determination (r^2) is used. The best fits that is, the ones with the highest r^2 value for all four variables are linear fits of the log-log scaled data and are shown in Figure 1. The corresponding fits are summarized in Equation (1) with the coefficients given in Table 2.

$$log_{10}A_{wet} = a \cdot log_{10}x + c \tag{1}$$

Table 2. Coefficients for log-log surface area fits.

x	a	c	r^2
$MTOW$	0.748	−0.689	0.986
n_{max}	0.940	0.887	0.963
MPL	0.855	−0.668	0.965
R_{des}	0.995	−0.417	0.859

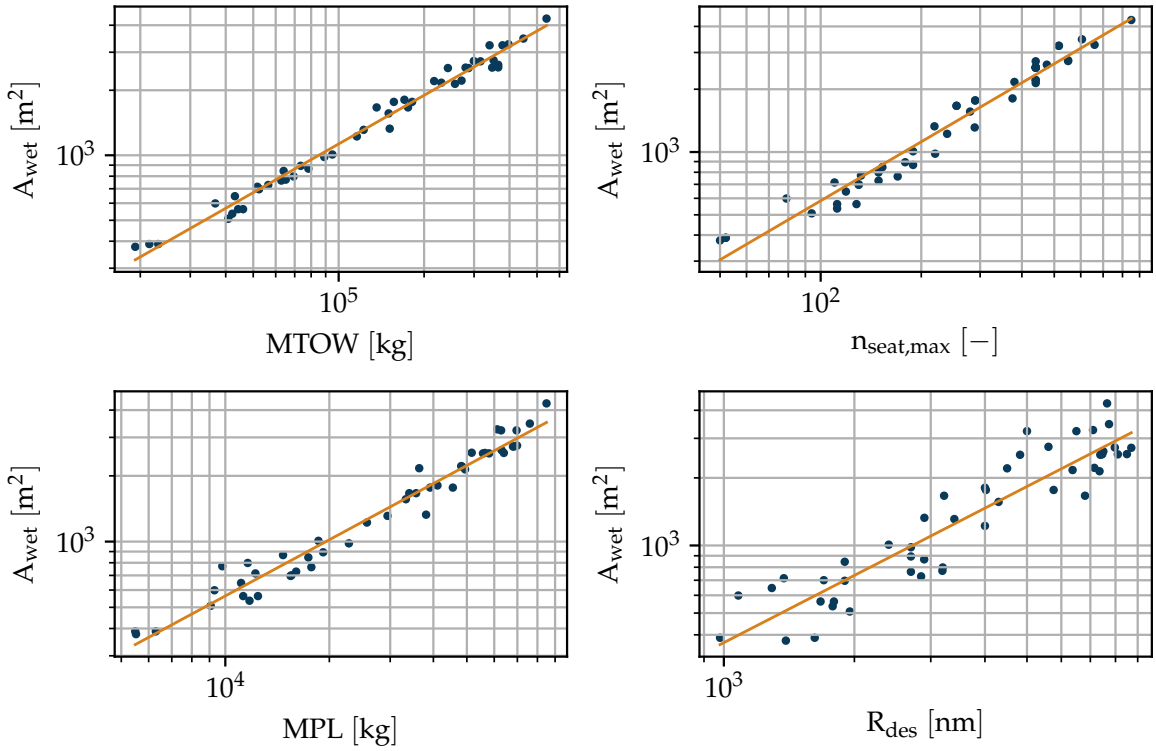

Figure 1. A_{wet} correlations with data from References [17–19].

The correlation of A_{wet} with R_{des} has a higher variance than the other three. A_{wet} correlates very well with $MTOW$, MPL and n_{max} ($r^2 > 0.95$). For this study, the $MTOW$ correlation is chosen because it has the highest r^2 value and $MTOW$ is the most general and robust aircraft parameter to compare against. It could also be used for retro fitted cargo aircraft, which is not possible for n_{max}. However,

the other correlations might be useful for a first A_{wet} assessment prior to the *MTOW* calculation in the conceptual design phase. The correlations are limited to their source data that is, they may not be used outside the range of the source data. They may be used for future aircraft that is, hybrid electric aircraft if no significant change in the respective correlation is expected due to for example technology changes. From the heat transfer modelling (cf. Section 3) it becomes apparent that solely knowing the total wetted area of the aircraft ($A_{wet,tot}$) is not sufficient even for the simple correlations that are used in this study. The distribution of $A_{wet,tot}$ among the component groups mentioned in Section 2.1 is investigated. No correlation is found with any of the x-parameters from Table 2. The share of each component of $A_{wet,tot}$ ($A_{wet,i}$) is rather constant. Therefore, a mean is applied and the results are listed together with the standard deviation (σ) for each mean in Table 3.

Table 3. $A_{wet,i}\,/\,A_{wet,tot}$ for each component.

Component	$A_{wet,i}/A_{wet,tot}$ (%)	σ (%)
Fuselage	49	3.80
Wing	31	3.55
Nacelles	7	1.49
Horizontal Tail	8	1.21
Vertical Tail	5	0.83

2.3. Propulsive Power

To put the available cooling power (Q_{av}) in perspective with the required cooling power (Q_{rq}) an estimation of the expected waste heat is necessary. The quantity of waste heat of a future propulsion system will depend on many factors, especially the propulsive power (P_{prop}), the transmission efficiency (η_{trans}), which includes all losses from shaft power (P_{shaft}) to P_{prop}, the Degree of Power Hybridization (H_P) [22] of the drive train and the overall electric efficiency (η_{ec}). Calculation of the exact heat loads over the entire mission are part of a detailed iterative design process. For a first estimation, simple methods are applied to estimate the waste heat during take-off, which is likely to be one of the most critical mission points with regards to cooling requirements. Starting from the take-off thrust (F_{TO}), which is available in the data set, Q_{rq} is derived:

$$Q_{rq} = (1 - \eta_{trans}) \cdot P_{prop} \cdot H_P \cdot (1 - \eta_{ec}) \tag{2}$$

with P_{prop} as:

$$P_{prop} = F_{TO} \cdot v_{TO} \tag{3}$$

With v_{TO} being the take-off velocity, which is calculated based on Sea Level (SL) conditions with $dT_{ISA} = 0$ and $Ma = 0.2$ as representative Ma_{TO}. The F_{TO} values are obtained from another linear fit of the log-log scaled data over *MTOW*. The resulting fit (Equation (4)) is shown in Figure 2. It has an r^2 value of 0.983.

$$log_{10}F_{TO} = 0.913 \cdot log_{10}MTOW + 0.895 \tag{4}$$

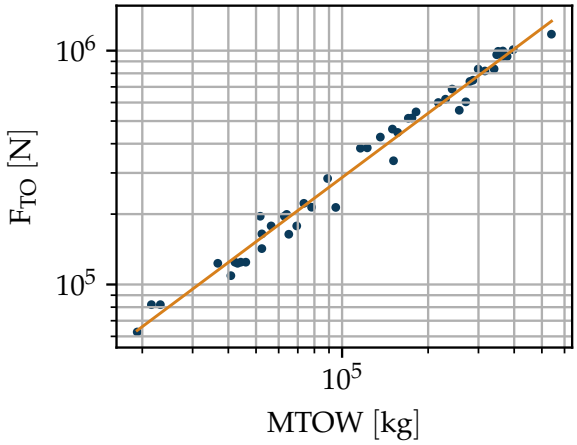

Figure 2. $MTOW$–F_{TO} correlation with data from References [17–19].

3. Surface Heat Transfer

In this section, the applied heat transfer models are described. The sensitivity of the methods to changes in geometry is tested and the impact of surface heating on drag is assessed.

3.1. Modeling

Flat plate models with uniform temperature distribution are used for heat transfer calculations for all components. Correlations for the local Nusselt number (Nu_x) from References [23–25] are applied to calculate local heat transfer coefficients (α_x), which requires a local discretization of the geometry in flow direction. The trapezoidal shaped components (wing and tail planes) are also discretized in span wise direction to account for the different flow lengths and corresponding Reynolds numbers (Re_x). Incoming solar radiation is accounted for in the overall heat balance by means of a material absorption coefficient and an incoming radiation power (P_{rad}) on all surfaces that are exposed to the sun. Unless stated otherwise an absorption coefficient of 0.25 typical of white paint and P_{rad} of 1362 W/m^2, which is the constant value outside earth's atmosphere [26] are assumed. For each component, half of A_{wet} is considered to be exposed to P_{rad}. Those are conservative assumptions since P_{rad} has a slightly lower value even at the highest flight levels than the above-mentioned value outside the atmosphere. Detailed descriptions of the used convection correlations and heat balances can be found in Reference [16]. The used 2D methods are less precise than for example 3D Computational Fluid Dynamics methods but they are sufficient for a first quantification of the surface cooling power in the conceptual design stage.

3.2. Sensitivities

The aforementioned local discretization of the heat transfer calculation depends on Re_x. Section 2.2 focuses on correlations of the total and component wise A_{wet}. However, to calculate Re_x more knowledge of the geometry is required. For example, two fuselages with the same A_{wet} have different Re_x distributions if their slenderness ratios (Λ) differ. To account for these effects, the geometric model of the components is refined. For cylindrical components (fuselage, nacelle) the sensitivity of Λ is studied:

$$\Lambda = l/d \tag{5}$$

With length (l) and diameter (d). Wing and tail components are modelled as single section trapezoids with no leading edge sweep. Their geometries, specifically the span-wise chord distribution can be fully defined with the help of their A_{exp}, aspect ratio (AR) and taper ratio (λ) [20]. The following sensitivity studies are conducted around TO conditions. It is one of the most critical conditions for TMS design, because of the low air flow velocities, high ambient temperatures (T_{amb}) and large cooling

demand (Q_{rq}) due to maximum propulsive power. Unless otherwise specified, the values in Table 4 are assumed for the wing sensitivity studies. The values are not specific to any aircraft but generally lie inside the range of the given data. $Re_{x,c}$ is the critical Reynolds number and T_{surf} the average surface temperature. In a real cooling application, the surface temperature would most likely not be uniform but have a gradient in the direction of a hot side flow underneath the surface. However, in this first approximation an average T_{surf} is assumed for simplification.

Table 4. Wing sensitivity study parameters.

Parameter	Value
A_{exp}	200 m^2
AR	12
λ	0.29
$Re_{x,c}$	5×10^5
T_{surf}	320 K

3.2.1. Transition Location

Flat plate heat transfer correlations distinguish between laminar and turbulent flow. They rely on the knowledge of a critical location (x_c) where transition occurs. Usually x_c is defined by $Re_{x,c}$ which according to Reference [24] is between 1×10^5 to 3×10^6 depending on free stream turbulence and surface roughness. Detailed transition modelling is a complex research area and beyond the scope of this work. However, a sensitivity study with varying $Re_{x,c}$ and Ma ranging from slow taxiing $Ma = 0.01$ to representative TO $Ma = 0.2$ is conducted. The results of the theoretically available cooling power (Q_{av}) as well as the relative Q_{av} compared to the Q_{av} at the lowest $Re_{x,c}$ for each Ma ($Q_{Re,x,c,min}$) are displayed in Figure 3.

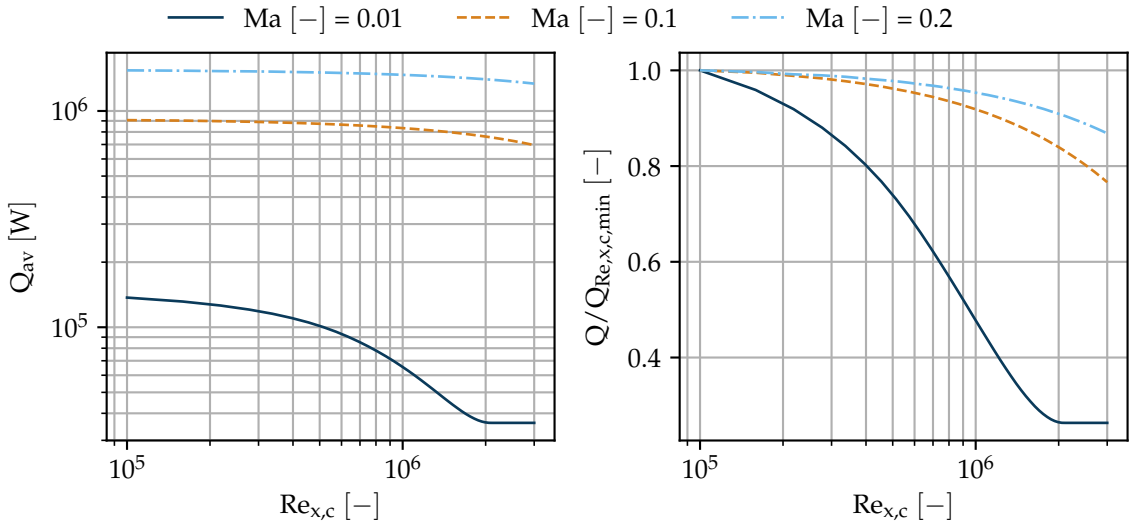

Figure 3. Transitional Reynolds number sensitivity.

An increased Ma results in increased Q_{av} because of the increased effects of forced convection. Shifting $Re_{x,c}$ to higher values, results in a decrease in Q_{av}. Turbulent flows favour heat transfer more than the structured flow in laminar regions because of the increased particle mixing within the boundary layer. With increased $Re_{x,c}$ the portion of A_{exp} with laminar flow increases. For very low Ma increasing $Re_{x,c}$ beyond 2×10^6 results in laminar flow on the entire surface. A further increase in $Re_{x,c}$ has no additional effect. The transition point has a large influence on Q_{av}. For 3D wings, transition is more complex than defining an $Re_{x,c}$ and assuming instantaneous transition. This study does not accurately account for real transition effects. The results in Section 4 assume fully turbulent

flow areas downstream the transition location. Therefore, the results of this study cannot directly be used for concepts with enhanced laminarity such as natural laminar flow (NLF) wings. Covering these advanced aerodynamic concepts is part of future work.

3.2.2. Wing Aspect Ratio

AR is varied from 6 to 18—a range that includes all aircraft used for the correlations in Section 2 and also leaves margin for possible future aircraft with increased AR. The results of Q_{av} as well as the relative Q_{av} compared to the Q_{av} at the lowest AR for each Ma ($Q_{AR,min}$) are displayed in Figure 4. For better comprehension of the trends in Figure 4, the effect of increasing AR on the local α_x distribution for the lowest and largest Ma are illustrated with heat maps in Figure 5.

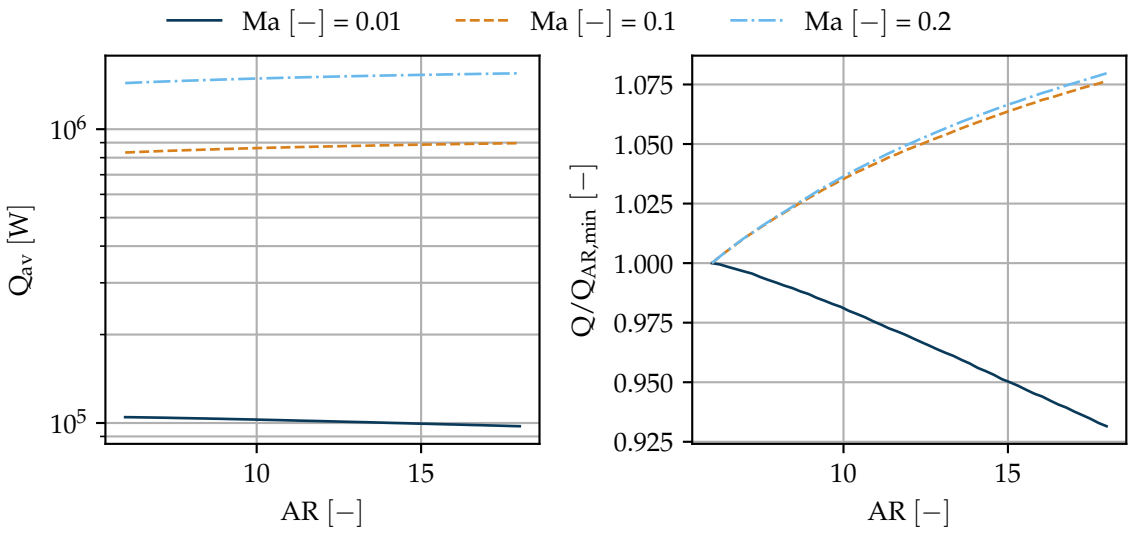

Figure 4. Wing aspect ratio sensitivity.

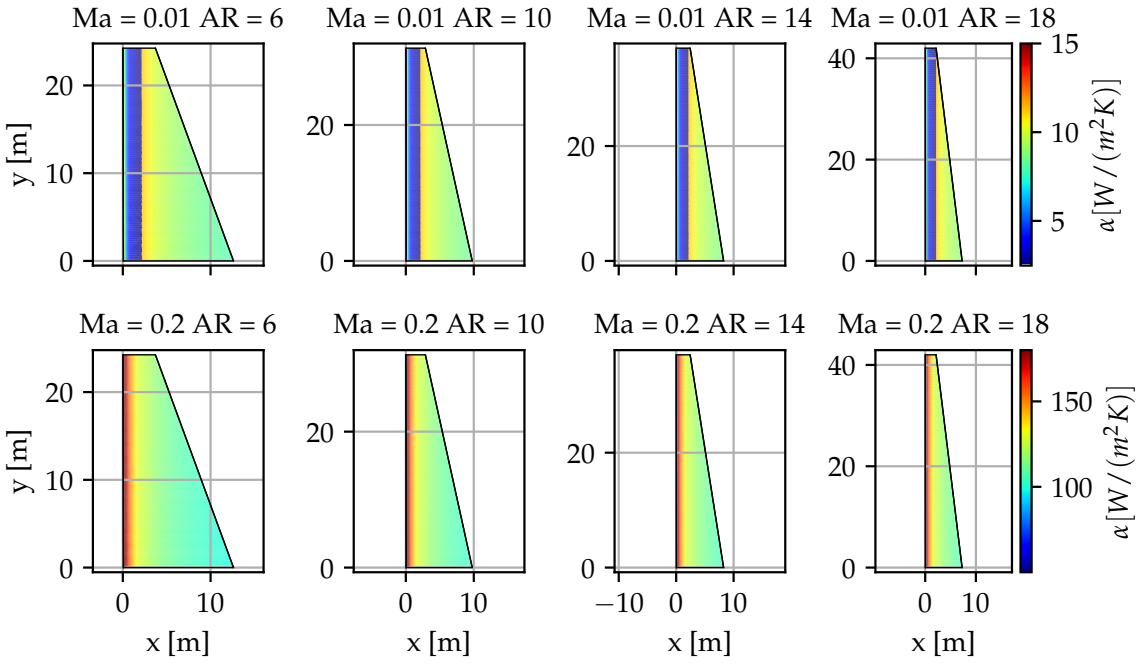

Figure 5. Local heat transfer coefficient for different Mach number–wing aspect ratio combinations.

Q_{av} increases with Ma, because the forced convection increases, due to increasing Re. Depending on Ma, Q_{av} increases or decreases with increasing AR. More specifically for the lowest Ma of 0.01, Q_{av} decreases with increasing AR. For all other Ma used in the study Q_{av} increases with AR. Two counteracting effects are the reason:

1. In general, α_x decreases along x because of the increasing thickness of the thermal boundary layer (δ_T). Therefore, higher AR favours heat transfer because for the same area, the average chord length is lower (cf. Figure 5 bottom graphs).
2. The front section of the wing is laminar, which results in small α_x. A higher AR increases the span and, thus, the laminar portion of the plate's total area (cf. Figure 5 top two graphs). The x_c depends on Ma. For low Ma the transition occurs further downstream, which means that this second effect contributes more.

Tripling the aspect ratio results in $\pm 8\%$ Q_{av} depending on Ma. The sensitivity is too weak for the expected precision of this study that aims to determine the order of magnitude of the surface cooling power. Hence, it is not regarded in the following studies.

3.2.3. Wing Taper Ratio

λ is varied between 0.1 and 1.0. The same Ma range as in the previous sections is applied. Variations in Q_{av} do not exceed $\pm 2\%$ with slight advantages for the non-tapered wings ($\lambda = 1.0$). The aforementioned effect of increasing flow length is positive for heat transfer of tapered wings near the wing tip but negative near the root, which leads to its equalization after integration over the entire span. As with the AR sensitivity, the effect is too small to be further considered in this work.

3.2.4. Fuselage Slenderness Ratio

For a fuselage with $A_{wet} = 1600\ \mathrm{m}^2$, Λ is varied from 5 to 15 within the same Ma range as the previous sensitivity analysis. Regardless of Ma, the change in Q_{av} from the lowest to the highest Λ value is around -8%, again due to the increasing flow length with increasing Λ. The effect is also within the expected precision of this study. For further investigations, $\Lambda = 12$ is used, which is conservative as it is one of the highest Λ values found in today's aircraft for example, for the Airbus A340-600.

3.3. Drag

For any aircraft component, which contributes to the aircraft's drag, local surface temperature can influence the aerodynamics of air passing the component surface at a certain velocity and with certain fluid characteristics. The two main occurring effects depending on the fluid's initial state are:

1. Transition delay of initially laminar flow
2. Drag alteration of fully turbulent flow

As the skin friction coefficient (c_f) is significantly smaller in laminar than in turbulent flow, total skin friction drag (D_f) of a surface can be decreased by moving the transition location downstream that is, by increasing the laminar length. During the last centuries, laminar flow control approaches have been studied intensively as a means to decrease drag. As such, surface temperature alteration can be employed to decrease the growth rate of unstable disturbances in the fluid and thus, to repress transition from laminar to turbulent flow [27]. The application of this method was shown in experiments by for example, References [27,28]. Two different approaches apply [29]:

1. Heating/cooling of the whole wetted surface area
2. Strategic heating/cooling of a part of the wetted surface area

In the two-dimensional case, Tollmien-Schlichting instabilities, which dominate the laminar boundary layer, are mitigated by cooling of the near wall boundary layer. In accordance with theory, flat plate experiments showed that the cooling of a surface leads to an increase of $Re_{x,c}$ and a

downstream movement of x_c [28]. The effect is reversed when the surface is heated: the destabilizing effect of the temperature increase in the boundary layer dominates and x_c moves upstream [27].

However, the stabilizing effect of cooling can also be utilized when a portion of the surface is heated at strategic locations. For a two-dimensional case, it was shown that heating a portion of a surface where stable laminar flow is present (preferably the leading edge) followed by a cool that is, unheated, "relaxation" surface downstream can lead to a preferable downstream movement of x_c. The heated wall has to be situated in the region where Tollmien-Schlichting waves start to develop in the laminar boundary layer. The temperature of the near wall boundary layer is increased and when the fluid reaches the cooler wall further downstream, the temperature of the boundary layer is higher than the wall temperature. The boundary layer is cooled down and the growth rate of the unstable disturbances is decreased. The transition point moves downstream. If the surface is heated in an unstable flow region, the effect is reversed [27,29,30].

In three-dimensional airflows, however, cross-flow instabilities determine the boundary layer. Dovgal et al. showed that in this case, a temperature increase of the near wall boundary layer fosters cross-flow instabilities no matter if the whole surface or only a part of the surface is heated. The transition location moves upstream resulting in an increased D_f [27,30]. Thus, for any three-dimensional aircraft component, localized and global surface heating in the laminar flow region facilitates laminar to turbulent transition and increases D_f.

In contrast, when the boundary layer is fully turbulent, different mechanisms govern the flow: Heating of the near wall boundary layer reduces the turbulent D_f. Kramer et al. conducted wind tunnel experiments and flight tests in 1999. They found that an increase of the near wall boundary layer temperature leads to a decrease of Re_x, which in turn leads to a reduced local skin friction force [31]. For a body similar to a fuselage, they showed that the heating of the fore body leads to a higher drag reduction than the heating of the aft body, whereas the heating of the whole body has the highest drag reduction potential. The findings are supported by a numerical evaluation of the effect of heating on the turbulent boundary layer flow over slender and bluff fuselage-like bodies conducted by Lin and Ash in 1986 [32]. The following theoretical deviation of D_f as a function of wall heating for a smooth flat plate is based on the deviation proposed by Reference [31].

The length Reynolds number is defined as:

$$Re_x = \frac{\rho \cdot v \cdot x}{\mu} \tag{6}$$

For $Re_x = 10^6 - 10^8$, the turbulent c_f for a flat plate of length x can be expressed with $K = 0.036$, $m = 6$ by Reference [33]:

$$c_f = \frac{K}{Re_x^{\frac{1}{m}}} \tag{7}$$

Total skin friction drag of a flat plate with the length x and total area A for a turbulent boundary layer is defined as [33]:

$$D_f = c_f \cdot \frac{1}{2} \cdot \rho \cdot v^2 \cdot A = \frac{0.036}{2} \cdot \frac{\rho}{\rho^{\frac{1}{6}}} \cdot \frac{v^2}{v^{\frac{1}{6}}} \cdot x^{\frac{1}{6}} \cdot \mu^{\frac{1}{6}} \cdot A. \tag{8}$$

Assuming a constant heated surface temperature (T_h) along x, the temperature ratio of unheated air (T_u) and T_h is defined as:

$$TR = \frac{T_h}{T_u} \tag{9}$$

Applying the ideal gas law leads to $\rho = f(1/T)$ and the dynamic viscosity of air can be simplified to $\mu = f(T)$. Thus:

$$\frac{\rho_h}{\rho_u} = \frac{T_u}{T_h} = \frac{1}{TR} \tag{10}$$

$$\frac{\mu_h}{\mu_u} = \frac{T_h}{T_u} = TR \tag{11}$$

$$\frac{Re_{x,h}}{Re_{x,u}} = \frac{\rho_h \cdot v_h \cdot \mu_u}{\rho_u \cdot v_u \cdot \mu_h} = \left(\frac{1}{TR}\right)^2 \tag{12}$$

When the wall is heated ($TR > 1$), Re_x decreases with increased temperature. In consequence, c_f increases. However, the change in ρ has a larger effect on D_f than the change in c_f:

$$\frac{D_{f,h}}{D_{f,u}} = \frac{\rho_h^{\frac{5}{6}}}{\rho_u^{\frac{5}{6}}} \cdot \frac{\mu_u^{\frac{1}{6}}}{\mu_h^{\frac{1}{6}}} = \left(\frac{1}{TR}\right)^{\frac{5}{6}} \cdot TR^{\frac{1}{6}} = \left(\frac{1}{TR}\right)^{\frac{2}{3}} \tag{13}$$

and therefore if $T_h > T_u \rightarrow D_{f,h} < D_{f,u}$. The higher the wall temperature compared to the ambient temperature, the higher the drag decreasing potential. All simplified relations are depicted in Figure 6.

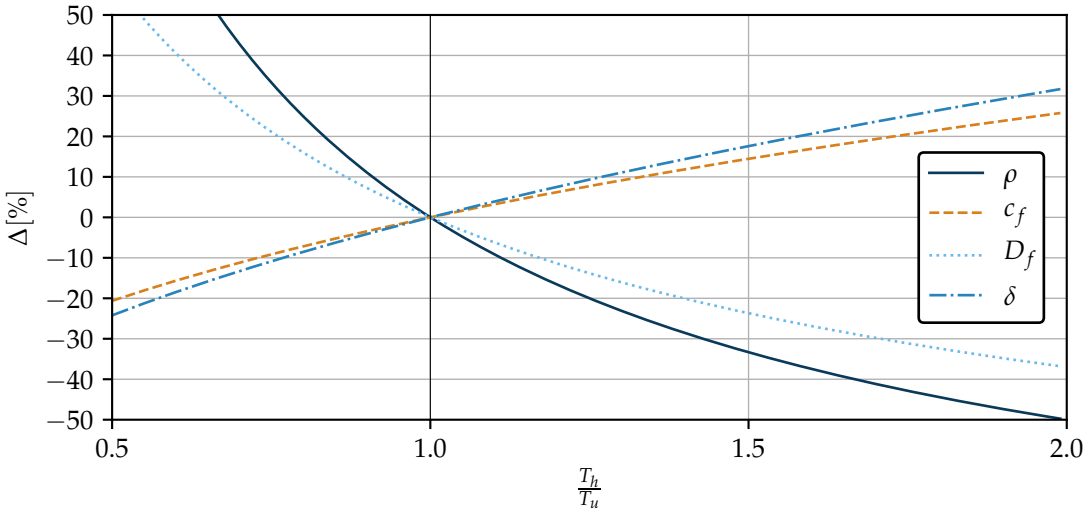

Figure 6. Theoretical impact of wall heating/cooling on a smooth flat plate turbulent boundary layer density, skin friction coefficient, skin friction drag force and boundary layer 99% thickness compared to an unheated wall. Valid for $Re_x = 10^6 - 10^8$.

Wall heating not only has an impact on skin friction drag but also effects the pressure drag. The turbulent boundary layer velocity profile thickens, because [34]:

$$\delta = \frac{0.37x}{Re_x^{\frac{1}{5}}}. \tag{14}$$

For a flat plate, the pressure gradient is zero at all locations. For a slender body (fuselage) or lifting surface (wing, tail planes), however, the pressure gradient varies in stream wise direction. Therefore, for a three-dimensional curved body, the heating of the wall has an effect on the (not-separated) pressure drag as shown by Lin and Ash. The heating of the wall increases the turbulent displacement thickness (δ^*), which in turn leads to a slight increase in pressure drag [32]. In addition, the boundary layer shape factor is increased. Thus, the adverse pressure gradient is increased, causing an earlier

flow separation [32,35]. The effect of wall heating on pressure drag is small compared to the effect on skin friction drag [32].

In summary, in regions in which the boundary layer is laminar, an increased temperature leads to an earlier transition and, thus, to an increase in total D_f. To make use of the beneficial effect of wall heating on the turbulent drag force, the surface of aircraft components should preferably be heated only in regions in which a fully turbulent boundary layer is present. This means that for example, the fuselage nose (cockpit area) or wing leading edge (slats etc.) should not be used for heat disposal. For aircraft concepts that unite different technologies, which emit excessive heat and aim at an increased laminar flow control, detailed studies have to be conducted, compromising excessive heat disposal and drag reduction approaches.

4. Surface Cooling Potential

For the following studies the simple correlations derived in Sections 2 and 3 are combined to estimate Q_{av} depending on $MTOW$. The calculated A_{wet} is reduced for each component to account for more realistic cases with unusable surface area in each component. These reductions are based on observations and estimations from drawings in manufacturer's documents such as in References [18,19].

4.1. Area Reduction Assumptions

In Section 3.3 it was shown that heating surfaces underneath laminar flow has a negative effect on aircraft drag. Therefore, areas at the front of each component are avoided as locations for surface heat exchangers. Independent of the size of the aircraft, the first 4 m of the fuselage are not used because cockpit, sensors and nose landing gear bay are located here. In addition, the contraction of this part is responsible for the overestimation of A_{wet} of the fuselage in Section 2. The rear 15% of the fuselage length are also not used because of the tail plane attachments, the auxiliary power unit (APU) and again the contraction that lead to an overestimation of A_{wet}. For the remaining fuselage middle section, a stripe of 0.5 m width is spared on both sides to account for the windows. Another 10% is subtracted from the total middle section area to account for passenger doors, cargo doors and landing gear doors as well as sensors and air openings. The wing leading edge and trailing edge (20% chord length each) cannot be used as a heat sink due to slats, flaps and other control surfaces. Only the forward 50% of the nacelle length is used to account for possible thrust reversers installed in the back. The rear 33% of the horizontal and vertical tail plane's chord length are not used because of the installed control surfaces. In the following, all remaining surfaces are employed for heat rejection.

4.2. Cooling Potential for Typical Operating Points

Q_{av} is investigated in multiple typical operating points: TO, HTO, CL and Cruise CR. The atmospheric conditions (Ma, alt and dT_{ISA}) of each operating point are listed in Table 5. The design space includes $MTOW$ over the entire range of the database used in Section 2.1 as well as T_{surf} ranging from 320 K to 400 K. T_{surf} has to be lower than the maximum allowed operating temperature of electric components, which for motors can be up to 180 °C [36] but are significantly lower for batteries. The actual T_{surf} depends on the installed drive train and the hot side of the cooling system. This study shows Q_{av} for a wide range of T_{surf} in Figure 7.

Table 5. Investigated operating points.

Opearting Point	Ma (-)	alt (m)	dT_{ISA} (K)
TO	0.2	0	0
HTO	0.2	0	+20
CL	0.5	5000	0
CR	0.8	10,000	0

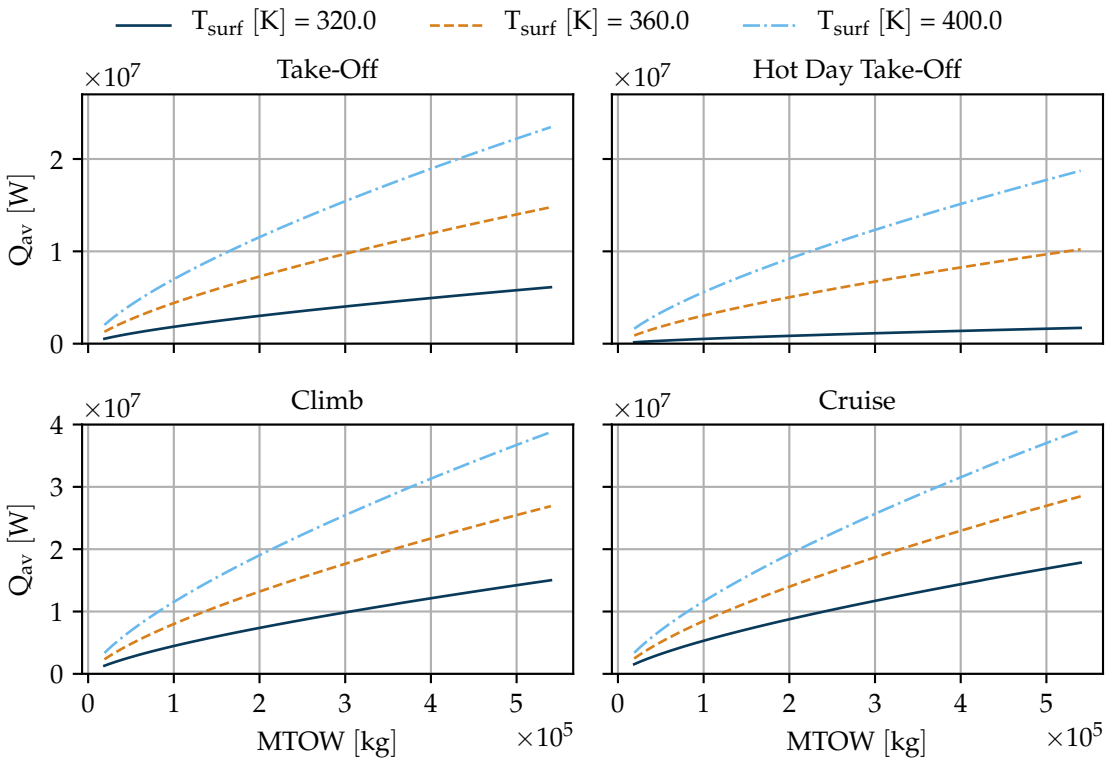

Figure 7. Q_{av} in multiple operating points for aircraft equipped with surface heat exchangers.

Figure 7 can be used to estimate Q_{av} of any tube and wing aircraft with known $MTOW$. For example, the A320 sized aircraft from Section 2.2 has an $MTOW$ of 71,000 kg. Assuming T_{surf} of 360 K an estimated Q_{av} of approximately 250 kW in HTO—the most critical condition—results. In contrast, the same aircraft with the same T_{surf} would be able to reject about 7 MW of heat in CR. In all operating points, Q_{av} increases with $MTOW$, because A_{wet} increases. The slope of Q_{av} decreases with $MTOW$, because the $MTOW$–A_{wet} correlation is weakly logarithmic and because aircraft with higher $MTOW$ have increased flow lengths on all surfaces, which results in lower α_x towards their rear ends (cf. Section 3.2). Q_{av} also increases with increasing T_{surf} due to the higher temperature difference to the ambient. In the HTO case, Q_{av} is about five times as large for $T_{surf} = 360$ K than the value corresponding with $T_{surf} = 320$ K over the entire $MTOW$ range. The high sensitivity is due to a relatively high ambient temperature (T_{amb}), resulting in an increase of heat transfer driving temperature difference (ΔT) from Δ12 K to Δ52 K (roughly factor five). For CL and CR the relative T_{surf} sensitivity is not as strong because T_{amb} is lower. Over the entire $MTOW$ range, Q_{av} is about twice as large for CR and CL compared to TO. The ratio even increases when comparing CR and CL to HTO. The reasons for this large difference are the lower T_{amb} in CL and CR compared to TO and HTO as well as the higher Ma that increases convection. The difference in Q_{av} between CL and CR is approximately 10% over the entire $MTOW$ range for $T_{surf} = 320$ K. The difference is less for higher T_{surf} and hardly noticeable for the largest T_{surf} of 400 K. CR has a lower T_{amb} than CL which results in a larger ΔT. The relative difference between ΔT_{CL} and ΔT_{CR} decreases with increasing T_{surf}. Also, for heat transfer, the total T_{amb} is relevant and due to the increased Ma in CR it is not smaller by the same ratio compared to CL as the static T_{amb}. The increased flight speed should additionally result in higher Nu in CR but the effect is reduced by the lower ρ_{amb}. More elaborate studies on the dependence of forced convection on flight conditions can be found in [16].

4.3. Hot Day Take-Off Performance

Results from the previous section indicate that HTO is the condition with minimum Q_{av}. Additionally, the propulsive power is usually at its maximum during TO, which means Q_{rq} is at its maximum as well.

For an aircraft application, the most relevant metric is the ratio of Q_{av} to Q_{rq} (C_Q). The following study is conducted for HTO conditions. Q_{rq} differs depending on the electric architecture and the mission profile amongst others. For the first part of this study a fully power hybridized aircraft ($H_P = 1$) is assumed with estimated values for the efficiencies required by the methods shown in Section 2.3 listed in Table 6. The effect of varying $MTOW$ over the entire range of the database (cf. Section 2.1) as well as T_{surf} ranging from 320K to 400K is investigated. The results are shown in Figure 8a. For the second part of the study different H_P values are assumed and the required T_{surf} to achieve $C_Q = 1$ that is, a Q_{av} that matches Q_{rq} is investigated. Figure 8b shows the results.

Table 6. Values for the estimation of Q_{rq}.

η_{trans}	0.5
η_{ec}	0.9
H_P	1.0
Ma_{TO}	0.2

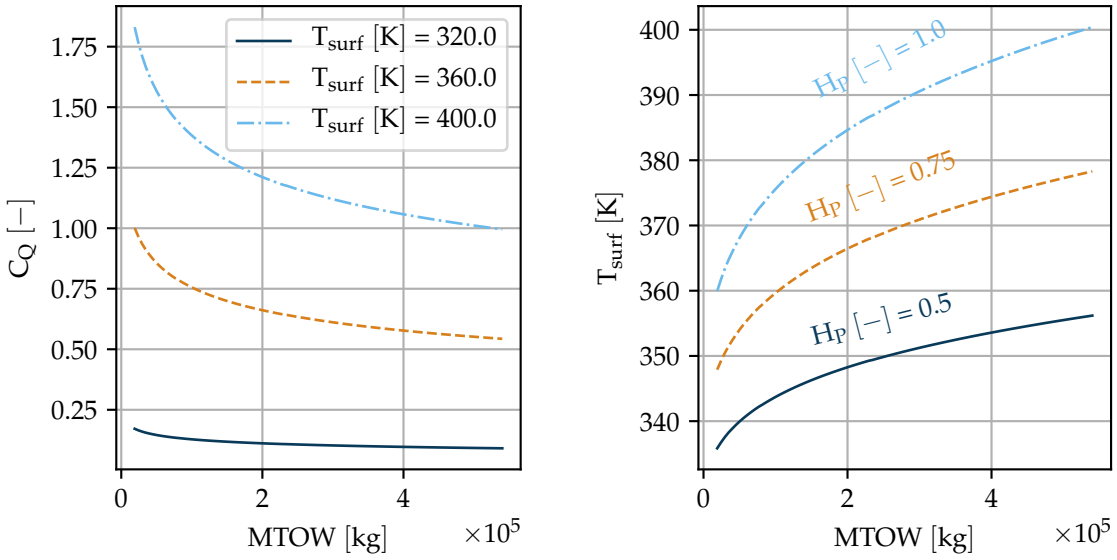

(**a**) (**b**)

Figure 8. Comparison of Q_{av} and Q_{rq} for hybrid electric aircraft in hot day take-off conditions. (**a**) Ratio of Q_{av} to Q_{rq} for different T_{surf}. (**b**) Required T_{surf} to achieve $C_Q = 1$.

A first observation is that Q_{av} and Q_{rq} are within the same order of magnitude during HTO. Within the used parameter ranges values above and below unity exist for C_Q. C_Q is decreasing linearly with T_{surf} and hyperbolically with $MTOW$. Smaller aircraft have a favourable C_Q. This is mainly due to the increased flow length on all surfaces of larger aircraft but also due to the weakly logarithmic behaviour of the $MTOW$–A_{wet} correlation. For the smallest considered aircraft, C_Q ranges between 0.2 and 1.8 depending on T_{surf}. In contrast, the C_Q range for the largest considered aircraft is between 0.1 and 1.0. In Figure 8b the required T_{surf} during HTO to achieve $C_Q = 1$ is depicted for different H_P. T_{surf} grows linearly with H_P because Q_{rq} increases proportionally to H_P. T_{surf} grows logarithmically with $MTOW$, which is expected from Figure 8a: Smaller aircraft have an advantage over large aircraft with regards to potential cooling via existing aircraft surfaces. Taking the A320 sized aircraft from Section 2.1 ($MTOW$ = 71,000 kg) as an example again with $H_P = 1$, Figure 8b shows that T_{surf} of about 370 K would be required during HTO to provide enough cooling power for the waste heat load of the drive train. Heating up the surface to an average T_{surf} of 370 K is going to be challenging in an application with low grade waste heat potentially involving artificial measures such as vapour compression cycles to increase the temperature at which heat is rejected. However, such systems add weight and need power, which might diminish the benefits from a surface cooling system on aircraft

level. A comparison of a conventional cooling system with a surface cooling system on aircraft level will be performed in future studies. The results shown in Figure 8 are for steady state cooling in the most adverse conditions. A dynamic model might reveal that requiring steady state cooling during TO is unnecessary because thermal inertia of components and fluids can cope with temporarily high heat loads that is, $Q_{rq} > Q_{av}$. The dynamic behaviour of surface cooling systems will also be part of future work. The feasibility of using surface heat exchangers for cooling highly depends on Q_{rq} and the requirements for T_{surf} are more relaxed for $H_P < 1$. For the aforementioned example reducing H_P to 0.5 results in a 30 K decrease in required T_{surf} to about 340 K. Thus, surface cooling might be a viable option for aircraft with lower H_P or can be used in combination with a conventional cooling system for aircraft with large electrification to reduce heat exchanger size and drag.

5. Conclusions and Outlook

The potential of using the existing aircraft surfaces as heat sink for the waste heat of a (hybrid-) electric drive train was investigated. First, empirical correlations were derived to predict an aircraft's wetted area (A_{wet}) from its maximum take-off weight ($MTOW$). The database included aircraft ranging from small regional aircraft to large twin aisle aircraft. The chosen correlation was a fit of the log-log scaled data that had a coefficient of determination (r^2) of 0.986. To assess the ratio of available cooling power to required cooling power (C_Q), a simple estimation of the waste heat based on take-off thrust was used. Heat transfer from wetted surfaces was modelled via flat plate correlations. To apply them, the total A_{wet} was divided into five component groups: fuselage, wing, nacelles, horizontal tail and vertical tail. The mean of the relative area share was calculated for each component.

Sensitivities of the heat transfer model were studied. The flow transition had a considerable impact on the predicted heat flow. The applied methods in this work did not include accurate transition prediction. The detailed analysis of the heat transfer potential of surfaces with large laminar shares are part of future work while the results of this study may be used for concepts where turbulent flow dominates. Other sensitivities investigated were wing taper ratio and aspect ratio as well as fuselage slenderness ratio. Their impact was too small to be further considered because it was below the expected uncertainty level from the modelling simplifications. A qualitative assessment of the impact of surface heating on the aircraft's drag was performed. When heat is added to a laminar flow region an increase in skin friction drag is expected. The opposite is true for fully turbulent flow regions where heat addition reduces skin friction drag. A quantification of the expected effects is part of future work. Combining the findings for the drag with the flow transition sensitivity of the heat transfer leads to the conclusion that surface heat exchangers should only be installed in fully turbulent flow regimes to avoid a negative impact of surface heating on the aircraft aerodynamics.

Additional area reductions to account for unusable surface area for example, windows, landing gear doors and cockpit were applied and available cooling power (Q_{av}) were calculated for a range of $MTOW$ over the entire database and average surface temperatures (T_{surf}) between 320 K and 400 K. Q_{av} was evaluated in four operating points: Take-off (TO), Hot Day Take-off (HTO), Climb (CL) and Cruise (CR). Q_{av} was largest in CR with about 7 MW for an A320 size aircraft and a medium T_{surf} of 360 K. The most critical operating point was HTO with Q_{av} of only 0.25 MW for the aforementioned aircraft and T_{surf}.

C_Q was calculated in HTO. The smallest aircraft showed an advantage over larger aircraft with C_Q values ranging from 0.2 to 1.8 depending on T_{surf} compared to 0.1 to 1.0 for the largest aircraft.

The results of this study may be used to quickly assess the feasibility of a surface cooling concept for a (hybrid-) electric aircraft. Future work will include more detailed models for surface heat transfer. Instead of assuming an average T_{surf}, surface heat exchangers with a hot side flow will be modelled. These models that can also be used in a dynamic simulation will allow a more detailed sizing of the thermal management system. To assess heat transfer more precisely in a 3D flow field, numerical methods will be developed Those methods may go beyond the scope of a conceptual aircraft analysis and are part of more in-depth studies later in the design process.

The impact of adding heat to the boundary layer has only been qualitatively assessed in this work. Numerical methods will help to quantify the effect. Together with improved drag predictions, mass and power estimations the concept will be compared to a similar aircraft with a conventional cooling system to quantify its benefits. In addition, structural integration of surface heat exchangers may be a challenge. The concept will be evaluated with regard to maintainability.

Author Contributions: Conceptualization, methodology, simulation, analysis and writing of all aspects of the research except for Section 3.3, H.K.; Conceptualization, methodology, simulation, analysis and writing of Section 3.3, A.L.H.; Supervision, M.H. All authors have read and agreed to the published version of the manuscript.

Funding: This research received funding as part of SynergIE, a research project supported by the Federal Ministry for Economic Affairs and Energy in the national LuFo V program. Any opinions, findings and conclusions expressed in this document are those of the authors and do not necessarily reflect the views of the other project partners.

Acknowledgments: The authors would like to thank Arne Seitz for his continued support of the research, his critical review and many fruitful discussions.

Conflicts of Interest: The authors declare no conflict of interest. The funders had no role in the design of the study; in the collection, analyses, or interpretation of data; in the writing of the manuscript, or in the decision to publish the results.

Abbreviations

SRIA	Strategic Research and Innovation Agenda
TMS	Thermal Management System
ISA	International Standard Atmosphere
TO	Take-off
HTO	Hot Day Take-off
CL	Climb
CR	Cruise
ACOC	Air Cooled Oil Cooler
SACOC	Surface Air Cooled Oil Cooler
APU	Auxilliary Power Unit
MTOW	Maximum Take-off Weight
MPL	Maximum Payload
Roman Symbols	
A	Area
dT	Temperature deviation
T	Temperature
alt	Altitude
Ma	Mach number
Q	Heat rate
n	Number
R	Range
r^2	Coefficient of determination
H	Degree of Hybrdization
P	Power
F	Thrust
v	Velocity
Nu	Nusselt Number
Re	Reynolds Number
AR	Aspect Ratio
l	Length
d	Diameter
x	Coordinate in flow direction
c	Coefficient
D	Drag Force
TR	Temperature Ratio
C_Q	Ratio of Heat Rates

Greek Symbols

σ	Standard deviation
δ	Boundary layer thickness
Δ	Difference
η	Efficiency
α	Heat transfer coefficient
λ	Wing taper ratio
Λ	Slenderness ratio
ρ	Density
μ	Dynamic Viscosity

Subscripts

wet	wetted
rq	required
exp	exposed
sim	simplified
act	actual
max	maximum
des	design
tot	total
av	available
trans	transmission
ec	electric
rad	radiation
surf	surface
c	critical
min	minimum
f	friction
h	heated
u	unheated
amb	ambient

References

1. Advisory Council for Aviation Research and Innovation in Europe. *Strategic Research and Innovation Agenda: Volume 1: 2017 Update*; Advisory Council for Aviation Research and Innovation in Europe: Brussels, Belgium, 2017.
2. Yakinthos, K.; Donnerhack, S.; Misirlis, D.; Flouros, M.; Vlahostergios, Z.; Goulas, A. Intercooled Recuperated Aero Engine: Early Development Stages and Optimization of Recuperation Based on Conventional Heat Exchangers. In Proceedings of the 2nd ECATS Conference, Athens, Greece, 7–9 November 2016.
3. Kaiser, S.; Kellermann, H.; Nickl, M.; Seitz, A. A Composite Cycle Engine Concept for Year 2050. In Proceedings of the 31st Congress of the International Council of the Aeronautical Sciences, Belo Horizonte, Brazil, 9–14 September 2018.
4. Jacob, F.; Rolt, A.; Sebastiampillai, J.; Sethi, V.; Belmonte, M.; Cobas, P. Performance of a Supercritical CO_2 Bottoming Cycle for Aero Applications. *Appl. Sci.* **2017**, *7*, 255. [CrossRef]
5. Rosero, J.A.; Ortega, J.A.; Aldabas, E.; Romeral, L. Moving towards a more electric aircraft. *IEEE Aerosp. Electron. Syst. Mag.* **2007**, *22*, 3–9. [CrossRef]
6. Pornet, C.; Isikveren, A.T. Conceptual design of hybrid-electric transport aircraft. *Prog. Aerosp. Sci.* **2015**, *79*, 114–135. [CrossRef]
7. Schlabe, D.; Lienig, J. *Model-Based Thermal Management Functions for Aircraft Systems*; SAE Technical Paper Series; SAE International: Warrendale, PA, USA, 2014. [CrossRef]
8. Wang, T.; Britcher, C.; Martin, P. Surface heat exchangers for aircraft applications—A technical review and historical survey. In Proceedings of the 37th Aerospace Sciences Meeting and Exhibit, Reno, NV, USA, 11–14 January 1999; American Institute of Aeronautics and Astronautics: Reston, VA, USA, 1999; p. 245. [CrossRef]

9. Wilkinson, S.P. Interactive wall turbulence control. In *Viscous Drag Reduction in Boundary Layers*; Bushnell, D.M., Hefner, J.N., Eds.; Progress in Astronautics and Aeronautics; American Institute of Aeronautics and Astronautics: Reston, VA, USA, 1990.
10. Sousa, J.; Villafañe, L.; Paniagua, G. Thermal analysis and modeling of surface heat exchangers operating in the transonic regime. *Energy* **2014**, *64*, 961–969. [CrossRef]
11. European Commission. *Surface Heat Exchangers for Aero-Engines*; European Commission: Brussels, Belgium, 2016.
12. European Commission. *Surface Heat Exchangers For Aero Engines 2*; European Commission: Brussels, Belgium, 2019.
13. European Commission. *Aerodynamic upgrade of Surface Air Cooled Oil Cooler*; European Commission: Brussels, Belgium, 2019.
14. Sakuma, Y.; Saito, H.; Watanabe, T.; Himeno, T.; Inoue, C.; Tomida, S.; Takahashi, N. Conjugate Heat Tansfer Analysis on Plate Fin Surface Air Cooled Oil Cooler. In Proceedings of the Shanghai 2017 Global Power and Propulsion Forum, Shanghai, China, 30 October–1 November 2017.
15. Liu, J.; Peck, J.; Yazawa, K.; Fisher, T.S.; Shih, T.I.P. Bypass, Loss, and Heat Transfer in Aircraft Surface Coolers. *Front. Mech. Eng.* **2019**, *5*, 219. [CrossRef]
16. Kellermann, H.; Habermann, A.L.; Vratny, P.C.; Hornung, M. Assessment of Fuel as Alternative Heat Sink for Future Aircraft. *Appl. Therm. Eng.* **2019**, under review.
17. Jenkinson, L.; Simpkin, P.; Rhodes, D. *Civil Jet Aircraft Design*; American Institute of Aeronautics and Astronautics, Inc.: Washington, DC, USA, 1999. [CrossRef]
18. Boeing Commercial Airplanes. *747-8 Airplane Characteristics for Airport Planning*; Boeing Commercial Airplanes: Seattle, WA, USA, 2012.
19. Airbus S.A.S. *A350 Aircraft Characteristics Airport and Maintenance Planning*; Airbus S.A.S.: Blagnac, France, 2016.
20. Torenbeek, E. *Synthesis of Subsonic Airplane Design: An introduction to the Preliminary Design of Subsonic General Aviation and Transport Aircraft, with Emphasis on Layout, Aerodynamic Design, Propulsion and Performance*; Springer: Dordrecht, The Netherlands, 2010.
21. Pornet, C.; Gologan, C.; Vratny, P.C.; Seitz, A.; Schmitz, O.; Isikveren, A.T.; Hornung, M. Methodology for Sizing and Performance Assessment of Hybrid Energy Aircraft. In Proceedings of the 2013 Aviation Technology, Integration, and Operations Conference, Los Angeles, CA, USA, 12–14 August 2013; American Institute of Aeronautics and Astronautics: Reston, VA, USA, 2013; p. 35. [CrossRef]
22. Lorenz, L.; Seitz, A.; Kuhn, H.; Sizmann, A. Hybrid Power Trains for Future Mobility. In Proceedings of the 62. Deutscher Luft- und Raumfahrtkongress, Stuttgart, Germany, 10–12 September 2013; Deutsche Gesellschaft für Luft- und Raumfahrt: Bonn, Germany, 2013.
23. Haaland, S.E. Simple and Explicit Formulas for the Friction Factor in Turbulent Pipe Flow. *J. Fluids Eng.* **1983**, *105*, 89. [CrossRef]
24. Incropera, F.P.; DeWitt, D.P.; Bergman, T.L.; Lavine, A.S. *Principles of Heat and Mass Transfer*, 7th ed.; International Student Version; Wiley: Singapore, 2013.
25. Schultz-Grunow, F. New frictional resistance law for smooth plates. *Luftfahrtforschung* **1940**, *1940*, 239–246.
26. Henninger, J.H. *Solar Absorptance and Thermal Emittance of Some Common Spacecraft Thermal-Control Coatings*; NASA Goddard Space Flight Center: Greenbelt, MD, USA, 1984.
27. Arnal, D.; Reneaux, J.; Casalis, G. Numerical and Experimental Studies Related to Skin Friction Drag Reduction Problems. Proceedings of the Colloquium Transitional Boundary Layers in Aeronautics. 1996. Available online: https://www.dwc.knaw.nl/DL/publications/PU00011219.pdf (accessed on 19 November 2019).
28. Reshotko, E. Drag Reduction by Cooling in Hydrogen-Fueled Aircraft. *J. Aircr.* **1979**, *16*, 584–590. [CrossRef]
29. Masad, J.A.; Nayfeh, A.H. Laminar flow control of subsonic boundary layers by suction and heat–transfer strips. *Phys. Fluids A Fluid Dyn.* **1992**, *4*, 1259–1272. [CrossRef]
30. Dovgal, A.V.; Levchenko, V.; Timopeev, V.A. Boundary Layer Control by a Local Heating of the Wall. In *Laminar-Turbulent Transition*; Springer: Berlin/Heidelberg, Germany, 1990; pp. 113–121.
31. Kramer, B.; Smith, B.; Heid, J.; Noffz, G.; Richwine, D.; Ng, T. Drag reduction experiments using boundary layer heating. In Proceedings of the 37th Aerospace Sciences Meeting and Exhibit, Reno, NV, USA, 11–14 January 1999. [CrossRef]
32. Lin, J.C.; Ash, R. Wall temperature control of low-speed body drag. *J. Aircr.* **1986**, *23*, 93–94. [CrossRef]

33. Hoerner, S.F. *Fluid-Dynamic Drag: Theoretical, Experimental and Statistical Information*; Hoerner Fluid Dynamics: Bakersfield, CA, USA, 1965.
34. Schlichting, H.; Gersten, K. *Boundary-Layer Theory*; Springer: Berlin/Heidelberg, Germany, 1979. [CrossRef]
35. Spalart, P.R.; Watmuff, J.H. Experimental and numerical study of a turbulent boundary layer with pressure gradients. *J. Fluid Mech.* **1993**, *249*, 337–371. [CrossRef]
36. Ohta, S. Temperature Classes of Electrical Insulators. *Three Bond Technical News*, 1 December 1985.

2.3 Assessment of Fuel as Alternative Heat Sink for Future Aircraft

The paper [3] presents methods and results for the assessment of fuel as a heat sink for aircraft using a 180-passenger hybrid electric aircraft as an application case. It is structured into five major sections.

The first section "Introduction" motivates the idea of using fuel as a heat sink with the increasing trend in waste heat production of future powertrains onboard aircraft. TMSs utilizing fuel could possibly operate drag-free and thereby have an advantage of R-HEXs. The state of the art is also discussed in Section 1 and the objective, as well as the procedure of the paper, is presented. Section 1 was conceptualized and written by Hagen Kellermann.

The second section "Conceptualization" presents the two concepts considered for fuel cooling. The WIFHE uses S-HEXs filled with fuel underneath the wing surfaces to cool previously heated fuel, which reenters the tanks. The second concept is the Tank with Internal Heating (TWIH): a HEX is placed inside the tank heating the fuel. Section 2 concludes with two paragraphs introducing the reference aircraft, which were written and conceptualized by Patrick Vratny. All other parts of Section 2 were written and conceptualized by Hagen Kellermann.

The third section "Concept modeling" explains the physical models that were developed for the different concepts of Section 2 as well as a reference R-HEX (Section 3.3) and the methods to estimate the overall aircraft level impact (Section 3.4). The models of the WIFHE and TWIH were a combination of mostly analytical fluid- and thermodynamic equations. The outer heat transfer via the wing surfaces was simplified by assuming flat plate convection. The internal heat transfer was modeled as forced convection in rectangular ducts for the WIFHE and natural convection inside a cavity for the TWIH. Together with the wall resistance, overall heat transfer coefficients were calculated. The models were spatially discretized. For the R-HEX, mainly empirical correlations were used to estimate the drag of the overall system consisting of a NACA inlet, diffuser, HEX, nozzle, and NACA outlet. The aircraft level impact was calculated via mass and drag trade factors. Section 3 was conceptualized and written by Hagen Kellermann, except for Section 3.3, which was conceptualized and written by Anais Habermann, and Section 3.4, which was conceptualized and written by Patrick Vratny.

The fourth section "Results and discussion" presents all findings. The first two subsections show the partial dependence analyses for the WIFHE (Section 4.1) and TWIH (Section 4.2) concepts respectively. All relevant input variables are varied and the model's response in the major output values is plotted. An understanding of the model is gained and some variables are excluded in future analyses due to their insignificance, e.g., the radial heat emission rate. The results of applying the two concepts to different operating points on the application case are presented in Section 4.3. The available Q is compared to the required Q in every operating point. Overall, the WIFHE concept can provide sufficient Q in all operating points except for TX due to the slow-moving ambient air. The TWIH concept can only provide a sufficient stationary Q in TO due to the poor natural convection inside the tank once it is not entirely full anymore. The drag coefficients of the R-HEX system are presented in Section 4.4. The R-HEX produces some thrust in TO and go-around and drag in all other operating points. Finally, the impact of the WIFHE on the overall aircraft level is discussed in Section 4.5. The TWIH is not further discussed due to its insufficient cooling rate. Assuming equal masses of R-HEX and WIFHE a 0.4% fuel burn advantage can be achieved by the WIFHE. Section 4 was conceptualized and written by Hagen Kellermann except for Section 4.4, which was conceptualized and written by Anais Habermann, and Table 8 and Fig. 14 in Section 4.5, which were created by Patrick Vratny including the generation of the aircraft level results.

The paper finishes with a conclusion and outlook summarizing the main findings of the paper and recommending a further investigation of the WIFHE hot side since it limited the heat transfer rate. Also, the limitations of the stationary model are outlined. Section 5 was written by Hagen Kellermann. The entire paper was reviewed by Mirko Hornung.

Author contributions in short: conceptualization, methodology, simulation, analysis, and writing of all aspects of the research except for all of the following: Sections 3.3, 3.4, 4.4, the paragraph on the reference aircraft in Section 2, the creation of Table 8 and Fig. 14 in Section 4.5: H.K.; conceptualization, methodology, simulation, analysis and writing of Section 3.3, 4.4: A.L.H.; conceptualization, methodology, simulation, analysis and writing of the paragraph on the reference aircraft in Section 2, creation of Table 8 and Fig. 14 in 4.5: P.C.V.; supervision and review: M.H.

Applied Thermal Engineering 170 (2020) 114985

Contents lists available at ScienceDirect

Applied Thermal Engineering

journal homepage: www.elsevier.com/locate/apthermeng

Assessment of fuel as alternative heat sink for future aircraft

H. Kellermann*, A.L. Habermann, P.C. Vratny, M. Hornung

Bauhaus Luftfahrt e.V., Taufkirchen, Germany

HIGHLIGHTS

- Fuel can be used as heat sink for future aircraft propulsion concepts in multiple ways.
- Active fuel circulation underneath exposed surfaces enables steady state cooling.
- Cooling demands of a hybrid electric aircraft with peak heat loads of 120 kW are met.
- On ground taxiing with low quantities of fuel left is the most challenging condition.
- Removed aircraft drag increment caused by the thermal management system.

ABSTRACT

Fuel is assessed as alternative heat sink for future aircraft applications to avoid excessive drag from conventional cooling systems. Two cooling concepts using fuel as a heat sink are investigated for a hybrid electric aircraft platform with entry into service of year 2035+, 180 PAX and a design range of 1300 nm. The hybrid electric propulsion system produces a maximum heat power of 126.1 kW. Concept 1 uses active hot fuel circulation underneath the wing surfaces for cooling, whereas Concept 2 uses heat exchangers placed inside the existing tanks. Concept 1 is subdivided based on the fuel flow architecture into series and parallel configuration. Thermodynamic modeling is based on semi empirical methods combining effects of internal and external convection, conduction and radiation to an overall heat transfer model. A partial dependence analysis is performed to ensure the model's integrity. The cooling power potential of both concepts is evaluated at five mission points for the reference aircraft. Concept 1 provides sufficient cooling power for all operating points within the operational limits of the fuel temperature except for the Taxi case, in which the required cooling power is 85% fulfilled. The series and parallel sub configurations of Concept 1 are capable of equal cooling powers in all operating points. The parallel option requires less than half the hydraulic power of the series option. The final system needs a pump providing 2.3 kW of hydraulic power. Concept 2 fails to provide the required cooling power at any mission point other than Take-Off due to low fuel fill levels. Concept 1 is compared to a reference cooling system using a ram air cooler on aircraft level. A mass and drag sensitivity assessment shows that Concept 1 performance is in the range of 0.0% to +0.6% in fuel burn compared to the ram air cooling system depending on the mass considerations for Concept 1.

1. Introduction

Research for next generation commercial aircraft is driven by ambitious goals to reduce the aircraft's environmental impact such as the European Commission's Strategic Research and Innovation Agenda (SRIA) [1]. The SRIA targets a 75% reduction in CO_2 emissions by the year 2050 compared to the year 2000. A powerful lever to achieve these targets is the propulsion system where both propulsive and core efficiency can be improved. Novel propulsion concepts with intercoolers [2] or bottoming cycles [3] are currently under investigation to further reduce the specific fuel consumption. Another promising approach is a higher electrification of the on-board systems or even the propulsion system. Examples are the more electric aircraft [4] or electric propulsion systems [5]. Many of these concepts lead to an increased need of emitting heat from the aircraft to ambient compared to today's aircraft. Conventional cooling concepts, which today are for example part of the environmental control system (ECS), require heat exchangers placed in the airflow path and thus induce drag [6]. An alternative option is to use fuel as a heat sink, which is common practice for high performance military aircraft [7].

Fuel has been utilized as heat sink in aircraft for many years. For commercial aircraft, a common application is the engine oil cooling by means of a fuel oil heat exchanger. If the required fuel flow for cooling is higher than the fuel flow demand of the engine, recirculation systems are installed [8]. This is especially the case in low thrust flight states such as descent and taxi. German developed a generic fuel heat sink model with recirculation and an additional fuel-air heat exchanger. They calculated the heat load capacity of the fuel by means of a thermal endurance for both adiabatic and non-adiabatic tank walls [9]. Pang et. al. continued work on thermal endurance for a high speed vehicle. They

* Corresponding author.
E-mail address: hagen.kellermann@bauhaus-luftfahrt.net (H. Kellermann).

https://doi.org/10.1016/j.applthermaleng.2020.114985
Received 16 April 2019; Received in revised form 2 October 2019; Accepted 22 January 2020
Available online 25 January 2020
1359-4311/

installed an additional consumptive coolant in case the fuel temperature reaches a critical value [10]. Alyanak et. al. investigated four thermal management system layouts with fuel as a heat sink using an as simple as possible approach. They considered systems with and without recirculation through a ram air heat exchanger [11]. Studies from the U.S. Air force showed that thermal endurance of modern fighter aircraft could be further increased by deploying a dual tank system with a dedicated recirculation tank. A ram air cooler was installed in the recirculation loop [12–14]. Zilio et. al. used computational fluid dynamics (CFD) to model a fuel tank thermal behavior with small heat loads (2 kW) over the entire mission. Particular emphasis was put on the assessment of fuel tank flammability hazards [15]. Roland and Rumpfkeil developed a method that solved mass and momentum equations separately from the energy equation to estimate heat transferred from a wing with internal heating of the fuel tank. They used a constant outer surface temperature of 400 K not taking into account thermal resistance from wall conduction and convection inside the tank. They demonstrated heat sink potential of wing tanks in the order of magnitude of 10^6 W [16]. In addition to the aforementioned research on the conceptualization of fuel cooled Thermal Management Systems (TMS), much work has been done on enhancing the fluid properties of jet fuel to increase its heat sink potential. A good summary of these sources is provided in [10].

Except for [16], the presented literature either had very small heat loads for the commercial applications or used additional, drag causing ram air coolers mainly in military applications. This paper aims to investigate using fuel as an alternative heat sink for waste heat of novel propulsion concepts such as a hybrid-electric propulsion system for a commercial aircraft avoiding any additional cooling drag.

For that purpose, a thermodynamic model of a cooling cycle with fuel as a heat sink is developed. Two concepts are investigated: One that actively cycles hot fuel below the wing surfaces to optimally use the available wing surface area for heat exchange with the ambient air and a second approach that adds heat to the fuel tanks via a liquid to liquid heat exchanger. The thermodynamic models are based on semi empirical methods for simplified geometries. A partial dependence analysis is performed for both concepts to ensure the integrity of the models. Both models account for heat transfer through convection, conduction and radiation. The consideration of the entire flight mission is of great importance as there is a large variance in boundary conditions over the course of it. Therefore, the maximum steady state heat flux is estimated for multiple operating points such as Take-Off (TO), End of Cruise (EoC), Go-Around after cruise (GA), Top of Climb Diversion (ToCD) and Taxi. The baseline aircraft for the study is a short range aircraft with an entry into service of year 2035. This time frame has been chosen, because it represents a potential point for aircraft fleet renewal and, therefore, introduction of new technologies [17]. Furthermore, it can be expected that electric components have been evolved in a way that they are getting interesting for hybrid-electric transport aircraft.

To display the relative size of the heat sink potential compared to the demand, the heat emission of a hybrid-electric propulsion system is estimated for the mentioned operating conditions. The study also provides a reference cooler model operated with ram air and estimates the expected increase in drag to show the impact of using fuel as heat sink on overall aircraft level. The expected mass difference between the fuel cooling concepts and the ram air cooler is taken into consideration.

2. Conceptualisation

Two different fuel cooling concepts are investigated. The first concept uses Wing Integrated Fuel Heat Exchangers (WIFHE) to actively pump warm fuel directly under the wing surfaces. WIFHEs are simple channels underneath the wing surface with the purpose to separate the warm fuel from the fuel mass inside the tank. The second concept uses Tanks With Internal Heating (TWIH). The concepts are sketched in Fig. 1.

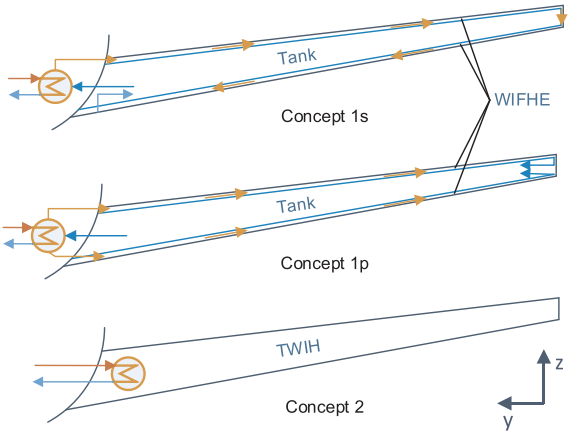

Fig. 1. Investigated fuel cooling concepts.

Concept 1 is divided into two subcategories: Series (1s) and Parallel (1p). Both use a liquid to liquid heat exchanger that transfers heat from the cooling fluid of the cooling system for the electric components to the fuel. The series configuration has only one fuel exit leading to the WIFHE in the upper wing surface. The hot fuel runs in span wise direction until it reaches the outer end where it is passed to the WIFHE in the lower wing. It is cooled further by flowing back towards the wing root where it ultimately reenters the storage tank. The parallel configuration has two outlets from the liquid – liquid heat exchanger: The first fuel mass stream enters the upper wing WIFHE and the second goes to the lower wing WIFHE. Both streams run parallel until they reach the maximum span wise location where they reenter the tank. Concept 2 places the liquid-liquid heat exchangers inside the existing fuel tanks. Without forced fuel flows the heat has to dissipate via natural convection.

The geometry for both concepts is shown in Fig. 2.

Tanks and WIFHE components occupy the same wing area because the WIFHEs are built into the existing tanks. For Concept 2, the tank is divided into three tanks: The inner tank can hold 3940 kg fuel at ISA conditions, the inner and outer TWIH 2134 kg and 552 kg respectively. The decisions leading to this setup are explained in Section 4.3.

The reference aircraft platform represents a parallel hybrid-electric short-range aircraft for an entry-into-service of year 2035+ based on [17,18] (cf. Fig. 3). It accommodates 180 PAX at 1300 nm. The used hybrid-electric topology is a discrete parallel hybrid propulsion system. It consists of conventional kerosene powered advanced Geared Turbofans (GTF) and Electric Ducted Fans (EDF) supplied by batteries. These thrust producing devices are arranged in a quad fan configuration on the wing with the GTF's location close to the wing root and the EDFs being placed further outboard. The two different thrust producing devices are not coupled allowing for an independent and optimized control of the combined propulsion system. For that purpose, this platform enables a comprehensive analysis of the impact of a pure propulsion hybridization without taking into account potential synergy effects such

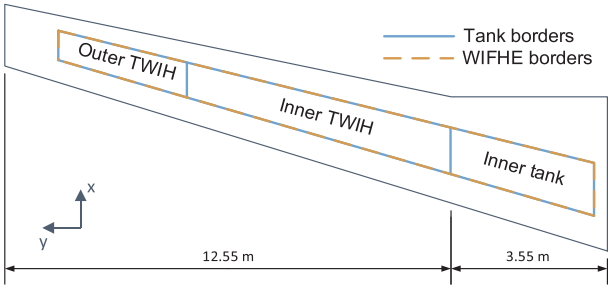

Fig. 2. Geometrical setup for all fuel-cooling concepts.

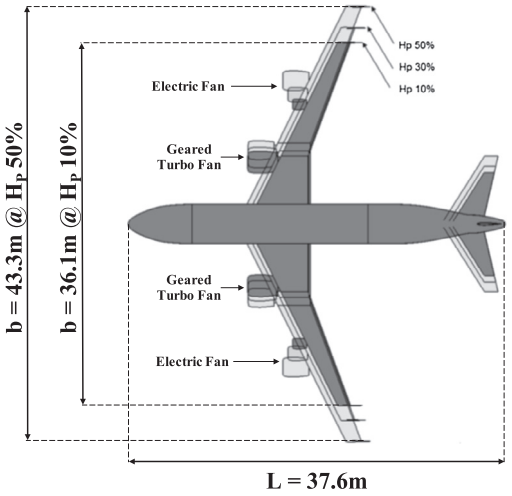

Fig. 3. Top view of the discrete parallel hybrid-electric reference aircraft.

as aerodynamic improvements. The electric power train consists of several high power electric components with different requirements for cooling based on [19,20]. In previous studies, the most eligible electric motor type with regard to overall mass and efficiency has been identified as a high temperature superconducting electric motor requiring an operating temperature of 50 K cooled by an active cryocooling system [21]. As energy and power supply, advanced lithium ion batteries are used assuming an optimum operating temperature of 298 K [19]. For the power management and distribution system multilevel inverters for the motor control, aluminum cables and solid-state protection switches are considered. The inverters and protection switches are actively cooled via a liquid cooling system with an operating temperature of 373 K [19]. The aircraft has been sized for a degree of power hybridization (H_P) of 20% in top-of-climb conditions, which have been identified in a previous study as a potential sizing point [20]. The H_P is defined as the ratio of the electric motor shaft power at a specific flight state to the overall propulsive shaft power. For the current aircraft configuration, this is equal to a total installed electric motor power of 2.6 MW at a minimum overall operating system efficiency of 95%. The electric system is operated at its maximum design power during the entire design mission, where possible. The residual required thrust in different flight states is delivered by the GTF. This mission hybridization strategy offers the most suitable performance with regard to block fuel reduction and Maximum Take-Off Weight (MTOW) increase.

Table 1 summarizes the most important aircraft parameters using a standard ram air heat exchanger. These aircraft parameters have been derived from the baseline concept described in [17,20]that neglected, in the first instance, the additional drag of the ram air heat exchanger of the thermal management system.

3. Concept modelling

The following sections describe the modelling of the most important components. Thermodynamic property models for air [22] and Jet A-1 fuel [23] were implemented. When using fuel as a heat sink safety must be taken into consideration. Therefore operational limits with regards to fuel ignition, coking and vaporization have to be defined. The auto ignition temperature (AIT) of Jet A-1 fuel at standard pressure is 511.15 K [23]. It increases with decreasing pressure. The thermal stability of aircraft petroleum fuels has breakpoint temperatures, which are typically above 483.15 K [24]. Jet A-1 fuel starts boiling at 448.15 K [23]. To avoid any unexpected fuel vaporization all studies in this work assume a fuel temperature limit of 400 K.

Table 1
Overview of relevant aircraft parameter of the hybrid-electric aircraft sized for a design degree of power hybridization of 20% based on [4].

Aircraft parameter	Value
MTOW [kg]	80,466
Release Fuel [kg]	5624
Battery [kg]	12,383
Block Fuel [kg]	4668
Wing Area [m^2]	125

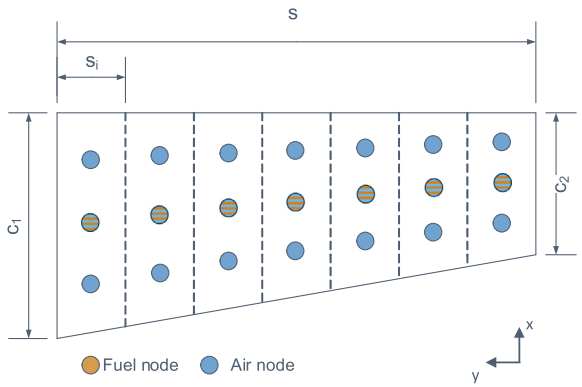

Fig. 4. WIFHE local discretization.

3.1. Wing integrated fuel heat exchanger

The model for the WIFHE was derived from first principal, as no standard methods for the special geometry are available. The geometrical set up is shown in Fig. 4. The heat exchanger is divided into finite elements in span wise (s) direction of the wing. These fuel nodes are further divided into multiple air nodes in chord wise (c) direction.

Fig. 5 shows the schematic drawing of one fuel node with all incoming and outgoing mass flows and heat fluxes. A 1D heat transfer analysis is performed. The inner wall facing the fuel tank is assumed as an insulation because the heat transferred via the outer wall is significantly larger due to the presence of forced convection. The temperature drop inside the fuel node is calculated with an energy balance:

$$T_{f,out} - T_{f,in} = \frac{\dot{Q}_{out}}{w_f \cdot c_v} \tag{1}$$

with c_v being the specific heat capacity of fuel, T_f the fuel temperature, w_f the fuel mass flow rate and $\dot{Q}$ the heat flow rate.

The total heat transfer rate of the WIFHE is calculated by summation of the local heat transfer rates of each fuel node:

$$\dot{Q}_{tot} = \sum^{n} \dot{Q}_i = \sum^{n} A_i \cdot q_i \tag{2}$$

With A_i being the effective heat exchange area of each fuel node and q_i the area specific heat transfer rate. For enhanced readability the suffix "i" is not written for the remainder of this section. However, all calculations are performed for one fuel node at a time. The thermodynamic properties of the fuel nodes are calculated subsequently and

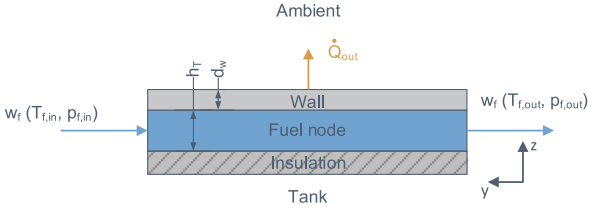

Fig. 5. WIFHE fuel node thermodynamic model.

$T_{f,in,i} = T_{f,out,\ i-1}$. q is split into two components: Convective – conductive heat transfer from the fuel to ambient (q_{cc}) and radiative heat transfer (q_{rad}). The radiation consists of two components, absorptance and emittance and can be calculated according to [25]:

$$q_{rad} = \epsilon_{em} \cdot \sigma \cdot (T_{w,o}^4 - T_{amb}^4) - \alpha \cdot P_{rad} \tag{3}$$

α is the absorption coefficient, P_{rad} the area specific incoming radiation power, ε_{em} the emissivity, σ the Stephan-Boltzmann constant, T_{amb} the static ambient temperature and $T_{w,o}$ the outer wall temperature. The specific overall convective and conductive heat transfer rate is calculated by means of an overall heat transfer coefficient (h).

$$q_{cc} = h \cdot \Delta T \tag{4}$$

With ΔT being the temperature difference between fuel and air. For high Mach numbers the total temperature of air ($T_{t,air}$) has to be used due to the no slip condition near the wall [26]. The overall heat transfer coefficient is calculated by combining the two convective heat transfer coefficients of fuel (h_{fuel}) and air (h_{air}) and the wall resistance:

$$\frac{1}{h} = \frac{1}{h_{fuel}} + \frac{\lambda_W}{d_W} + \frac{1}{h_{air}} \tag{5}$$

With λ_w being the thermal conductivity of the wall and d_w being the wall thickness [27]. For comparison, the temperature effectiveness on the hot side is used:

$$\epsilon = \frac{T_{f,in} - T_{f,out}}{T_{f,in} - T_{t,air}} \tag{6}$$

A flat plate model is used for the airside neglecting the pressure gradient occurring around the perimeter of an aerodynamic profile. For most operating points free convection can be neglected and only forced convection is taken into account. In those cases, the local Nusselt numbers are calculated as described in [27] depending on the character of the flow regime. For laminar flows ($Re_x < 500{,}000$, $0.01 < Pr < 1000$):

$$Nu_x = 0.332 \cdot Re^{\frac{1}{2}} \cdot Pr^{\frac{1}{3}} \tag{7}$$

For turbulent flows ($Re_x > 500{,}000$; $0.6 < Pr < 1000$):

$$Nu_x = 0.296 \cdot Re_x^{0.8} \cdot Pr^{\frac{1}{3}} \tag{8}$$

Re is the Reynolds number and Pr the Prandtl number. If an unheated starting length is present, the local Nusselt number is corrected with methods from [28].

The local airside heat transfer coefficient is obtained via the definition of the Nusselt number:

$$h_{air,x} = Nu_x \cdot \frac{\lambda_{air}}{x} \tag{9}$$

With λ_{air} being the thermal conductivity of air. The average heat transfer coefficient for each fuel node (h_{air}) is the mean of all local (- air node) coefficients.

On the fuel side, internal flow inside a rectangular duct is considered. Constants from [26] are used to determine the Nusselt number and friction coefficient (f) in the laminar flow regime ($Re < 2000$). They depend on the aspect ratio of the rectangular cross section of the duct through which the fuel flows.

The friction factor in the turbulent regime f_t is calculated via Haaland's [29] explicit formulation of Colebrook's formula:

$$f_t = \left(-1.8 \log\left(\left(\frac{\xi}{3.7 D_h}\right)^{1.11} + \frac{6.9}{Re}\right)\right)^{-2} \tag{10}$$

With ξ being the wall roughness and D_h the hydraulic diameter of the cross section. Gnielinski's approximation gives the Nusselt number in the turbulent regime [27]:

$$Nu = \frac{\frac{f_t}{8} \cdot (Re - 1000) \cdot Pr}{1 + 12.7 \cdot \left(\frac{f_t}{8}\right)^{0.5} \cdot \left(Pr^{\frac{2}{3}} - 1\right)} \tag{11}$$

The transitional regime is not well understood. For this study the correlation provided by [30] is used to determine the friction factor in the transitional region of the flow. The entry region is neglected due to the large length to width ratio of the duct.

To calculate the hydraulic pumping power (P_{hyd}) required to move the fuel through the WIFHE components, both the head loss (HL) in the duct as well as the potential height difference have to be taken into account. The head loss is calculated via the Darcy-Weisbach equation [31]:

$$HL = \frac{f \cdot l \cdot u^2}{2 D_h \cdot g} \tag{12}$$

With l being the duct length, u being the flow velocity and g the gravitational constant. By adding the power for the height difference, the total hydraulic power is obtained:

$$P_{hyd} = (h_l + \Delta h \cdot \rho \cdot g) \cdot w_f / \rho \tag{13}$$

3.2. Tank with internal heating

A 1D heat transfer analysis is performed. The tank geometry is simplified by a cuboid. It is divided into four zones: Upper wall, air, fuel and lower wall as shown in Fig. 6. In reality the air zone consists of an air fuel mixture, but for a first approximation the thermodynamic properties of pure air are assumed. It is a conservative assumption as the air fuel mixture has a higher thermal conductivity.

Fig. 6 shows the modelling approach chosen in this work for a TWIH. The heat exchanger is mounted close to the lower wall to ensure it is submerged in fuel even when the fill level (FL) is low. The heat exchanger is not modelled in detail but a constant temperature near the heat exchanger is assumed (T_0). Adding the heat source near the bottom of the tank is also beneficial for the internal heat transfer as the temperature difference between T_0 and the temperature at the fuel air boundary ($T_{f,a}$) induces natural convection in the fuel zone. Similarly, the temperature gradient between $T_{f,a}$ and the temperature at the inside of the upper wall ($T_{w,i,u}$) causes natural convection in the air zone. To obtain the heat transfer coefficients for fuel and air zone the correlations for natural convection inside cavities from [32] are applied:

$$Nu = \left[\left(1 + 1.446 \cdot \left(1 - \frac{Ra_c}{Ra}\right)\right)^{15} + \left(Ra \cdot \frac{f(Pr)}{1420}\right)^5\right]^{\frac{1}{15}} \tag{14}$$

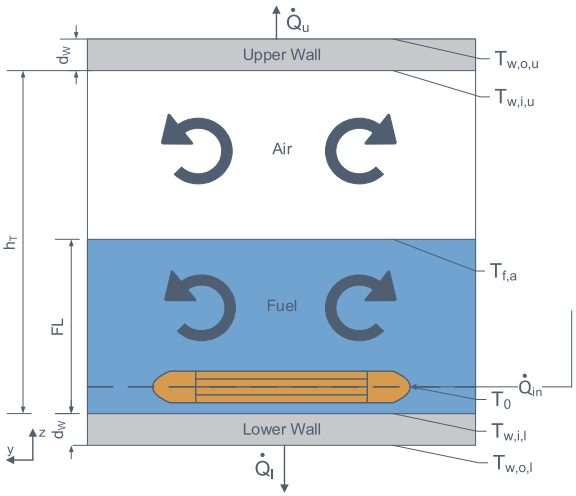

Fig. 6. TWIH thermodynamic model.

With Ra being the Rayleigh number and Ra_c the critical Rayleigh number.

Heat transfer through the walls is modelled via conduction and the heat transfer coefficient on the free stream airside of the wing is obtained with the methods described in Section 3.1. The overall heat transfer rate is again calculated with (2) adding upper ($\dot{Q}_u$) and lower ($\dot{Q}_l$) side.

In heat transfer problems such as the present, often the incoming heat flow is set and the resulting temperatures are calculated. However, since this work investigates the potential of fuel as a heat sink and the maximum fuel temperature is restricted, the developed method is set up to use the maximum fuel temperature (T_0) as input and calculate the resulting heat flow. The dependence of the internal heat transfer coefficients on the unknown temperature differences entails the need for an iterative solution. A trust region reflective algorithm is used [33].

3.3. Reference ram air heat exchanger

To compare the described heat sink concepts against a conventional heat sink approach, a ram air heat exchanger system is modelled. The system is based on a ram air cooler commonly applied with environmental control systems (ECS) of commercial aircraft, such as the Boeing 747-8 [34]. It is assumed, that the ram air system is the source of pressure drag, which effects the overall aircraft performance (Section 4.4).

A simplified, non-dimensional heat transfer analysis is performed. It is based on an adaption and extension of an ECS optimization approach introduced by [35], which has been applied by [36]. The ram air heat exchanger system is sketched in Fig. 7. It is located inside the belly fairing of the fuselage. The inlet is situated forward of the wing leading edge at the root section.

The modelling of the core system consisting of adiabatic diffuser, heat exchanger and adiabatic nozzle, is adapted from [35]. A compact cross-flow heat exchanger with unmixed fluids is modelled with heat transfer surface properties proposed by [35] and design methods from [37]. The thermodynamic properties of the cooling fluid (air) are modelled depending on the given flight conditions [22]. A potassium formate solution (40:60 wt) is chosen as a coolant, since it has favourable physical properties for the cooling of electronic devices [19]. The temperature dependent properties of the coolant are calculated according to [38]. The diffuser and nozzle are described by their adiabatic efficiencies and mass balance equation. The efficiencies of the components are approximated by [35] as $\eta_{adiabatic} = 0.95$.

Total pressure losses in the heat exchanger are mainly responsible for the ram air system drag. The occurring losses and the dimensions of the heat exchanger directly translate into the external drag of ram air inlet and outlet. A submerged NACA inlet is chosen. This type of inlet is widely applied for ECS of commercial aircraft, as it is known for its favourable drag characteristics. The drag increment of the inlet is calculated as a function of mass flow through the inlet and free stream Mach number based on an interpolation of experimental data presented by [39]. As the experimental data is given for a fighter airplane model, the resulting drag values are scaled to the commercial reference aircraft

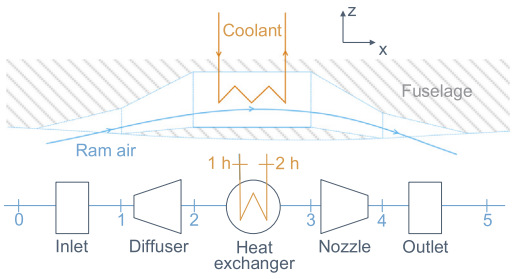

Fig. 7. Reference ram air heat exchanger system.

Table 2
Fixed ram air system design parameters.

Parameter	Value
dT_{ISA} [K]	10
$T_{coolant,in}$ [K]	373
$M_{air,hx,cruise}$ [–]	0.1

by making use of inlet and wing reference areas.

As a first approximation, a 60° inclined, squared, ducted outlet is modelled according to experimental data presented by [40]. The thrust ("negative drag") produced by the outlet is a function of freestream air properties, air mass flow through the system, ram air properties and outlet duct size. The ram air properties at the outlet are a direct outcome of the airflow through the dimensioned heat exchanger and the corresponding losses in total pressure. The total external drag of the system thus yields to:

$$\Delta c_D = c_{D,inlet} - c_{D,outlet} \quad (15)$$

In addition to the heat exchanger specifications by Perez-Grande & Leo (see [35] for further details), the following design parameters are defined: ISA temperature deviation (dT_{ISA}), coolant temperature at station 1 h ($T_{coolant,in}$) and ram air Mach number at station 2 ($M_{air,hx,cruise}$). The values are listed in Table 2.

3.4. Impact on overall aircraft

The aircraft level assessment was performed with the aircraft preliminary design framework Pacelab APD [41]. It was used to derive trade factors covering sensitivities of mass and drag changes with regard to MTOW, block fuel and battery mass. The trade factor approach allows a quick assessment of the cooling impacts covering all sizing snowball effects on aircraft level. For that purpose, the method used by [20] has been extended. The method equally distributes additional weights to all components and does not consider the exact location of the additional weight. Consequently, positive effects such as placing additional masses inside the wing and thereby lowering the root bending moment are not reflected. However, within the range of the considered mass increases, this effect can be neglected in the first instance.

4. Results and discussion

The following two sections describe the results of the partial dependence analysis for Concept 1 and 2. Only the results for Concept 1s are shown and discussed because the trends for the parallel configuration are the same. The difference between series and parallel configuration in Concept 1 is highlighted in Section 4.3.1.

4.1. Wing integrated fuel heat exchanger

Fig. 8 shows the partial dependence analysis of the WIFHE component model. For this single component study the upper surface of the tank section between fuselage and kink of the wing was used for the geometry (Fig. 2). Appropriate space for high lift devices was considered by only using the section between 25% and 75% chord length. The impact of multiple design variables on the three output parameters total heat transfer rate (Q) total pumping power required (P_{hyd}) and heat exchanger effectiveness (ε) were investigated. For ease of interpretation, the values were related to the values at the reference point of the partial dependence analysis, which are summarized in Table 3. Each column of Fig. 8 displays the influence of two design variables. The pairs were formed according to the highest inter variable influence.

The first column in Fig. 8 has Mach number (Ma) and altitude (alt) as variables. The investigated field exceeds the borders of a typical

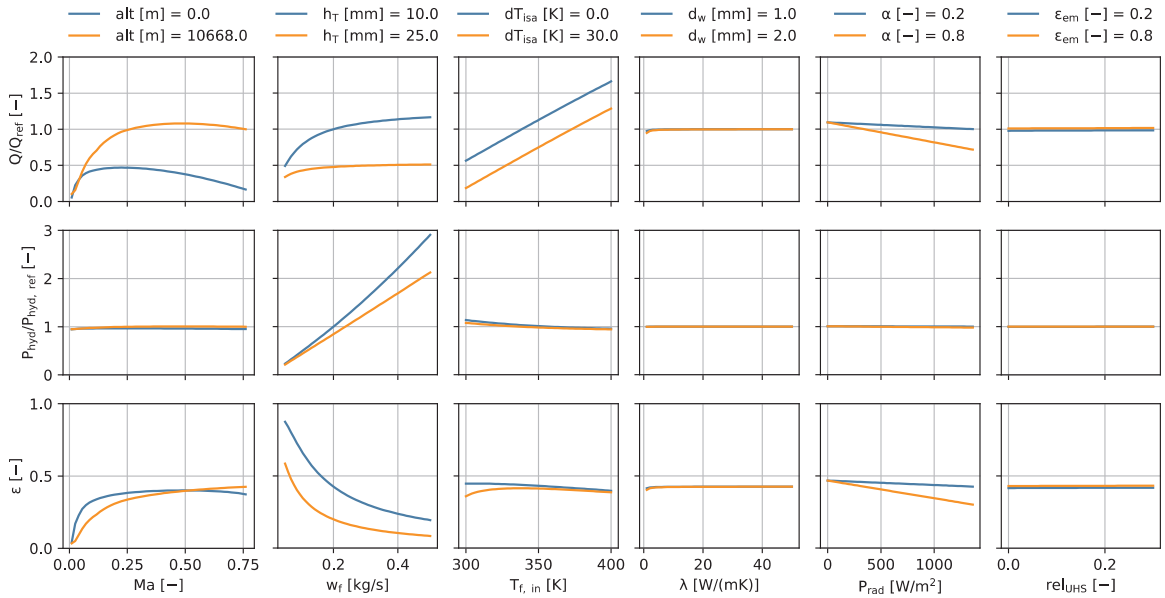

Fig. 8. Partial dependence analysis of WIFHE series system.

Table 3
Reference point values for partial dependence study.

Ma [–]	0.76	λ_w [W/(mK)]	240
alt [m]	10,668	d_w [mm]	1.5
w_f [kg/s]	0.2	P_{rad} [W/m^2]	1100
h_T [mm]	15	α [–]	0.25
$T_{f,in}$ [K]	350	rel_{UHS} [–]	0.25
dT_{isa} [K]	10	$ε_{em}$ [–]	0.5

flight envelope intentionally to account for all possible flight conditions in this early design analysis. The model predicts an increase in Q for increasing Ma up to 0.5 at cruise altitude. At higher Ma, Q decreases slightly. At sea level, the maximum Q is located around Ma 0.25 and Q decreases with further increasing Ma. This is to be expected because both Re_{air} and $T_{t,air}$ are influenced by Ma. An increase in Re_{air} positively influences h_{air} but a higher $T_{t,air}$ leads to a lower overall temperature difference driving the heat transfer (cf. (4)). For lower Ma the positive effect of increasing Re_{air} is dominating, but for higher Ma it is overcome by the negative effect of $T_{t,air}$. For a lower altitude with higher air density, the maximum Q is reached at lower Ma because density has a larger impact on $T_{t,air}$ than on Re_{air}. Q strongly depends on both Ma and alt with differences between minimum and maximum values of 90%. The results indicate that low Mach numbers and low altitudes are the most challenging conditions with regards to Q. ε shows a strong asymptotic behaviour for both altitudes with high gradients at low Ma that fall of at higher Ma. At sea level the initial gradient is stronger than at cruise altitude and an ε optimum exists around a Mach number of 0.5. At cruise altitude, the effectiveness increases monotonously up to the cruise Ma 0.76. This does not contradict with the observed Q maximum at cruise altitude because $T_{t,air}$ also affects ε (cf (6)). The impact of Ma and alt deviations on P_{hyd} is very small.

The second column shows the impact of fuel flow (w_f) and component height (h_T) (cf. Fig. 5). Increasing h_T results in decreased Q values due to the higher hydraulic diameter. Increasing w_f shows an asymptotic behaviour with regards to Q: The gradient for small w_f values is high but rapidly flattens from a certain w_f value that also depends on h_T. The ε diagram provides the explanation for the relationship: At high w_f, ε is low meaning the exit fuel temperature is close to the inlet temperature. Increasing the fuel flow further does not increase the heat exchange area with high ΔT between fuel and airside much further, whereas at low w_f with high ε an increase of w_f leads to more area (or more “span”) being exposed to high ΔT. This behaviour is interesting because the designer might be willing to accept low effectiveness to get high Q. Increasing w_f and decreasing h_T both result in more required P_{hyd}. Thin heat exchangers have a higher dP_{hyd}/dw_f value and thus are more sensitive to changes in fuel flow. In an applied system, h_T is most likely a parameter fixed by the realized construction whereas w_f may be varied during operation and therefore could be a control parameter. The system should be designed with an optimal balance between Q and P_{hyd} and a w_f range with good control capabilities to be able to react to increased cooling demands or changed environmental conditions. However, there is a limitation to the possible Q increase by increasing w_f.

In the third column the influences of inlet fuel temperature ($T_{f,in}$) and temperature ISA deviation (dT_{ISA}) are shown. Increasing $T_{f,in}$ linearly increases Q. Q also shows a linear dependency on dT_{ISA} with higher dT_{ISA} values leading to decreased Q values. ε decreases slightly and linearly with increasing $T_{f,in}$ for $T_{f,in} > 350$ K. For those high temperatures there is also almost no difference between the two dT_{ISA} values. For lower $T_{f,in}$ values the curves of constant dT_{ISA} split with the $dT_{ISA} = 30$ K curve starting to decrease in ε with decreased $T_{f,in}$. When $T_{f,in}$ nears $T_{t,air}$ ε converges towards 0 because in the absence of a driving temperature difference, there would be no heat transfer anymore. For the $dT_{ISA} = 0$ K curve this effect will only be visible for $T_{f,in}$ values lower than the minimum in the diagram. Influence on P_{hyd} is negligible for dT_{ISA} but P_{hyd} can be reduced by increasing $T_{f,in}$ due to decreased fuel viscosity. Over the chosen range of $T_{f,in}$, P_{hyd} changes by 20%.

Column 4 shows the dependencies on wall thickness (d_w) and thermal conductivity of the wall material (λ_w). Both have negligible influence on all three evaluation parameters except for very low λ_w where Q decreases slightly. However, aluminium which is typically used for the wing skin has λ_w values of about 210 W/(mK) [42]. Wall conduction is not the system's bottleneck with regards to heat transfer, yet thin walls are preferable to reduce the overall system mass.

In column 5, the influence of incoming solar radiation is shown. The maximum radiation power (P_{rad}) was set to 1362 W/m^2, which is the power outside of the earth's atmosphere [43]. Increasing P_{rad} decreases Q linearly. The absorption coefficient is the slope of the resulting line, which was expected from (3). At high levels of P_{rad} the difference between a good and a poor absorbing material may cause up to 25% discrepancy in Q. Therefore the wing surface material should be carefully chosen and preferably have light colours. Radiation's influence on P_{hyd} is negligible. ε shows the same dependence on P_{rad} and α as Q

because a lower Q value results in a higher exit temperature with unchanged ambient conditions.

The last column has the material emissivity (ε_{em}) and the relative unheated starting length (rel_{UHS}) as variables. It was found that rel_{UHS} has up to 8% influence on h_{air} but for the overall system, it is negligible. Radiative heat emission is also negligible due to the relatively low overall temperature differences.

Additionally, a study was performed where instead of the flight Mach number a Mach number closer to the actual local Mach number on a super critical profile was used. A difference in h_{Air} around 10% was found but similarly to rel_{UHS} the effect on the overall system was negligible. Roland [16] provides an in depth analysis of profile dependent air side convection for incompressible flow. In the present study, keeping the simple flat plate model is reasonable due to the low influence on the overall system. Also, any 2D effects on the wing surface especially with regards to sweep angle were neglected.

4.2. Tank with internal heating

For the tank with internal heating, the partial dependence analysis of the previous section is performed as well. The reference values were adopted from Table 3 except for w_f, which is not applicable for this concept, and h_T, which is set to 0.3 m. Additionally, the reference fill level (FL) is set to 0.5. The results are shown in Fig. 9. The TWIH does not need extra pumping power and does not have an effectiveness in the same sense as the WIFHE concept. Therefore, Q is the only evaluation parameter used. Because the results confirmed the negligibility of λ_w, d_w, ε_{em} and rel_{UHS} for this model similar to the WIFHE concept the respective diagrams are not shown here. h_T is investigated separately with the fill level (FL) in Fig. 10.

The Ma - alt dependencies are very similar to the ones of the WIFHE. This was to be expected as both variables influence the airside convection, which is modeled in the same way for both concepts. The Ma dependence for the TWIH is slightly higher. This shows in the slightly larger maxima and their location at lower Ma. The reason is the dependence of h_{fuel}, which for the TWIH uses a natural convection model, on the temperature differences.

The influence of both dT_{ISA} and T_0 show the same trend as for the WIFHE $dT_{ISA} - T_{f,in}$ diagram. They both are stronger again because of the temperature dependence of the natural convection.

Solar radiation has a negligible influence on Q for the TWIH according to Fig. 9. Because the tank is only half full, the heat transfer at the bottom surface dominates the overall Q. Since the bottom surface is not significantly exposed to solar radiation, the influence is very small.

If the tank is not full the air layer acts as an insulation for the heat transfer. In Fig. 10, the influences of the tank fill level (FL) and the overall tank height (h_T) are shown.

Q is drastically – by a factor of 3.5 – higher for a full tank compared to a partially filled tank. The driving temperature difference for the natural convection inside the fuel is between the temperature close to the heat source near the bottom (T_0) and the temperature of the fuel air boundary (T_{fa}) (cf. Fig. 6). For a full tank, the air layer does not exist and T_{fa} is equal to the temperature of the upper inner wall surface ($T_{w,i,u}$), which is very cold due to the external airside convection and wall conduction. When there is an air layer inside the tank, the heat transfer through the upper surface is significantly decreased because of

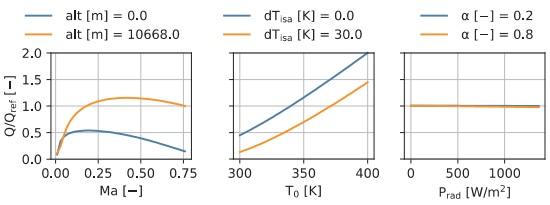

Fig. 9. Partial dependencies of TWIH.

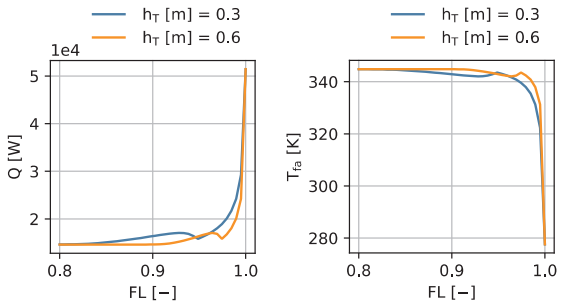

Fig. 10. Tank size and fill level.

the low thermal conductivity of air. Additionally h_{fuel} is drastically decreased because of the much lower driving temperature difference, which results in a decreased heat transfer rate through both upper and lower side. Overall Q is reduced by 70% when the fill level is decreased from 100% to 80%.

The tank height has an influence on the transitional regime between 80% and 100% FL. A small local Q maximum can be observed at a certain fill level for each tank height where the air layer becomes too thin for natural convection to occur. The intersection of the lines is due to the choice of a relative FL on the x - axis. The Q maximum depends on a certain absolute thickness of the air layer inside the tank. For the larger tank (h_T = 0.6 m) this absolute thickness occurs at a higher relative value and therefore the Q maximum is shifted to the right compared to the thin tank (h_T = 0.3 m).

The results imply that when designing an applied system the tanks should be compartmentalized to ensure that the heated tanks can remain full for most of the flight mission.

4.3. Application on the reference aircraft

The heat loads of the hybrid-electric reference aircraft described in Section 2 at selected points of the mission with their respective Mach number and flight altitude are shown in Table 4. Additionally, it lists the total on board fuel mass at each mission point. Selected mission points are TO, EoC, GA, ToCD and Taxi.

4.3.1. Concept 1 – WIFHE

The partial dependence analysis for the WIFHE suggested $T_{f,in}$ and w_f as control parameters for the system. Therefore, design studies are carried out over a range of those two parameters. All other design parameters are fixed at reasonable but not optimized values and summarized in Table 5. The minimum amount of fuel required on board to fill the entire system ($m_{f,min}$) is a result of the component dimensions and the fuel density. This value does only account for the WIFHE components and no additional ducts and pumps that also need to be filled with fuel. For the later aircraft level assessment study, an additional amount of 220 kg fuel is assumed. This fuel is not designated for the propulsion system, but has to be on board even after a diversion and the following landing plus taxi run to ensure the cooling capability of the system.

Ma and alt were adopted according to each mission point. 0.1 was selected as an averaged Ma for the TO segment. The design studies with

Table 4
Heat removal demand over mission.

	Ma [–]	alt [ft]	Q_{req} [kW]	m_{fuel} [kg]
TO	0.10	1500	106.5	5695
EoC	0.76	35,000	126.1	967
GA	0.20	1500	87.9	967
ToCD	0.65	15,000	120.5	597
Taxi	0.01	0	73.0	220

Table 5
Fixed WIFHE design parameters.

dT_{ISA} [K]	10	d_w [mm]	1.5
h_T [mm]	3.0	λ_w [W/mK]	240
P_{rad} [W/m^2]	1100	$m_{f,min}$ [kg]	212
α_{abs} [–]	0.25	m_{WIFHE}[kg]	122

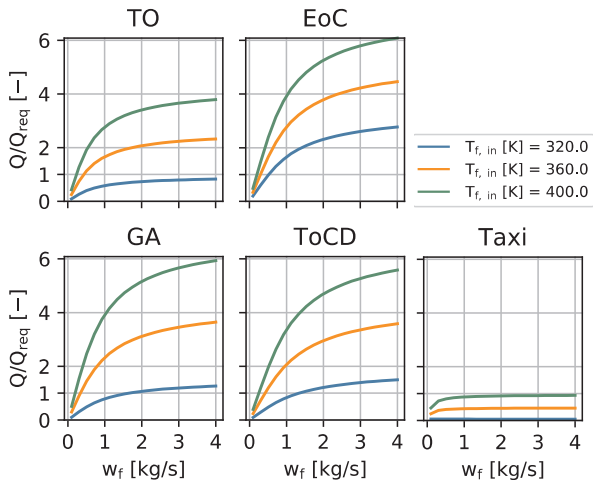

Fig. 11. WIFHE series system mission evaluation.

both control parameters for each mission point for the series configuration (Concept 1s) are shown in Fig. 11. The system's cooling power was scaled by the cooling power required at each mission point (Q_{req}). The final system needs to have at least a value of one for Q/Q_{req} for each mission point to be able to fulfil the cooling demand in a steady state manner.

Most fixed design parameters in Table 5 were adopted from the reference point of the partial dependence analysis (cf. Table 3). However, h_T was decreased to 3 mm to increase Q. The additional system mass from the WIFHE components (m_{WIFHE}) and $m_{f,min}$ are direct results of the geometries in Fig. 2, h_T and the chosen wing skin material "Al2024-T351" [42].

A first general observation when comparing Fig. 11 to Fig. 8 is the gradient of increasing w_f. In column two of the partial dependence analysis, the lines showed strong asymptotic tendencies for w_f values higher than 0.5 kg/s. The WIFHE series system still has a notable slope for a w_f of 4 kg/s except for the Taxi mission point because multiple WIFHE components are in series and thus extend the effective heat exchange area so that the w_f limit is higher.

The TO heat load can be fully rejected for a fuel flow of 0.45 kg/s within the WIFHE at a $T_{f,in}$ value of 360 K. For very low inlet temperatures of 320 K the required heat load is not matched even for high w_f of 4 kg/s. Using a maximum $T_{f,in}$ value of 400 K reduces the required w_f to 0.25 kg/s.

At EoC, Mach number and altitude are high providing a very good external heat transfer coefficient and low ambient temperature. Therefore the heat load demand can be met even with low $T_{f,in}$ values of 320 K at moderate fuel flows of 0.5 kg/s. For higher $T_{f,in}$ the fuel flow value becomes even less.

At GA the shape of the lines of constant $T_{f,in}$ is similar to the previously discussed mission points. The $T_{f,in}$ sensitivity is the largest of all mission points mainly because of the low altitude and thus relatively high ambient temperature and the comparably low Q_{req} value. At GA the heat can be removed even with the lowest $T_{f,in}$ value of 320 K. However, a rather large w_f of 1.5 kg/s is required. Using a moderate $T_{f,in}$ value significantly reduces the minimum w_f value to 0.4 kg/s.

ToCD temperature lines are almost an exact copy of the ones in the GA case even though the cooling power demand is 50% higher. The increased Q_{req} value is balanced by the better external heat transfer coefficient due to the high Mach number and moderate altitude.

The taxi case differs from all other cases. Even with the maximum allowable $T_{f,in}$ for very high w_f the cooling demand is not fulfilled and no more than 90% of Q_{req} can be provided. For a moderate $T_{f,in}$ cooling power is roughly 50% of the required value. $T_{f,in}$ values below 350 K provide hardly any cooling power because of the very low Ma and alt.

The mission design study indicates that Taxi and TO are the most critical points, which is in good accordance with Section 4.1. Therefore, the study is repeated for these two points with the most adverse conditions for the cooling system, which are hot and low (h&l). Hot and high (h&h) is typically one of the most adverse cases in aircraft design, especially for engines due to the high air temperature and low air density. However, for the WIFHE the impact of the ambient temperature out scales the density's one so that the higher ambient temperatures at h&l compared to h&h cause h&l to be most critical. For this adverse condition, dT_{ISA} is set to 20 K. At TO the minimum w_f value for a $T_{f,in}$ of 360 K slightly increases to 0.5 kg/s. At h&l taxi, the maximum Q value decreases to 85% of Q_{req}. Cooling with $T_{f,in}$ of 320 K becomes impossible due to radiation heat at the top wing surface.

The design study is repeated for the parallel configuration (Concept 1p). Only very marginal differences with regards to Q are found for every mission point compared to the series configuration. The main difference between series and parallel configuration is the fuel flow velocity for a given w_f. The parallel configuration's velocity is half the velocity of the series configuration for the same w_f. Since in both cases Reynolds numbers are too low for any turbulent flow to occur, flow velocity has no influence on the Nusselt number and thus h_{fuel}. The velocity does have an impact on the friction factor and therefore on P_{hyd} as shown in Fig. 12. It displays P_{hyd} over w_f and $T_{f,in}$ for the parallel and series WIFHE system configuration at TO conditions. The external conditions have very limited effect on P_{hyd} (cf. Fig. 8), therefore Fig. 12 represents the characteristic at all mission points.

P_{hyd} is larger for the series compared to the parallel configuration at any given w_f – $T_{f,in}$ combination. At the same w_f value, the series configuration has twice the flow velocity, which causes a higher friction factor. The quadratic nature of the flow velocity – P_{hyd} dependence results in P_{hyd} being more than twice as large for the series configuration. Because of the significantly lower P_{hyd} value and equal Q values, a parallel configuration is chosen for the subsequent aircraft assessment. The system will have a design w_f of 1.0 kg/s but a pump providing a maximum hydraulic power of 2.3 kW – enough for a w_f of 1.5 kg/s already implementing a safety factor of 1.5. The design w_f allows TO at $T_{f,in} \geq 340$ K, GA as well as ToCD with fuel inlet temperatures just above 320 K and EoC at even less than 320 K. The system does not always have to run at the design w_f, but may be adjusted to cooling power demands. There seems to be no solution for the Taxi case within the given design range. However, a good argument can be made for operational solutions with the existing concept: All evaluations

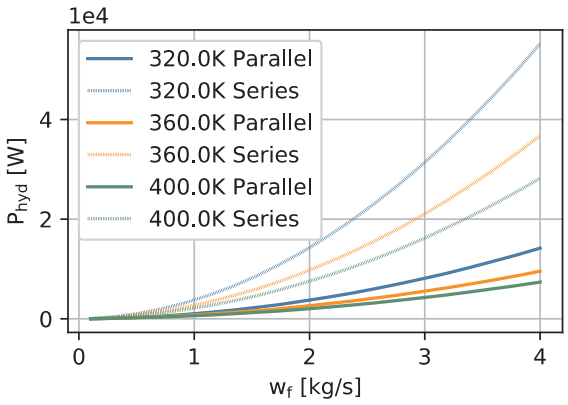

Fig. 12. Hydraulic power of parallel and series WIFHE system in TO.

Table 6
TWIH fill levels at selected mission points.

	$m_{f,outer}$ [kg|%]		$m_{f,inner}$ [kg|%]	
TO	2 × 552	100	2 × 2134	100
EoC	2 × 110	20	2 × 363	17
GA	2 × 110	20	2 × 363	17
ToCD	2 × 298	54	2 × 0	0
Taxi	2 × 99	18	2 × 0	0

presented in this work are stationary at few discrete points in time. An integrated time resolved model however, could use the full potential of the fuel heat sink. During Taxi – out excess heat that cannot be removed to ambient may be temporarily added to the fuel mass stored in the tank. The amount of heat required to increase the temperature of a quantity of fuel by 1 K is easily obtained via (1). For the fuel mass present at TO (cf. Table 4), this gives a heat value of 10.97 MJ – enough to remove the taxiing heat load for 150 s. In other words: A 15 min Taxi – out run would cause a 6 K increase in fuel temperature if zero heat loss to ambient was assumed. Taxi – in especially after a diversion is more complicated due to the small remaining fuel amount. Optimized solutions will be part of future work.

4.3.2. Concept 2 – TWIH

The TWIH does not have w_f as a parameter and therefore one less degree of freedom. The Q/Q_{req} evaluation for all mission points was performed in the same way as for Concept 1. Prior to evaluating Concept 2 at the different mission points, the fill levels of each tank have to be defined. They are shown in Table 6. The inner tank is not listed because no heat exchanger is installed. This decision stems from the results of the TWIH partial dependence analysis with regards to the fill level. The largest tank is the hardest to keep at a high FL. The inner tank also has the worst area to volume ratio and during operation, its fuel would be the first to be used. At TO, outer and inner TWIH are full and the rest of the fuel is in the inner tank. At EoC and GA the remaining fuel is too little to fill up the inner and outer TWIH entirely. Therefore, it is distributed between the two, so that they have an almost equal relative fill level. This ensures that the heat exchangers are still submerged in the fuel and offer the greatest surface area. At ToCD and Taxi only the outer tanks can be used since there is very little fuel left. The results of the TWIH mission design studies are shown in Fig. 13.

At TO all TWIH components are filled up and therefore can use their maximum potential. At T_0 just above 370 K the TO Q_{req} is met. Increasing T_0 to the set limit temperature of 400 K allows exceeding Q_{req} by 50%. At EoC no tank is filled anymore, which according to Fig. 10 leads to a large decrease in Q. Only 70% of EoC Q_{req} can be provided even at the highest T_0. At GA heat loads are lower due to the slower flight speed, but that also decreases the heat transfer rate. GA Q_{req} can be met up to 75% at the maximum T_0 however, it falls of more rapidly with decreasing T_0 compared to EoC. ToCD and Taxi have such low fuel levels that there is only some fuel left in the small outer TWIH. Therefore, the respective Q_{req} values can only be satisfied by 15% and 2.5% for the highest possible T_0 value.

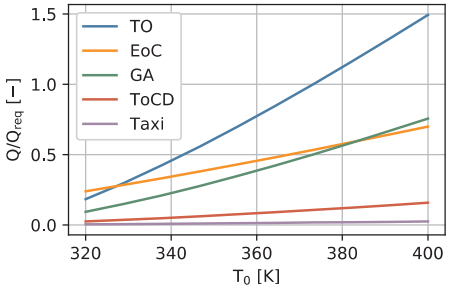

Fig. 13. TWIH design at selected mission points.

The current model of Concept 2 is clearly not adequate to cope with the presented heat demands. However, this may be mostly attributed to the nature of the used model: Real tanks are not at rest, but constantly subject to accelerations causing enhanced movement in the fuel. There also might be mixing due to inter tank fuel transfer. Furthermore, in the present model the dihedral angle was ignored. With dihedral angle the air layer occurring at less than 100% fill level does not cover the full span at relatively high fill levels. Considering all these phenomena would increase h_{fuel}. The presented model is therefore very conservative.

The TWIH concept would benefit from a fully time resolved method as the entire fuel mass is used in contrast to the fraction in the WIFHE model and therefore the heat capacity is much larger. Another way to significantly increase heat transfer for concept 2 is mounting the heat exchanger on the lower TWIH surface, so that it has direct contact with the wing surface material. Lower side heat transfer is then conductive combined with external convection and not dependent on the fuel natural convection. Also forcing a permanent movement of the fuel inside the tank increases the fuel side heat transfer coefficient. This can be realised with stirring devices or by using the fuel system to constantly pump fuel between the different tanks.

4.4. Reference heat exchanger

To evaluate the effect of the fuel cooling concepts against the reference ram air heat exchanger system on overall aircraft level, the reference system is dimensioned for the determining flight condition (EoC, cf. Section 4.3) aiming at a minimum external drag at a reasonable heat exchanger volume. Once the system is dimensioned, its geometrical features are held constant and the remaining flight conditions are calculated. The resulting drag values are integrated in the overall aircraft performance analysis.

For low Mach numbers (ground operations as well as the early take-off phase), the operation of a ram air fan is assumed. Its effect on the ram air system is neglected in this study.

The properties of the resulting system (ram air mass flow ($\dot{m}_{air}$), coolant mass flow ($\dot{m}_{coolant}$), heat exchanger volume (V_{hx}), total system length (L_{total}), diffuser outlet area (A_2) and coolant temperature delta over heat exchanger ($\Delta T_{coolant}$)) are presented in Table 7.

The corresponding drag increments at the selected mission points with reference to the overall aircraft are given in Table 8. According to the underlying experimental data for inlet and outlet, inlet drag of NACA inlets approaches zero, while the outlet produces a small amount of thrust at low Mach numbers. Therefore, a negative drag coefficient (i.e. thrust) is reached for take-off and go-around condition.

Due to the lack of available validation data, the non-dimensional heat transfer model of the reference ram air heat exchanger system could not be validated. Therefore, the presented data serves as a first estimation to evaluate trends when comparing heat sink technologies rather than pursuing the goal of optimizing a ram air heat transfer system.

4.5. Impact on overall aircraft level

Based on the system level results, Concept 1 was investigated on overall aircraft level. At its current state, Concept 2 proved to be thermodynamically insufficient for the necessary cooling power and is therefore not assessed on aircraft level. For Concept 1 the ram air cooler was replaced by the WIFHE system. Consequently, drag associated with

Table 7
Resulting ram air system design parameters.

$\dot{m}_{air}$ [kg/s]	3.35	L_{total} [m]	1.83
$\dot{m}_{coolant}$ [kg/s]	8.17	A_2 [m^2]	0.23
V_{hx} [m^3]	0.86	$\Delta T_{coolant}$ [K]	5.00

Table 8
Incremental pressure drag counts of the ram air system at selected mission points.

	Ma [–]	c_D [–]*		Ma [–]	c_D [–]*
TO	0.00	–	GA	0.20	− 0.78
	0.20	− 0.78	ToCD	0.65	0.45
EoC	0.76	0.99	Taxi	0.01	–

* With respect to the reference aircraft wing area.

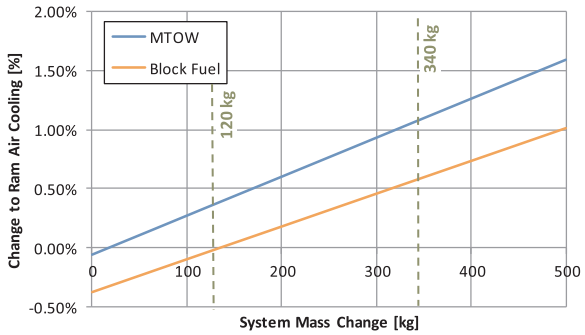

Fig. 14. Mass sensitivity analysis of Concept 1 compared to ram air cooling concept.

the ram air cooler system was set to zero and the mass of the WIFHE components was added. A mass impact of the down sized ram air inlet and in turn heat exchanger has been neglected in the first instance. The results of this approach are given in Fig. 14 showing the impact of a variation of the additional system masses. It marks the two variants of Concept 1: the 120 kg basic variant (only structural mass) and the 340 kg variant considering the additional required fuel demand for taxiing. The basic variant results in a similar performance as the ram air cooling concept. The MTOW increases by 0.3% compared to the ram air cooling concept and the block fuel maintains the same. However, considering the additional required fuel that is not accounted in the block fuel, but required for cooling during Taxi – in after the diversion, the MTOW further increases to 1.1% and block fuel increases by 0.6%.

5. Conclusion and outlook

Two concepts using fuel as a heat sink for a future aircraft were investigated and compared to a ram air based cooler. One concept actively cycled fuel underneath the wing surface while the other transferred heat to the fuel by placing a heat exchanger inside the tank. The reference aircraft platform was a hybrid-electric aircraft supplied by kerosene and batteries designed for 180 passengers, a design range of 1300 nm and a design cruise Mach number of 0.76. Thermodynamic modelling of the concepts was based on semi empirical methods. The system model's integrity was confirmed by means of a partial dependence analysis. The systems were designed to meet heat removal requirements for the presented aircraft system at five relevant mission points. The required cooling rate at each mission point (Q_{req}) was given as input parameter. A liquid based cooling system for the electric components was assumed, but not modelled in full detail. All assessments were made for steady state heat flow at discrete time points. Concept 1 using Wing Integrated Fuel Heat Exchangers (WIFHE) could provide Q_{req} in all mission points within the set design range for the two control parameters fuel flow (w_f) and fuel inlet temperature ($T_{f,in}$) except for the Taxi case. In End of Cruise (EoC), Go Around after cruise (GA) and Top of Climb Diversion (ToCD) relatively low $T_{f,in}$ could be used allowing relaxed design constraints for the hot side system. For Taxi only 85% of Q_{req} were achieved. The installed system added 120 kg structural mass on the wings. For the Taxi – in case 220 kg of additional fuel need to be on board at all time to ensure the cooling capability of the system.

Concept 2 used Tanks With Internal Heating (TWIH) and the fuel – side heat transfer coefficient (h_{fuel}) was based on a natural convection model. The model proved to be extremely sensitive to fill level (FL) near the maximum FL. The potential cooling rate (Q) was decreased by 70% when reducing the FL of a TWIH from 100% to 80%. Q_{req} could only be met in TO. In EoC and GA Q_{req} was fulfilled by 70% and 75% respectively. ToCD and Taxi conditions led to 15% and 2.5% Q/Q_{req} values.

The reference cooler was modelled as a ram air system with NACA inlet and a compact cross-flow heat exchanger. It was dimensioned based on the requirements of the EoC operating point of the reference aircraft. The resulting geometry was applied to the relevant operating conditions and incremental drag values were calculated and integrated into the overall aircraft performance evaluation. Aircraft trade studies showed that Concept 1 would break even with a conventional ram air cooler in terms of fuel burn if no additional cooling fuel is required. The addition of 220 kg fuel for cooling purposes at Taxi – in lead to a 0.3% increase in fuel burn.

Future work on concept 1 may include a better solution for the critical Taxi – in case than adding 220 kg of fuel. A fully integrated time resolved model is required including a model for the hot side cooling system. With the knowledge of all fluid masses it may be possible to use the heat capacity of the fluids to absorb peak heat loads temporarily (e.g. TO) and reject them in later flight stages. With a liquid hot side system it may be possible to keep the cooling fluid́s temperature low until all fuel is used and then use the cooling fluid́s heat capacity to store the Taxi – in heat load. This is only required for unusual mission cases where the reserve fuel is used up. A detailed model for the liquid cooling system of the electric components is also required to obtain typical temperature levels. This study investigated cooling concepts using fuel with fuel temperatures up to 400 K while the proposed cooling system only had an operating temperature of 373 K.

The WIFHE was limited by the fuel side convection because the laminar duct flow has poor heat transfer capabilities compared to the turbulent external airflow. Artificially adding turbulence to the fuel flow could greatly increase the system's effectiveness. A free convection model on the air side could be useful to estimate adverse conditions i.e. the aircraft being at rest at an airport at hot and low conditions.

Concept 2 could be improved by investigating possibilities to constantly keep the fuel in motion inside the tanks either by inter tank fuel transfer or by mechanical mixers. It will also greatly benefit from using a fully time resolved model to use the large heat capacity of the entire fuel mass for heat removal. Inclusion of the dihedral angle would benefit free convection at high but not full fill levels.

The aircraft level assessment is very mass sensitive. The impact of added masses due to Concept 1 was overestimated because the favourable location of the added masses was not considered. For a better prediction of the aircraft level impact of the different cooling concepts, mass estimations for the entire systems are required in addition to structural models that are sensitive towards the location of added masses.

For some of the aforementioned proposed future work the simple semi empirical methods that were used in this research are not sufficient, which leads to the need of higher fidelity methods. This research was a first exploratory work on different options to use fuel as a heat sink for commercial aircraft with hybrid electric propulsion systems. In the future, both concepts should be evaluated with numerical 2D and 3D methods to increase accuracy and investigate secondary effects for example the effect on friction drag from the heated surfaces. In a next step, an experimental investigation should be performed to validate the developed models.

Declaration of Competing Interest

The authors declared that there is no conflict of interest.

Acknowledgements

We would like to thank Christoph Falter for fruitful discussions and his insights on thermal modelling. Furthermore, we thank Arne Seitz, Fabian Peter and Jochen Kaiser for their continued support of this work and their critical questions.

Funding

This research did not receive any specific grant from funding agencies in the public, commercial, or not-for-profit sectors.

Appendix A. Supplementary material

Supplementary data to this article can be found online at https://doi.org/10.1016/j.applthermaleng.2020.114985.

References

[1] Advisory Council for Aviation Research and Innovation in Europe, in: Strategic Research and Innovation Agenda: Volume 1. 2017 Update. Brussels, 2017.
[2] K. Yakinthos, S. Donnerhack, D. Misirlis, Flouros, M., Vlahostergios, Z., and A. Goulas, "Intercooled Recuperated Aero Engine: Early Development Stages and Optimization of Recuperation Based on Conventional Heat Exchangers," in: 2nd ECATS Conference: Making Aviation Environmentally Sustainable, Athens, Nov. 2016.
[3] F. Jacob, et al., Performance of a supercritical CO2 bottoming cycle for aero applications, Appl. Sci. 7 (3) (2017) 255.
[4] J.A. Rosero, J.A. Ortega, E. Aldabas, L. Romeral, Moving towards a more electric aircraft, IEEE Aerosp. Electron. Syst. Mag. 22 (3) (2007) 3–9.
[5] A. Isikveren, A. Seitz, P. Vratny, C. Pornet, K. Plötner, Conceptual Studies of Universally-Electric Systems Architectures Suitable for Transport Aircraft, 61. Deutscher Luft- und Raumfahrtkongress, Berlin, Sep. 2012, (2012).
[6] D. Schlabe, J. Lienig, Model-based thermal management functions for aircraft systems, in: SAE Technical Paper Series, 2014.
[7] C.N. Gray, M.W. Shayeson, Aircraft Fuel Heat Sink Utilization, Ohio, Jul. 1973.
[8] H. Streifinger, Fuel/oil system thermal management in aircraft turbine engines, in: Design principles and methods for aircraft gas turbine engines: Papers presented at the RTO Applied Vehicle Technology Panel (AVT) Symposium (organized by the former AGARD Propulsion and Energetics Panel (PEP)), held in Toulouse, France, 11 - 15 May 1998 = Les principes et méthodes de conception des turbomoteurs.
[9] B.J. German, Tank heating model for aircraft fuel thermal systems with recirculation, J. Propul. Power 28 (1) (2012) 204–210.
[10] L. Pang, et al., Influence of the design parameters of a fuel thermal management system on its thermal endurance, Energies 11 (7) (2018) 1677.
[11] E.J. Alyanak, D.L. Allison, Fuel thermal management system consideration in conceptual design sizing, in: AIAA SciTech: 57th AIAA/ASCE/AHS/ASC Structures, Structural Dynamics, and Materials Conference, San Diego, California, USA, 2016.
[12] D.B. Doman, Fuel flow topology and control for extending aircraft thermal endurance, J. Thermophys. Heat Transf. 32 (1) (2018) 35–50.
[13] D. Sigthorsson, M.W. Oppenheimer, D.B. Doman, Aircraft thermal endurance optimization part I: using a mixed dual tank topology and robust temperature regulation, in: AIAA Scitech 2019 Forum, San Diego, California, 2019.
[14] D. Sigthorsson, M.W. Oppenheimer, D.B. Doman, Aircraft thermal endurance optimization part II: using a simple dual tank topology and robust temperature regulation, in: AIAA Scitech 2019 Forum, San Diego, California, 2019.
[15] C. Zilio, et al., CFD analysis of aircraft fuel tanks thermal behaviour, J. Phys. Conf. Ser. 923 (2017) 12027.
[16] J. Roland, M.P. Rumpfkeil, Wing fuel-tank heat-sink calculation for conceptual aircraft design, J. Aircraft 54 (3) (2017) 1172–1188.
[17] C. Pornet, A.T. Isikveren, Conceptual design of hybrid-electric transport aircraft, Prog. Aerosp. Sci. 79 (2015) 114–135.
[18] C. Pornet, S. Kaiser, A.T. Isikveren, M. Hornung, Integrated fuel-battery hybrid for a narrow-body sized transport aircraft, Aircraft Eng. Aerospace Tech. 86 (6) (2014) 568–574.
[19] P.C. Vratny, H. Kuhn, M. Hornung, Influences of voltage variations on electric power architectures for hybrid electric aircraft, CEAS Aeronaut J. 8 (1) (2017) 31–43.
[20] P.C. Vratny, Conceptual Design Methods of Electric Power Architectures for Hybrid Energy Aircraft," Dissertation, Fakultät für Maschinenwesen, Technische Universität München, Munich, 2018.
[21] P. Vratny, P. Forsbach, A. Seitz, M. Hornung, Investigation of universally electric propulsion systems for transport aircraft, 29th ICAS Congress, (2014).
[22] I.H. Bell, J. Wronski, S. Quoilin, V. Lemort, Pure and pseudo-pure fluid thermophysical property evaluation and the open-source thermophysical property library coolprop, Ind. Eng. Chem. Res. 53 (6) (2014) 2498–2508.
[23] Coordinating Research Council, Handbook of aviation fuel properties. Atlanta, Ga, 1983.
[24] L.E. Faith, G.H. Ackermann, H.T. Henderson, Heat Sink capability of Jet A Fuel: Heat Transfer and Coking Studies, Cleveland, OH, Jul. 1971.
[25] H.D. Baehr, K. Stephan, Wärme- und Stoffübertragung, (ger), Springer Lehrbuch, 2004.
[26] W.M. Kays, M.E. Crawford, Convective Heat and Mass Transfer, third ed., McGraw-Hill, New York, 1993.
[27] Verein Deutscher Ingenieure; VDI-Gesellschaft Verfahrenstechnik und Chemieingenieurwesen, VDI-Wärmeatlas: Mit 320 Tabellen, 11th ed., Springer Vieweg, Berlin, 2013.
[28] F.P. Incropera, D.P. DeWitt, T.L. Bergman, A.S. Lavine, Principles of Heat and Mass Transfer, seventh ed., Wiley, Singapore, 2013.
[29] S. Genic, et al., A review of explicit approximations of Colebrook's equation, FME Trans. 39 (2011) 67–71.
[30] N.-S. Cheng, Formulas for friction factor in transitional regimes, J. Hydraul. Eng. 134 (9) (2008) 1357–1362.
[31] Y. Nakayama, R.F. Boucher, Introduction to Fluid Mechanics, Butterworth Heinemann, Oxford, Boston, 1999.
[32] E.U. Schlünder (Ed.), Heat Exchanger Design Handbook: HEDH, VDI-Verl, Düsseldorf, 1983.
[33] M.A. Branch, T.F. Coleman, Y. Li, A subspace, interior, and conjugate gradient method for large-scale bound-constrained minimization problems, SIAM J. Sci. Comput. 21 (1) (1999) 1–23.
[34] A. Brasseur, W. Leppert, A. Pradille, Inside the 747–8 new environmental control system, Boeing Aeromagazine 1 (2012) 19–25.
[35] I. Pérez-Grande, T.J. Leo, Optimization of a commercial aircraft environmental control system, Appl. Therm. Eng. 22 (17) (2002) 1885–1904.
[36] P. Feliot, Y. Le Guennec, J. Bect, E. Vazquez, Design of a commercial aircraft environment control system using Bayesian optimization techniques, in: 5th International Conference on Engineering Optimization.
[37] W.M. Kays, A.L. London, Compact heat exchangers, third ed., Krieger, Malabar, Fla., 1998.
[38] T. Elmer, A Novel SOFC Tri-generation System for Building Applications, Springer International Publishing, Cham, 2016.
[39] C.F. Hall, F. Dorn Barclay, An Experimental Investigation of NACA Submerged Inlets at High Subsonic Speeds, Washington, Jun. 1948.
[40] P.E. Dewey, A.R. Vick, An Investigation of the Discharge and Drag Characteristics of Auxiliary-Air Outlets Discharging, Washington, Jul. 1955.
[41] Pace GmbH, Pacelab APD, Pace GmbH, Berlin, 2011.
[42] MatWeb, Material Property Data Aluminum. [Online] Available: http://www.matweb.com/search/DataSheet.aspx?MatGUID=0cd1edf33ac145ee93a0aa6fc666c0e0&ckck=1 (accessed on: Sep. 25 2019).
[43] J.H. Henninger, Solar Absorptance and Thermal Emittance of Some Common Spacecraft Thermal-control Coatings, NASA, Greenbelt, 1984.

2.4 Design of a Battery Cooling System for Hybrid Electric Aircraft

The paper [4] presents methods and results for the design of battery TMSs onboard aircraft. A 19-seat regional aircraft is used as an application case. The paper is structured into seven sections.

The first section "Introduction" motivates the topic of battery TMSs as particularly difficult due to the low operating temperatures of batteries, which in combination with HDTO conditions result in the need for a heat pump. The state of the art is summarized and the aim of the paper to provide a battery TMS for adverse operating conditions is stated. Section I was conceptualized and written by Samuel Fuhrmann and edited by Hagen Kellermann.

The second section "Technology Assessment" presents different technologies, which would allow heat rejection of the battery at temperatures lower than ambient. The majority of the technologies are heat pumps. Most of the more than 30 considered technologies are quickly dismissed for various reasons, e.g., technology readiness, and expected mass, but seven technologies are investigated more in-depth. A detailed qualitative discussion combined with a rough quantitative assessment of the expected aircraft impact is conducted and finally, Thermoelectric Modules (TEMs) are selected. Section II was conceptualized and written by Samuel Fuhrmann and edited by Hagen Kellermann.

The third section "Battery Thermal Management System Model" presents the three component models of the battery TMS. The TEM consists of analytical and semi-empirical methods. It consists of multiple thermocouples and can be scaled to any heat load. Besides its mass, the electrical input power is the main output value of interest. The implemented model is compared to an existing model from the literature. The second component is a single-fluid finned R-HEX. The model is derived from a two-fluid R-HEX by introducing an additional geometric ratio to compensate for the additional geometric degree of freedom. Lastly, a simple heat pipe model is presented, which can be used to scale the heat pipe mass to a given heat load. It uses simple empirical correlations based on existing heat pipes. The initial part of Section III.A (TEM) was conceptualized and written by Samuel Fuhrmann. The TEM model was reworked, and the entire Section was rewritten by Hagen Kellermann. Section III.B (HEX) was conceptualized and written by Hagen Kellermann and Section III.C (heat pipe) was written and conceptualized by Samuel Fuhrmann.

The fourth section "Application Case: High-Performance Battery of the E19" summarizes the main information on the studied aircraft and the assumptions for the battery, most importantly the power demand of the different operating points and the temperature limits of the battery. Section IV was conceptualized and written by Michael Shamyieh except for the last paragraph which was written by Hagen Kellermann.

The fifth section "Sensitivity Analysis" presents partial dependence analyses for the TEM and the HEX model. They are conducted for all relevant variables of both models in a one-dimensional matter. Besides mass and power, the base area is a critical output parameter of both models since they have to be similar in the final assembled TMS. For the TEM, the overall temperature difference between the hot and cold side is the most influential parameter, especially with regard to the required electrical power. Section V was conceptualized and written by Hagen Kellermann.

The sixth section "Design of the Battery Thermal Management System for the Application Case" presents the setup and results of the final design study. The optimization procedure is explained and detailed results of the final TMS, which was designed for HDTO conditions are presented. The final results show electric power, system mass, and an expected overall mass including additional battery mass required to provide the power for the TMS. Within the given design space of varying ambient temperature, battery efficiency, and allowed battery temperature, the relative MTOM increase ranges from 2% to 16%. Besides the top-level results, more in-depth results are presented to provide explanations for the observed trends. No off-design calculations were performed but a qualitative discussion of the possible impacts of a dynamic model is at the end of the section. Section VI was conceptualized and written by Hagen Kellermann.

The paper closes with a combined conclusion and outlook section summarizing the main findings and recommending future work. As the main improvement the consideration of snowball effects, which can only be regarded in an iterative procedure, is recommended. The final section was written by Hagen Kellermann. The

entire paper was reviewed by Mirko Hornung. The Master Thesis of Samuel Fuhrmann, who was supervised by Hagen Kellermann and Mirko Hornung was the basis for the paper.

Author contributions in short: conceptualization, methodology, simulation, analysis, and writing of all aspects of the research except Section I, II, III.C, IV, the initial draft of III.A: H.K.; Review, editing of Section I, II, III.C, IV: H.K.; conceptualization, methodology, simulation, analysis and writing of Section I, II, III.C, the initial draft of III.A: S.F. conceptualization and writing of Section IV: M.S.; supervision and review: M.H.

Design of a Battery Cooling System for Hybrid Electric Aircraft

Hagen Kellermann,* Samuel Fuhrmann,† Michael Shamiyeh,‡ and Mirko Hornung§
Bauhaus Luftfahrt e.V., 82024 Taufkirchen, Germany

https://doi.org/10.2514/1.B38695

A battery thermal management system (BTMS) for a hybrid electric aircraft is designed. Hot-day takeoff conditions are assumed, resulting in an ambient temperature higher than the allowed battery temperature. Thus, a heat pump has to be employed in the BTMS. All available heat pump technologies are assessed and compared. In a qualitative downselection process, thermoelectric cooling is chosen as heat pump technology. A computational model of the thermoelectric modules (TEMs), as well as a finned ram air heat exchanger with a puller fan (HEX) as heat sink, and a simple heat pipe model for heat acquisition from the battery are developed. Sensitivity analyses of the TEM and HEX models are conducted for comprehension of the relevant design variables. Finally, a BTMS is designed and optimized for a 19-seat hybrid electric aircraft with an all-electric design mission and a combustion engine for range extension. The temperature deviation from the International Standard Atmosphere, the battery operating temperature, and the battery efficiency span a three-dimensional design space rather than being defined to three discrete values. The most adverse combination of these three parameters results in an optimized BTMS that increases the maximum takeoff mass of the aircraft by 16% without the consideration of any snowball effects, whereas the most advantageous combination leads to a 2% increase.

Nomenclature

A	=	area, m^2
A_{base}	=	total base plate area of the heat exchanger, m^2
A_{front}	=	frontal area of the heat exchanger, m^2
B	=	width, m
C_R	=	heat capacity ratio
c_p	=	specific heat capacity at constant pressure, $J \cdot kg^{-1} \cdot K^{-1}$
d_H	=	hydraulic diameter, m
H	=	height, m
I	=	electric current, A
K	=	thermal conductance, $W \cdot K^{-1}$
L	=	length, m
Ma	=	Mach number
m	=	mass, kg
P	=	electric power, W
p	=	pressure, Pa
Q	=	heat flow, W
R	=	electric resistance, $V \cdot A^{-1}$
T	=	temperature, K
t	=	thickness, m
w	=	mass flow, $kg \cdot s^{-1}$
α	=	Seebeck coefficient, $V \cdot K^{-1}$
γ	=	aspect ratio defined as height to width or length to width
Δ	=	absolute difference
δ	=	relative difference
ϵ	=	heat exchanger effectiveness
λ	=	thermal conductivity, $W \cdot m^{-1} \cdot K^{-1}$
Π	=	pressure ratio defined as outlet pressure to inlet pressure
ρ	=	density, $kg \cdot m^{-3}$
ρ_e	=	electric resistivity, $V \cdot m \cdot A^{-1}$
σ	=	ratio of free flow to frontal area

Subscripts

AS	=	air side
amb	=	ambient
bat	=	battery
c	=	cold side
chan	=	channel
e	=	electric
HS	=	hot side
h	=	hot side
m	=	arithmetic mean
mat	=	material
max	=	maximum
n	=	negative doted type
p	=	positive doted type
tc	=	thermocouple
w	=	wall
ϕ	=	value at maximum COP
1	=	at inlet
2	=	at outlet

Presented as Paper 2021-3138 at the AIAA Aviation 2021 Forum, Washington, DC (Online), August 2–6, 2021; received 8 November 2021; revision received 28 January 2022; accepted for publication 23 February 2022; published online Open Access 29 April 2022.

*Research Engineer, Bavaria; hagen.kellermann@bauhaus-luftfahrt.net. Student Member AIAA (Corresponding Author).

†Master's Thesis Student, Bavaria; also Master's Student, Technical University of Munich, Germany, TUM Department of Aerospace and Geodesy; samuel.fuhrmann@tum.de.

‡Research Engineer, Bavaria; michael.shamiyeh@bauhaus-luftfahrt.net.

§Executive Director of Research and Technology, Bavaria; mirko.hornung@bauhaus-luftfahrt.net. Senior Member AIAA.

I. Introduction

AMBITIOUS goals for particle and noise emission reductions in aviation were set by European and U.S. organizations (Advisory Council for Aeronautics Research in Europe [ACARE] and NASA respectively) at the beginning of the past decade [1,2]. Among the multiple technologies that are proposed to achieve these goals, the partial or full electrification of the propulsion system has been a focus of research in the last years. Potential benefits such as emission-reduced or emission-free flight can be realized. However, a remaining challenge for (hybrid) electric aircraft [(H)EAC] is thermal management [3–6]. Despite their generally high efficiencies, electric components do not have a natural heat sink such as the exhaust jet of a gas turbine.

Of the many components of an electric drive train, batteries are particularly difficult to cool because of the low and narrow optimal temperature range of high-performance batteries. For lithium-ion batteries, 15 to 35°C is a common range of the recommended operating temperature [7]. Considering hot-day takeoff conditions with ambient temperatures higher than 35°C, common air- or liquid-based heat transfer cooling concepts are most likely not sufficient. The battery cooling system must include a heat pump with a cold side at a temperature lower than ambient.

The objective of this study is threefold: First, potential heat pump technologies are investigated. Using qualitative and first-order quantitative methods, the most promising technology candidate for a (H)EAC is selected. Second, the battery cooling system with the chosen heat pump technology is modeled to a degree that allows the prediction of mass and power off-take added to the aircraft. Third, this model is used to size a battery cooling system for a (H)EAC application case. The aircraft considered for the case study is the so-called E19 concept: a hybrid electric 19-seater with an all-electric range of 190 km and a combustion engine for range extension [8].

The thermal management system (TMS) is widely acknowledged in research as essential subsystem of (H)EAC [3–6]. However, several conceptual (H)EAC studies either neglect the TMS in their quantitative concept assessment or use very simplified assumptions (e.g., [9,10]). Others investigated TMS for (H)EAC in more detail although the focus was on the thermal management of motors, generators, power electronics, and cables [11] or alternative heat sinks available on the aircraft [12,13]. The specific challenges of battery thermal management systems (BTMS) on aircraft have only been addressed quite recently. In [14], an open reverse Brayton cycle on the system level and heat pipes on the component level are proposed and a proof-of-concept is given. A sophisticated study incorporating a BTMS on a (H)EAC was presented in [15]. It is an update of an earlier TMS concept [16] based upon the N+4 2035 Refined SUGAR by Boeing. The TMS consists of three separate pumped liquid coolant loops: a fuel- and bypass-air-cooled oil loop for higher temperature engine loads and two propylene-glycol-based coolant loops for lower temperature loads (one for the battery, one for the motor drive) with ram air as the final heat sink. The concept does not require a heat pump because the battery is allowed to heat up during takeoff and climb until the maximum operating temperature of 40°C is reached, which does not happen before the aircraft is already at higher altitudes with low ambient temperatures. It assumes precooling of the batteries on the ground for hot-day takeoff conditions. In [17], additional sensitivity studies are conducted for the concept, finding TMS weight reductions for an increase of TMS design altitude or an increase of battery efficiency. In [18], integrated motor drive units are cooled by an air-cooled oil cooler and the BTMS is covered by the existing environmental control system (ECS). To avoid an oversized ECS, the battery is allowed to heat up to a limit temperature of 45°C (thermal storage). The ECS is sufficient for battery cooling if it operates at maximum load during the entire mission, and an averaged battery heat generation is assumed throughout the mission. This results in a neutral mass balance and a 1.4% block fuel burn penalty.

All research on BTMS for (H)EAC up to this point depends on several strong assumptions regarding battery thermal capacity and idealized operating conditions. This work aims to provide a reliable, independent BTMS considering adverse operating conditions.

II. Technology Assessment

The technology assessment was done to identify all technologies available to solve the challenge of cooling an electric component with a maximum allowed temperature near or below adverse ambient conditions. The boundary conditions for the technology assessment included a maximum T_{bat} of 35°C, $Q_{bat} = 100$ kW, and a deviation from the International Standard Atmosphere (ISA) temperature of +30 K, which corresponds to $T_{amb} = 45$°C at sea level. The temperature lift requirement for the heat pump was set to 25 K. This leaves some temperature difference for TMS internal heat transfer and for sufficient temperature difference to the ambient.

For a better understanding of the technology assessment, Fig. 1 shows a sketch of a general BTMS. The battery heat load is named Q_i because it is the input to the BTMS. Q_i is transferred to the heat acquisition system (HAS), which is a general term used for the specific technology collecting the heat from the direct vicinity of the battery pack. A HAS can be as simple as direct air contact outside the pack, but also sophisticated technology such as heat pipes inside the pack or liquid cooling channels. Depending on the selected technology of the cooler, there may be several options for a suitable HAS. From the HAS, the cold side heat load Q_c, which may be larger than Q_i depending on the HAS used, is transferred to the cooler. The cooler is the core technology of the BTMS to ensure that the battery does not exceed its temperature limits. Most cooler technologies are some form of heat pump due to the aforementioned requirement of $T_{bat} < T_{amb}$ on hot days. A heat pump needs a work input that results in $Q_h > Q_c$ for most coolers. The hot side heat load Q_h is transferred to the heat sink system (HSS), which is the component transferring the heat to the ambient (Q_o), e.g., a radiator. HAS, cooler, and HSS together are the BTMS. All components of the BTMS may require power P if they are not passive components. The technology assessment in this section only addresses the cooler, and it is assumed that HAS and HSS are chosen accordingly.

Initially, 32 technologies were considered for the cooler of which the majority were heat pumps. Most were disregarded quickly either because they were not expected to be available in 2035, or were unsuitable for the given application case, or because they rely on thermal rather than electrical or mechanical power to operate. The last criterion needs further explanation. A metric for any cooling technology is the coefficient of performance (COP):

$$\text{COP} = \frac{\text{heat removed by the system}}{\text{work required by the system}} = \frac{Q_c}{Q_h - Q_c} = \frac{Q_c}{P_{\text{Cooler}}} \quad (1)$$

Consequently, thermally driven systems either need to have a large COP value or a thermal load from another source that exceeds the cooling load, i.e., the battery heat load, largely in quantity. For the given application, the battery is expected to be the most inefficient component of the electric drive train and therefore has the highest thermal load. Also, thermally driven systems usually have small COP values. Single effect absorption or adsorption refrigerators, e.g., have a COP of well below 1 [19,20]. Ejector refrigeration has a COP of around 0.2 [21]. Furthermore, thermally driven cooling technologies may tend to increase system complexity. The disregarded thermally driven technologies are absorption cooling, adsorption cooling, metal-hydride cooling, ejector refrigeration, and Vuilleumier cycle cooling.

All other technologies that were among the quickly discarded are summarized with a short explanation on the working principle, the reason for their dismissal, and some available literature on them in the Appendix of the conference version of this paper [22]. In the remainder of this section, seven cooling technologies are further investigated and compared in order to reach a well-founded decision on which technology to use in the following detailed assessment. In a first step, a rough quantitative estimation is conducted based on literature research. Then each technology is discussed in depth and finally one of them is selected.

Table 1 lists the seven technologies considered for the battery cooling system with an estimation of potential COP and mass values. The estimated mass is exclusively for the cooler technology, and the masses of the additional components are not considered.

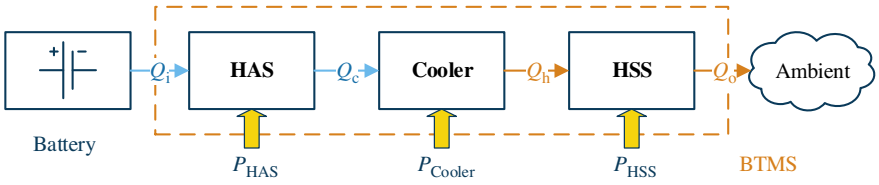

Fig. 1 Scheme of the general battery thermal management system.

Table 1 Comparison of most relevant cooling technologies (technology assessment boundary conditions considered)

Technology	COP	Mass, kg	Additional components	Sources
Air cycle machine	0.1–0.7	80–290	HAS, piping	[21,23–25]
Vapor cycle machine	2.3–4.4	330–600	HAS, HSS	[21,26], MR
Expendable cooling	N/A	30–300	HAS, storage	[27]
Vortex tube cooling	0.01–0.13	50–85	HAS, piping, compressor	[28,29], MR
Thermoelectric cooler	0.2–1.2	10–30	HAS, HSS, electric leads	[26,30–32], MR
Magnetocaloric cooler	0.5–9.7	340–610	HAS, HSS, magnet, motor, pump, piping	[28,33,34]
Phase change material	N/A	400–510	HSS, matrix	[35,36]

The additional components are listed and their impact is discussed. The values given for COP and mass are literature values scaled to the selected Q_{bat} where available. Otherwise, small market researches were conducted using the product information of companies as indicated by "MR" in Table 1. In those cases, the product information sheets available on the websites of one or multiple companies offering products for the respective technologies were consulted to estimate the possible COP and mass ranges.

The following discussion includes additional qualitative criteria. Especially a technology's impact on (airport) infrastructure, its capability to also heat the battery if needed, the technology maturity, and the availability of cooling power during the charge phase on ground are mentioned if they are a disadvantage for the respective technology.

A. Air Cycle Machine

The air cycle machine (ACM) uses the Joule–Brayton cycle known from gas turbines in reverse. Ram air taken from the ambient is compressed, which increases its temperature. The compressed air is cooled by a secondary flow of uncompressed ambient air. Afterward the compressed air is expanded again, which results in a temperature drop below ambient, enabling it as coolant for the battery. ACMs are already widely used in aircraft as ECS. This technology is rather lightweight, especially because the HSS is already part of the considered system mass. Further advantages are its robustness, reliability, minor leakage concerns because air is used as medium, a wide operable temperature range, and a COP that increases with increasing temperature lift [14,21,31,37]. Using air as cooling medium also presents the major disadvantage of the ACM. The simplest HAS would be direct air cooling of the battery, which might not ensure the required constant and uniform temperature of the battery modules [38]. Furthermore, dehumidification devices and filters may be required in order to protect the battery, adding mass and maintenance effort to the system. Mufflers might have to be provided to attenuate the noise of the air compressor [21]. More complex HAS would be possible but add mass and thermal resistances to the BTMS. In [18] the concept of using the ECS for battery cooling was already used in simulation.

B. Vapor Cycle Machine

The vapor cycle machine (VCM) is one of the most common cooling technologies in the world. It employs a closed cycle. In an evaporator, the cooling fluid absorbs heat from a source with a temperature lower than ambient. The gaseous coolant is then compressed, resulting in a further temperature increase above ambient, allowing it to be cooled and condensed in a second heat exchanger. Besides its maturity level even in aircraft operation where it is used as ECS in small aircraft, the high COP value is the largest advantage of the VCM. It increases with temperature lift as well [21,34,37]. The large mass numbers for the VCM in Table 1 are partly due to the industrial application cases in the literature and market research. Adaptions to aircraft requirements may result in a significant reduction of the system mass, but because of the additionally required HAS and HSS, the VCM is still expected to be among the heavier technologies. It is vital to avoid leakage of the two-phase coolant. This might result in even heavier and more complex system layouts or increased maintenance effort. Without additional systems, no heating is possible with a VCM, resulting in challenges to keep the battery above the lower allowable temperature during cruise or when switched off on ground. When operating at full power, a VCM can produce a significant noise level [21,24,34].

C. Expendable Cooling

For expendable cooling, liquefied gas with beneficial properties (high heat of vaporization and high heat capacity), e.g., liquefied hydrogen, is used. It flows by the heat source and evaporates before either being burned in a combustion chamber or ejected to the environment. To estimate the mass values in Table 1, the properties of H_2, O_2, CO_2, He, N_2, and CH_4 were considered. In case of an aircraft concept that uses the liquefied gas for propulsion, expendable cooling may be the best choice because the calculated coolant mass would, at least to some extent, already be accounted for as fuel and the airport would have the infrastructure to refuel the coolant. Also, when very low temperatures are required, e.g., in cryogenic applications, expendable cooling may be the preferred choice over employing a heavy cryo-cooler.

For battery cooling, the low gas evaporation temperature is a challenge that needs to be carefully considered to prevent the battery from being cooled too much. Also, expendable cooling does not offer a heating capability, and if the coolant is not used as fuel, the additionally required infrastructure is a large cost and certification factor. The cooling system has to operate during battery charging on ground and it might cause problems related to releasing the evaporated gas (unburned) at the airport.

D. Vortex Tube

The vortex tube passively expands pressurized air in a way that the incoming air stream is divided into a hotter and a colder jet. The colder one can be used for cooling purposes. Vortex tube cooling (VTC) has advantages: having an adjustable cooling temperature and no moving parts, and being lightweight, compact, and commercially available. Furthermore, the hot air produced as by-product could be made use of (e.g., in galley) [29,39,40].

VTC shares most disadvantages with the ACM, because of its use of air as coolant (issues with cooling uniformity, dehumidification, filtering). In addition, VTC requires the provision of highly compressed air (about 7 bar) and a lot of piping is necessary to supply the installed vortex tubes (several dozens) with air. It is not trivial to distribute the produced cool air streams because they are very focused (thin diameter). Furthermore, the COP of this technology is very low and a high noise level is expected at high power operation [39,40].

E. Thermoelectric Cooling

For thermoelectric cooling (TEC), solid-state Peltier elements (flat squares with side lengths of a few centimeters) are used. When a voltage is applied to a Peltier element, it pumps heat from its one side to the other. TEC offers advantages such as compact size, small weight, robustness, noiselessness, reliability, easy control, lack of moving parts, and therefore low maintenance effort. It is well established in other industry segments and of moderate cost. Heating of the battery is possible by inverting the direction of the applied electric current. And for very large temperature gradients, e.g., with very cold ambient air during cruise, the Peltier elements can be used as thermoelectric generators as well [32,34,37,41]. The major disadvantage of the TEC is its comparably low COP value, which decreases with

increasing temperature lift. The advantage of accurately controlling each Peltier element and thereby the temperature distribution results in complex controls requiring a significant amount of cabling [32,34,41].

F. Magnetocaloric Cooling

Magnetocaloric cooling (MCC) uses materials that heat up when exposed to a magnetic field and cool down again when the field is removed. This phenomenon can be used in a cyclic manner to create a heat pump. An additional coolant is used to transport the heat between magnetocaloric materials and the heat exchangers with heat source and sink. Research shows large potential COP values of up to 10, which is the major advantage of MCC [26,33].

Up to now, the maturity level of MCC is low. The existing research prototypes are heavy, bulky, of high complexity, and far from first industrial applications. MCC employs a magnetic field of considerable strength (about 1 T), which requires shielding. Whether the system weight can be reduced enough to become viable for mobile and especially flying applications is uncertain. Today, magnetocaloric materials are expensive as well [28,37].

G. Phase Change Material

Phase change materials (PCMs) have a very high latent heat capacity. They can absorb large amounts of heat at a characteristic, constant temperature. When the heat transfer to the ambient is possible, the PCM rejects the heat. If this is not the case, the PCM can store the energy for a longer time. The battery modules can be embedded into the PCM, so no further HAS is required. Additionally, a very constant and uniform battery temperature is assured hereby. PCMs are a passive system, so no energy is required for operation and no moving parts exist [35,42].

Being a passive system, PCMs lack operational flexibility. They or the aircraft would have to be stored in an environment with controlled temperature to avoid the PCM heating up before takeoff. Unexpected delays on the ground during a hot day could lead to the cancellation of a flight. Also, the PCM would need to be cooled after charging again. The mass calculated in Table 1 already implies an exchangeable system, where the PCM can be sized only for the mission. Further disadvantages are the risk of PCM leakage as well as inhomogeneity issues of the PCM occurring after repeated melting/solidifying cycles, which have to be settled by research to ensure the reliability of this cooling technology [36,42]. PCMs cannot actively heat the battery.

H. Comparison and Decision

The seven considered technologies have unique advantages and disadvantages. To reach a final decision, the assumed application case is considered. Because the aircraft does not operate with liquefied gas as fuel, expendable cooling is disregarded. The EIS 2035 leaves too little time for the maturation of MCC. PCMs are an interesting technology to dampen peak heat loads. As standalone cooling technology they are disregarded due to their lack of operational flexibility and requirement for additional infrastructure. They should, however, be considered by future research on the matter as enhancement of the HAS, for example. The high weight of the VCM, combined with the lack of heating capabilities as well as noise and leakage issues, makes this technology less favorable. ACM and VTC share many properties and therefore advantages and disadvantages. In direct comparison, especially the need for highly compressed air and the lower expected COP values are arguments against VTC, and it is therefore disregarded. The choice between ACM and TEC is not definitive. For a final assessment, both technologies would have to be modeled in full detail for the application case. For this study, TEC is chosen due to its outstanding operational flexibility.

III. Battery Thermal Management System Model

The scheme of a general BTMS structure is already shown in Fig. 1 and explained at the beginning of Sec. II. Figure 2 shows a sketch of the proposed layout of the BTMS. Thermoelectric modules (TEMs) are used as cooler technology. The HAS is attached to their cold side and the HSS to their hot side. Heat pipes are assumed for the HAS. A finned ram air heat exchanger model (HEX) with rectangular channels is developed for the HSS. Figure 2 shows a front view of the BTMS on the left (the air flows through the HEX into the plane) and a top view on the right. Especially for Sec. V, some geometrical parameters are important: H_{HS} is the height of the hot side, including the HAS with TEMs on both sides; H_{chan} the height of one cold side channel, and H_{stack} the height of one stack of the BTMS. L_{leg} is the length of one thermocouple leg (cf. Sec. V.A and Fig. 3b). $A_{\mathrm{TEM},i}$ and $A_{\mathrm{base},i}$ are the surface areas of one TEM and one section of the HEX, respectively. The matching of the total A_{TEM} and A_{base} is discussed in the later sections. The later mentioned A_{front} refers to the total frontal area of the BTMS. In the following section the working principles of the component models including all relevant simplifications and assumptions are given.

A. Thermoelectric Module

Because TEC was chosen as the heat pump technology, a TEM is modeled for the cooler of the BTMS (cf. Fig. 1). Three thermoelectric effects are the physical basis of a TEM: the Peltier effect (cooling or heating can be observed at the junction of two conductors of different material when an electric current runs through them), the Seebeck effect (an electromotive force can be observed when the junction of these two conductors is heated), and the Thomson effect (reversible cooling or heating occurs at a conductor with a temperature gradient and an electric current applied to it). Peltier and Seebeck effects are basically the inverse of one another. More detailed explanations of the thermoelectric working principle can be found in fundamental textbooks such as [43].

A TEM consists of multiple thermocouples that are the smallest entity of a Peltier element. Figure 3 provides basic sketches of a TEM and a thermocouple. Figure 3a shows the entire TEM with a magnification of one thermocouple, and Fig. 3b depicts the working principle of a thermocouple. TEM and thermocouple models are available in literature, e.g., [44–46]. In [47] different models for a single thermoelectric "leg" (cf. explanation below) are compared and divided into four categories: simplified models, analytical models, electrical analogy models, and numerical models based on FEM, with increasing level of detail. For the given simulation application, namely, the first design of a BTMS for a conceptual aircraft design, the simplified model is sufficient and serves as basis for the implemented TEM model [47]. Depending on the direction of the applied

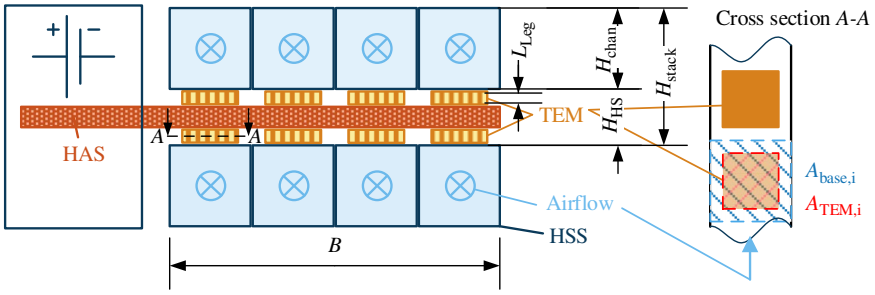

Fig. 2 Sketch of the proposed battery thermal management system.

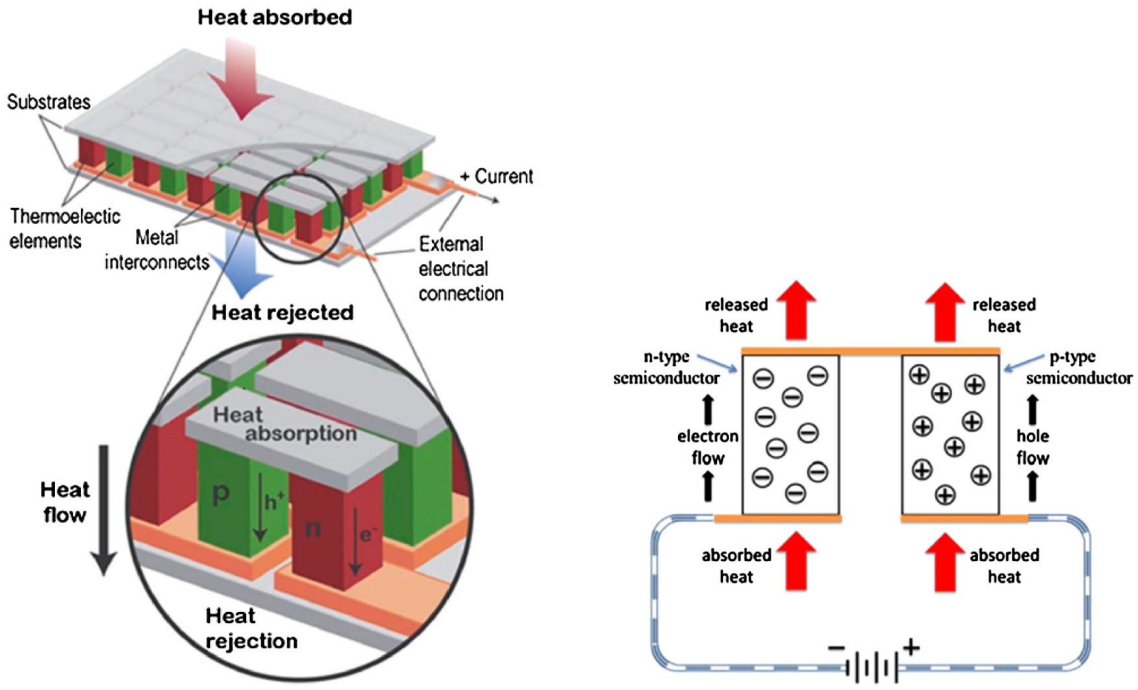

a) Thermoelectric module, build up from multiple thermocouples. Reprinted with permission from [48] ©2012 Elsevier Ltd

b) Schematic of the working principle of a single thermocouple. Reprinted with permission from [49] ©2013 Elsevier Ltd

Fig. 3 Sketches of the thermoelectric module.

electric current, the temperature on the heat rejecting side may be higher than on the heat absorbing side. As shown in Fig. 3b, the two conductors are a p-type and an n-type semiconductor called legs connected by a small metal strip on one side and linked to a DC voltage on the other side. Bi_2Te_3 is chosen as semiconductor material because it is a well-known material for TEMs [43], and the properties are adapted from [47]. Using the same material as [47] also allows the direct comparison of the implemented model to the original one. In later studies, more advanced thermoelectric materials should be investigated as well for a potential performance improvement of the BTMS. The heat flow on the cold and hot sides of the thermocouple can be calculated with [43]:

$$Q_c = (\alpha_p - \alpha_n) I T_c - (K_p + K_n)(T_h - T_c) - 0.5 I^2 (R_p + R_n) \tag{2}$$

$$Q_h = (\alpha_p - \alpha_n) I T_h - (K_p + K_n)(T_h - T_c) + 0.5 I^2 (R_p + R_n) \tag{3}$$

They depend on the current and temperature as well as the legs' Seebeck coefficients α; thermal conductance [43]

$$K_{p/n} = \left[\frac{\lambda A}{L}\right]_{p/n} \tag{4}$$

with the legs' thermal conductivity λ, cross-sectional area A, and length L; and the legs' electric resistance [43]

$$R_{p/n} = \left[\frac{\rho_e L}{A}\right]_{p/n} \tag{5}$$

with the legs' electric resistivity ρ_e. To assess the performance, the electric power and the COP are calculated [43]:

$$P = (\alpha_p - \alpha_n) I (T_h - T_c) + I^2 (R_p + R_n) \tag{6}$$

$$\mathrm{COP} = \frac{Q_c}{P} \tag{7}$$

In theory, a single thermocouple could be operated to achieve a variety of required cooling loads. This would require impractically high electric currents. Therefore, several thermocouples are linked electrically in series and thermally in parallel and form a TEM as shown in Fig. 3a [43].

With the equations above, the performance of a thermocouple is known. To match the battery heat load, the number of thermocouples per TEM and the number of TEMs can simply be adjusted. Additional thermal and electric resistances for the ceramic plates (called "Substrates" in Fig. 3a) and metal connectors as well as their junctions are considered. Temperature-dependent material properties are evaluated at arithmetic mean temperature T_m. The Thomson effect is neglected due to the moderate temperature lifts, and the Joule effect is assumed to be symmetrically distributed over both legs. For mass calculations, only the ceramic plates and the legs are considered with detailed geometric calculations, whereas metal connectors and cabling are added with a constant accessory weight per thermocouple. As shown in Fig. 3a the area of the ceramic plates is higher than the cross-sectional area of both legs combined (i.e., leg area perpendicular to the electron/hole flow cf. Fig. 3b; $A_{\mathrm{leg},p}$ and $A_{\mathrm{leg},n}$). To account for the difference a simple spacing factor is used:

$$\delta A = \frac{A_{\mathrm{thermocouple}}}{A_{\mathrm{leg},p} + A_{\mathrm{leg},n}} \tag{8}$$

For numerical robustness, a slight adaptation is made to the input parameter I_{tc}. Rather than providing it directly, the deviation from the optimal I_{tc} is used:

$$\delta I_\phi = I_{\mathrm{tc}} / I_\phi \tag{9}$$

I_ϕ corresponds to the maximum possible COP of a TEM and can be calculated with [43]

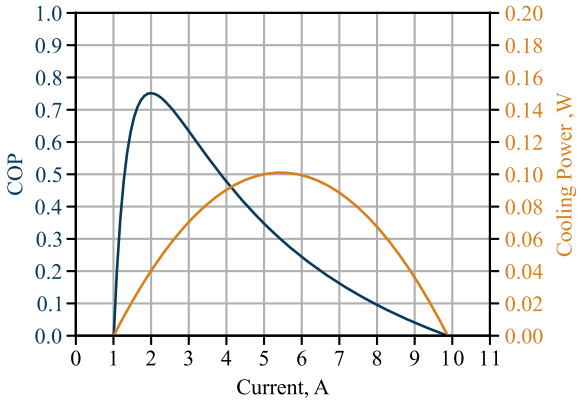

Fig. 4 COP and cooling power of the implemented TEM model with inputs from [47].

$$\mathrm{COP}_{\max} = \frac{T_c\left(\sqrt{1+ZT_m} - (T_h/T_c)\right)}{(T_h - T_c)\left(\sqrt{1+ZT_m}+1\right)} \tag{10}$$

$$I_\phi = \frac{(\alpha_p - \alpha_n)(T_h - T_c)}{(R_p + R_n)\left(\sqrt{1+ZT_m}-1\right)} \tag{11}$$

$$Z = \frac{(\alpha_p - \alpha_n)^2}{(K_p + K_n)(R_p + R_n)} \tag{12}$$

To ensure the correct implementation of the TEM model, the data provided in [47] were used. Leg geometries, material data, temperatures, and electric currents are given. Figure 4 shows COP and Q_c over I_{tc}. The graphs resemble the results for the simplified model from Fig. 4 in [47] exactly, which was expected because no new model was developed, but the existing one from [47] was implemented. The values apply for a single leg. A TEM consisting of many thermocouples with two legs each has a much higher cooling power.

B. Finned Ram Air Heat Exchanger

The sketch in Fig. 2 already shows a cross-sectional view of the developed HSS. A finned ram air heat exchanger (HEX) is selected, and the model is derived from the compact HEX in [50]. The HEX here is simpler because it only has one fluid and heated walls, rather than two fluids. For a detailed understanding, study [50] and the original source for the HEX methods [51] should be consulted. Only a brief outline of the design process is presented here.

Inputs to the model are the air inlet properties (T, p, Ma), wall temperature (assumed to be uniform over the base plates), heat load, effectiveness, and pressure ratio, as well as the geometric properties of the cross section of the channels (d_H, γ_{chan}). The main outputs are the required air mass flow, the air outlet properties, the overall dimensions of the HEX (L, H, B, A_{base}), and its mass. All fluid properties are estimated at T_m from [27]. Outlet temperature and air mass flow can be calculated immediately [51,52]:

$$T_2 = \epsilon(T_w - T_1) + T_1 \tag{13}$$

$$w = \frac{Q}{c_p(T_2 - T_1)} \tag{14}$$

With only one fluid present, $C_R = 0$ and therefore the number of transfer units (NTU) can be calculated [51]:

$$\mathrm{NTU} = -\log(1-\epsilon) \tag{15}$$

From here the algorithm follows the exact procedure described in [50,51], with the exception that only one core-mass-velocity/pressure-ratio pair has to be iterated until convergence. This adds a degree of freedom regarding the width-to-length ratio of the HEX. Therefore an input variable is added fixing the ratio (cf. Fig. 2):

$$\gamma_{\mathrm{HEX}} = \left[\frac{L}{B}\right]_{\mathrm{HEX}} \tag{16}$$

For the mass calculation, a simple geometric approach is chosen; σ is the ratio of the free flow to the frontal area on one side of a HEX. For the air side, σ_{AS} can be calculated as described in [51]. There is no second fluid, and thus no second free flow area but only the hot side consisting of TEM and HAS. The mass of these components is already accounted for in the respective component models. Therefore, it is necessary to define:

$$\sigma_{\mathrm{HS}} = \frac{H_{\mathrm{HS}}}{H_{\mathrm{HS}} + H_{\mathrm{chan}} + 2t_w} \tag{17}$$

Starting with a block volume for the entire HEX and reducing it by the air side volume and the hot-side volume leads to the mass formula. Aluminum is assumed to be the HEX material.

$$m_{\mathrm{HEX}} = A_{\mathrm{front}} L_{\mathrm{HEX}} (1 - \sigma_{\mathrm{AS}} - \sigma_{\mathrm{HS}}) \rho_{\mathrm{mat}} \tag{18}$$

C. Heat Pipes

Several options for the HAS, namely, direct-contact, air- and liquid-based systems, PCMs, immersion cooling, and heat pipes were considered [38,53,54]. The disadvantages of PCMs were discussed in Sec. III.G. PCMs should be kept in mind for transient models but are not suited for the steady-state assessment in this work. With immersion cooling, the battery is inserted into a liquid that is designed to boil off at about the required battery maximum temperature and that is then condensed at the cooler interface and recirculated back to the battery. This HAS type is dismissed because of its high weight as well as geometrical constraints and in accordance with [55], where the necessity of notable superheat temperature difference between wall and fluid as well as large minimum spaces between adjacent cells for prevention of vapor lock are listed as arguments against it. The disadvantages of an air-based HAS were already discussed in Sec. II, and the chosen heat pump technology (TEC) allows the choice of an alternative HAS without penalty. Direct contact solutions may result in local hotspots inside the battery pack and are therefore not selected here despite them being the most lightweight solution [54]. Liquid systems achieve good thermal uniformity and can reliably cool batteries at high discharge rates [38]. A liquid HAS has a comparatively high weight and with no liquid involved in any other part of the BTMS; it would add an additional leakage problem. Also, as an active system, it would require additional power and would add complexity and maintenance effort to the BTMS [56,57].

Heat pipes are selected for the HAS because they offer good temperature uniformity, high heat transfer rates, high technology maturity and no additional power requirement [54,57,58]. The length of heat pipes is limited. For an application case with the heat sink location far from the battery, another HAS solution might be preferable. A common heat pipe consists of a sealed thin metal tube with a working fluid and a wick structure inside. The application of heat at one end of the pipe causes the fluid to evaporate and move to the other end, where it rejects the absorbed heat and condenses. The capillary forces in the wick transport the liquid back to the start [58]. Because there is no detailed battery model available (cf. Sec. IV), a detailed heat pipe model is not implemented. Given the very high heat transfer coefficients of common heat pipes between 1000 and

$10{,}000\,\mathrm{W \cdot m^{-2} \cdot K^{-1}}$ [14,54,59], the temperature difference between both ends is simply assumed to be 5 K. Further explanations on this assumptions are provided at the end of Sec. IV. To account for the mass of the HAS, the online accessible product data of several commercial heat pipes from Advanced Thermal Solutions, Inc., were considered (compare https://www.qats.com/products/heat-pipes). The selected heat pipes were at the upper end of the offered lengths (0.5 m) and at high power levels (65–80 W). An average specific mass of $8 \times 10^{-4}\,\mathrm{kg \cdot W^{-1}}$ was calculated. In future research with detailed battery models, a detailed heat pipe or other HAS model should be implemented. More detailed studies on HAS for batteries as well as visualizations of their connections to the battery cells can be found in [55].

IV. Application Case: High-Performance Battery of the E19

The application case is a 19-seat (H)EAC called "E19." It has an all-electric design mission and uses a combustion engine for range extension. The aircraft has a maximum takeoff mass (MTOM) of 8618 kg. The mission profile of the thermally more challenging all-electric mission of the E19 is shown in Fig. 5 [8].

The power train and the battery are designed based on state-of-the-art technology assumptions [8]. The lithium-ion battery pack has a total mass of 2018 kg and a specific energy of $230\,\mathrm{W \cdot h \cdot kg^{-1}}$ and can be discharged with a maximum C-rate of 3 C, which corresponds to a total output power of 1352 kW. The maximum power is decisive for the battery sizing in this case. The pack is operated within a state of charge range of 90–20% during regular missions [8].

For a valid TMS design, an operating temperature of the battery has to be specified. The permissible temperature range specified by the manufacturers for discharging lithium-ion batteries is typically stated as between −20 and +60°C [60]. However, operation at room temperature is in most respects ideal for the battery; an operating range between 15 and 35°C is recommended [7,61]. Below and above this range, several effects have a negative impact on battery performance. At lower temperatures, the capacity of the battery decreases significantly due to inhibited electrochemical processes, and maximum power output is limited by an increase of internal resistance [60]. Both a reduced capacity and reduced power output have a direct negative impact on aircraft performance. Cycling of the battery below the specified range must therefore be prevented by the TMS. Operation at elevated temperatures reduces the cycle life of the battery due to a loss of cyclable lithium and the reduction of active material in the cell [60]. To prevent excessive degradation, the maximum discharge rate should be limited when operating at temperatures above 35°C. Cycling experiments with lithium-iron phosphate-based batteries at 40°C showed a reduction in cycle life of about 27% compared to operation at room temperature (25°C) [62]. Whereas operation between 35 and 40°C already represents a compromise between cooling effort and battery cycle life, higher temperatures would presumably shorten battery life to an unacceptable degree. Cycling at even higher temperatures above 60°C may lead to fast degradation and irreversible damage of the cell. Moreover, the risk of a thermal runaway and thus a catastrophic failure of the battery system increase [60].

The waste heat of a battery is significantly influenced by the discharge rate and the internal resistance of the cell. This depends on the cell type, the state of charge, and the state of health of the cell and the operating temperature. Cells optimized for power generally have lower internal resistance and produce less waste heat—especially at higher discharge currents—than energy-optimized cells. Operation at higher temperatures reduces waste heat production due to a decreased internal resistance [60,63]. As the discharge process and service life progress, the internal resistance and thus the waste heat increase steadily; this effect is intensified at higher operating temperatures [62]. In the application considered, the battery is discharged at a maximum C-rate of 3 C. Experimental studies have reported average waste heat amounts between 5 and 10% of the discharge power for different cell types and different operating temperatures between 25 and 40°C [64,65]. Whereas operation at higher temperatures reduces the heat to be dissipated, the increasing waste heat over the lifetime must be considered for the design of the TMS. Therefore, for the given application case, the design point of the TMS is assumed to be between 5 and 10% of the maximum battery power. In a future more detailed study, a more precise battery heat generation model should be implemented.

For the required temperature difference over the heat pipe in the previous section, the available cell surface had to be estimated. Assuming a cell-to-pack efficiency rate of 0.728 for a battery pack assembled by standard 18,650 cylindrical cells [66], the pack of the application case has a pure cell mass of 1469 kg. Considering 0.045 kg mass, 0.018 m diameter, and 0.06 m height per single cell [67], this results in about 31,937 cells with a total outer surface area A_{cell} of 117.39 $\mathrm{m^2}$. With a heat pipe with a heat transfer coefficient of $1000\,\mathrm{W \cdot m^{-2} \cdot K^{-1}}$ (most conservative value of the range from Sec. III.C), the assumed 5 K temperature difference would result in a maximum possible heat transfer rate for the HAS of

$$Q_{\mathrm{HAS,max}} = \alpha_{\mathrm{HAS}} \times \Delta T \times A_{\mathrm{cell}} = 1000\,\mathrm{W \cdot m^{-2} \cdot K^{-1}} \times 5\,\mathrm{K} \times 117.39\,\mathrm{m^2} = 568.95\,\mathrm{kW} \tag{19}$$

With the lowest battery efficiency assumption from above of 0.9 the maximum heat load of the battery is 135.2 kW. Thus, about a fourth of A_{cell} would be sufficient as cooling area. This value decreases in the likely case that α_{HAS} is larger than $1000\,\mathrm{W \cdot m^{-2} \cdot K^{-1}}$, which makes $\Delta T = 5$ K a very conservative assumption. Due to the superficial HAS model used, it was kept,

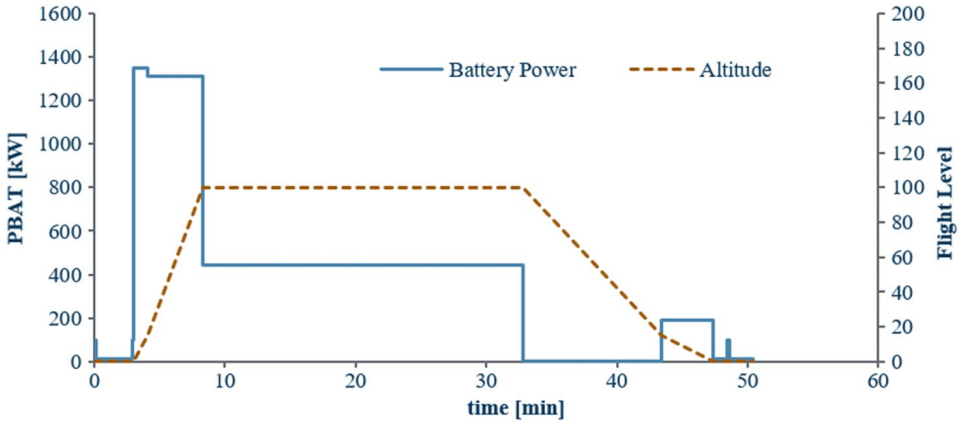

Fig. 5 Mission profile of the all-electric mission of the E19 [8].

but it can probably be reduced in a future study with a more detailed HAS model.

V. Sensitivity Analysis

The sensitivity analysis has multiple purposes. It promotes a better understanding of component and system models. The dependency of multiple output parameters on various input parameters can be assessed qualitatively and quantitatively. It is a means of validation, because implementation errors could reflect in wrong trends. Additionally, the information gained can be used in later optimization studies, e.g., by selecting only relevant variables to be free variables or by choosing reasonable initial values to enhance numerical performance. In the following section, sensitivity analyses of the component models for the TEM and the HEX are performed.

A. Thermoelectric Module Sensitivities

For the TEM sensitivity analysis, six variable input parameters and four outputs are considered. The results are shown in Fig. 6. For each of the input variables, a value range was defined. The lower and upper ends are labeled at the end of the lines in the diagrams. The sensitivity analysis is one-dimensional, which means that only one input variable is varied at a time. The other variables are held constant at the mean value of their respective value range, e.g., T_h is set to 335 K during the sensitivity analysis of the other variables because it ranges from 320 to 350 K. At the intersection of all lines, each variable is at its mean value. The one-dimensional nature of the sensitivity study limits the conclusions that can be drawn from Fig. 6. In particular, the results cannot be used to manually optimize a TEM because dependencies between the input variables exist, but are not considered in the 1D analysis. The selected outputs are mass and electric power, because they both have a direct effect on the aircraft's performance, electric current, because the simplified TEM model loses accuracy at $I > 5$ A [47], and the A_{TEM}, because it needs to be in the same order of magnitude as the HEX A_{base} (cf. Fig. 2).

Mass, power, and area all increase linearly with increasing Q_c. Increasing Q_c simply results in an enlargement of the TEM; i.e., the number of thermocouples increases. Increasing δI_ϕ causes an increase in I_{tc}. The area decreases monotonically because the entire δI_ϕ value range results in I_{tc} values lower than the one for maximum cooling power (cf. Fig. 4). The area trend is directly reflected in the mass. The power seems to be almost constant for very low δI_ϕ values and exponentially increases for higher values. It very well reflects the COP characteristic from Fig. 4. The strong increase in mass toward low values especially suggests that $\delta I_\phi < 1$ is of little interest except if very large areas are required.

The curves for T_c and T_h are very similar because the temperature difference is more relevant than the absolute temperature for the sensitivities of the TEM parameters. An explanation can be found in the TEM defining equations (2), (3), (6), (10), and (11), where the temperature difference is present as either difference or ratio. A detailed understanding of the mass sensitivity can only be gained by rearrangement of all those equations. In short, the visible mass minimum corresponds to a maximum in heat transferred per thermocouple. The trend in electric power is understood more easily: It increases exponentially with ΔT because of the lower maximum COP [cf. Eq. (10)]. Inversely, TEMs with little ΔT require very low amounts of power. Both $T_c = 290$ K and $T_h = 350$ K have the same ΔT value of 45 K. However, there is a significant difference in electric current and power, because T_m is different and Bi_2Te_3 has temperature-dependent properties, e.g., α and ρ_e.

The geometric properties of the legs (L_{leg}, A_{leg}) have no direct influence on the power but solely on the mass of the system. Longer legs increase the mass linearly because they linearly contribute to the volume of the legs and also increase TEM area due to the lower heat transfer per unit area. I_{tc} decreases with increasing L_{leg}, but the maximum COP value does not, hence the unchanged power in this one-dimensional sensitivity with constant δI_ϕ. Equations (10–12) allow an explanation: L_{leg} is included in K and R. It can be shown that after some rearrangements in Eq. (10) L_{leg} cancels out, whereas in Eq. (11) it does not. Similarly, I_{tc} increases with A_{leg}, but COP and thus power remain constant. Also, the TEM area remains unchanged by A_{leg} because for larger A_{leg} values the number of thermocouples decreases at the same rate. The small mass benefit for larger A_{leg} originates in the constant accessory mass assumed for each thermocouple; i.e., with fewer thermocouples the total accessory mass is lower.

In summary, none of the investigated variables should be neglected in a later optimization process as they all have a relevant influence on at least one relevant output parameter.

B. Heat Sink Sensitivities

The heat sink sensitivities were carried out at common takeoff conditions, i.e., sea level and $Ma = 0.2$. As for the TEM sensitivity analysis, four output parameters were investigated: m_{HEX}, P_{HEX},

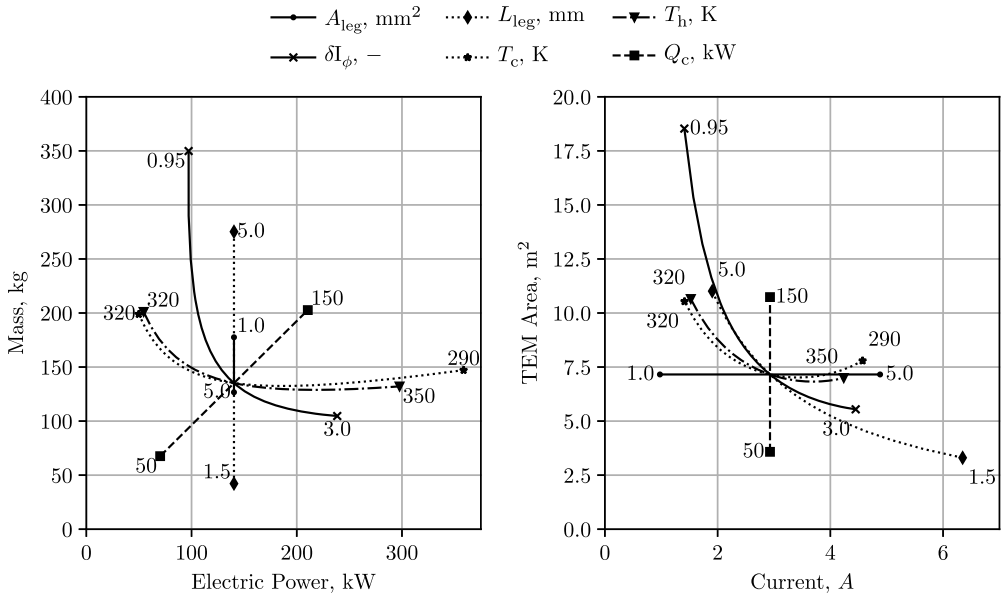

Fig. 6 Sensitivity analysis of the thermoelectric module.

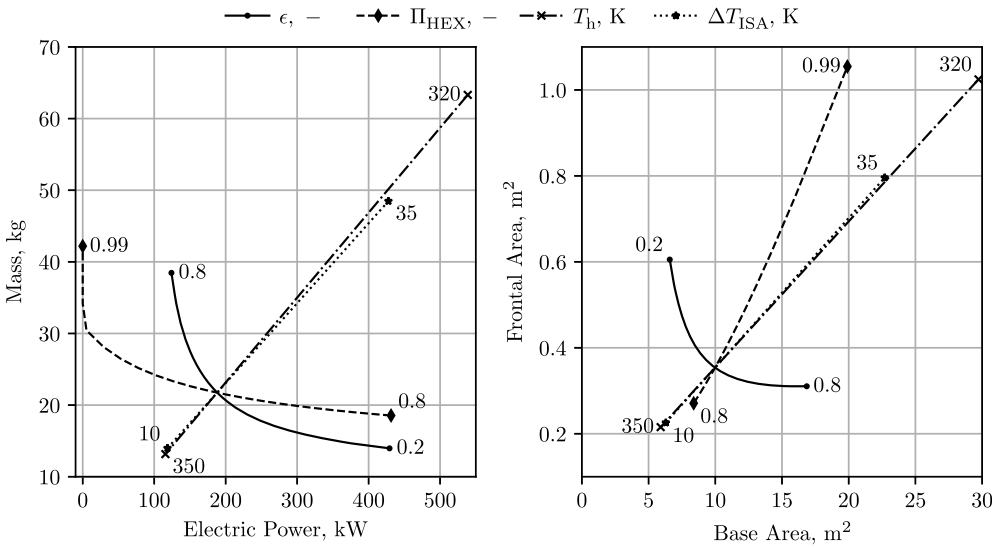

Fig. 7 Heat exchanger sensitivity analysis part 1: thermodynamic parameters.

A_{base}, and A_{front}. To assess P_{HEX}, a simple fan installed behind the HEX with an efficiency of 0.7, which is a typical value for fans in air heat exchangers [68], was assumed to bring the air exiting the HEX back to atmospheric pressure. The understanding of A_{base} is important because it needs to be of similar size as A_{TEM} in the following design optimization. A_{front} is a good indicator for the difficulty of integrating the HEX into the aircraft. The procedure was the same as for the TEM sensitivities. Because of the higher number of regarded input variables, the results were split into Figs. 7 and 8, which show the same output parameters on x and y axis but with different scales for enhanced perceptibility.

Note that ϵ has a direct influence on L_{HEX} because a more effective HEX needs to be longer to allow the passing fluid to heat up more and thus have a higher exit temperature. HEXs with higher ϵ have lower heat transfer rates at the end of the flow length because the ΔT between wall and fluid is lower there. Therefore, HEXs with high ϵ generally need more heat transfer area and are heavier as shown in Fig. 7. P_{HEX} decreases with increasing ϵ because more energy is added to the fluid, compensating the momentum loss due to friction better—the so-called Meredith effect. With increasing ϵ an increase in A_{base} can be observed due to the increasing L_{HEX} and, with constant γ_{HEX}, accordingly increasing B_{HEX}. The resulting reduction in H_{HEX} and thereby number of plates needed do not compensate these effects. However, it does show a reduction in A_{front} but at a declining rate toward higher ϵ. This behavior is common for HEX: ϵ approaching 1 results in exponential increases in mass and dimensions.

Increasing Π_{HEX} decreases the required power because less pressure is lost over the HEX and consequently the fan needs to work less. With Π_{HEX} approaching 0.99, the need for a fan disappears due to the dynamic pressure from the moving aircraft; m_{HEX} increases, as well as both A_{base} and A_{front}, mainly, because for higher Π_{HEX} values with constant channel geometries, the air must move slower, which results in smaller heat transfer coefficients and therefore more heat transfer area. Mainly, H_{HEX} grows with Π_{HEX} and thereby both A_{base} and A_{front} increase. The mass increase is exponential toward high Π_{HEX} values.

T_h was set to the same value range as in Fig. 6. For the HEX, it has the opposite effect regarding mass and power: high T_h result in lighter HEX because ΔT between HEX walls and fluid is higher and also in less P_{HEX} due to the higher outlet temperatures and the Meredith effect. Accordingly, both regarded areas decrease. The effect of varying ΔT_{ISA} is analog but vice versa because

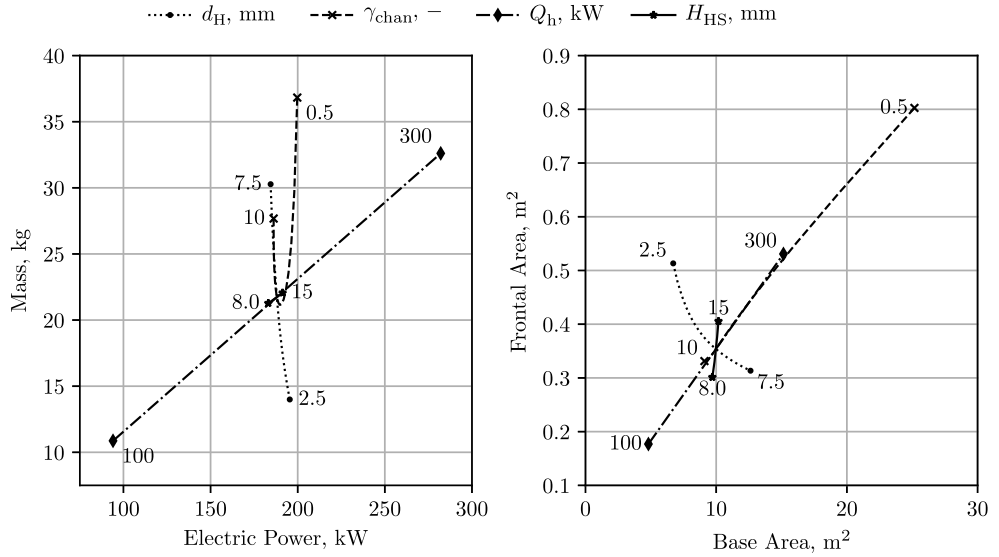

Fig. 8 Heat exchanger sensitivity analysis part 2: geometric parameters and heat load.

increasing the air temperature reduces the ΔT between HEX walls and fluid.

Smaller d_H values are generally favorable for the heat transfer coefficient, which results in less required heat transfer area and thus mass. A_{front} increases because with constant Π_{HEX}, smaller d_H values require slower air flow. This also explains why a slightly higher P_{HEX} is required for smaller d_H: With a larger A_{front}, the inlet Ma is lower, and therefore the static pressure at the HEX inlet is higher. Since Π_{HEX} is the relative static pressure ratio, the total pressure loss is higher here, which results in more work required by the fan.

Note that γ_{chan} controls the fin height. For low γ_{chan} values, the fins are very short. Therefore, the ratio of A_{base} to A_{fin} is large, resulting in large A_{base} values. A_{front} is also large, as the low σ value for short fins results in a significant acceleration of the airflow when entering the channels, and therefore the HEX has to be short if Π_{HEX} is constant. A shorter HEX needs more plates stacked on top of each other and thus is taller to have a sufficient heat transfer area. A HEX with more stacked plates consequently has more hot side elements stacked and, therefore, a disproportional high A_{front}. Hence, when γ_{chan} is increased from 0.5 to higher values, m_{HEX} decreases rapidly. Eventually the mass decreasing trend stops because the further increase in fin height reduces the heat transfer coefficient. P_{HEX} is hardly affected by γ_{chan} and the small sensitivity is due to the difference in A_{front} and thereby static inlet pressure as mentioned before.

Q_h was set to double the amount of Q_c in Fig. 6, which assumes a COP of 1. The sensitivities of all output parameters are directly proportional to Q_h as an increase in Q_h simply requires an up-scaling of the HEX. H_{HS} changes, e.g., if L_{leg} in the TEM model is changed. The effect on HEX mass and power is caused by the increased A_{front}, but comparatively small.

In summary, all observed trends match the expectations and are in good accordance with the sensitivities shown for the two-fluid HEX in [50]. Comparing TEM and HEX sensitivities, some are counteracting, e.g., T_h, which implies that an optimization can only be successful when both components are optimized together. A_{base} and A_{TEM} are within the same order of magnitude in the sensitivity analysis, but the matching of both areas may add constraints to the optimization.

VI. Design of the Battery Thermal Management System for the Application Case

A. Numerical Setup

In the previous sections, many variables influencing the BTMS design have been identified. While many are a free choice for the BTMS designer, ΔT_{ISA}, T_{bat}, and η_{bat} depend on ambient conditions and the chosen battery technology. Moreover, Sec. IV showed that the battery parameters change over the lifetime of the battery. Rather than assuming discrete values for these three parameters, a design space exploration is conducted, highlighting the sensitivity of the optimized systems toward them. The boundaries of the design space are listed in Table 2.

The battery analysis in Sec. IV indicated a preferable range for T_{bat} between 288 and 308 K. In the design space, slightly higher limits were chosen to anticipate possible improvements in battery technology; η_{bat} covers the expected battery performance and ΔT_{ISA} ranges from a common summer day (+15 K) to a very hot day (+35 K). For the optimization, a well-known sequential least square method was used [69]. Of all the variables investigated in Sec. V, d_H, γ_{chan}, γ_{HEX}, ϵ, Π_{HEX}, T_h, A_{leg}, L_{leg}, and δI_ϕ are free design variables. The others are covered either directly (ΔT_{ISA}) or indirectly (Q_h, Q_c, T_c) by Table 2 or are geometric relations (H_{HS}, cf. Fig. 2). In a small exploration, it became apparent that the optimal values for A_{leg} and γ_{chan} were always very close to 5.0 mm^2 and 6.0, respectively. To increase computational performance, these two variables were fixed. The following constraints were invoked:

$$0.2 < \frac{H_{\text{HEX}}}{B_{\text{HEX}}} < 5.0 \tag{20}$$

$$0.67 < \frac{A_{\text{TEM}}}{A_{\text{base}}} < 1.5 \tag{21}$$

$$0.2\ \text{m} < L_{\text{HEX}} \tag{22}$$

$$1 \times 10^{-3}\ \text{m} < L_{\text{leg}} \tag{23}$$

All constraints are geometric. Constraint (23) limits the shortness of L_{leg}, because no information on the possibilities of manufacturing such short legs is available. Constraint (22) prevents the HEX from becoming unreasonably short. If left unconstrained an optimization of the HEX often results in very low L_{HEX} values because lower Π_{HEX} at higher air velocities and thus heat transfer coefficients are possible. In exchange, either B_{HEX} or H_{HEX} or both increase to provide sufficient heat transfer area, resulting in a stick-shaped or flat-plate-shaped HEX. Constraint (21) covers the aforementioned required similarity of A_{TEM} and A_{base}. The allowed deviation of 50% is expected to have a negligible influence on the heat transfer characteristics because of the very good thermal conductivity of the used HEX material aluminum. For confirmation of this assumption, however, a model that accounts for lateral heat conduction as well would have to be implemented. Constraint (20) ensures a certain compactness of the HEX. In the single fluid HEX, B_{HEX} and H_{HEX} are interchangeable, meaning that their only thermodynamic effect is the increase in heat transfer area. Therefore, this constraint is not a particular challenge and easily matched by appropriate variation of γ_{HEX}. The target function of the optimization was

$$m_{\text{tot}} = m_{\text{BTMS}} + 0.69\ \text{kW} \cdot \text{kg}^{-1} P_{\text{BTMS}} \tag{24}$$

To find a balance between P_{BTMS} and m_{BTMS}, which both negatively affect the aircraft's performance, the battery power density from [8] was used to calculate the additional battery mass required for the cooling system. This results in a first-order assessment. In later more detailed studies, iterative procedures would have to be applied taking into account the additional waste heat generated by the additional batteries. The following section shows the results of the design space exploration.

Table 2 Design space parameter boundaries

Parameter	Lower value	Upper value
ΔT_{ISA}, K	15	35
T_{bat}, K	295	325
η_{bat}	0.90	0.95

B. BTMS Design Results

The results of P_{BTMS}, m_{BTMS}, and m_{tot} are displayed in Fig. 9; additional details such as A_{front} and the relative shares of the components in the total mass and power in Fig. 10 and some of the corresponding TEM parameters are shown in Fig. 11. For η_{bat} and T_{bat}, only the values of the boundaries of the design space are displayed for clarity. The complete results with all values in between can be seen in Fig. A1 in the Appendix, but the trends are similar. The relative mass and power shares in Fig. 10 are defined as

$$\delta P_{\text{component}} = \frac{P_{\text{component}}}{P_{\text{BTMS}}} \tag{25}$$

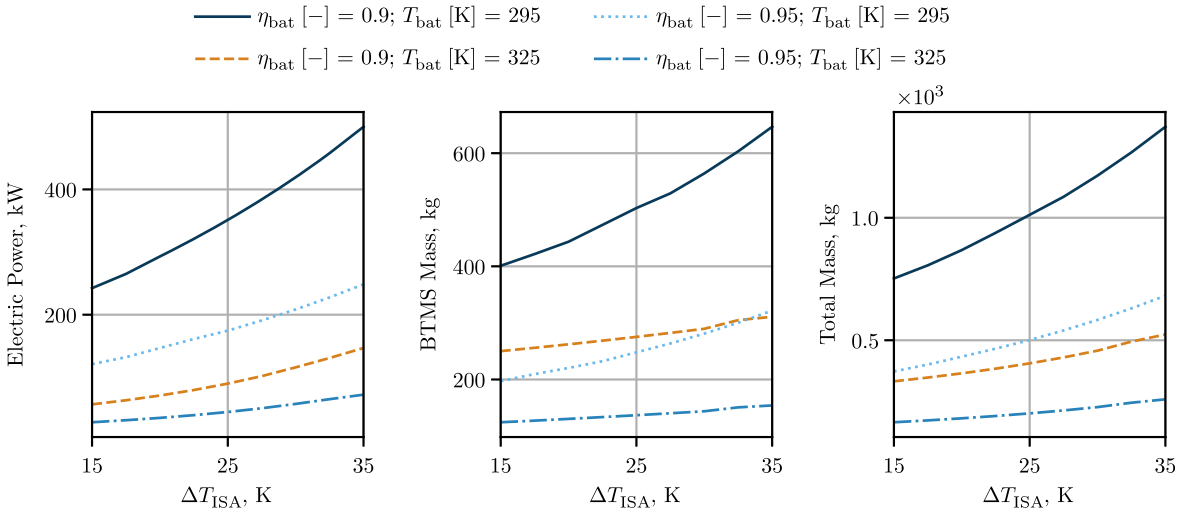

Fig. 9 Top-level optimization results of the final BTMS design space exploration.

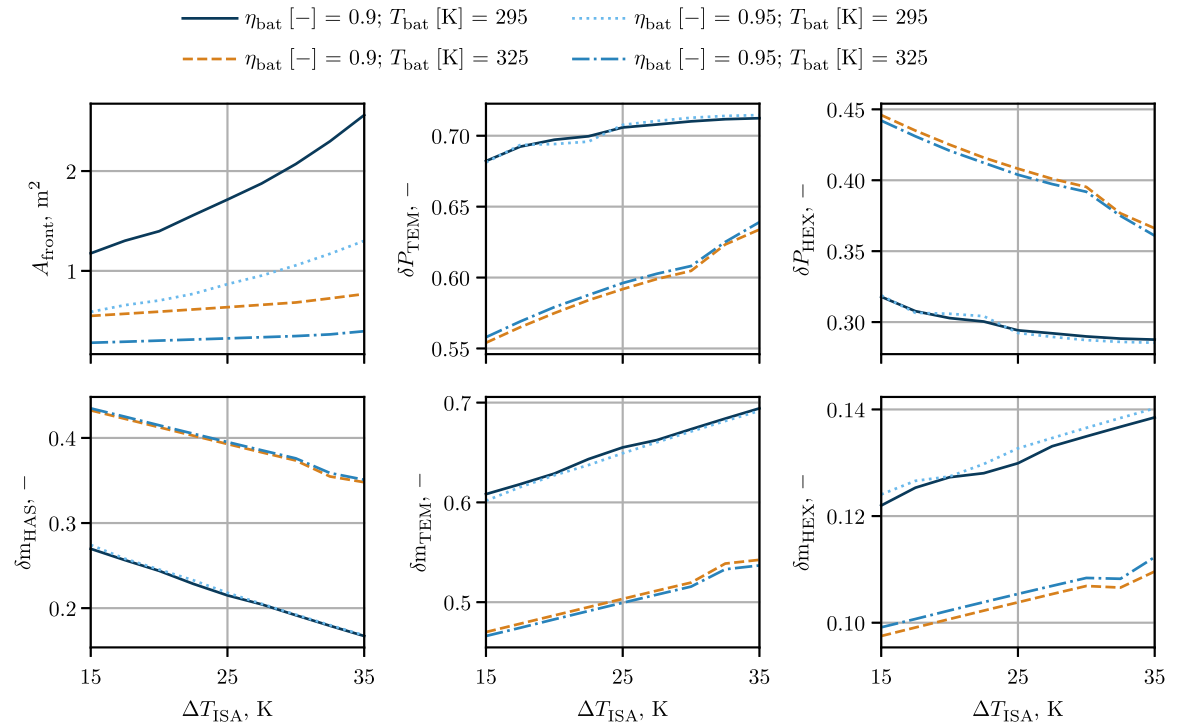

Fig. 10 HEX frontal area and BTMS ratio of component mass and power to total mass and power in the final BTMS design space exploration.

$$\delta m_{\text{component}} = \frac{m_{\text{component}}}{m_{\text{BTMS}}} \tag{26}$$

There was no clear trend toward one limit of the compactness constraint (20), showcasing the aforementioned interchangeability of H_{HEX} and B_{HEX}. The lower limit of the area similarity constraint (21) was reached in the entire design space. Due to air and its associated low thermal conductivity as fluid, rather large A_{base} values are necessary, presenting a difficulty for the BTMS to match A_{base} and A_{TEM} appropriately. As predicted, L_{HEX} reached its constrained value in Eq. (22) over the entire design space. The L_{leg} Constraint (23) is discussed later in the analysis.

The most adverse or challenging conditions for the BTMS are at high ΔT_{ISA}, low T_{bat}, and low η_{bat} values. The combination of high ambient and low battery temperature results in the highest required temperature lift for the heat pump and the low battery efficiency value in the highest heat load. The sensitivity analysis showed that the heaviest and most power consuming systems can be expected from this combination.

As a first observation, each parameter increases exponentially with ΔT_{ISA}. For P_{BTMS} the relative increase using $\Delta T_{ISA} = 15$ K as a reference increases with T_{bat}, i.e., a factor of about 2 between $\Delta T_{ISA} = 15$ K and $\Delta T_{ISA} = 35$ K for $T_{bat} = 295$ K, but a factor of 3 if $T_{bat} = 325$ K. The trends and factors can be explained with the T_h and COP values (cf. Fig. 11): For $T_{bat} = 295$ K, the limiting factor for T_h is a sufficient ΔT to the ambient inside the HEX for the entire range of ΔT_{ISA}. The temperature lift over the TEM is 32 K for $\Delta T_{ISA} = 15$ K and 51 K for $\Delta T_{ISA} = 35$ K. Because the initial temperature lift is already quite high, the relative change in COP is smaller: a decrease from 0.82 to 0.38 over the given ΔT_{ISA} range.

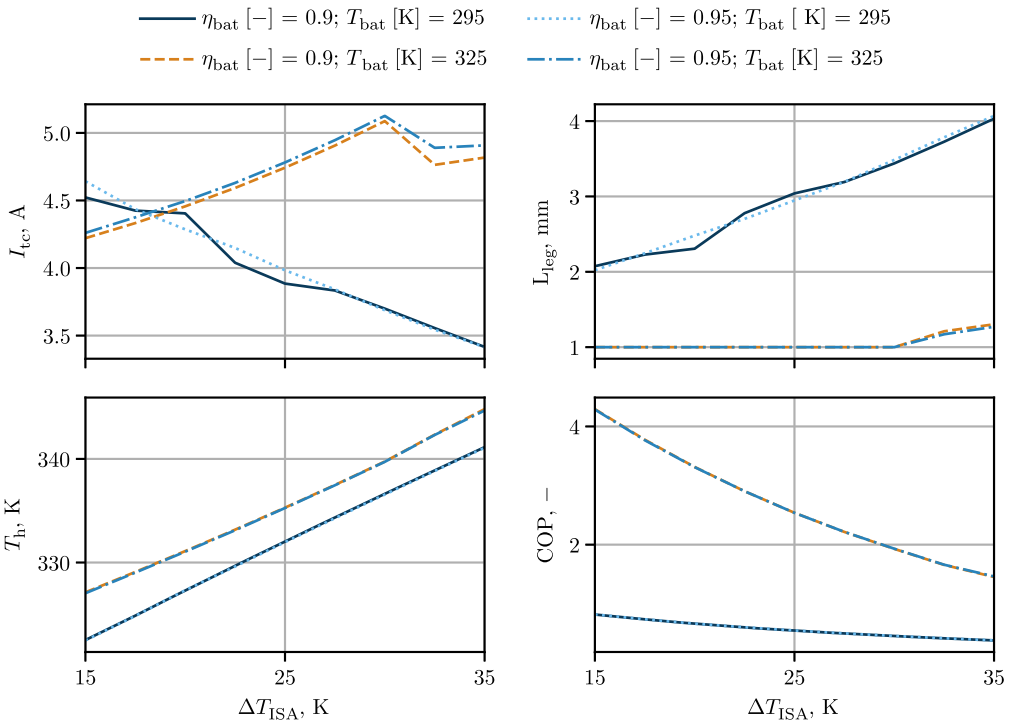

Fig. 11 Selection of TEM parameters in the final BTMS design space exploration.

For $T_{bat} = 325$ K, the temperature lift over the TEM for low ΔT_{ISA} can be very small, because the difference to ambient is sufficient already due to the high allowed T_{bat}. T_h increases from 327 to 344 K, and thereby the temperature lift over the TEM changes from 7 to 24 K. This results in a significant reduction in COP from 4.3 to 1.5 and therefore a large increase in P_{BTMS}. The overall lower COP values for $T_{bat} = 295$ K result in the overall higher P_{BTMS}. The COP values do not depend on η_{bat}, but because the heat load is higher for low η_{bat} values P_{BTMS} is higher as well. The increased P_{BTMS} for lower T_{bat} is mainly driven by the TEM as seen in Fig. 10. However, the installed fan has a significant power share ranging between 30 and 45%.

For m_{BTMS}, low η_{bat} and low T_{bat} are clearly the most adverse conditions over the entire ΔT_{ISA} range as well. Comparing the medium conditions where one of T_{bat} and η_{bat} is near its upper and the other near its lower value reveals a difference compared to the trends observed for P_{BTMS}. At lower ΔT_{ISA} values, a low η_{bat} combined with a high T_{bat} (dashed orange line) results in a higher m_{BTMS} than the opposite combination (dotted light blue line). This is mainly due to the difference in HAS mass that has a high relative mass of 43% for the first combination at $\Delta T_{ISA} = 15$ K. Only at the highest ΔT_{ISA} values, the second combination becomes heavier than the first, due to the increasing m_{TEM}, which is mainly caused by the increasing L_{Leg} and A_{TEM}.

Note that δm_{HEX} is comparatively small, ranging between 10 and 15%, because the modeled HEX only consists of a thin-walled aluminum structure filled with air. The HEX is heavier for low T_{bat} values because the lower COP value results in a higher heat load for the HEX. This is also the reason for the values of L_{leg} in Fig. 11. For low T_{bat} values the increased heat load on the HEX results in larger A_{base} values. Through constraint (21), L_{leg} is forced to higher values to increase A_{TEM} despite the penalty in m_{TEM} (cf. Fig. 6). For high T_{bat} values, L_{leg} can stay at the lower constrained value from its constraint (23) for all ΔT_{ISA} values up to 30 K without violating the area similarity constraint (21). I_{tc} is equal to I_ϕ for the entire design space except when L_{leg} is at the constrained value. Here, slightly higher I_{tc} are possible to reduce A_{TEM} and thus m_{BTMS} while slightly increasing P_{BTMS}. The benefit from the reduced m_{BTMS} in the objective function outweighs the penalty from increased P_{BTMS} in this case. The HAS mass is independent of ΔT_{ISA} but the relative mass decreases with increasing ΔT_{ISA} due to the increase in m_{TEM} and m_{HEX}. The relative TEM mass ranges between 47 and 70% largely depending on T_{bat}.

The resulting total mass including the additional battery mass in Fig. 9 is basically a superposition of the mass and power diagram. Low η_{bat} combined with low T_{bat} values are clearly the most disadvantageous conditions for the BTMS, whereas the opposite conditions are favorable. The difference at the highest ΔT_{ISA} value is large: 1371 kg for the first combination compared to 259 kg for the second, which equals a factor of 5.3 in between. For $\Delta T_{ISA} = 15$ K the adverse battery conditions result in a total mass of 752 kg compared to 165 kg for the more favorable battery conditions.

To put these numbers into perspective, they should be compared to the battery mass (2018 kg) and the MTOM (8618 kg) of the application case. Adding 1371 kg to the MTOM would be an increase of 16% without considering any snowball effects on aircraft level or the additional heat load of the 700 kg additional battery, which is a 35% increase in battery mass. The performance of the aircraft would be impacted significantly and a redesign would be necessary. There is a possibility that the entire concept becomes unfeasible. On the other hand, 258 kg, would be equal to a 3% increase in MTOM without the consideration of aircraft level growth factors, which could possibly already be covered by a small range reduction. Regarding the favorable battery parameters at $\Delta T_{ISA} = 15$ K, the MTOM increase would only be 2% without growth factors.

In addition to the negative impact on the aircraft through the additional mass, the integration of the BTMS is not trivial. With A_{front} reaching up to 2.6 m^2, the HEX would not fit into the fuselage. Again, the size of the HEX heavily depends on T_{bat} and η_{bat}. More advantageous values for these two battery parameters result in the reduction of A_{front} to below 0.3 m^2. Also, by increasing the minimum L_{HEX} in Eq. (22), A_{front} could be lowered further.

Especially in Figs. 10 and 11, nondifferentiable points exist in the graphs. For L_{leg} in Fig. 11 with $T_{bat} = 325$ K the cause is the L_{leg} constraint (23). In all other cases these points result from the numerical optimization process. Because there were seven free

design variables, different values may achieve very similar solutions of the objective function. The nondifferentiable points do not exist in the output of the objective function (cf. Fig. 9) except for the one caused by constraint (23).

Some of the free variables are not shown in any of the figures. Their variation was numerically important to comply with the constraints and also, the target function was sensitive to them, but the resulting values are in narrow ranges for the entire design space; ϵ ranges from 0.47 to 0.50, d_H from 3.7 to 4.0 mm, and Π_{HEX} from 0.980 to 0.987; γ_{HEX} varies from 0.1 to 0.5, but has little effect on the BTMS performance and only helps to not violate the compactness constraint (20).

C. Additional Considerations Beyond the Static Model

Deliberately, this study did not choose discrete values for the battery and ambient conditions. The results show clearly that, even with an optimized BTMS, there are combinations of these conditions that result in such high levels of m_{BTMS} and P_{BTMS} that the aircraft concept may be unfeasible, whereas on the other hand more advantageous conditions result in feasible BTMS designs. There are several considerations for the interpretation and further use of the presented results:

T_{bat} seems to be the most significant factor for the sizing of the BTMS. Operating the battery near room temperature is optimal for the battery itself, but the additional size required for the BTMS outweighs the benefit gained from it. The assessment in Sec. IV showed that there is a positive synergy between higher T_{bat} and η_{bat} so that from a BTMS point of view, the highest T_{bat} should be chosen as long as it does not drastically decrease the battery lifetime.

The choice of ΔT_{ISA} should be carefully considered. Safety has the highest priority in aviation, and designing aircraft that are not able to fly in hotter parts of the world or only on colder days is economically questionable. Therefore, usually high ΔT_{ISA} values are assumed in the design process to ensure that the system can operate on any day anywhere. However, in this design study, only a static analysis was performed. A future dynamic model should investigate a more realistic distribution of hot days and the effect on the battery's lifetime. In Sec. IV, the different temperature limits for T_{bat} were discussed. One strategy might be to design a BTMS for a low average ΔT_{ISA} of 15 K and a T_{bat} near the upper end of the optimal temperature range of 313 K. On hotter days the BTMS would have to ensure that T_{bat} does not reach the absolute temperature limit where thermal runaway starts. This may be possible because it is considerably higher than 313 K and there are also operational measures available such as increasing I_{tc} on a hot day. Of course, these hot days would reduce the battery's lifetime. A dynamic model would be helpful to assess this strategy in detail alongside any off-design scenario and should be part of future work.

Off-design performance was not regarded in this study. For the particular application case, the BTMS designed for a hot-day takeoff would be sufficient in all other operating points as well, due to the significantly lower P_{bat}, and thus Q_{bat}, and higher altitudes, and thus lower ambient temperatures, in those points (cf. Fig. 5). In a cold climate, even heating may be necessary during cruise, where P_{bat} is low, or before takeoff. With TEMs, heating is easily possible. The detailed analysis of all relevant off-design points should be included in future work.

If all off-design points are considered, the drag of the TMS has to be analyzed as well. In this study, only takeoff was considered, and earlier studies with a ram-air HEX and a puller fan showed that during takeoff the TMS may actually produce thrust due to the high power load of the fan [50]. During cruise, it may be possible to reduce the power of the fan to idle or zero and TMS drag becomes relevant for the BTMS assessment on overall aircraft level.

VII. Conclusions

A BTMS for a (H)EAC was designed under the assumption that the ambient temperature may be higher than the allowed battery operating temperature on hot days. As a result, the BTMS had to implement a heat pump to overcome a positive temperature gradient. In a first step, all existing technologies capable of transferring heat from a lower to a higher temperature level were assessed. With a qualitative elimination process the number of considered technologies was reduced to seven. A more refined assessment then identified the ACM and the TEM as most suitable technologies. The TEM was chosen over the ACM due to its superior operational flexibility.

With the technology chosen, a numeric model was developed to quantitatively analyze battery thermal management problems. The model consists of a TEM, a finned ram air heat exchanger (HEX) as heat sink, and a very simplified heat pipe as HAS. A simple fan model was also implemented as part of the HEX to increase the air mass flow through the HEX. Sensitivity analyses for both the TEM and the HEX model were conducted identifying a total of six relevant design parameters for the TEM and eight design parameters for the HEX. The sensitivity analysis allowed a comprehensive understanding of the behavior of the models and thus the setup of a numerical optimization.

Lastly, a BTMS for an application case was designed. The (H)EAC was a 19-seater short range aircraft with an all-electric design mission and a combustion engine for range extension. To increase the results' usability, a value range rather than discrete values was chosen for the temperature deviation from the ISA (ΔT_{ISA}), the battery discharge efficiency η_{bat}, and the battery operating temperature T_{bat}. These three parameters depend strongly on assumptions and battery technology development. The final BTMS design for the most adverse combination of the three parameters ($\Delta T_{\text{ISA}} = 35$ K, $T_{\text{bat}} = 295$ K, $\eta_{\text{bat}} = 0.90$) resulted in a 16% increase in aircraft MTOM without considering any snowball effects, whereas the most advantageous combination ($\Delta T_{\text{ISA}} = 15$ K, $T_{\text{bat}} = 325$ K, $\eta_{\text{bat}} = 0.95$) only caused a 2% increase in MTOM. The mass increase considered additional battery mass required to power the BTMS on a first-order basis, meaning that the additional heat load from the additional battery mass was not considered or were any other mass increases, e.g., in the aircraft's structure. A major challenge was the proper matching of TEM surface area and HEX base area because the HEX tended to have larger areas due to the poor heat transfer properties of air.

Because this work was a first design space exploration of a BTMS, there are many interesting possibilities for future work. The aforementioned first-order analysis of additional battery mass is not sufficient, especially when up to 35% of battery mass is added to the aircraft. An iterative design that also considers the additional battery heat load is necessary as well as an integration into the overall aircraft design process to properly account for aircraft level snowball effects. Also, the TEM model is a single-stage model. A multistage TEM can achieve higher COP values for larger temperature lifts [43] and thus could improve the BTMS performance for lower T_{bat}. For a more homogeneous level of modeling detail, a more detailed heat pipe model or an alternative HAS should be implemented. The simplified model showed that the heat pipes have a significant share in the overall BTMS mass. Therefore, a further optimization might result in a better BTMS. The design of the BTMS was tailored toward the most adverse point of the mission. Off-design performance was only discussed qualitatively, but showed potential in further reductions in BTMS mass. To properly assess this potential, a dynamic model of the entire system that also considers battery heating if required is necessary. Finally, the choice between ACM and TEM was so close that only a quantitative assessment of the ACM with the same level of detail as the presented TEM model can answer the question which technology is more beneficial for a BTMS for the given application case.

Appendix

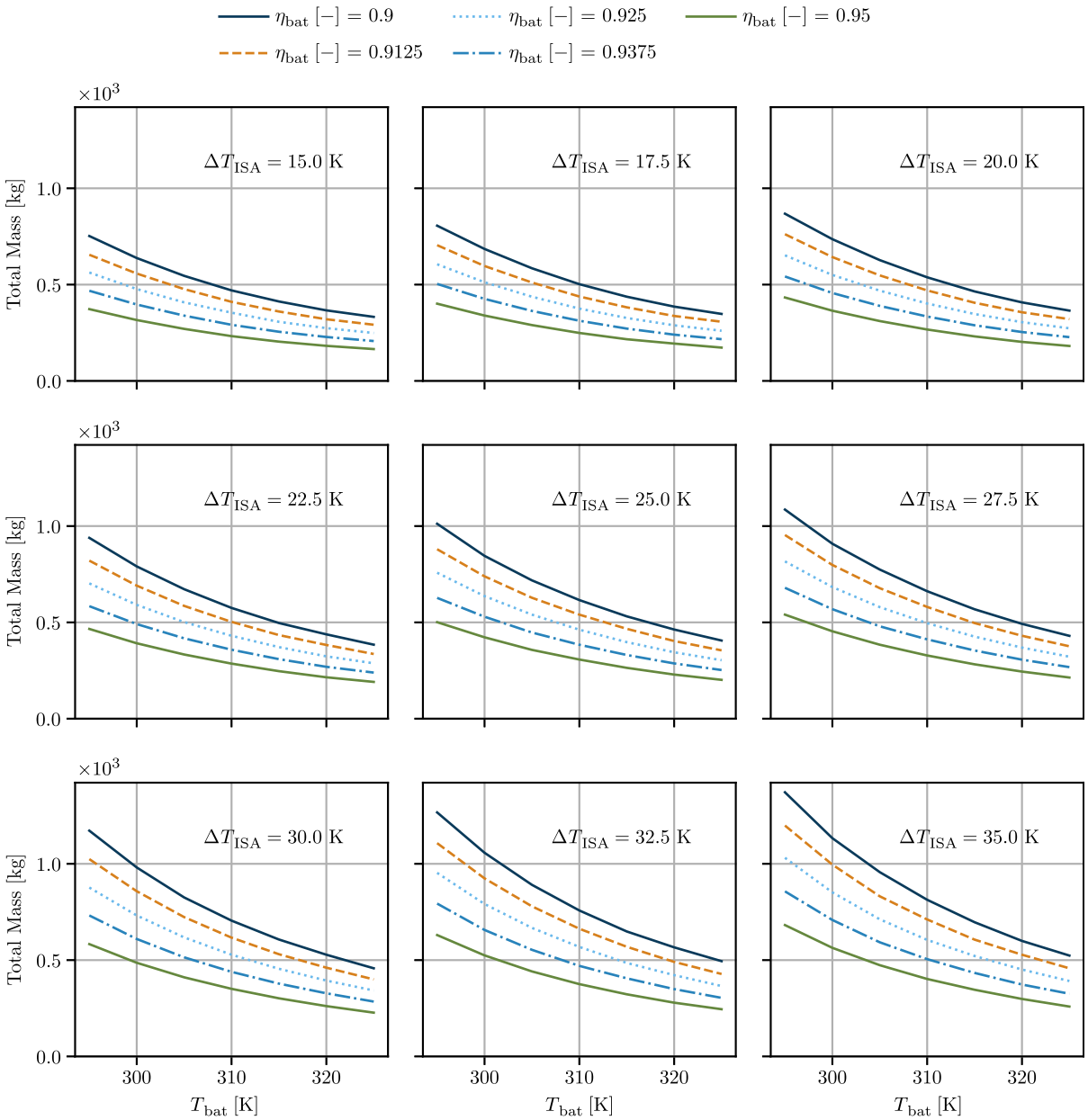

Fig. A1 Full results of the final design space optimization.

Acknowledgments

This research received funding as part of the IVekLu project, a research project supported by the Federal Ministry for Economic Affairs and Energy in the German national LuFo program. We would like to thank Frederick Berg, Romain Berthet, Jorge Carretero-Benignos, Borja Molera, Santosh Nalangula, Peter Rostek, Robert Schoell, and Arne Seitz for the fruitful discussion on possible battery thermal management system technologies. This work is based on the master's thesis of Samuel Fuhrmann, conducted at Bauhaus Luftfahrt e.V., and includes the original publication of the findings of this thesis.

References

[1] "Strategic Research & Innovation Agenda: 2017 Update, Volume 1," Advisory Council for Aviation Research and Innovation in Europe TR, 2017, https://www.acare4europe.org/documents/strategic-research-innovation-agenda-2017-update.

[2] Suder, K. L., "Overview of the NASA Environmentally Responsible Aviation Project's Propulsion Technology Portfolio," *48th AIAA/ASME/SAE/ASEE Joint Propulsion Conference & Exhibit*, AIAA Paper 2012-4038, 2012.

[3] Bowman, C. L., Felder, J. L., and Marien, T. V., "Turbo- and Hybrid-Electrified Aircraft Propulsion Concepts for Commercial Transport," *AIAA/IEEE Electric Aircraft Technologies Symposium*, AIAA Paper 2018-4984, 2018.

[4] Brelje, B. J., and Martins, J. R., "Electric, Hybrid, and Turboelectric Fixed-Wing Aircraft: A Review of Concepts, Models, and Design Approaches," *Progress in Aerospace Sciences*, Vol. 104, Jan. 2019, pp. 1–19. https://doi.org/10.1016/j.paerosci.2018.06.004

[5] Freeman, J., Osterkamp, P., Green, M., Gibson, A., and Schiltgen, B., "Challenges and Opportunities for Electric Aircraft Thermal Management," *Aircraft Engineering and Aerospace Technology: An International Journal*, Vol. 86, No. 6, 2014, pp. 519–524. https://doi.org/10.1108/AEAT-04-2014-0042

[6] Vratny, P. C., "Conceptual Design Methods of Electric Power Architectures for Hybrid Energy Aircraft," Dissertation, Technical Univ. of Munich, Munich, 2018.

[7] Buidin, T. I. C., and Mariasiu, F., "Battery Thermal Management Systems: Current Status and Design Approach of Cooling Technologies," *Energies*, Vol. 14, No. 16, 2021, p. 4879. https://doi.org/10.3390/en14164879

[8] Atanasov, G., van Wensveen, J., Peter, F., and Zill, T., "Electric Commuter Transport Concept Enabled by Combustion Engine Range Extender," *68th German Aerospace Congress (DLRK)*, German Aerospace Soc. (DGLR), Darmstadt, Germany, 2019, https://elib.dlr.de/132771/.

[9] Jansen, R. H., Bowman, C., and Jankovsky, A., "Sizing Power Components of an Electrically Driven Tail Cone Thruster and a Range Extender," *16th AIAA Aviation Technology, Integration, and Operations Conference*, AIAA Paper 2016-3766, 2016.

[10] Pornet, C., and Isikveren, A. T., "Conceptual Design of Hybrid-Electric Transport Aircraft," *Progress in Aerospace Sciences*, Vol. 79, Nov. 2015, pp. 114–135. https://doi.org/10.1016/j.paerosci.2015.09.002

[11] Schiltgen, B. T., Freeman, J., and Hall, D. W., "Aeropropulsive Interaction and Thermal System Integration within the ECO-150: A Turboelectric Distributed Propulsion Airliner with Conventional Electric Machines," *16th AIAA Aviation Technology, Integration, and Operations Conference*, AIAA Paper 2016-4064, 2016.

[12] Kellermann, H., Habermann, A. L., and Hornung, M., "Assessment of Aircraft Surface Heat Exchanger Potential," *Aerospace*, Vol. 7, No. 1, 2020, p. 1. https://doi.org/10.3390/aerospace7010001

[13] Kellermann, H., Habermann, A. L., Vratny, P. C., and Hornung, M., "Assessment of Fuel as Alternative Heat Sink for Future Aircraft," *Applied Thermal Engineering*, Vol. 170, April 2020. https://doi.org/10.1016/j.applthermaleng.2020.114985

[14] Kabir, R., McCluskey, P., and Kizito, J. P., "Investigation of a Cooling System for a Hybrid Airplane," *AIAA/IEEE Electric Aircraft Technologies Symposium*, AIAA Paper 2018-4991, 2018.

[15] Rheaume, J. M., Macdonald, M., and Lents, C. E., "Commercial Hybrid Electric Aircraft Thermal Management System Design, Simulation, and Operation Improvements," *AIAA Propulsion and Energy 2019 Forum*, AIAA Paper 2019-4492, 2019.

[16] Rheaume, J. M., and Lents, C. E., "Design and Simulation of a Commercial Hybrid Electric Aircraft Thermal Management System," *AIAA/IEEE Electric Aircraft Technologies Symposium*, AIAA Paper 2018-4994, 2018.

[17] Rheaume, J. M., and Lents, C. E., "Commercial Hybrid Electric Aircraft Thermal Management Sensitivity Studies," *AIAA/IEEE Electric Aircraft Technologies Symposium*, AIAA Paper 2020-3558, 2020.

[18] Perullo, C., Alahmad, A., Wen, J., D'Arpino, M., Canova, M., Mavris, D. N., and Benzakein, M. J., "Sizing and Performance Analysis of a Turbo-Hybrid-Electric Regional Jet for the NASA ULI Program," *AIAA Propulsion and Energy 2019 Forum*, AIAA Paper 2019-4490, 2019.

[19] Nikbakhti, R., Wang, X., Hussein, A. K., and Iranmanesh, A., "Absorption Cooling Systems–Review of Various Techniques for Energy Performance Enhancement," *Alexandria Engineering Journal*, Vol. 59, No. 2, 2020, pp. 707–738. https://doi.org/10.1016/j.aej.2020.01.036

[20] Ashok Kumar, K., and Kapilan, N., "Studies on the Feasibility of Adsorption Cooling Technologies," *Journal of Physics: Conference Series*, Vol. 1473, March 2020, Paper 012050. https://doi.org/10.1088/1742-6596/1473/1/012050

[21] Merzvinskas, M., Bringhenti, C., Tomita, J. T., and de Andrade, C. R., "Air Conditioning Systems for Aeronautical Applications: A Review," *Aeronautical Journal*, Vol. 124, No. 1274, 2020, pp. 499–532. https://doi.org/10.1017/aer.2019.159

[22] Kellermann, H., Fuhrmann, S., Shamiyeh, M., and Hornung, M., "Design of a Battery Cooling System for Hybrid Electric Aircraft," *AIAA Aviation 2021 Forum*, AIAA Paper 2021-3138, 2021.

[23] Matulich, D., "High-Temperature Bootstrap Compared with F-15 Growth Air Cycle Air Conditioning System," *SAE Transactions*, Vol. 98, 1989, pp. 349–360. https://doi.org/10.4271/891436

[24] Nowacki, J.-E., Dar, U., and Aerosystems, S., "An Electric Cooling System for an UAV," *25th Congress of the International Council of the Aeronautical Sciences*, ICAS, Bonn, Germany, 2006, pp. 3592–3599.

[25] Santos, A. P., Andrade, C. R., and Zaparoli, E. L., "A Thermodynamic Study of Air Cycle Machine for Aeronautical Applications," *International Journal of Thermodynamics*, Vol. 17, No. 3, 2014, pp. 117–126. https://doi.org/10.5541/ijot.538

[26] Bansal, P., Vineyard, E., and Abdelaziz, O., "Status of Not-in-Kind Refrigeration Technologies for Household Space Conditioning, Water Heating and Food Refrigeration," *International Journal of Sustainable Built Environment*, Vol. 1, No. 1, 2012, pp. 85–101. https://doi.org/10.1016/j.ijsbe.2012.07.003

[27] Bell, I. H., Wronski, J., Quoilin, S., and Lemort, V., "Pure and Pseudo-Pure Fluid Thermophysical Property Evaluation and the Open-Source Thermophysical Property Library CoolProp," *Industrial & Engineering Chemistry Research*, Vol. 53, No. 6, 2014, pp. 2498–2508. https://doi.org/10.1021/ie4033999

[28] Brown, J. S., and Domanski, P. A., "Review of Alternative Cooling Technologies," *Applied Thermal Engineering*, Vol. 64, Nos. 1–2, 2014, pp. 252–262. https://doi.org/10.1016/j.applthermaleng.2013.12.014

[29] Subudhi, S., and Sen, M., "Review of Ranque–Hilsch Vortex Tube Experiments Using Air," *Renewable and Sustainable Energy Reviews*, Vol. 52, Dec. 2015, pp. 172–178. https://doi.org/10.1016/j.rser.2015.07.103

[30] Atta, R. M., "Thermoelectric Cooling," *Bringing Thermoelectricity into Reality*, IntechOpen, London, U.K., 2018, pp. 247–267, https://www.intechopen.com/chapters/60452. https://doi.org/10.5772/intechopen.75791

[31] Lewis, J. S., Chaer, I., and Tassou, S. A., "Fostering the Development of Technologies and Practices to Reduce the Energy Inputs into the Refrigeration of Food: Reviews of Alternative Refrigeration Technologies," Centre for Energy and Built Environment Research, School of Engineering and Design, Brunel Univ. TR, 2007, http://www.grimsby.ac.uk/documents/defra/tech-newrefrigetechs.pdf.

[32] Radermacher, R., Yang, B., and Hwang, Y., "Integrating Alternative and Conventional Cooling Technologies," *ASHRAE Journal*, Vol. 49, No. 10, 2007, pp. 28–35.

[33] Chaudron, J.-B., Muller, C., Hittinger, M., Risser, M., and Lionte, S., "Performance Measurements on a Large-Scale Magnetocaloric Cooling Application at Room Temperature," *Thermag VIII—International Conference on Caloric Cooling*, International Inst. of Refrigeration, Paris, 2018, pp. 137–142.

[34] Kitanovski, A., "Energy Applications of Magnetocaloric Materials," *Advanced Energy Materials*, Vol. 10, No. 10, 2020, Paper 1903741. https://doi.org/10.1002/aenm.201903741

[35] Malik, M., Dincer, I., and Rosen, M. A., "Review on Use of Phase Change Materials in Battery Thermal Management for Electric and Hybrid Electric Vehicles," *International Journal of Energy Research*, Vol. 40, No. 8, 2016, pp. 1011–1031. https://doi.org/10.1002/er.3496.

[36] Lu, M., Zhang, X., Ji, J., Xu, X., and Zhang, Y., "Research Progress on Power Battery Cooling Technology for Electric Vehicles," *Journal of Energy Storage*, Vol. 27, Feb. 2020, Paper 101155. https://doi.org/10.1016/j.est.2019.101155

[37] Qian, S., Nasuta, D., Rhoads, A., Wang, Y., Geng, Y., Hwang, Y., Radermacher, R., and Takeuchi, I., "Not-in-Kind Cooling Technologies: A Quantitative Comparison of Refrigerants and System Performance," *International Journal of Refrigeration*, Vol. 62, Feb. 2016, pp. 177–192. https://doi.org/10.1016/j.ijrefrig.2015.10.019

[38] An, Z., Jia, L., Ding, Y., Dang, C., and Li, X., "A Review on Lithium-Ion Power Battery Thermal Management Technologies and Thermal Safety," *Journal of Thermal Science*, Vol. 26, No. 5, 2017, pp. 391–412. https://doi.org/10.1007/s11630-017-0955-2

[39] Cox, T. G., and Weiss, C. F., "An Investigation of Two Cooling Technologies as Applied to a Distributed Propulsion Control Architecture," *Turbo Expo: Power for Land, Sea, and Air*, American Soc. of Mechanical Engineers Paper 91-GT-341, 1991.

[40] Sharma, T. K., Rao, G. A. P., and Murthy, K. M., "Numerical Analysis of a Vortex Tube: A Review," *Archives of Computational Methods in Engineering*, Vol. 24, No. 2, 2017, pp. 251–280. https://doi.org/10.1007/s11831-016-9166-3

[41] Salah, W. A., and Abuhelwa, M., "Review of Thermoelectric Cooling Devices Recent Applications," *Journal of Engineering Science and Technology*, Vol. 15, No. 1, 2020, pp. 455–476.

[42] Kim, J., Oh, J., and Lee, H., "Review on Battery Thermal Management System for Electric Vehicles," *Applied Thermal Engineering*, Vol. 149, Feb. 2019, pp. 192–212. https://doi.org/10.1016/j.applthermaleng.2018.12.020

[43] Goldsmid, H. J., *Introduction to Thermoelectricity*, Springer Series in Materials Science, Vol. 121, Springer, Berlin, 2010.

[44] Chang, Y.-W., Chang, C.-C., Ke, M.-T., and Chen, S.-L., "Thermoelectric Air-Cooling Module for Electronic Devices," *Applied Thermal Engineering*, Vol. 29, No. 13, 2009, pp. 2731–2737. https://doi.org/10.1016/j.applthermaleng.2009.01.004

[45] McCarty, R., "A Comparison Between Numerical and Simplified Thermoelectric Cooler Models," *Journal of Electronic Materials*,

Vol. 39, No. 9, 2010, pp. 1842–1847.
https://doi.org/10.1007/s11664-010-1075-x

[46] Huang, H.-S., Weng, Y.-C., Chang, Y.-W., Chen, S.-L., and Ke, M.-T., "Thermoelectric Water-Cooling Device Applied to Electronic Equipment," *International Communications in Heat and Mass Transfer*, Vol. 37, No. 2, 2010, pp. 140–146.
https://doi.org/10.1016/j.icheatmasstransfer.2009.08.012

[47] Fraisse, G., Ramousse, J., Sgorlon, D., and Goupil, C., "Comparison of Different Modeling Approaches for Thermoelectric Elements," *Energy Conversion and Management*, Vol. 65, Jan. 2013, pp. 351–356.
https://doi.org/10.1016/j.enconman.2012.08.022

[48] Saidur, R., Rezaei, M., Muzammil, W. K., Hassan, M. H., Paria, S., and Hasanuzzaman, M., "Technologies to Recover Exhaust Heat from Internal Combustion Engines," *Renewable and Sustainable Energy Reviews*, Vol. 16, No. 8, 2012, pp. 5649–5659.
https://doi.org/10.1016/j.rser.2012.05.018

[49] Zhu, W., Deng, Y., Wang, Y., and Wang, A., "Finite Element Analysis of Miniature Thermoelectric Coolers with High Cooling Performance and Short Response Time," *Microelectronics Journal*, Vol. 44, No. 9, 2013, pp. 860–868.
https://doi.org/10.1016/j.mejo.2013.06.013

[50] Kellermann, H., Lüdemann, M., Pohl, M., and Hornung, M., "Design and Optimization of Ram Air-Based Thermal Management Systems for Hybrid-Electric Aircraft," *Aerospace*, Vol. 8, No. 1, 2021, p. 3.
https://doi.org/10.3390/aerospace8010003

[51] Shah, R. K., and Sekulić, D. P., *Fundamentals of Heat Exchanger Design*, Wiley-Interscience, Hoboken, NJ, 2003.

[52] Kays, W. M., and London, A. L., *Compact Heat Exchangers*, 3rd ed., Krieger, Malabar, FL, 1998.

[53] Zhang, C.-W., Xu, K.-J., Li, L.-Y., Yang, M.-Z., Gao, H.-B., and Chen, S.-R., "Study on a Battery Thermal Management System Based on a Thermoelectric Effect," *Energies*, Vol. 11, No. 2, 2018.
https://doi.org/10.3390/en11020279

[54] Zhang, C., Xia, Z., Wang, B., Gao, H., Chen, S., Zong, S., and Luo, K., "A Li-Ion Battery Thermal Management System Combining a Heat Pipe and Thermoelectric Cooler," *Energies*, Vol. 13, No. 4, 2020, p. 841.
https://doi.org/10.3390/en13040841

[55] Annapragada, S. R., Macdonald, M., Sur, A., Mahmoudi, R., and Lents, C., "Hybrid Electric Aircraft Battery Heat Acquisition System," *AIAA/IEEE Electric Aircraft Technologies Symposium*, AIAA Paper 2018-4992, 2018.

[56] Doumin, A. M., Daud, Z. H. C., Asus, Z., Mazali, I. I., Kameil, M., Hamid, A., Said, M. F. M., and Chrenko, D., "Recent Studies on Lithium-ion Battery Thermal Behaviour for Electric and Hybrid Electric Vehicles: A Review," *Journal of Advanced Research in Fluid Mechanics and Thermal Sciences*, Vol. 61, No. 2, 2019, pp. 262–272.

[57] Jaguemont, J., and van Mierlo, J., "A Comprehensive Review of Future Thermal Management Systems for Battery-Electrified Vehicles," *Journal of Energy Storage*, Vol. 31, Oct. 2020.
https://doi.org/10.1016/j.est.2020.101551

[58] Dinçer, İ., and Kanoglu, M., *Refrigeration Systems and Applications*, 2nd ed., Wiley, Hoboken, NJ, 2010, Chap. 7.

[59] Iradukunda, A.-C., Huitink, D., and Luo, F., "A Review of Advanced Thermal Management Solutions and the Implications for Integration in High-Voltage Packages," *IEEE Journal of Emerging and Selected Topics in Power Electronics*, Vol. 8, No. 1, 2019, pp. 256–271.
https://doi.org/10.1109/JESTPE.2019.2953102

[60] Ma, S., Jiang, M., Tao, P., Song, C., Wu, J., Wang, J., Deng, T., and Shang, W., "Temperature Effect and Thermal Impact in Lithium-Ion Batteries: A Review," *Progress in Natural Science: Materials International*, Vol. 28, No. 6, 2018, pp. 653–666.
https://doi.org/10.1016/j.pnsc.2018.11.002

[61] Khan, M. R., Swierczynski, M. J., and Kær, S. K., "Towards an Ultimate Battery Thermal Management System: A Review," *Batteries*, Vol. 3, No. 1, 2017, p. 9.
https://doi.org/10.3390/batteries3010009

[62] Omar, N., Monem, M. A., Firouz, Y., Salminen, J., Smekens, J., Hegazy, O., Gaulous, H., Mulder, G., van den Bossche, P., Coosemans, T., and van Mierlo, J., "Lithium Iron Phosphate Based Battery—Assessment of the Aging Parameters and Development of Cycle Life Model," *Applied Energy*, Vol. 113, Jan. 2014, pp. 1575–1585.
https://doi.org/10.1016/j.apenergy.2013.09.003

[63] Pesaran, A., Santhanagopalan, S., and Gi-Heon, K., "Addressing the Impact of Temperature Extremes on Large Format Li-Ion Batteries for Vehicle Applications," *30th International Battery Seminar*, National Renewable Energy Lab., NREL/PR-5400-58145, 2013.

[64] Saw, L. H., Somasundaram, K., Ye, Y., and Tay, A., "Electro-Thermal Analysis of Lithium Iron Phosphate Battery for Electric Vehicles," *Journal of Power Sources*, Vol. 249, March 2014, pp. 231–238.
https://doi.org/10.1016/j.jpowsour.2013.10.052

[65] Liu, G., Ouyang, M., Lu, L., Li, J., and Han, X., "Analysis of the Heat Generation of Lithium-Ion Battery During Charging and Discharging Considering Different Influencing Factors," *Journal of Thermal Analysis and Calorimetry*, Vol. 116, No. 2, 2014, pp. 1001–1010.
https://doi.org/10.1007/s10973-013-3599-9

[66] Löbberding, H., Wessel, S., Offermanns, C., Kehrer, M., Rother, J., Heimes, H., and Kampker, A., "From Cell to Battery System in BEVs: Analysis of System Packing Efficiency and Cell Types," *World Electric Vehicle Journal*, Vol. 11, No. 4, 2020, p. 77.
https://doi.org/10.3390/wevj11040077

[67] Quinn, J. B., Waldmann, T., Richter, K., Kasper, M., and Wohlfahrt-Mehrens, M., "Energy Density of Cylindrical Li-Ion Cells: A Comparison of Commercial 18650 to the 21700 Cells," *Journal of the Electrochemical Society*, Vol. 165, No. 14, 2018, Paper A3284.
https://doi.org/10.1149/2.0281814jes

[68] Purushothama, B., "Air Handling Units in Textile Industry," *Humidification and Ventilation Management in Textile Industry*, Woodhead Publishing India Pvt. Ltd, 2009, pp. 41–86.

[69] Kraft, D., "A Software Package for Sequential Quadratic Programming," DLR German Aerospace Center—Inst. for Flight Mechanics DFVLR-FB 88-28, Cologne, Germany, 1988.

T. Lee
Associate Editor

3 Discussion

The four papers above can be utilized together for a complete stationary heat flow analysis of the TMS of any (H)EP-aircraft. In [1], design methods for the most conventional heat sink – a R-HEX – are presented. One of the largest advantages of the R-HEX is its infinite scalability. It can be designed for any heat flow even though the resulting HEX may become too heavy or spacious for the aircraft. For any conceptual (H)EP-aircraft design study, the procedure from [1] can be utilized for an assessment of the necessary corresponding TMS. Contrary to other studies with fixed components, e.g., HEXs with fixed internal geometries, the results of the analysis are optimized to a degree and scale accurately with the thermal requirements.

In [2], the aircraft surfaces were considered as an alternative heat sink. With relatively simple methods a quick estimation of the cooling potential of the surfaces of any aircraft is possible. The advantage of using existing surfaces is less drag or even an aerodynamic benefit from the TMS and a possibly lighter TMS due to multi-use surfaces and structures. The procedure outlined in [2] may be applied in any aircraft conceptual design study to quickly assess the heat sink potential of the aircraft surfaces. Combined with an estimation of the expected heat loads of the propulsion system or other heat sources a decision on whether to pursue a surface cooling system as an alternative to the conventional R-HEX system can be established quickly.

A full stationary model of surface HEXs utilizing fuel as coolant was developed in [3]. The WIFHE and the TWIH are two detailed heat rejection component models that match the modeling depth of the R-HEX presented in [1]. With a few adaptions, the WIFHE model was transformed into the more general WISH model (cf. section 1.4.2) that allows quantitative comparison of an R-HEX to an S-HEX system.

Finally, the special challenge of heat sources with very low temperatures, e.g., a battery, was discussed in [4] and a possible cooling method was presented with TEMs. The TEM was chosen as the most suitable heat pump technology through a qualitative assessment of many possible technologies. Again, the modeling depth of the new component was set to allow an assessment of all three parasitic effects of the TMS.

Combined, the four papers and thus the main body of this thesis provide methods to assess a large variety of thermal management challenges in conceptual aircraft studies. A combined application enables a comparison of different heat sinks and allows the selection of the most suitable one. It is possible to optimize the TMS towards aircraft target functions. All four publications included application cases to demonstrate the feasibility of the developed methods and to provide a specific TMS assessment for their respective application case. Due to the difference in application cases, it is not possible to directly compare the final results of the papers to each other. The following sections demonstrate in an exemplary matter how to utilize the methods of the papers together to perform a large assessment of the TMS for one application case. First, the overall procedure is outlined, second, the application case is introduced, and, last, the TMS assessment is performed.

3.1 Procedure of the exemplary thermal management system assessment

The four models are combined to design and optimize a TMS for one application case. The design procedures will allow an estimation of the TMS impact within the aircraft conceptual design phase. If coupled with other disciplines, e.g., the propulsion system design, the TMS design can be incorporated at an early stage of the aircraft design process, thereby ensuring a more optimized final design. Similar to the sizing of conventional engines, where performance maps are used for the conceptual aircraft design, the outcome of the TMS should ideally have a similarly low level of implementation effort. While the simplification and optimization of the TMS design and performance methods for a computationally performant aircraft design loop is not part of this thesis, the results will be presented in the form of simple graphs or data tables that could be used within an aircraft design loop. The final analysis procedure is threefold:

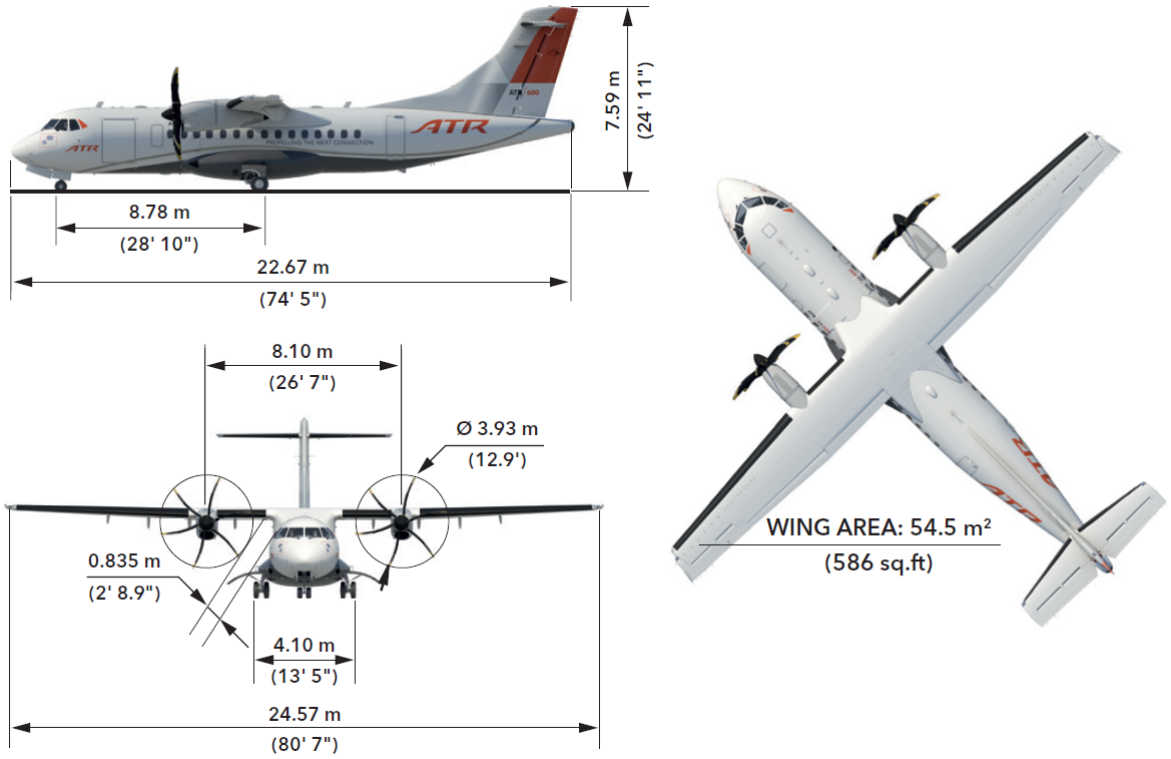

Figure 3.1 Drawings of the ATR 42-600 [72]

1. **Initial assessment of surface cooling potential**
   Based on the actual geometry of the aircraft the surface cooling potential assessment from [2] is conducted followed by a more detailed analysis for S-HEXs with enhanced methods based on [3].

2. **Design of a R-HEX based TMS for a range of possible heat loads**
   With broad assumptions, e.g., on the possible hybridization strategy, a design space for possible propulsion system heat loads is opened. R-HEX based TMSs are designed and optimized for the design space with methods from [1] and possibly [4] depending on the temperature assumptions.

3. **Design and optimization of a final TMS**
   The results from the above two points are combined to design a final TMS tailored towards the minimum impact on the aircraft by means of mass, drag, and power requirements.

3.2 The application case: a partially electrified regional aircraft

The TMS design procedure can be applied to any aircraft application. To showcase the applicability of the developed methods, an exemplary application is selected. To choose a relevant example, a smaller regional aircraft is considered since (partial) electrification has a higher potential for smaller aircraft [42]. In a current, EU-funded project named "IMOTHEP" [71], the ATR 42-600 is used as a reference application for a hybrid-electric aircraft concept. The baseline aircraft is sized according to similar Top Level Aircraft Requirement (TLAR)s. Figure 3.1 shows the reference aircraft from three sides with some geometric parameters.

At this time, the propulsion system design is only preliminary and key parameters relevant for a detailed final design of the TMS are not yet specified, such as the degree of hybridization, which has a direct impact on the emitted waste heat. Instead of using one value, large ranges are defined for the heat loads of the components, which allow the design of a range of TMSs. The results of the TMS assessment can later be implemented in the aircraft conceptual design process to account for a potential TMS even at the early stages of the design process.

Table 3.1 Input parameters from the electric propulsion system for the TMS [73]

Component	Parameter	Value
Battery	T_{out}	328 K
	Q	90 kW - 180 kW
PMAD	T_{out}	370 K
	Q	25 kW - 50 kW
Motors	T_{out}	370 K
	Q	20 kW - 40 kW

The propulsion system has two electric motors: one powering one or multiple compressor stages and the other partially powering the propeller on the main shaft. The electric power is provided by a battery and there is a Power Management and Distribution System (PMAD). The assumptions for the range of required cooling systems are presented in Table 3.1 [73]. The outlet temperature (T_{out}) of each component is the temperature of the coolant entering the TMS. Due to the similar T_{out} of the motors and the PMAD their heat loads are combined resulting in an overall range of 45 kW - 100 kW. For the remainder of the thesis, the TMSs are referred to as battery and motor TMS for simplicity. With the given T_{out} in Table 3.1 and the hot day assumption of ΔT_{ISA}= 30 K, there is no direct need for a heat pump. Thus, the assessment is carried out with the models from [1–3].

Additionally, a fuel burn sensitivity with regards to a fictional TMS mass (m_{TMS}) and drag (D_{TMS}) increase was derived from a model of the ATR 42-600 to serve as a target function for TMS optimizations as in [1]. The relative fuel burn increase is [73]:

$$\delta FB = \frac{3\%}{1\,000\,\text{kg}} m_{\text{TMS}} + \frac{2.45\%}{376.4\,\text{N}} D_{\text{TMS}} \tag{3.1}$$

3.3 Assessment of the surface cooling potential

3.3.1 Setup, procedure, and assumptions

The first step in assessing the cooling potential of the existing aircraft surfaces is the definition of the surfaces. While a MTOM based empirical correlation was used in [2] to estimate the surface areas of the components for general aircraft, more refined geometries are usually at hand if the application case is known. In this case, the ATR 42-600 geometries are used even though a later aircraft with (H)EP would have slightly different surfaces. As shown in [2] the potential assessment can accept a rather large uncertainty because the goal is not to define the final detailed TMS. All assumed geometric properties are shown in Table 3.2. Some simplifications include the modeling of the geometries of nacelles and fuselage as straight cylinders, the wing as a double trapezoid with one rectangular section inboard and a tapered section outboard, and the tail planes as single trapezoids. The wing box section above the fuselage is not counted for the wing as the area is already included in the fuselage calculations. The values are either directly obtained from [72, 74] or derived from the drawings within those sources. [74] may be used for that purpose even though it concerns the earlier version of the ATR 42, i.e. Model 500, however, the Model 600 has the same geometries as shown by comparing [72] with [75]. The constant parameters for the S-HEX assessment are listed in Table 3.2. In accordance with [2] some areas of the aircraft are excluded such as the control surfaces, flaps, and slats. The radiation settings were adopted from [3] and the exposed relative area $(\delta A)_{\text{exp}}$ was set to 50% since, for symmetric components, only about half of the total surface area is exposed to solar radiation. Radiation emission from the surfaces was neglected in accordance with the results from [3]. Four typical operating points were selected to assess the surface cooling potential for the mission. They are listed in Table 3.3 [73]. In all operating points, a ΔT_{ISA} of 30 K was assumed.

For a potential assessment at the beginning of an analysis, certain design variables need a broad space rather than fixed values to allow flexibility during the aircraft design process. T_{surf} has to cover a broad range to allow different heat source temperatures. In this study, it was set between 320 K and 420 K. The usable δA_{fslg} is hard to define due to the many interruptions of the smooth surface, e.g., connections to other components, windows,

Table 3.2 Input setting for the surface cooling assessment partly derived from [72, 74]

Parameter	Value	Parameter	Value
Fuselage		**Horizontal tail plane**	
d	2.63 m	c_{root}	2.05 m
L	22.67 m	c_{tip}	1.25 m
Nacelles		S	3.65 m
d	0.97 m	δc_{cts}	40%
L	3.55 m	**Vertical tail plane**	
Wing		c_{root}	3.58 m
c_{root}	2.57 m	c_{tip}	2.12 m
c_{kink}	2.57 m	S	4.44 m
c_{tip}	1.41 m	δc_{cts}	0.35
$S_{root-kink}$	3.68 m	**Radiation**	
$S_{kink-tip}$	7.44 m	P_{solar}	1 100 W m^{-2}
δc_{slat}	0%	δA_{exp}	50%
δc_{flap}	15%	β	0.25

Table 3.3 Operating points [73]

Operating point	Altitude [m]	Ma [−]	F_N [N]
TX	0.0	0.01	1400
TO	0.0	0.16	61968
CL	3282	0.31	29184
CR	6705	0.46	13877

and doors. Therefore, a broad spectrum between 25% and 75% was chosen in this study. The results of this parameter variation combination are shown in Figure 3.2 and explained in Section 3.3.2.

In [2] and [3] it became clear that TX is a particularly difficult operating point for any surface cooling system due to the low velocities of the aircraft and, therefore, the very limited forced convection around the surfaces. One advantage of open-rotor aircraft such as the ATR 42-600 is the existence of a slipstream behind the propellers, which causes an increased flow velocity over some of the aircraft's surfaces. The effect of the slipstream on the heat transfer rate is analyzed with respect to two parameters: F_N and the relative wing-span covered by the propeller slipstream (δS_{slip}). F_N was varied between 0 kN and 80 kN and δS_{slip} was set to three values between 0.2 and 1.0. The results are shown in Figure 3.3 for all four operating points and in Figure 3.4 for TX over a lower F_N range. The chosen range between no and maximum F_N results in sections of the graph that are not operable, e.g., the maximum F_N of 80 kN cannot be achieved in CR. For a better orientation, the typical F_N from Table 3.3 is added to the graphs. The slipstream propeller model introduced in Section 1.4.2 was used to calculate the slipstream velocity. In Figure 3.5, the distribution of Q over the different aircraft components is presented for $\delta S_{slip} = 0.353$, which is the value corresponding to a straight slipstream behind the current ATR 42-600 propellers with a diameter of 3.93 m.

3.3.2 Surface cooling potential in different operating points

The results in Figure 3.2 show linear dependencies between the two input variables (δA_{fslg} and T_{surf}) and Q, which is expected from the fundamental heat transfer equations. In TX, two interesting observations are the presence of negative Q values, i.e., surface heating instead of cooling, and the intersection of the lines representing different δA_{fslg} values. The assumed ΔT_{ISA} corresponds to an ambient temperature (T_{amb}) of 318 K in TX and the low Ma value does not result in any significant total temperature (T_{tot}) increase. Therefore, convectional cooling is possible for any T_{surf} above 318 K. The negative Q values observed for T_{surf} below 332 K to 333 K depending on δA_{fslg} are caused by solar absorption. At the intersection of the three δA_{fslg} lines at $T_{surf} = 336$ K, absorption and convection heat rates have equal magnitudes but opposite signs for the

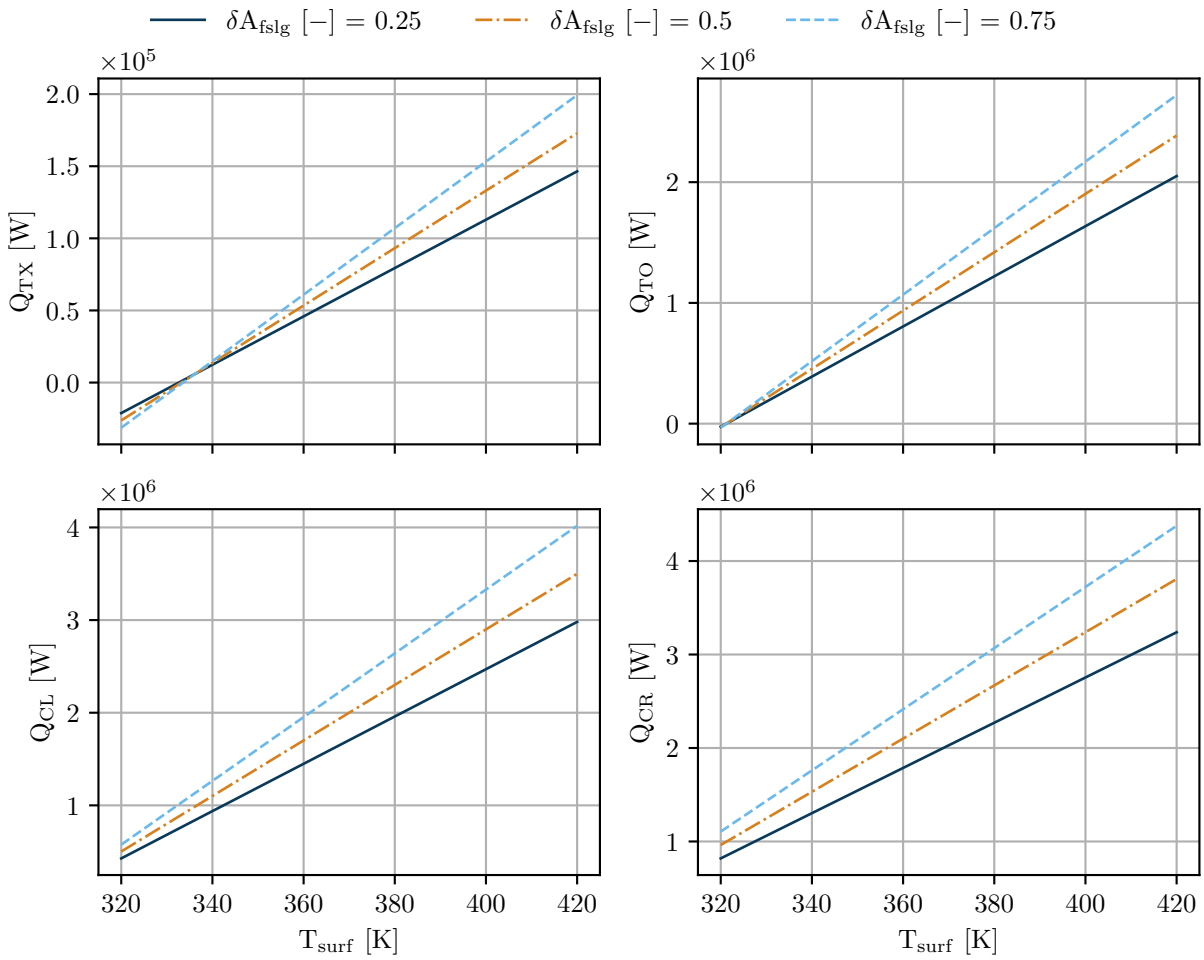

Figure 3.2 Influence of surface temperature and usable fuselage surface area on the surface cooling potential

fuselage. The intersection is located at T_{surf} values with positive Q values, i.e., cooling for the entire aircraft since other components, e.g., wings and tail planes, have their "equilibrium" T_{surf} at different values. Mainly the thermal boundary layer thickness is responsible for the difference. Short components have thinner average thermal boundary layers and therefore provide better convective cooling.

The influence of the solar absorption decreases with increasing Ma. In TO, all operating conditions are equal to TX except for Ma (cf. Table 3.3). The absorbed Q is equal to the value in TX, but the convectional Q has increased significantly. The 0-crossing is close to the lowest T_{surf} of 320 K. The total Q increased by an order of magnitude. In TO, 1 MW of heat can be removed for T_{surf} between 357 K and 369 K depending on δA_{fslg} while in TX, the maximum Q value for the maximum T_{surf} of 420 K ranged between 0.15 MW and 0.20 MW.

This effect is further increased in CL and CR and enhanced by the increasing altitude and thus decreasing T_{amb}. Even for T_{surf} = 320 K, Q values between 0.43 MW and 0.58 MW in CL and between 0.82 MW and 1.11 MW in CR are possible. At maximum T_{surf}, these ranges increase to 2.99 MW to 4.02 MW and 3.24 MW to 4.37 MW respectively.

The first objective of the S-HEX assessment was achieved with the rough estimation of the surface cooling potential of the given aircraft application for the most relevant operating points. The trend observed in [2] and [3] with regards to the criticality of TX and TO for the TMS was confirmed for the application at hand. The large increase in Q between TX and TO strengthens the assumption that TX may not be as critical since the time spent between the end of TX and the selected TO point lasts less than a minute depending on the application case. During this time, the thermal capacities of the electric components as well as the components of the TMS may be capable of absorbing the peak heat loads until stationary cooling is provided by the increased convection. This assumption has to be confirmed by a detailed dynamic TMS analysis for every application and it is only valid if the application's heat load is within the available Q for the later operating points.

As part of the surface cooling potential assessment, the increase in Q due to the forced flow in the propeller slipstream was analyzed as well. The results in Figures 3.3 and 3.4 were generated using the mean values for the variables from Figure 3.2, i.e., T_{surf} = 370 K and δA_{fslg} = 0.5. The general square-root shape of Q over F_N is rooted in (1.2). The relative increase in Q with F_N is stronger for operating points with low flight speeds. In TX, without any propeller slipstream (F_N = 0), Q is 40.5 kW. At the typical F_N value of 1 400 N, Q is increased by 43% for δS_{slip} = 0.2 and by 184% for δS_{slip} = 1.0, i.e., a wing with full distributed propulsion. At the beginning of TO, i.e., before the selected TO conditions from Table 3.3, F_N would be increased to its maximum value. From Figure 3.3, an increase of Q to 178 kW - 646 kW depending on δS_{slip} can be observed corresponding to a 339% - 1 495% increase in Q compared to the value without slip stream consideration. In CR, the relative increase in Q for the typical F_N only ranges from 0.3% to 1.3%, which are the lowest relative values of all operating points.

Figure 3.5 provides further details on the distribution of Q on the different aircraft components. The assumptions for T_{surf} and δA_{fslg} are equal to those in Figures 3.3 and 3.4 and additionally δS_{slip} is set to 0.353. As a first observation, the component-wise Q-split is different for TX compared to the other operating points. When no slip-stream is considered, the fuselage has the largest Q-share followed by the wing. For all other operating points, the wing has a larger Q-share due to the area considered for heat transfer. With the assumption of δA_{fslg} = 0.5, the wing area is larger than the fuselage area, which reflects in the distributions for TO, CL and CR. In TX, the low Ma leads to laminar flow on the wing, but towards the rear fuselage section, the Reynolds number (Re) is above the critical Re, resulting in a turbulent flow and thus significantly increased heat transfer. In all other operating points, the increased Ma results in turbulent flow on (parts of) all components, which decreases the advantage of the fuselage. The laminar-turbulent transition is also the reason for the large relative benefit of the propeller slipstream in TX. The high slipstream velocity leads to turbulent flow in the propeller wake on the wing, which increases Q_{wing} by a factor of about four. In all other operating points, an increase in Q_{wing} is visible when considering the slipstream, however, the relative impact on the overall Q is smaller and becomes negligible for CR.

Overall the analysis of the propeller slipstream impact on the surface cooling potential showed a significant benefit for operating points with very low speeds. The strategic placement of surface HEXs in the propeller wake can help with peak heat loads during TX and the beginning of TO. For operating points with higher flight

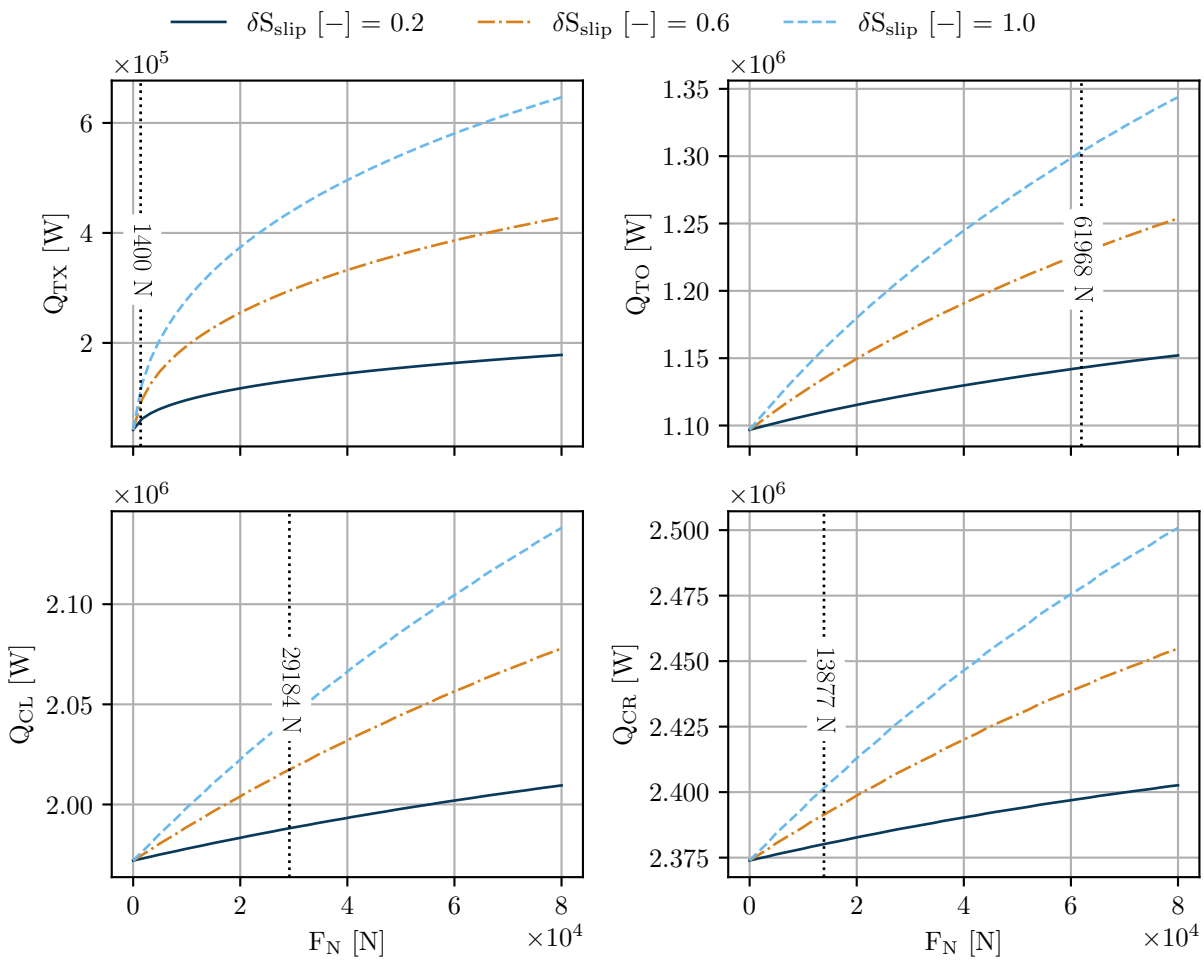

Figure 3.3 Influence of relative wing span covered by the propeller slipstream and thrust on the surface cooling potential

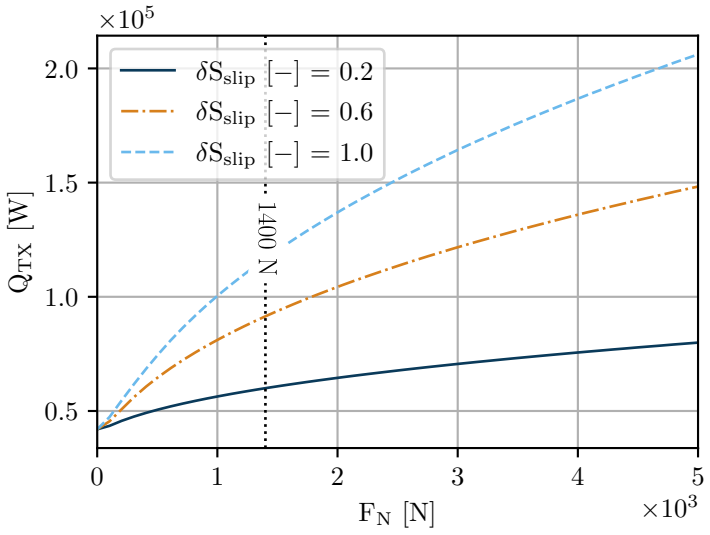

Figure 3.4 Influence of relative wing span covered by the propeller slipstream and thrust on the surface cooling potential during taxi

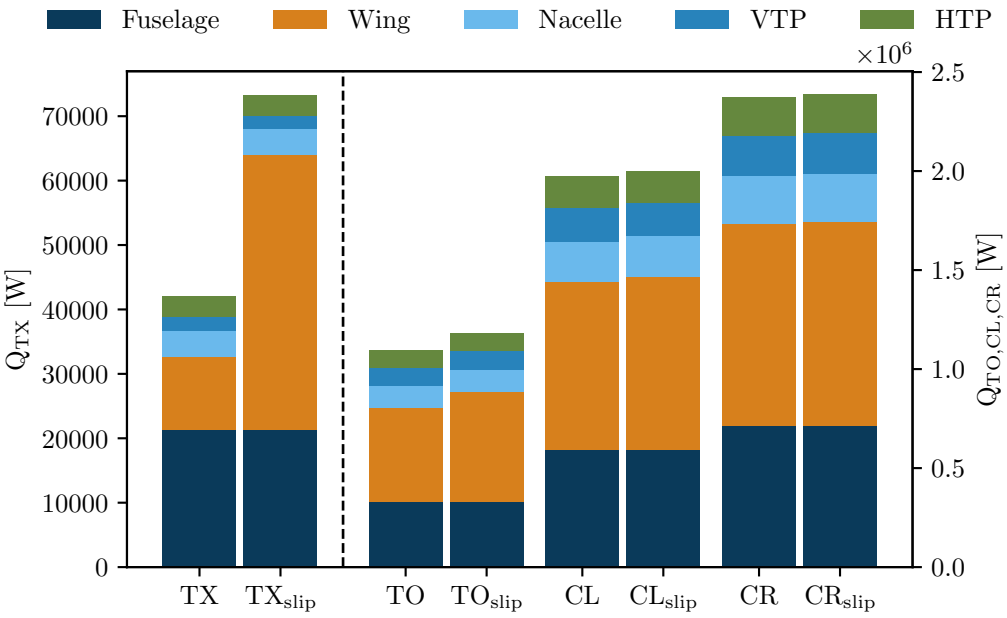

Figure 3.5 Comparison of heat rejection per component with and without slipstream consideration. $\delta S_{slip} = 0.353$; F_N: typical values from Table 3.3

velocities, the Q increase beyond values expected from a surface HEX assessment without the consideration of the propeller slipstream is very limited.

Relating the results of the surface cooling assessment to the Q-ranges in Table 3.1 reveals that the cooling potential of the existing surfaces exceeds the sum of the heat loads of the propulsion system by an order of magnitude for CL and CR. In TO, and TX, the cooling potential is limited especially for low T_{surf} and, therefore, especially the battery TMS presents a challenge. Overall, the results of the potential assessment suggest that the use of S-HEXs as part of the TMS is a viable option, thus, a detailed assessment in Section 3.5 further investigates the design of S-HEXs for the application case including a quantification of the weight and fuel burn impact of S-HEXs on the aircraft.

3.4 Design and performance of a ram-air based thermal management system

The ram-air-based system is designed with the methods presented in [1]. It is the most commonly used system in current applications and in future studies (cf. Section 1.3). A cooling potential assessment similar to the one performed in Section 3.3 is not required since the R-HEX has a theoretical infinitesimal scaling ability, i.e., it can be designed for any heat load requirement as long as the hot side inlet temperature is above the cold side inlet temperature. Therefore, it is possible to meet the first priority for TMSs in aircraft of the objectives of this thesis (cf. Section 1.2) in any case. There are combinations of heat loads and inlet conditions that lead to large and heavy R-HEXs, which consequently have a large negative impact on the aircraft's performance, however, they would meet the required heat load. Therefore, unlike the surface cooling assessment from Section 3.3, the assessment of the R-HEX-TMS begins with the second priority of the objectives section, i.e., minimizing the negative impact of the TMS on the aircraft.

3.4.1 Setup, procedure, and assumptions

The TMS sketched in [1] is simplified for this analysis as shown in Figure 3.6. A hot fluid flowing from the electric components enters the hot side of the HEX according to the specifications in Table 3.1. All piping of the hot side is substituted by one pipe component, which has a length set to the estimated sum of the hot side piping length. After the pump, the coolant leaves the system with a new colder temperature and at the same

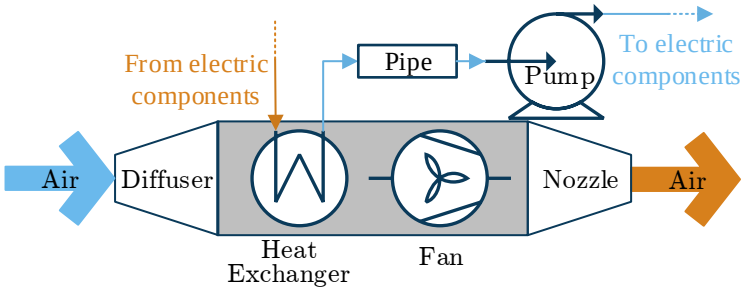

Figure 3.6 Sketch of the simplified ram-air TMS

pressure as at the hot side inlet. Both outlet temperatures in Table 3.1 are below the boiling temperature of water. With its high heat capacity and good thermal conductivity, water is usually the preferred coolant choice for low-quality waste heat. In most applications, a water-glycol mixture is used to protect the cooling system from damage through ice formation in cold conditions. Here, 50% "Zitrec M" - a water–ethylene glycol mixture [76] - is used as hot side fluid.

The study in [1] showed that the performance of the TMS is heavily influenced by the operating conditions. Therefore, it is important even for aircraft conceptual design to provide information on the impact of the TMS for the most critical operating points. Here, ToC is chosen as the design point for the TMS. ToC has operating conditions representative for the entire CR, which is the most relevant segment with regards to drag. Additionally, HDTO is expected to be the most critical off-design point due to its adverse combination of large heat loads and high ambient temperatures. The performance of each design-TMS is also assessed in HDTO. The final result is a multidimensional set of data with some design and some off-design variables that allow a quick choice of an appropriate TMS during the aircraft conceptual design process. Due to the two different outlet temperatures in Table 3.1, the following study is executed once for each temperature, i.e., for the battery and motor TMS, resulting in two sets of results.

For the design of the TMS, the optimization procedure from [1] is applied. In [1] the hot side hydraulic power (P_h) was neglected in the optimization target function since the power required to increase an incompressible fluid's pressure is usually negligible compared to the power required for moving the compressible fluid (air) on the cold side. This leads to the optimization trending towards the lower bound of the hot side pressure ratio (Π_h). The results in [1] showed that no fan (i.e. power) was required for the TMS in the design conditions and the drag could be reduced to almost zero questioning whether P_h should be neglected. Therefore, P_h is added to (3.1):

$$\delta FB = \frac{3\%}{1\,000\,\mathrm{kg}}\,\Delta m + \frac{2.45\%}{376.4\,\mathrm{N}}\,\Delta D\,\left(1 + \frac{P_\mathrm{h}}{\Delta D\,u_\infty}\right) \tag{3.2}$$

The P_h sensitivity is added to the drag-related part of the sensitivity equation. It is normalized by the power required to overcome the drag, i.e., it is assumed that providing hydraulic power (e.g. through a pump) is as costly for the aircraft as providing propulsive power. This assumption is not accurate due to different overall efficiencies between the energy source and the propeller or pump, however, it is sufficient as a first-order approximation. It is not important or possible for the optimization target function to be entirely accurate at this conceptual design stage simply because the aircraft will change throughout the design process. The main purpose of the target function is to provide a balance between those output parameters of the TMS, which negatively impact the aircraft.

The free design variables of the system are listed in Table 3.4 with their respective selected minimum and maximum bounds. The hot side outlet temperature ($T_{2,h}$) is not a free design variable as in [1], but is fixed to a range of values. $T_{2,h}$ is the inlet coolant temperature of the electric components. The details of the electric component's internal cooling system are unknown. Therefore, the results are produced for a range of $T_{2,h}$ to allow a later selection of a TMS with the desired $T_{2,h}$. For each inlet temperature level ($T_{1,h}$) the total heat load range was split into two equal parts, i.e., two symmetric TMSs were designed for redundancy reasons. The

Table 3.4 Free variables of the ram-air TMS design study

Parameter	Symbol	Unit	Bounds
Diffuser pre-entry area ratio	$(A_0/A_1)_{diff}$	–	0.5 – 1.0
Ratio of heat capacities C_c / C_h	C_R	–	0.5 – 1.0
Hot side hydraulic diameter	$d_{H,h}$	mm	0.1 – 5.0
Cold side hydraulic diameter	$d_{H,c}$	mm	1.0 – 100
Hot side pressure ratio	Π_h	–	0.5 – 0.999
Cold side pressure ratio	Π_c	–	0.5 – 0.999

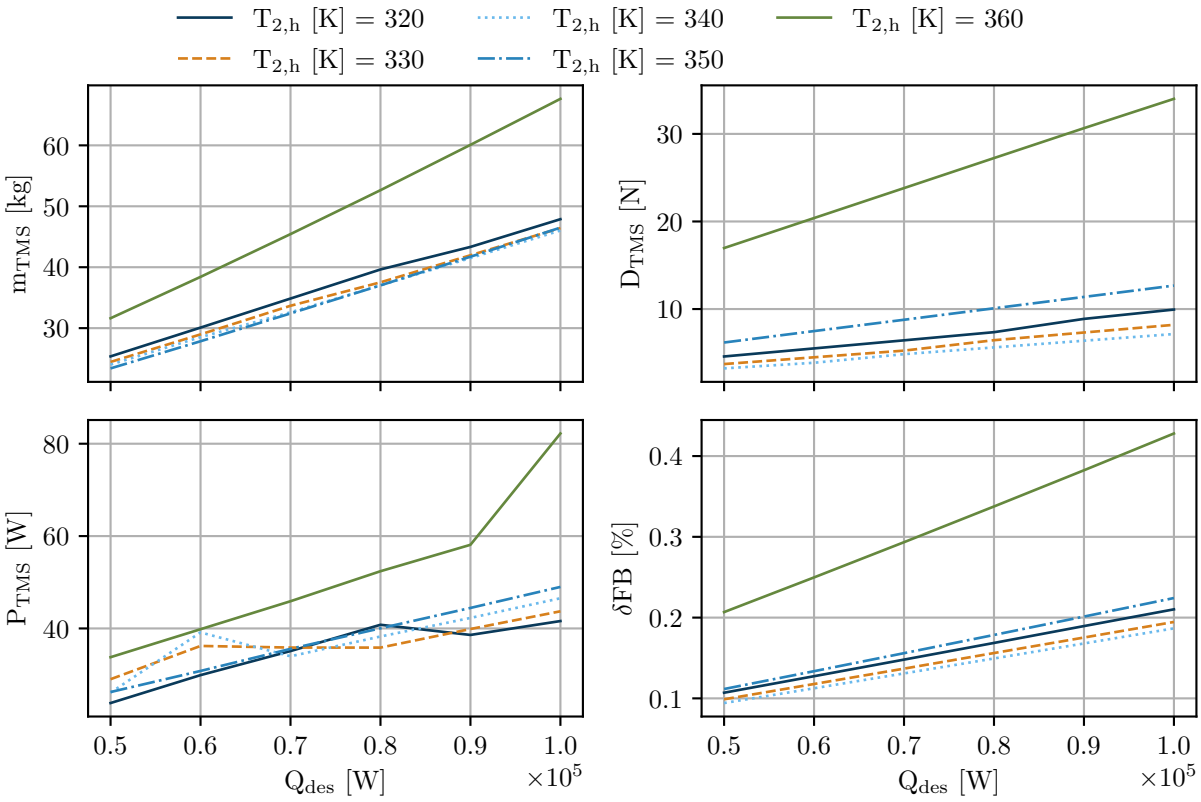

Figure 3.7 Final optimization results for the motor TMS with the most relevant parameters for the aircraft

outlet diffuser aspect ratio was set to equal the inlet aspect ratio of the HEX. For the piping, a total length of 2 m was assumed. All components with analytic mass estimations, i.e. all components except the fan and pump, had aluminum as assumed material with plate thicknesses of 1 mm and the HEX fins were set to 0.1 mm thickness.

For off-design, HDTO was assumed (cf. Table 3.3 TO with ΔT_{ISA}= 30 K). For the off-design assessment, different design systems were used and for each of them, the mass flows on both sides were varied. On the hot side, the mass flow was set relative to the design mass flow (δw_h), and on the cold side it was varied by choosing different pressure ratios for the fan (Π_{fan}). In addition, $T_{1,h}$ was varied from the design value to a temperature 20 K larger than the design value. This accounts for a possible operating scenario where temporarily larger temperatures in TO conditions are accepted.

3.4.2 Design results of the ram-air based thermal management system

The results of the three TMS parameters negatively impacting the aircraft (m_{TMS}, D_{TMS}, P_{TMS}) together with their resulting δFB are displayed in Figure 3.7 for the motor TMS. Figure 3.8 shows the distribution of m_{TMS} on the individual components of the TMS at Q_{DES} = 100 kW. The relative distribution is nearly independent of the heat load.

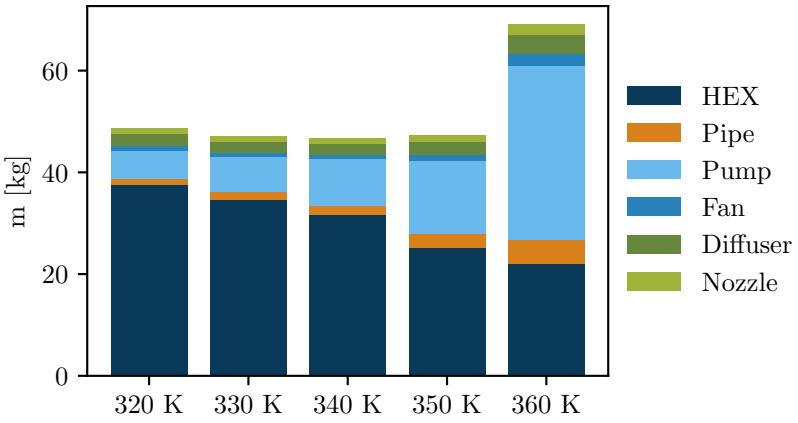

Figure 3.8 Mass distribution for $Q_{\mathrm{DES}} = 100\,\mathrm{kW}$ and different $T_{2,h}$

Table 3.5 Q_{DES} specific values for the motor TMS parameters

$T_{2,h}$ [K]	m/Q [kg kW^{-1}]	D/Q [N kW^{-1}]	P/Q [W kW^{-1}]	$\delta FB/Q$ [% kW^{-1}]
320	0.50	0.092	0.51	0.0021
330	0.47	0.078	0.48	0.0020
340	0.46	0.070	0.48	0.0019
350	0.46	0.126	0.50	0.0022
360	0.65	0.340	0.66	0.0042

All parameters have a proportional relationship to Q_{DES} for each $T_{2,h}$, i.e. m_{TMS}, D_{TMS}, and P_{TMS} scale linearly with Q_{DES} and, therefore, δFB as well. Simple specific values can be obtained for each parameter and are listed in Table 3.5. They were calculated by linear interpolation since, for P_{TMS} especially, but also for D_{TMS} and m_{TMS}, there are slight inconsistencies in the linear trend. The reason is the presence of local minima very close to the global minimum as proven by the fact that there is no visible inconsistency in the results for the target function δFB. The values from Table 3.5 cannot be transferred to other TMSs in other aircraft configurations unless the aircraft flies at the same design conditions and the same assumptions for the TMS are applied.

With regards to δFB, the best $T_{2,h}$ is 340 K. There appears to be an optimal $T_{2,h}$ between 330 K and 350 K. All investigated $T_{2,h}$ except 360 K have similar δFB values. The large offset of 360 K is also visible in the graphs of the three parameters (m_{TMS}, D_{TMS}, P_{TMS}) contributing to δFB. For a better understanding, the six free variables from Table 3.4 are displayed in Figure A.1. One of the reasons for the observed weakness of the sensitivity of δFB towards $T_{2,h}$ is the change in C_R. The three highest $T_{2,h}$ have C_R values at its lower bound of 0.5, whereas for the two lower $T_{2,h}$ values, C_R increases with $T_{2,h}$. This results in almost equal w_{c} values for $T_{2,h}$ values between 320 K and 340 K, which is one of the most influential parameters for D_{TMS}. w_{h} decreases linearly with $T_{2,h}$, but P_{TMS} is similar for the different $T_{2,h}$ values due to the larger Π_{h} values for larger $T_{2,h}$.

The m_{TMS} trend of the system is displayed in detail in Figure 3.8. The HEX mass decreases with $T_{2,h}$ since, with a fixed $T_{1,h}$, the effectiveness of the HEX decreases. The HEX mass decreases since the mean temperature difference between the hot and cold sides is larger. An increase in $T_{2,h}$ also results in an increase of w_{h} and, with fixed C_R, also w_{c}. Therefore, the mass of all piping, ducting, and the fluid moving parts pump and fan increases. Especially the pump weight dominates the overall system mass at larger $T_{2,h}$. A careful evaluation of future pumps optimized for the aircraft industry could probably decrease the pump weight, which is based on an empirical correlation of currently existing pumps (cf. (1.5)).

Despite the main properties mass, drag, and power, the dimensions of the system are also relevant for the aircraft since the TMS has to be integrated inside the existing structure if possible. The three dimensions of the HEX (L_{h}, L_{c}, $\mathrm{H}_{\mathrm{HEX}}$), its frontal area on the cold side ($A_{frontal,c}$) as well as diffuser and nozzle length are shown in Figure A.2. The overall cold side length consists of L_{diff}, L_{c}, and L_{nozz}. It is mainly influenced by

Table 3.6 Q_{DES} specific values for the battery TMS parameters

$T_{2,h}$ [K]	m/Q [kg kW^{-1}]	D/Q [N kW^{-1}]	P/Q [W kW^{-1}]	$\delta FB/Q$ [% kW^{-1}]
290	0.80	0.31	0.76	0.0044
300	0.73	0.26	0.77	0.0040
310	0.73	0.25	0.85	0.0038
320	1.01	0.52	1.03	0.0065

$T_{2,h}$ since L_{c} increases with the hot side exit temperature and the resulting increase in HEX effectiveness. In this study, no constraints on the ratio of the HEX dimensions were invoked contrary to [1] and [4]. The ratios of L_{h} and $\mathrm{H_{HEX}}$ seem acceptable. The ratio of $\mathrm{H_{HEX}}$ to L_{h} is large especially for high Q_{DES} and $T_{2,h}$ values. However, when building a HEX, the stack can be compartmentalized into multiple stacks and rearranged for example in the hot side direction, thereby, adjusting the $\mathrm{H_{HEX}}$ to L_{h} ratio. This rearrangement does not result in any changes to the thermodynamic properties of the HEX. Therefore, no attempt is made in this conceptual study to change the dimensions of the HEX.

Combined, the results for the motor TMS indicate that if possible a $T_{2,h}$ between 320 K and 340 K should be selected. With a $T_{1,h}$ of 370 K a 30 K temperature rise over the electric component would be required for 340 K. At this stage, the possible temperature increase over the electric component is unknown and can only be determined after the details of the internal cooling systems of the electric components are established. The values in Table 3.5 cover a broad range of $T_{2,h}$ and thus allow a proper selection of a TMS in the later aircraft design process. Also, the indicated trends can be considered in the detailed design of the electric component's internal cooling architecture, e.g., if a temperature increase of 10 K was found as the optimal choice for the electric component, the large consequence for the TMS could be considered to find a balance between the requirements of the electric component and the TMS. The results can be extrapolated to higher or lower Q_{DES} if required due to their linear behavior.

The same design process was repeated for the battery TMS with a lower $T_{1,h} = 328$ K. The main results are displayed in Figure 3.9 with similar trends as the motor-TMS (cf. Figure 3.7) and specific values for the main parameters are calculated in Table 3.6. Again, the P_{TMS} graph shows small kinks, which do not reflect in the results of the target function (δFB). Figure A.3 visualizes the values of all free variables of the optimization study. They are independent of Q_{DES}, however, the origin of the kinks is found in Π_{h} and $d_{H,h}$. There are local minima in the δFB function close to the global optimum. Options to prove this hypothesis are the use of a global optimization algorithm or an elaborate selection of more suitable starting values. Since the effect on the aircraft is negligible in δFB, the problem is not further investigated. Figure A.4 completes the design analysis of the battery TMS with the overall TMS dimensions.

Comparing Tables 3.5 and 3.6 reveals the importance of considering the different temperature levels. The best specific δFB value of the battery TMS is about double the value of the motor TMS (0.003 8 % kW^{-1} versus 0.001 9 % kW^{-1}). When comparing the three specific parameters (mass, drag, and power) contributing to δFB, the specific mass and power only increase by about 60%, but the drag increases by about 250%. The reduced $T_{1,h}$ and $T_{2,h}$ of the battery TMS compared to the motor TMS result in an overall smaller temperature difference between the hot and cold sides ($T_{1,c}$ is equal for both systems since the same flight conditions are present). Therefore, a larger airflow is required per Q resulting in significantly increased drag. Also, the lower hot side temperatures lead to lower outlet temperatures on the air side and, thus, a smaller Meredith effect.

Overall, the complex task of designing an optimized TMS for an aircraft application has been performed and the results were simplified to a set of top-level parameters that can be implemented in the aircraft design process at a very little computational cost. Since the TMS has to operate in all conditions, off-design performance is evaluated in the next Section.

3.4.3 Hot-day take-off performance of the ram-air based thermal management system

With two degrees of freedom in design (Q_{DES}, $T_{2,h}$) and three degrees of freedom in off-design (δw_{h}, Π_{fan}, $T_{1,h}$), the off-design results of each parameter (Q, D, P, $\delta FB)_{od}$ are five dimensional arrays. Per the objective

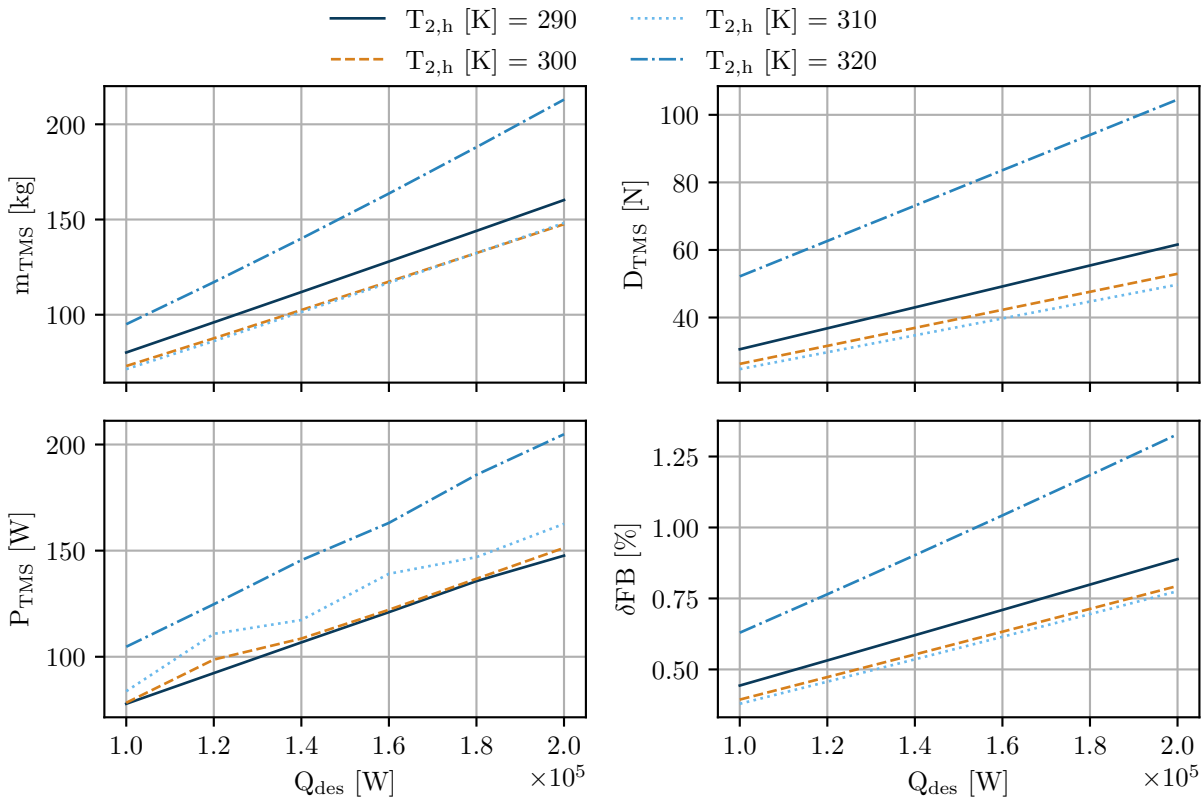

Figure 3.9 Final optimization results for the battery TMS with the most relevant parameters for the aircraft

section, the most relevant parameter is the heat load in off-design followed by drag and power. Therefore, first, the resulting Q_{OD} is analyzed. For general correlations, which are more useful in aircraft conceptual design, the absolute values are not as interesting as the relative value compared to the design value. Therefore, a ratio is defined as:

$$Q_{\mathrm{R}} = \frac{Q_{\mathrm{OD}}}{Q_{\mathrm{DES}}} \tag{3.3}$$

For any aircraft conceptual design, the five-dimensional data at hand is already sufficient. Regardless of the number of dimensions, interpolation over the regular grid is fast enough to be implemented in a design loop. For a better understanding of the data, this analysis visualizes and discusses the data. Since visualization of five-dimensional data is complicated, a piece-wise analysis is conducted. Figures A.5 and A.6 show that Q_{R} is nearly independent of Q_{DES} and only slightly dependent on $T_{2,h,des}$. Therefore, the off-design results are visualized in Figure 3.10 at one design point with $Q_{\mathrm{DES}} = 100\,\mathrm{kW}$ and $T_{2,h,des} = 330\,\mathrm{K}$.

As expected, Q_{R} increases with δw_{h}, Π_{fan} and $T_{1,h,od}$. The correlation is linear with $T_{1,h,od}$, due to the resulting increase in temperature difference between the hot and cold sides. The correlations of Π_{fan} and δw_{h} with Q_{R} are more complicated and interdependent. Π_{fan} and δw_{h} control the mass flows on both sides of the HEX and therefore influence C_R, which is a key parameter for the HEX effectiveness. Near the minimum δw_{h} value, an increase of Π_{fan} results in only a slight increase in Q_{R} since C_{c} is much larger than C_{h}. On the other side, increasing δw_{h} towards its maximum values has only a small effect on Q_{R} for $\Pi_{\mathrm{fan}} = 1.0$, but a more substantial one for $\Pi_{\mathrm{fan}} = 1.05$ since C_{R} is smaller. The inconsistencies which are visible in each line of the Q_{R} graphs are located near $C_R = 1.0$. They result from an inaccuracy in the model: C_R is calculated using heat capacities with mean fluid properties, while Q_{max} is calculated from the actual possible enthalpy difference. C_R in combination with the NTU results in the HEX effectiveness. Q is calculated from the effectiveness and Q_{max}. The enthalpy-based method is more accurate, but cannot be used for the C_R calculation. The inconsistencies are accepted since their overall effect on the results is small. Within the chosen parameter range, it is possible

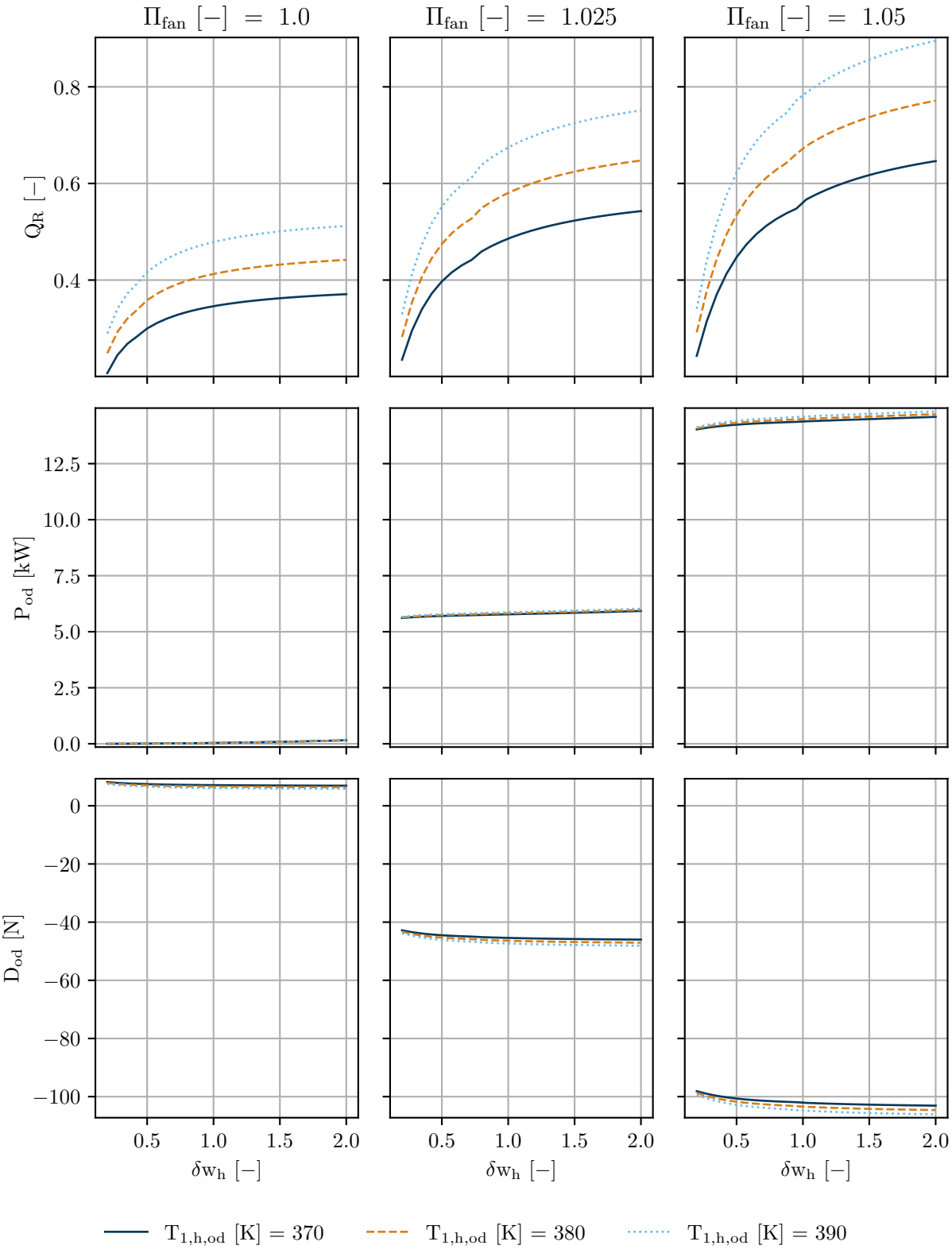

Figure 3.10 Motor TMS off-design results in HDTO for Q_{DES} = 100 kW and $T_{2,h,des}$ = 330 K

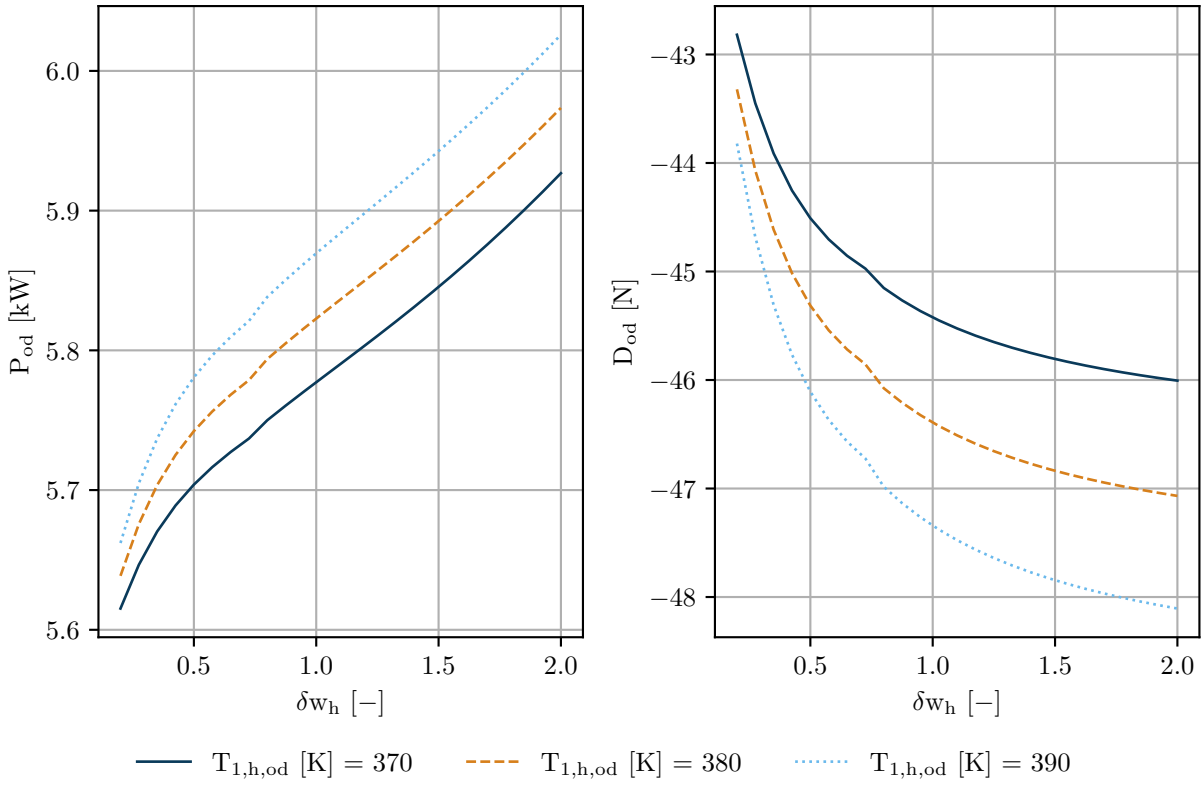

Figure 3.11 Motor TMS P_{OD} and D_{OD} in HDTO for Q_{DES} = 100 kW, $T_{2,h,des}$ = 330 K, Π_{fan} = 1.025

to reach Q_R values of nearly 0.9, i.e., Q_{HDTO} is 90% of Q_{DES}, despite the less favorable operating conditions in HDTO. When not allowing an increase of $T_{1,h}$ beyond the design value, the maximum Q_R value is about 0.65.

P_{OD} and D_{OD} mainly depend on Π_{fan}. Increasing Π_{fan} changes P_{OD} by two orders of magnitude compared to the design case without a fan. This power is not lost, but a significant amount of thrust (negative drag values) is produced. It is therefore hard to quantify the negative impact of an increased P_{OD}. A fan is most likely not as efficient in generating thrust as the main propulsion device, however, the thrust resulting from it allows the main propulsors to consume less power. To display the effect of δw_{OD} on P_{OD} and D_{OD}, Figure 3.11 provides a zoom of Figure 3.10 for a fixed Π_{fan} = 1.025. Increasing δw_h results in increased pump power. Additionally, increasing δw_h leads to an increased $T_{2,c}$ and thus more power required by the fan to produce the given Π_{fan}. The same effect explains why larger $T_{1,h,od}$ values require slightly more power. The entire range of δw_h has P_{OD} values within a 0.4 kW range whereas the increase of Π_{fan} from 1.0 to 1.025 resulted in about a 6 kW increase in P_{OD}. D_{OD} mirrors Q_{OD} due to the Meredith effect. An increased heat transfer recovers some of the lost momenta over the HEX for the airflow and results in less drag, i.e., more thrust. In the mass calculations, currently, no electric motor to drive the fan is considered but only the fan itself. In a more detailed analysis, a motor with appropriate maximum power should be added to the weight balance. However, in that future analysis, the mass of the main electric motor could be reduced due to the thrust of the TMS. Again, these trade-offs are probably not of equal magnitude but are neglected in this conceptual study.

Figure 3.12 shows the off-design assessment for the battery TMS. The results are similar to the ones for the motor TMS, but the maximum Q_R values are lower, mainly due to the larger difference between design and off-design temperature difference of the HEX between hot and cold side. Especially if $T_{1,h}$ is limited to the design value, Q_{OD} cannot exceed 20% of Q_{DES} even if w_h is increased to the maximum value. The roughly 50% larger P_{OD} of the selected battery TMS compared to the selected motor TMS is caused by the selected design points. The chosen motor TMS has a lower C_R value and thus smaller w_c values.

With the results at hand, it is possible to quickly evaluate the possible off-design heat load in HDTO. Reverse engineering of the design case is possible. For illustration purposes, a simple example is given: For one propulsion configuration, equal heat loads in design and off-design are expected for the motor at

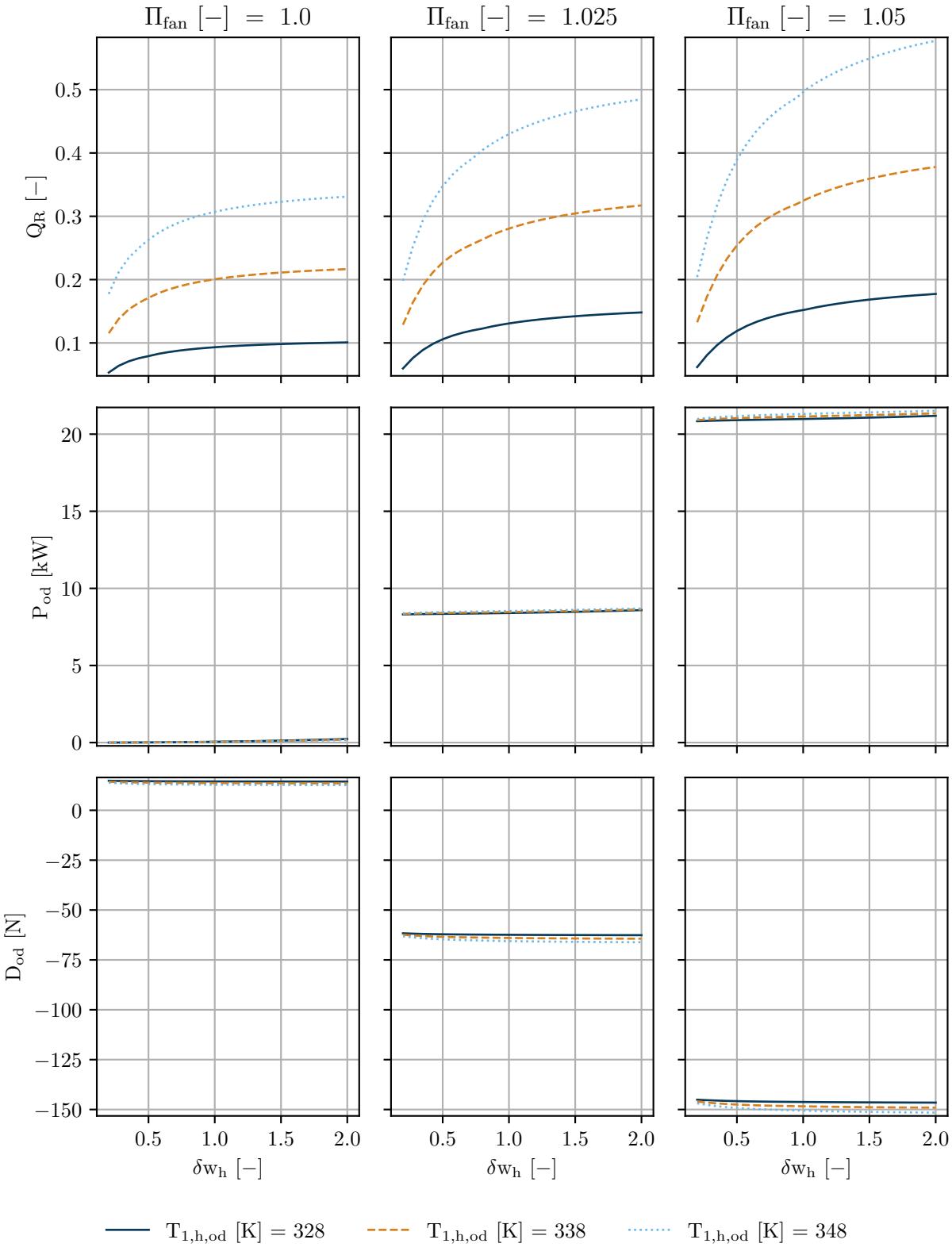

Figure 3.12 Battery TMS off-design results in HDTO for Q_{DES} = 100 kW and $T_{2,h,des}$ = 300 K

$Q_{DES} = Q_{HDTO} = 50\,kW$. Since there are no points in Figure 3.10 with $Q_R = 1$, HDTO is the critical case. For the example, it is assumed that Π_{fan} should not exceed 1.025 , δw_h is limited to 1.5 , and $T_{1,h,od}$ has its maximum allowed value at 380 K. From Figure 3.10, $Q_R = 0.63$ follows and with (3.3) $Q_{DES} = 79.4\,kW$ is calculated. Now, m_{TMS}, D_{TMS} and P_h can be read from Figure 3.7 or Table 3.5 and are available for the aircraft conceptual design. With the data available as a five-dimensional regular grid, the above-described process can be automated within an aircraft conceptual design loop.

3.5 Design and performance of a surface heat exchanger thermal management system

The assessment of the surface cooling potential in Section 3.3 showed that for the given application case, the existing aircraft surfaces offer heat rejection at an order of magnitude larger than required. Therefore, the WISH model from [3] is applied to estimate mass and hydraulic power required by a surface TMS. Since modifications to the WISH model were implemented since the publication of [3], i.e., a more detailed hot side geometry and the addition of a propeller slipstream model (cf. Section 1.4.2), a partial dependence analysis is conducted first to understand the sensitivities of the model.

3.5.1 Partial dependence analysis of the wing integrated surface heat exchanger

The partial dependence analysis is conducted in HDTO conditions and with 50% water-glycol as coolant. The hot side inlet temperature ($T_{1,h}$) was set to 350 K. Four variables are investigated, which were partly not yet considered in the partial dependence analysis in [3], namely the hydraulic diameter (d_H), the hot side mass flow (w_h), the relative slip stream span (δS_{slip}), and the relative unheated chord length at the leading edge (δc_{uh}). The latter is used to control the extension of the WISH in chord direction and, thus, the overall size of the WISH. Spanwise, the WISH extends over the entire wing. In a real application, the shape of the WISH could be altered arbitrarily, but for this academic analysis, only one dimension is varied for simplicity. Span-wise, the WISH is segmented to increase the overall Q while keeping the system complexity (additional feed lines and valves) acceptable. The segments have equal shares of w_h. Similar to the sensitivity analyses in [1–4], one parameter is varied at a time while the others are held constant.

The results are shown in Figure 3.13. In addition to heat, mass, and power, the hot side outlet temperature ($T_{2,h}$) is displayed. It is important to ensure that the fluid returning to the tank or reservoir is sufficiently cold to further be used as a coolant. Decreasing d_H increases Q. The relationship is slightly stronger than linear. Two α_h-increasing effects occur: decreasing d_H directly results in an increased α_h, which leads to decreased $T_{2,h}$. Also, the hot side flow-velocity increases, since, with constant channel aspect ratio and overall width (chord), a decrease in d_H results in a decrease in channel height and thus overall flow cross-section area. At smaller d_H, the increase in flow velocity causes P_{TMS} to increase exponentially due to the increased pressure loss. The mass of the WISH decreases with decreasing d_H mainly due to the reduction in fin height.

Increasing w_h directly increases Q_{TMS} with a declining rate towards larger w_h. The main consequence of an increased w_h is an increased flow velocity and thus α_h. Since the wall resistance and α_c remain unchanged, the influence of increasing α_h on the overall α is limited. The observed mass increase is based on the increase in pump mass with increasing w_h. As discussed in Section 3.4, the sensitivity of the empirical pump correlation is questionable and the share of the pump mass would probably decrease for an optimized pump. P_{TMS} increases with w_h due to the increased flow velocity and $T_{2,h}$ increases due to the increased heat capacity of the hot side.

In Figure 3.14, the outer wall (surface) temperature of the WISH ($T_{w,o}$) is shown at selected points of the partial dependence analysis to further illustrate the described effects. $T_{w,o}$ decreases from inlet to outlet of each segment. At equal d_H the average $T_{w,o}$ is larger for larger w_h due to the increased heat capacity and thus slower cooling of the hot side. Towards the wing tip, $T_{w,o}$ at the end of the segment (right side of each segment) is larger than for segments towards the wing root. Due to the wing taper, the flow velocity in the tip segments is higher, resulting in less exposure time. Comparison of the results for different d_H at equal w_h shows a lower average $T_{w,o}$ for larger d_H. The lower α_h of larger d_H increases the overall thermal resistance of the WISH.

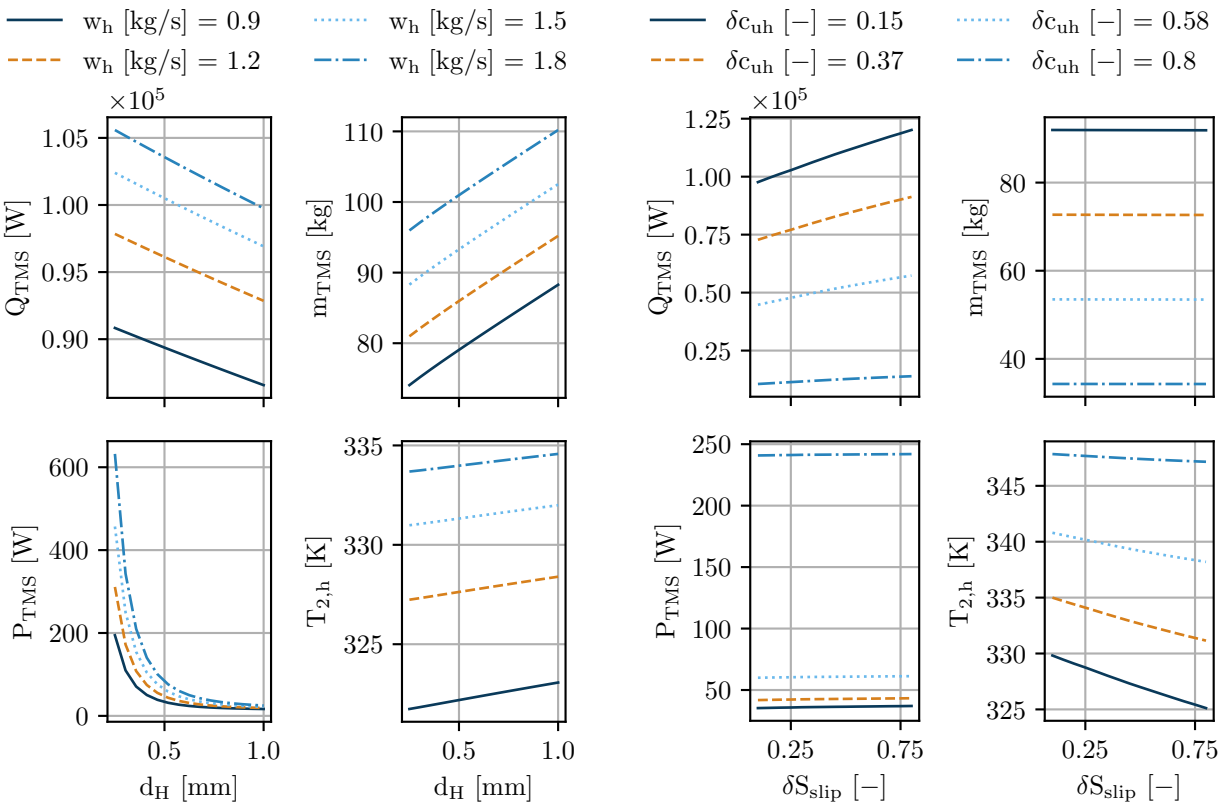

(a) Hydraulic diameter and hot side mass flow

(b) Relative slip stream span and relative unheated chord length

Figure 3.13 Partial dependence analysis of the WISH

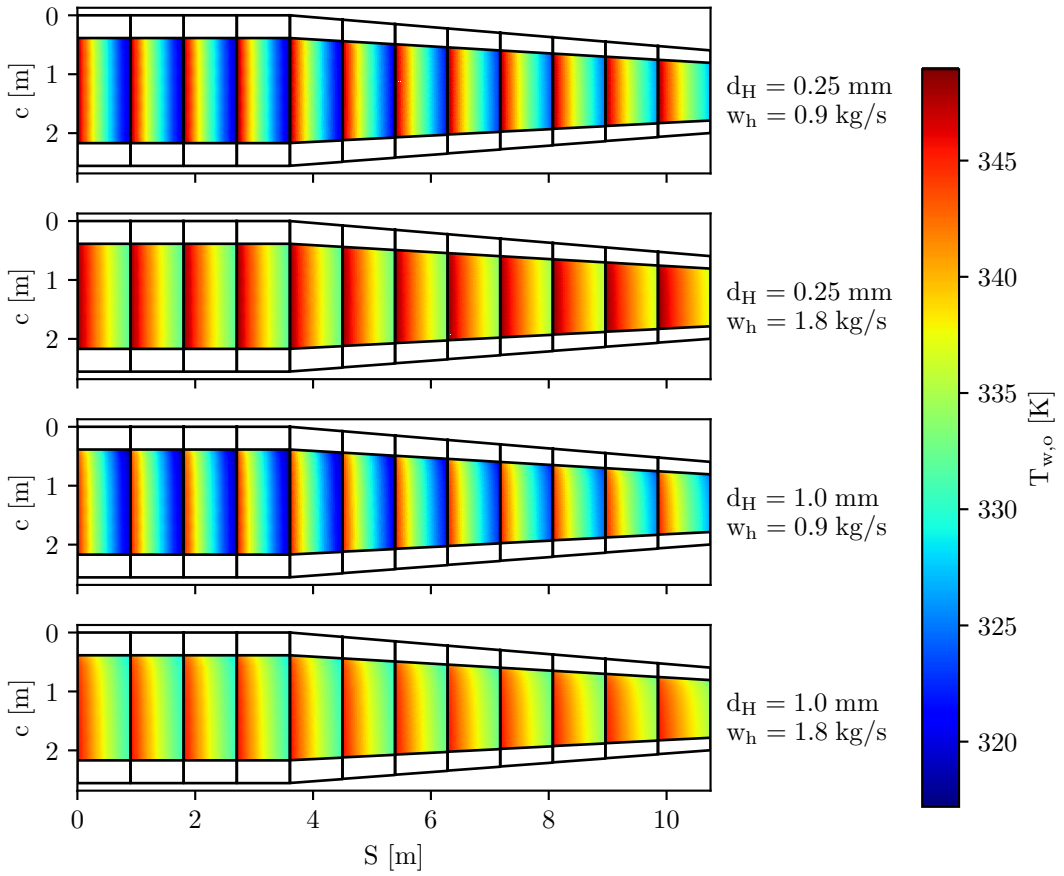

Figure 3.14 Distribution of the outer surface temperature of the WISH

Lastly, an increase of $T_{w,o}$ downstream in airflow direction is visible due to the increasing thickness of the thermal boundary layer on the air side.

The second part of the partial dependency analysis in Figure 3.13b shows that δS_{slip} has no influence on m_{TMS} and P_{TMS} since it is an airside variable. Increasing δS_{slip} results in an increase of Q_{TMS} due to the increased α_{c} in the slipstream. As a direct consequence, $T_{2,h}$ decreases. Varying δc_{uh} alters the overall size of the WISH and thus an increase results in a linear decrease of m_{TMS} and Q_{TMS} (δc_{uh} corresponds to the unheated, i.e., white section of the wing at the leading edge visible in Figure 3.14). The decrease in Q_{TMS} is reflected in $T_{2,h}$ since w_{h} is left constant. To ensure, that the addition of a detailed hot side convection model, has no influence on the sensitivity of the surface HEX on δS_{slip} and F_N, which was investigated earlier (cf. Figure 3.3), the study was repeated with the detailed WISH model. The results are shown in Figure B.1 and resemble the trends in Figure 3.3. The absolute values differ by an order of magnitude in the WISH analysis since only the top surface of one wing is considered rather than the entire aircraft. This also results in the relatively small difference in Q between TX and TO. Figure 3.14 shows the span-wise flow on the hot side. A chord-wise flow from the trailing to the leading edge, i.e., counter flow towards the airflow would be technically possible. Due to the iterative nature of solving the counterflow process, the corresponding model would have a significantly larger complexity level. A further improvement of the heat transfer characteristics can be expected for a counterflow option and the quantification of the effect should be investigated in future work.

Overall, the partial dependence analysis showed that an optimization of the WISH needs a target function combining a maximization of Q_{TMS} and a minimization of the aircraft parasitic effects. d_{H} and w_{h} are free design variables. δS_{slip} and δc_{uh} should be set as pre defined parameter ranges since δS_{slip} depends on the aircraft application and δc_{uh} controls the overall size of the TMS. A parameter range over δc_{uh} serves analogously to varying Q_{DES} in Section 3.4 since Q_{DES} cannot be controlled directly for the WISH model.

Table 3.7 Design space range for the WISH design study

Parameter	Symbol	Unit	Range
Hot side inlet temperature	$T_{1,h}$	K	328, 370
Relative slip stream span	δS_{slip}	–	0.353 – 1.0
Relative unheated chord length at the leading edge	δc_{uh}	–	0.15 – 0.8

3.5.2 Setup, procedure, and assumptions

The design procedure for the WISH is kept as similar as possible to the design procedure of the ram-air-based system in Section 3.4.1. However, some modifications are necessary due to the different characteristics of a surface-based TMS. First, the WISH is assumed to have zero drag. This assumption has been qualitatively discussed in [2], but the quantitative impact of heating the aircraft's surfaces on its drag remains an open question. The optimization target function (3.2) is rewritten without drag and the rejected heat was added to the target function. Contrarily to the R-HEX model, Q is an output variable instead of an input to the WISH model. Therefore, an optimization target function, which balances the priorities of a TMS (cf. Section 1.2) by maximizing the heat transfer rate and minimizing the negative impact on the aircraft, was developed:

$$y = \left(\frac{3\%}{1\,000\,\text{kg}} \Delta m + \frac{2.45\%}{376.4\,\text{N}} \frac{P_{\text{h}}}{u_\infty} \right) \frac{3.33 \times 10^8}{Q_{\text{TMS}}} - \frac{Q_{\text{TMS}}}{10^5} \tag{3.4}$$

The resulting target function (3.4) consists of two terms: the left part represents δFB normalized by Q and a numeric weighting factor and the right part consists of Q including a second numeric weighting factor. The weighting factors were established after some preliminary studies.

For simplicity, the entire design study was conducted on one WISH on the upper surface of one wing. The aircraft has a total of four wing surfaces available (top and bottom for two wings). The results below, therefore, represent only one-fourth of the maximum available Q. For cases with higher required Q, an extension would be possible. There are only two free variables in the optimization study: w_{h} and $d_{H,h}$. They were left unbound. Material and strength assumptions were adapted from Section 3.4.1. An overall piping length equal to the wing span was assumed. The substitute piping model is capable of transporting the entire w_{h}, and therefore provides a reasonable mass estimation. In a more detailed model, the exact inlet and outlet piping lengths of each WISH segment should be considered together with the locations of the heat sources. Three other parameters listed in Table 3.7 were used to span a design range.

$T_{1,h}$ has two values corresponding to the battery and the motor TMS respectively. δc_{uh} is used to control the size and thus maximum Q of the WISH to enable a comparison with the required Q. It is preferable to vary δc_{uh} instead of δc_{flap}, since α_{air} benefits from the increased turbulence downstream. δc_{flap} is kept constant at 0.15. δS_{slip} is set to different values to show the effect of the propeller slipstream, e.g., for an aircraft with fully distributed propulsion. In off-design, HDTO conditions are assumed and w_{h} is varied as in Section 3.4.3.

3.5.3 Design results of the wing integrated surface heat exchanger

The main optimization results of the WISH designed for ToC are displayed in Figure 3.15. δS_{slip} is set to the lowest value from Table 3.7 corresponding to a propeller similar to the ATR42-600. In the high-velocity ToC conditions, the influence of δS_{slip} was expected to be low from Section 3.5.1 and Figure B.1. Figure B.2 shows a negligible influence of δS_{slip} on the optimization results for the battery cooling system. δS_{slip} may still be of interest in the later analysis of the TMS performance in HDTO conditions.

Q decreases with δc_{uh} since the width of the WISH decreases (cf. Figure 3.14: the unheated section at the leading edge increases). Consequently, the main attributes mass and power of the TMS also decrease. The power decrease as well as the decrease in the pipe and pump mass are well explained by the smaller w_{h}. Additionally, the mass of the WISH decreases due to the smaller size. According to Figure 3.13a, the slight increase in d_{H} towards larger δc_{uh} values increases the mass. However, this effect is not visible due to the other previously described mass-decreasing effects. δFB is a direct result of m_{TMS} and P_{TMS} (cf. left part of the target function 3.4).

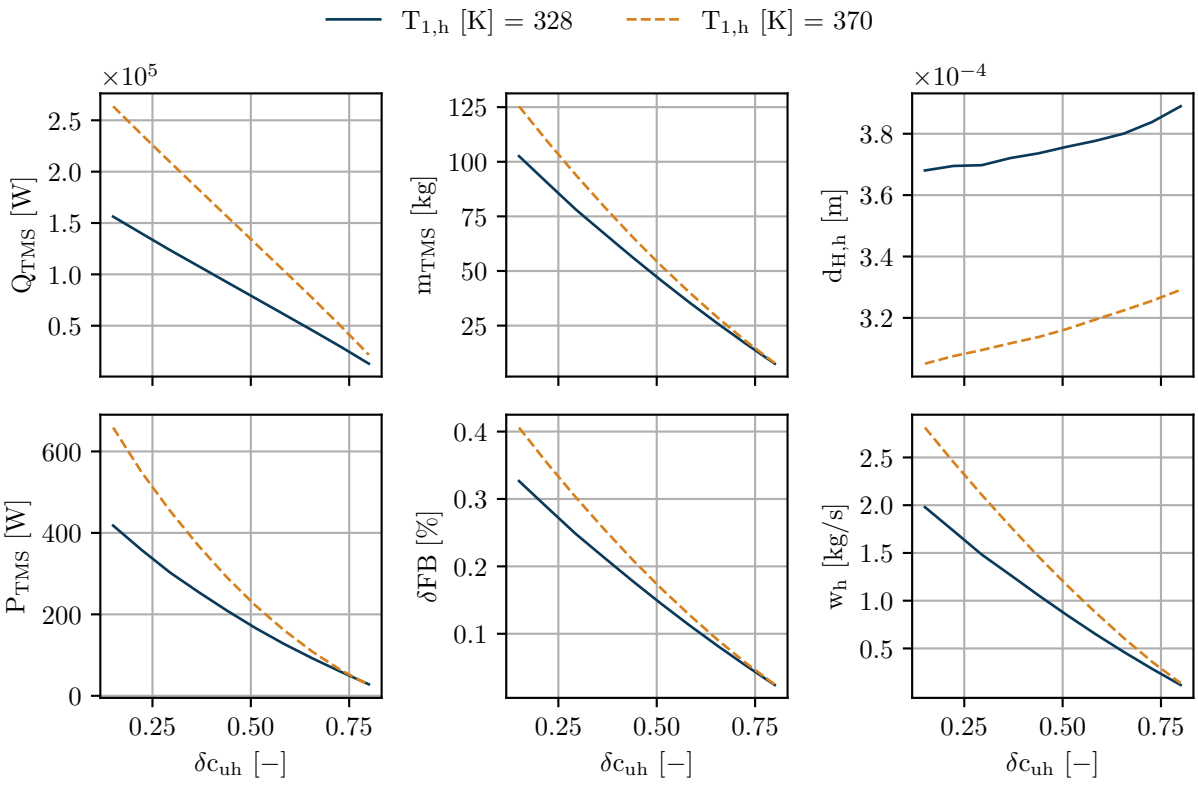

Figure 3.15 Final optimization results of the WISH heat transfer rate, mass, power, and fuel burn for $\delta S_{\text{slip}} = 0.353$

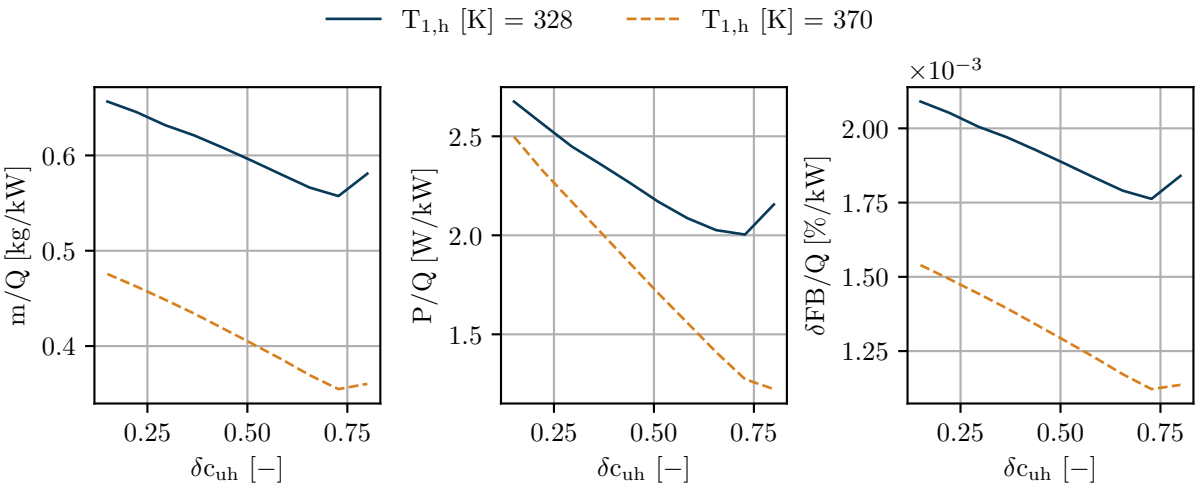

Figure 3.16 WISH final optimization results normalized by the heat transfer rate for $\delta S_{\text{slip}} = 0.353$

The slightly logarithmic decreases in m_{TMS} and P_{TMS} with δc_{uh} are partly explained by the similarly shaped w_{h} curves. Additionally, the maximum δc_{uh} value of 0.8 corresponds to a WISH covering only 5% of the chord length. For smaller chord lengths, the aspect ratio of the overall hot side geometry is lowered and, therefore, the portion of material directly conducting heat to ambient is smaller. Figure 3.16 shows the relevant aircraft level parameters normalized by the heat load. All specific values are decreasing for increasing δc_{uh} up to a value of about 0.7 where the above-described effect causes an increasing trend of Q-specific mass, power, and fuel burn. At δc_{uh} values below 0.7 the shorter flow length on the air side leads to a lower average thermal boundary layer thickness, increasing α_{air} for increasing δc_{uh}. Between battery and motor cooling system, an average Q-specific δFB advantage of $0.000\,5\,\%\,\mathrm{kW}^{-1}$ for the motor cooling system is observed due to the higher temperature difference between hot and cold side.

With a maximum Q of about 250 kW (cf. Figure 3.15), the WISH for the motor TMS would exceed the expected maximum required Q by a factor of 2.5. Therefore, the motors of the aircraft could be cooled with WISHs occupying only fractions of the available chord or span close to the motors' locations. For the battery cooling system, the maximum Q of 150 kW does not match the maximum required Q of 200 kW completely. However, using two WISHs would provide Q above one-third of the required Q. For the entire range in Table 3.1, a TMS consisting of WISHs is feasible for the design conditions (ToC). In an aircraft design process, Figure 3.15 and 3.16 can be utilized to match Q_{TMS} to the required Q and directly read mass, power, and fuel burn caused by the resulting TMS.

3.5.4 Hot-day take-off performance of the wing integrated surface heat exchanger

Similar to Section 3.4.3, the off-design analysis of the WISH leads to a multi-dimensional data structure. Each WISH-TMS (battery and motor) has two design variables (δS_{slip} and δc_{uh}) and two off-design variables (w_{h} and $T_{1,h}$) resulting in a four-dimensional data set. The main output parameters are Q_{R} as defined in (3.3) and P_{R} which is defined analogously to Q_{R} for the required power of the TMS. Since there is no additional fan for the WISH system, the powers in HDTO and ToC are within the same order of magnitude. The final results for battery and motor TMS are displayed in Figure 3.17 and 3.18 respectively. The visualization lacks the fourth dimension since δc_{uh} is set to the lowest value of 0.15. In the appendix, Figures B.3, B.4, and B.5 show the influence of δc_{uh} on Q_{R} and P_{R} for the motor WISH at different δw_{h} values. In general, Q_{R} and P_{R} are more sensitive towards δw_{h} and $T_{1,h}$ than δc_{uh}. There is an observable sensitivity of P_{R} towards δc_{uh} at large δc_{uh} values, which is caused by the relatively high design w_{h} values (cf. Figure 3.15).

The first observation in Figures 3.17 and 3.18 is the very limited available Q of the WISH in HDTO compared to ToC. Without allowing an increased $T_{1,h}$ or w_{h} and for the basic δS_{slip} of 0.353 , the battery WISH provides only 7.5% of Q_{ToC}, while the motor WISH reaches 35%. An increase of δw_{h} to its maximum value only achieves an increase of Q_{R} to 8% for the battery and 37% for the motor WISH, indicating, that α_{air} limits Q. The air side is influenced by δS_{slip}. Both, battery and motor WISH show a slight increase in Q_{R} with δS_{slip}. To understand the full potential of an increased slipstream effect on the WISH, the absolute Q values in HDTO are shown in Figure B.6. At $\delta w_{\mathrm{h}} = 1.0$, an increase of Q_{HDTO} between 7% – 10% can be observed when comparing the maximum to the minimum δS_{slip} value.

On the hot side, allowing an increased $T_{1,h}$, results in large increases in Q_{R}. Especially for the battery WISH (cf. Figure 3.17), the effect is substantial as Q_{R} increases by more than a factor of 3 when increasing $T_{1,h}$ by 20 K. For the motor WISH (cf. Figure 3.18), the same $T_{1,h}$ increase leads to a Q_{R} increase by a factor of 1.5. The effect is larger for the battery WISH since the lower inlet temperatures are close to the ambient temperature and, thus, an increase of the hot side inlet temperature results in a larger relative temperature difference to ambient increase. P_{R} increases exponentially with δw_{h} as expected from the quadratic dependency of internal pressure loss on flow velocity. For the battery WISH, P_{R} is slightly lower for higher $T_{1,h}$ values due to the higher average viscosity of the coolant. The same effect is not observed for the motor WISH since there is a viscosity minimum of the coolant near 380 K. To reduce the required oversizing of the TMS, $T_{1,h}$ should be lower in ToC compared to HDTO.

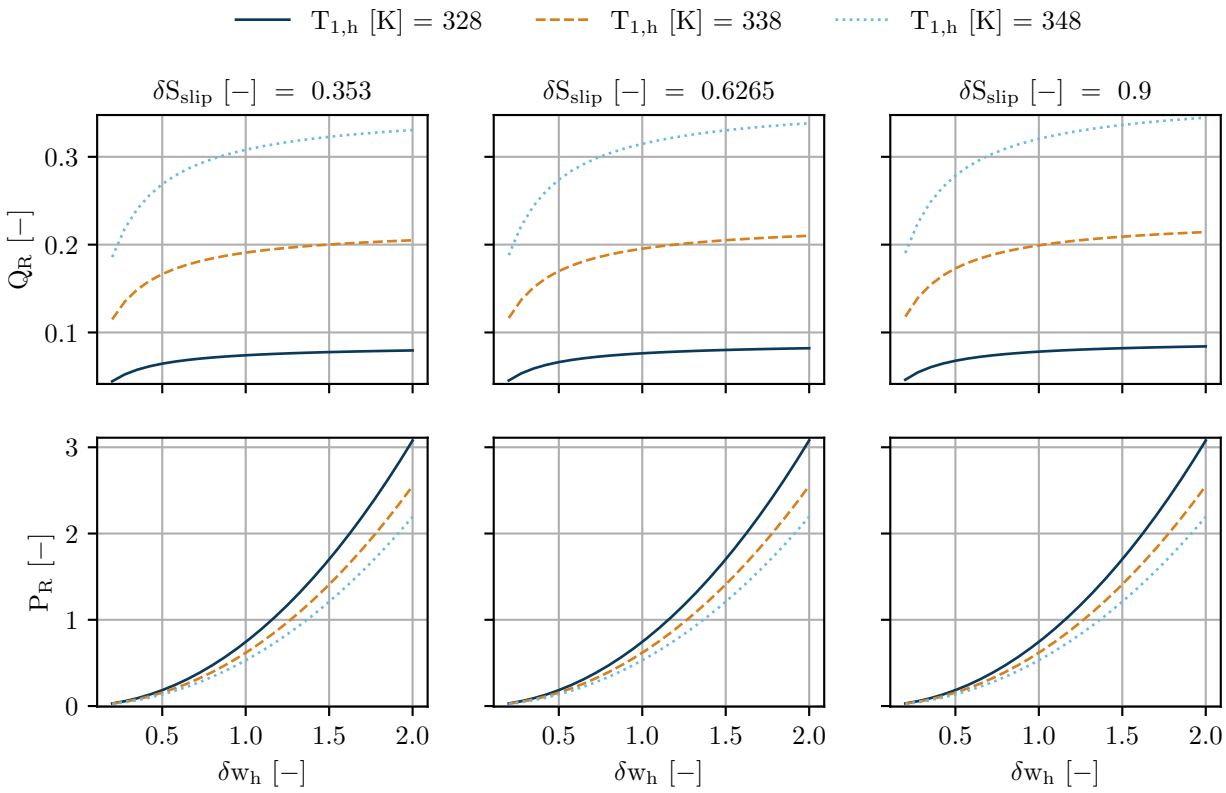

Figure 3.17 Hot day take-off performance of the battery WISH with $\delta c_{uh} = 0.15$

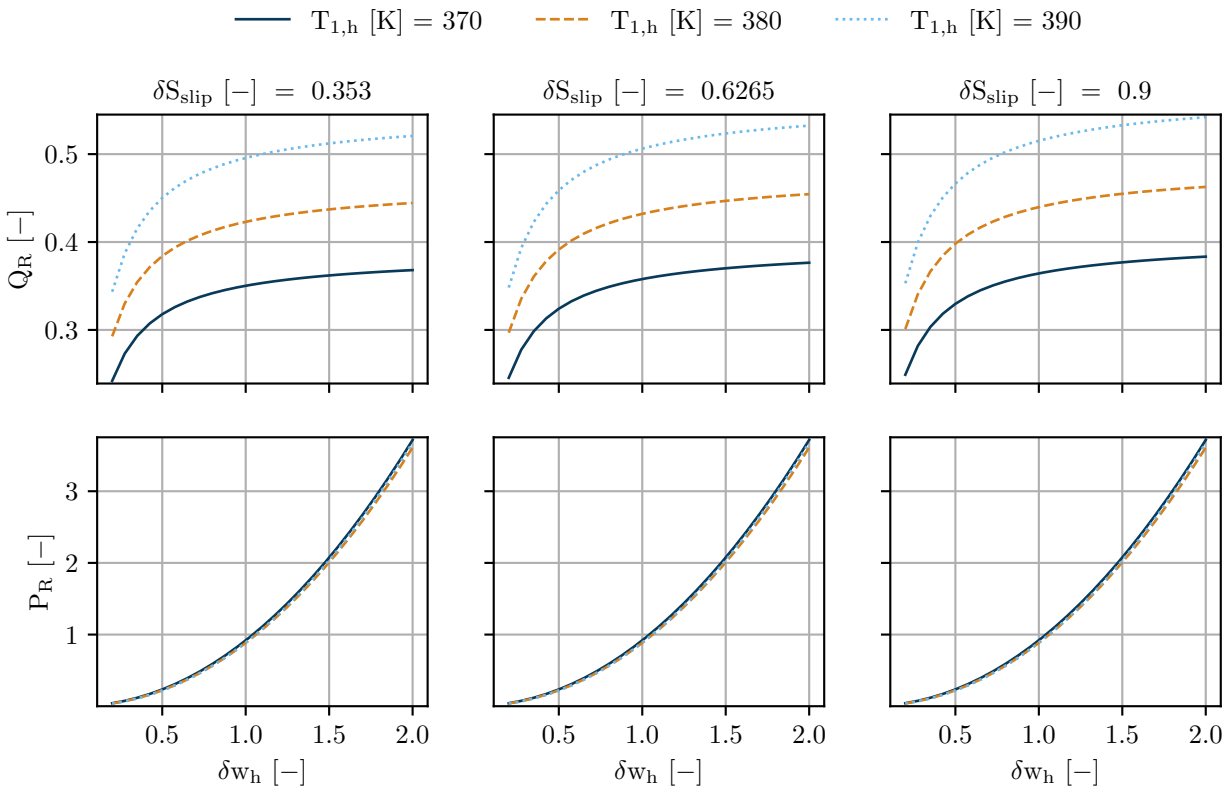

Figure 3.18 Hot day take-off performance of the motor WISH with $\delta c_{uh} = 0.15$

3.6 Comparison of thermal management solutions for the application case

Sections 3.4 and 3.5 provided detailed models of possible TMS solutions for the given application case and the results were discussed individually. This section starts with a general comparative discussion of the results. The second part demonstrates the use of the simplified data that was generated to create different combinations of TMSs for an exemplary propulsion system of the application case.

3.6.1 Comparison of the results for the ram-air heat exchanger with the wing integrated surface heat exchanger

In the analyses in Sections 3.4 and 3.5, a TMS was sized for ToC and the off-design performance in the most critical conditions (HDTO) was assessed. With regards to the priorities in Section 1.2, the available Q is compared before any other parameters are considered. Both systems were capable of providing sufficient Q in design and had Q_{HDTO} values significantly smaller than their respective Q_{ToC}. This discrepancy, expressed in a Q_{R} value smaller than one (cf. Figures 3.10, 3.12, 3.17, 3.18), is generally larger for the battery TMSs than for the motor TMSs due to the very low temperature-difference to ambient resulting from the restricted battery temperature and HDTO conditions. Without an additional fan for the R-HEX ($\Pi_{\mathrm{fan}} = 1.0$), the Q_{R} values are very similar to the WISH for both, battery and motor TMS. However, the addition of a fan enhances the R-HEX substantially, allowing it to reach Q_{R} values, which are about 100% larger than the Q_{R} values of the WISH for the battery TMS and 50% larger for the motor TMS. If a large Q_{R} value is required the R-HEX is advantageous. However, the required Q_{R} depends heavily on the hybridization strategy of the application and the thermal capacity of the propulsion components as well as the TMS. The consideration of the thermal capacity is not part of this explicitly stationary analysis and would have to be considered in a future dynamic simulation.

Since both systems were able to meet the first priority of the objectives their expected impact on the aircraft (priority two) is compared. For the optimization procedure, similar target functions were used even though an adaption was necessary for the WISH. A different weighting of Q and δFB in (3.4) could possibly lead to slightly different results for the WISH. Tables 3.5 and 3.6 indicate minimum $\delta FB/Q$ values of about $0.003\,8\,\%\,\mathrm{kW}^{-1}$ and $0.001\,9\,\%\,\mathrm{kW}^{-1}$ for the battery and motor R-HEX respectively. According to Figure 3.16, the battery WISH can achieve $\delta FB/Q$ values of $0.002\,1\,\%\,\mathrm{kW}^{-1}$ if the maximum chord length is utilized and values as low as $0.001\,8\,\%\,\mathrm{kW}^{-1}$ if only a small fraction of the chord length is used. However, this reduction would also cause a reduced Q. Therefore, for the remainder of this discussion, the lowest δc_{uh} value will be used in Figure 3.16. For the battery TMS, the WISH concept would have 45% less δFB than the R-HEX if they are sized for the same Q_{ToC}. However, it may be necessary to oversize the WISH more due to its smaller Q_{R} in HDTO as illustrated by the example in the next section.

For the motor TMS, the same comparison results in 16% smaller $\delta FB/Q$ values for the WISH compared to the R-HEX unless it is possible to use only a fraction of the chord length for the WISH, which would lead to values as low as $0.001\,2\,\%\,\mathrm{kW}^{-1}$, i.e., 37% less than the R-HEX. The most obvious reason for the advantage of the WISH is the absence of any drag. Comparing the battery TMSs, the WISH has a 11% smaller m/Q value than the R-HEX and a 214% larger P/Q value, but still outperforms the R-HEX with regards to δFB. This advantage decreases with an increase in the hot side temperature, i.e. for the motor TMS, since the R-HEX benefits from the Meredith effect. For the motor TMSs, the WISH has a δFB advantage despite an almost equal specific mass and a 400% higher specific power compared to the R-HEX. In other words, the absence of any drag overcompensates the higher power demand of the WISH resulting from its longer hot side flow lengths.

There are a few qualitative aspects that should be considered for future more detailed work. First, the theoretical benefit of a S-HEX over a R-HEX heavily depends on the utilized air-side flow length. In general, S-HEXs should have small air-side flow lengths to prevent the formation of a thick thermal boundary layer. This analysis only considered a WISH. However, the same Q could be split on multiple smaller S-HEXs distributed over the aircraft, e.g., a battery in the fuselage could use ring-shaped S-HEXs with hot-side inlets close to the battery location. An in-depth analysis of the effect of the resulting interrupted thermal boundary layers would lead to a more detailed solution for Q as well as indicate the influence on the aircraft drag. Such an analysis would require higher fidelity (i.e. CFD) methods, which are beyond the scope of the thesis at hand. Additionally, so far, the mass calculation for the WISH and possibly other S-HEXs was conservative since no

structural integration benefits were considered. A S-HEX could possibly be integrated into the existing aircraft structure and, therefore, have a lower mass than an isolated component.

3.6.2 Thermal management system selection for an exemplary electric powertrain of the application case

The application case introduced in Section 3.2 does not yet have a fully designed propulsion system, but only rough estimates of the resulting heat loads are available. With the results generated in the previous sections, the TMS design can be included in the sizing of the powertrain. This section provides a small example of how to use the available data and quickly assess the TMS of a given application system. For that purpose, an exemplary propulsion system within the range of Table 3.1 is assumed. The assumed values are summarized in Table 3.8. The assumed heat loads are the mean values of the ranges presented in Table 3.1 and equal heat loads in ToC and HDTO conditions are assumed. Furthermore, an increase of 10 K of the coolant temperature as well as a 25% increase in w_h is accepted in HDTO. These arbitrary assumptions are necessary since the final design of the powertrain is not yet available, but they can be quickly adapted to more precise inputs from a detailed electric propulsion system as long as the inputs are within the bounds of the simulated data.

In addition to the assumptions in Table 3.8, the Q_R values for the WISH and R-HEX can be obtained from the respective Figures and are listed in Table 3.9. Since all Q_R values are smaller than one, the different TMS options have to be oversized in ToC to meet the HDTO heat load requirements. Six different scenarios are considered for the motor and the battery TMS. The scenarios are split into two groups: the first group called OD splits the off-design heat load (Q_HDTO) between R-HEX and WISH. Both heat sinks are then sized using their respective Q_R values. The second group called DES splits the design heat load (Q_ToC) between R-HEX and WISH. The total available off-design heat load is then calculated using the Q_R values. The missing off-design heat load is filled with an additional R-HEX. It is assumed that this additional R-HEX can be shut off after TO and its air feeding ducts can be closed so that they do not produce any drag apart from additional induced drag through their mass or consume any power during the majority of the flight. Both groups, DES and OD have three scenarios with 0%, 50%, and 100% Q share for the WISH. The example calculation uses simple steps to utilize the existing data:

1. Calculate Q_ToC from Q_HDTO with the Q_R values in Table 3.9 and (3.3). For the DES scenarios, this step is only required for the additional R-HEX.

2. Calculate mass and power for WISH and R-HEX as well as drag for the R-HEX with the specific values from Tables 3.5 and 3.6, and Figure 3.16 (assuming the minimum δc_uh value). For the DES scenarios, only the portion of the R-HEX Q_ToC is used that is actually required after TO to calculate drag and power as it is assumed that the additional R-HEX can be shut off.

3. Calculate δFB with (3.1).

The final results are shown in Table 3.10. To emphasize the difference between the OD and the DES scenarios, the installed Q (Q_inst) is listed. Additionally, the Q_ToC column in the R-HEX section shows the active R-HEX during ToC. For the WISH section of Table 3.10, Q_inst always equals Q_ToC as no scenario allows a partial shutoff of the WISH.

For the battery TMSs, the comparison of the OD configurations 0%, 50%, and 100% shows a slight δFB advantage for TMSs with larger Q_HDTO shares for the WISH. For the motor TMSs, the trend is the opposite favoring systems with a high share of Q_HDTO for the R-HEX. The result aligns well with the previous comparative discussion in Section 3.6.1. First of all, a higher WISH participation results in an increased overall Q_inst due to the lower Q_R values of the WISH. The better specific mass, power, and drag values of the WISH overcompensate this disadvantage for the battery TMS. For the motor TMS, the Meredith effect helps to reduce the drag of the R-HEX to almost zero, which was previously observed in [1], thereby decreasing the disadvantage of the R-HEX compared to the WISH.

The DES scenarios combine the advantages of both systems. For the DES-100% case, the WISH is sized to be capable of removing all heat in ToC, and the R-HEX with its superior Q_R is used to "boost" the off-design

Table 3.8 Values of the selected exemplary propulsion system

Parameter	Unit	Value
Q_{Bat}	kW	150
Q_{mot}	kW	75
ΔT_{HDTO}	K	10
δw_{HDTO}	–	1.25
$\Pi_{\mathrm{fan,HDTO}}$	–	1.05
δS_{slip}	–	0.353

Table 3.9 Q_{R} values from Figures 3.17, 3.18, 3.10, 3.12 with inputs from Table 3.8

Thermal Management System	Q_{R} [–]
WISH, motor	0.43
WISH, battery	0.20
R-HEX, motor	0.71
R-HEX, battery	0.35

Table 3.10 Results of the different TMS options for the exemplary electric powertrain of the application case

Configuration		WISH			R-HEX					TMS	
Split	%-WISH	Q_{inst} [kW]	m [kg]	P [kW]	Q_{inst} [kW]	m [kg]	Q_{ToC} [kW]	P [kW]	D [N]	Q_{inst} [kW]	δFB [%]
Battery TMS											
OD	0	0	0	0	429	313	429	0.36	107	429	1.65
OD	50	381	250	1.02	214	156	214	0.18	53	595	1.62
OD	100	761	499	2.04	0	0	0	0	0	761	1.59
DES	0	0	0	0	429	313	150	0.13	38	429	1.19
DES	50	75	49	0.20	386	282	75	0.06	19	461	1.13
DES	100	150	98	0.40	344	251	0	0	0	494	1.07
Motor TMS											
OD	0	0	0	0	106	49	106	0.05	7	106	0.20
OD	50	87	41	0.22	53	24	53	0.03	4	140	0.23
OD	100	174	82	0.43	0	0	0	0	0	174	0.27
DES	0	0	0	0	106	49	75	0.04	5	106	0.18
DES	50	38	18	0.09	83	38	38	0.02	3	121	0.19
DES	100	75	36	0.19	60	28	0	0	0	135	0.20

performance of the TMS. This scenario results in a reduction of δFB by 0.58%-points (corresponding to a 35% decrease) for the battery TMS compared to the OD-0% scenario, which can be seen as reference scenario as it presents the simplest TMS solution. The largest part of the benefit is caused by the drag and power reduction of the R-HEX after TO. The DES-0% scenario also exclusively utilizes R-HEXs but allows the shutoff of parts of the R-HEX during the mission. This measure already reduces δFB by 0.46%-points. The replacement of the R-HEXs that are required during the entire mission by WISHs then further improves the TMS. The DES-100% scenario has a slightly more oversized TMS compared to the DES-0% scenario (Q_{inst} of 494 kW compared to 429 kW). This disadvantage is overcompensated by the advantageous specific mass, power, and drag of the WISH.

For the motor, again the ability to shut off parts of the R-HEXs is beneficial as the DES-0% scenario results in a δFB value of 0.18% compared to the 0.20% of the OD-0% scenario. Contrary to the battery TMS, adding a WISH does not improve the DES scenarios for the motor TMS. The additional system mass due to the more oversized TMS outweighs the slight drag and power advantages of the DES 50% and 100% WISH scenarios.

Overall, the results of the example calculation suggest the DES 100% scenario as the best option for the battery TMS. For the motor TMS, a simple TMS comprised of only R-HEXs should be chosen since the addition of a WISH does not further reduce δFB. For the battery and motor TMSs the shutoff of any not required R-HEXs during parts of the mission leads to performance improvements. The results are highly specific to the various assumptions taken before the example calculation. More important than the exact numeric values is the simplicity of achieving aircraft-level results from the prepared design and off-design TMS data. Calculations such as the example above can be implemented in aircraft conceptual design calculations, thereby allowing the consideration of the TMS already at the early stages of the aircraft analysis. The methods developed in this thesis can be used to prepare design and off-design "decks" for arbitrary aircraft and propulsion systems similar to the generation of engine decks, which is common practice in aircraft design.

4 Conclusion

The thesis at hand investigated Thermal Management Systems (TMSs) of future aircraft with a focus on (partly) electrified propulsion systems. The main body of the thesis consists of four papers [1–4]. A modular computer simulation was developed to analyze the impact of TMSs on the overall aircraft level. The component models include analytical and semi-empirical methods to calculate thermodynamic properties such as heat flow rate (Q) as well as the main parasitic effects mass (m), drag (D), and power (P) of a TMS affecting the aircraft. Two main heat sinks were considered: Ram-Air Heat Exchangers (R-HEXs) and Surface Heat Exchangers (S-HEXs). The following conclusion summarizes the findings of the thesis with regard to the initially raised questions in the objectives Section 1.2.

For all system models, the mass, drag, and power, thus the most influential parameters of the TMS on overall aircraft level were quantified. In all cases, it was impossible to optimize the TMS without a multi-variable target function since for some variables, the TMS showed opposing trends in the resulting mass, drag, and power. One example is the cold side pressure loss in the R-HEX: the reduction of the pressure loss reduced the drag of the TMS but increased its mass. With optimization functions derived from selected application cases, it was possible to design TMSs with a good balance between all parasitic effects. For most investigated application cases, including the final comparative case in this thesis, the estimated fuel burn increase by the TMS was below 2%. However, this result is specific to the assessed cases with their respective propulsion systems. For the application case in [4] with an all-electric design mission, no fuel burn increase could be calculated but the estimated Maximum Take-off Mass (MTOM) increase of up to 16% indicates a comparatively larger impact of the TMS. Furthermore, it was not only possible to assess the TMS impact in a detailed study after the conceptual design of the aircraft, but instead, larger data maps were generated that could be used in an aircraft conceptual design loop. The procedure is similar to the well-known implementation of substitute models for aircraft engines in the aircraft design loop. It allows consideration of the TMS at an early stage of the aircraft conceptual design process and, therefore, adds precision to the assessment of (hybrid) electric configurations. Since the TMS only adds parasitic effects to the aircraft an earlier recognition of infeasible or insufficient configurations is possible.

Large sensitivity studies were conducted for the different system models to understand the influence of varying internal and external input parameters for the optimization of a TMS. With regards to the parasitic effects on aircraft level, the most influential parameters are Q and the temperature difference (ΔT) between the hot and cold side ($\Delta T = T_h - T_c$). For all detailed system models (R-HEX [1], Thermoelectric Module (TEM) [4] and Wing Integrated Surface Heat Exchanger (WISH) / Wing Integrated Fuel Heat Exchanger (WIFHE) [3]), the system mass scaled linearly with Q. There are some scaling effects that were not yet considered, e.g., the modeling of component accessories. Taking these scaling effects into consideration would weaken the linear trend. ΔT showed complex interactions with all aspects of the TMS. Generally, a larger ΔT value reduced all parameters negatively impacting the aircraft. The trend is more complicated than the linear behavior of Q. Towards smaller ΔT, mass and drag increased exponentially and for very small or negative ΔT values, some systems could not meet the Q requirements, and other more complex technologies such as TEMs had to be implemented. Each individual model had stronger and weaker sensitivities towards selected parameters. The R-HEX was very sensitive towards the Heat Exchanger (HEX) surface geometries, i.e., the hydraulic diameters, and the pressure losses on both sides. The WISH depended heavily on the ambient conditions since it did not have measures to increase the heat transfer coefficient on the outside. The TEM required power in a different order of magnitude compared to R-HEX and WISH. It was very sensitive to the required temperature increase from cold to hot side and the applied electric currents.

Since all papers [1–4] used different application cases, a direct comparison of the heat sinks was only possible in a final additional study. Since no discrete design of the propulsion system was available, TMSs for a range of possible heat loads were designed in Top of Climb (ToC) and the performance was assessed in the most critical off-design conditions Hot-Day Take-Off (HDTO). Two different systems were investigated: one for the

cooling of the battery and another one for the cooling of the motors and the Power Management and Distribution System (PMAD) due to their different temperature requirements. The above-described process of designing TMS substitute models for design and off-design conditions was applied and their use was illustrated with the arbitrary choice of the design and off-design heat loads. For the battery, 150 kW heat was assumed for ToC and HDTO, and for the motors including the PMAD, the heat load was set to 75 kW. Both values were located in the middle of the assumed Q ranges. Due to the difference in operating conditions, the TMSs had to be oversized in ToC to meet the heat load requirements in HDTO. Two different strategies were employed: the first split the heat load evenly in HDTO and oversized each heat sink in ToC, while the second split the heat load in ToC and filled the missing HDTO heat load with an additional R-HEX. This additional R-HEX was assumed to be shut off after Take-Off (TO) including the closure of any air-feeding ducts. For the battery TMS using the first strategy, a S-HEX system was preferable to a R-HEX system due to the lack of drag of the S-HEX. The S-HEX system had a relative fuel burn increase (δFB) of 1.59% compared to the 1.65% of the R-HEX. The employment of the second strategy with only R-HEXs lead to a reduction of δFB to 1.19%. A combined system of a S-HEX sized for ToC and a R-HEX supplementing the missing Q in HDTO further reduced the δFB value to 1.07%. For the motor and PMAD TMS, a R-HEX system had lower δFB values compared to the S-HEX system due to the better ratio of off-design to design Q in both strategies. Using the second strategy, i.e., allowing parts of the R-HEX to be shut off, reduced the δFB value from 0.2% to 0.18%.

Overall the thesis provided models and methods for TMS design and performance calculations, which can be used as early as aircraft conceptual design. They are not bound to a specific aircraft concept and can be used for an arbitrary application case with arbitrary heat loads. The results are beneficial for any future aircraft concept with a propulsion system with new or unusual heat loads. Accounting for the TMS at the conceptual design stage already may save valuable resources as unsuitable candidates are identified faster. A more realistic estimation of the benefits of future aircraft can be provided by including the TMS in the assessment.

5 Outlook

After the completion of the thesis, there are several issues, which could be of interest to future research in the field of aircraft TMS. First, the analysis at hand used strictly steady-state methods to allow a fast assessment of different systems. The actual thermal load of an aircraft throughout its mission is dynamic, however. Other research in the field already implemented dynamic models but they could only be used for very specific use cases. In the future, a general assessment of the distribution of heat loads over the aircraft mission and the thermal capacities of the components could help to provide better inputs for the methods presented in the thesis at hand. From a dynamic analysis with lumped capacity models, for example, a distribution between stationary heat load requirements in different operating points could be derived and used for the assessment of the overall TMS via the previously calculated data tables.

Each of the presented component models could be enhanced to increase the precision of the results. Some important examples are the empirical pump model, which seems to predict very large pump masses for increasing fluid flows, or the rough model of a heat pipe in [4]. These models are on a lower level of detail compared to some of the other models since initially they were expected to be less important. Also, the models, which were the focus of the thesis, i.e., R-HEX and WISH could be improved. The R-HEX mass does not yet consider accessories for example and the WISH benefit would be amplified if it could use parts of the existing structure. The latter improvement would require the consideration of multiple disciplines, e.g., the integration of the WISH calculation in a wing structure analysis.

Despite improvements to the developed models, their applications could be widened in future studies. For example, the R-HEX model is capable of implementing parameterized surface geometries on both sides, but in this thesis, only rectangular channels were considered due to their comprehensible nature. Any experimental surface with potentially enhanced heat transfer capabilities could be investigated. Also, the thesis successfully developed a TMS substitute data set for a range of TMSs that could be included in aircraft conceptual design. This range is currently bounded but a future study could introduce a large design space to develop a large TMS database, which could be used by any aircraft concept for a quick preliminary assessment of their TMS.

Fuel fed to the engines was excluded as a potential heat sink in this thesis since the current gas turbines already utilize their full heat sink capacity and there is no indication of a change in future gas turbines. The fuel flowing to the gas turbine is potentially the most attractive heat sink since the liquid-to-liquid heat exchanger does not contribute to the drag and has a low specific mass due to the good heat transfer characteristics of liquid mass flows. The exclusion of the fuel flow as a heat sink was done for kerosene. Recently, hydrogen as a fuel alternative for future aircraft has gained high levels of attention from the research community. It can be utilized either in gas turbines or fuel cells. From a TMS perspective, its heat sink capacity is of interest. Figure 5.1 shows a comparison of the heat sink capacity of a hydrogen fuel flow compared to a kerosene fuel flow with equal chemical energy rates, i.e., aircraft with equal energy consumption was assumed. An arbitrary kerosene fuel flow of $1\,\mathrm{kg\,s^{-1}}$ was chosen and the chemical energy flow rate was calculated with the Lower Heating Value (LHV) ($43.6\,\mathrm{MJ\,kg^{-1}}$ [77]). An equivalent hydrogen fuel flow of $0.36\,\mathrm{kg\,s^{-1}}$ resulted from the LHV of hydrogen ($120\,\mathrm{MJ\,kg^{-1}}$ [76]). For the comparison, it was further assumed, that liquid hydrogen would exit the tank at 20 K and kerosene would be available at 270 K. Figure 5.1 shows the heat flow rate that can be added to the fuel mass flows if they are heated from their respective initial temperatures to a maximum temperature (T_{max}). First of all, at the highest T_{max}, the Q value for hydrogen is about 1.75 MW compared to the 0.25 MW of the kerosene fuel flow, i.e., the total heat capacity of the hydrogen flow is larger by a factor of 7 despite the three times smaller mass flow rate. The two obvious reasons are the larger available temperature increase of the hydrogen flow as well as its larger heat capacity values (e.g. $14\,180\,\mathrm{J\,kg^{-1}\,K^{-1}}$ for hydrogen [76] versus $1\,847\,\mathrm{J\,kg^{-1}\,K^{-1}}$ for kerosene [77] at 270 K). Therefore, the above assumption could be questioned for future hydrogen gas turbines since they are not likely to have significantly higher waste heat loads than gas turbines fed with kerosene. The second difference is the available Q at lower temperatures. The latent heat of evaporation

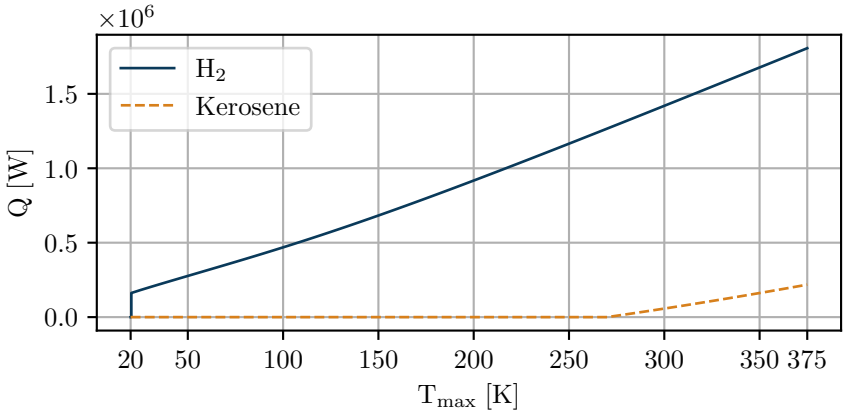

Figure 5.1 Comparison of heat sink capacities of fuel flows with chemical energy flow rates equivalent to the energy flow rate of 1 kg s^{-1} kerosene

of the hydrogen fuel flow in this example provides a Q value similar to the total Q of the kerosene fuel flow. This heat sink capacity is available at the boiling temperature of hydrogen around 20 K and could be utilized for cooling of high-temperature super-conducting electric components. Therefore, the introduction of hydrogen is not only interesting from a TMS perspective due to its larger overall heat capacity but also due to its ability to have superconducting components onboard without heavy cryo-coolers. The potential should be investigated in future studies including detailed models of heat-exchanging components with hydrogen as a heat sink.

Lastly, the thesis did not investigate methods of waste heat recovery due to the low quality of the waste heat. The option to potentially recycle a part of the lost energy should be kept in mind in future investigations of aircraft TMS.

A Additional figures for the ram-air based thermal management system

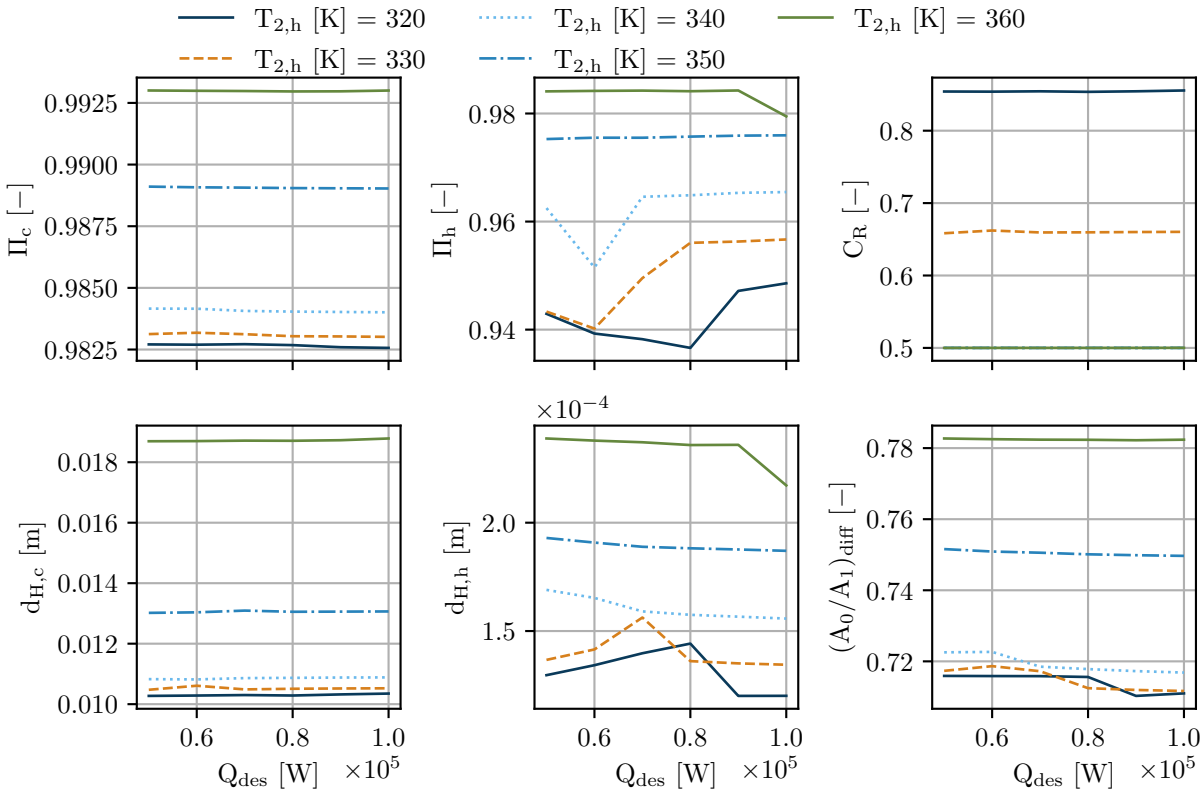

Figure A.1 Free design variables of the motor-TMS design study

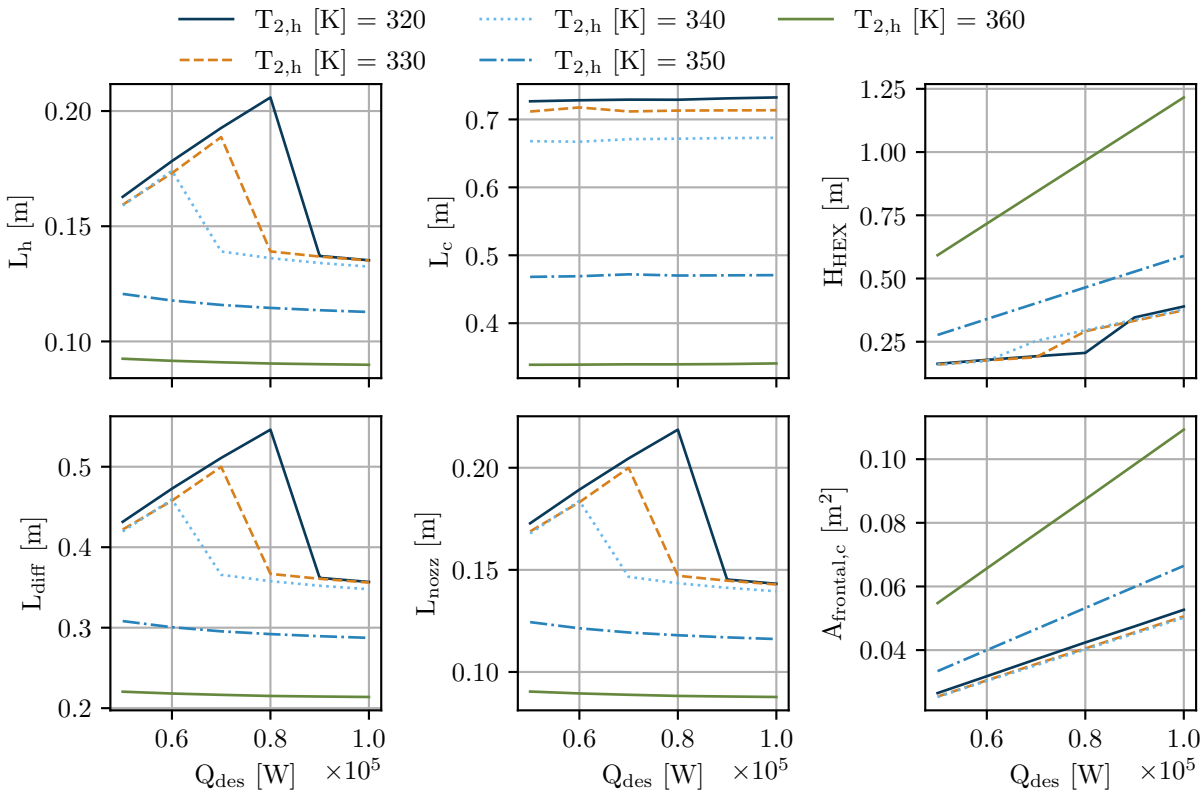

Figure A.2 Dimensions of the motor TMS

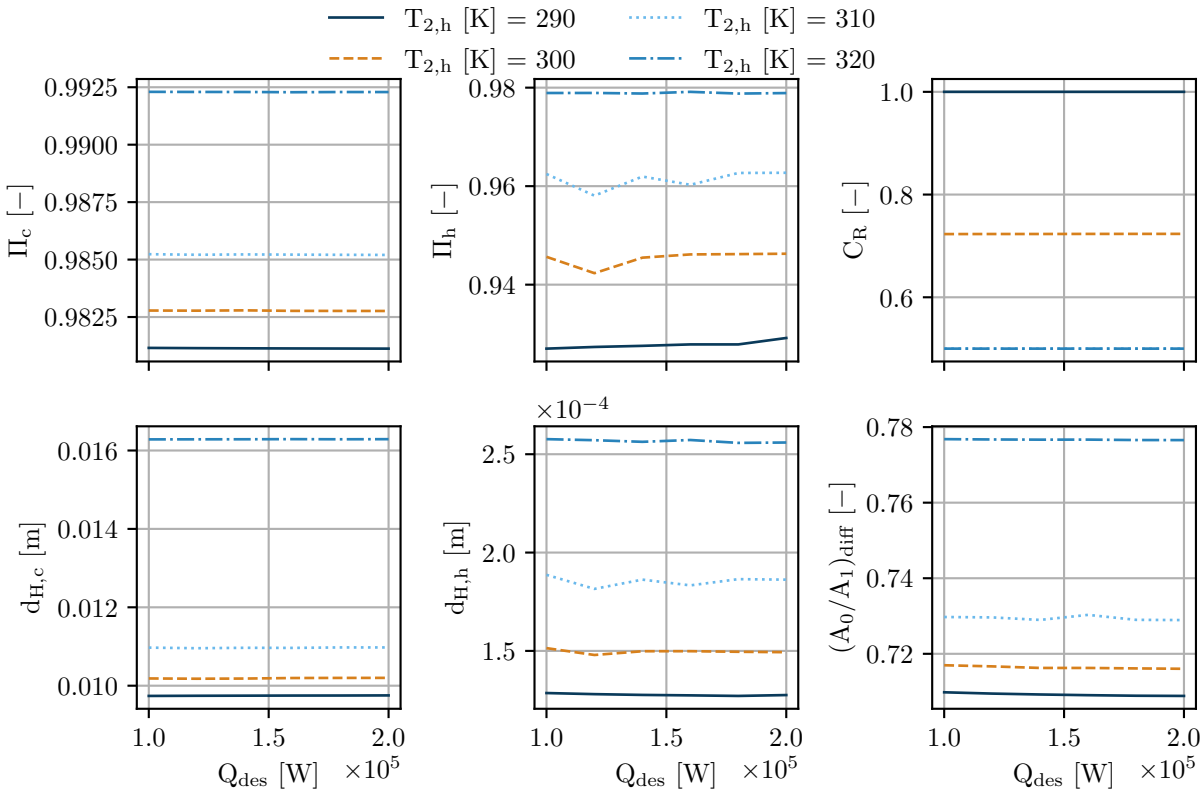

Figure A.3 Free design variables of the battery TMS design study

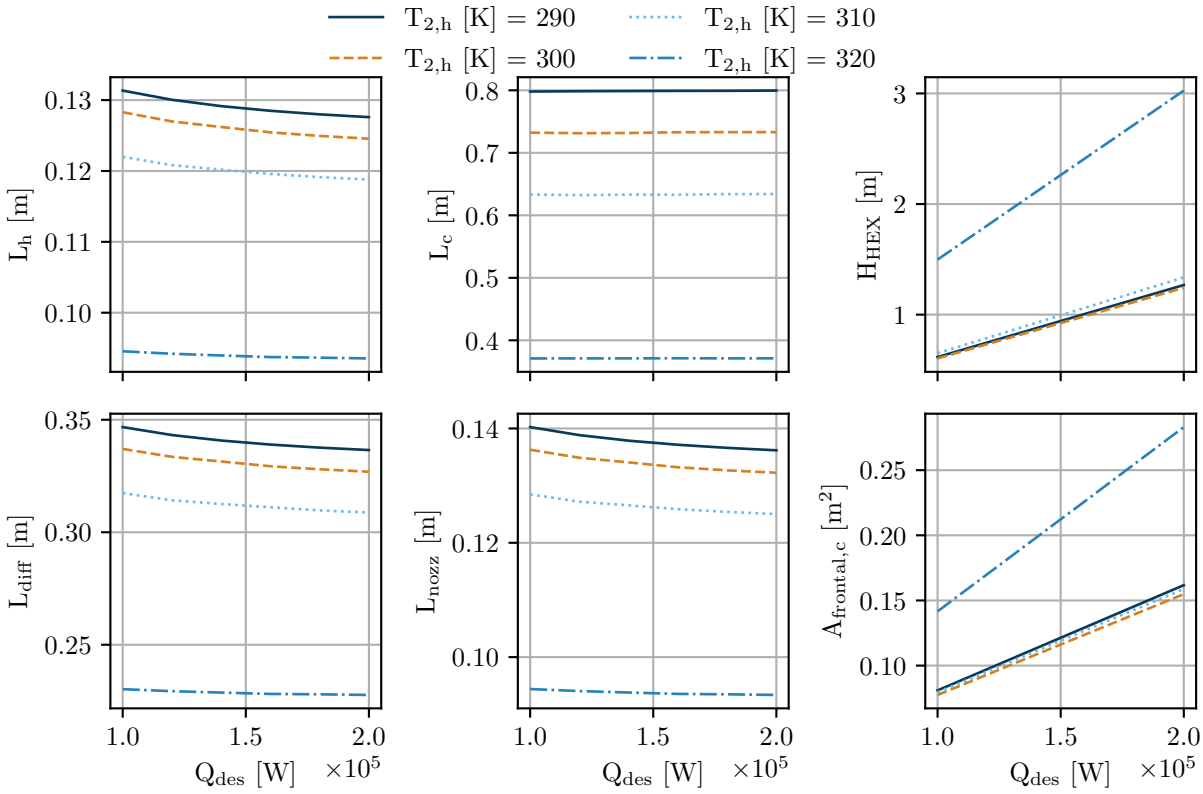

Figure A.4 Dimensions of the battery TMS

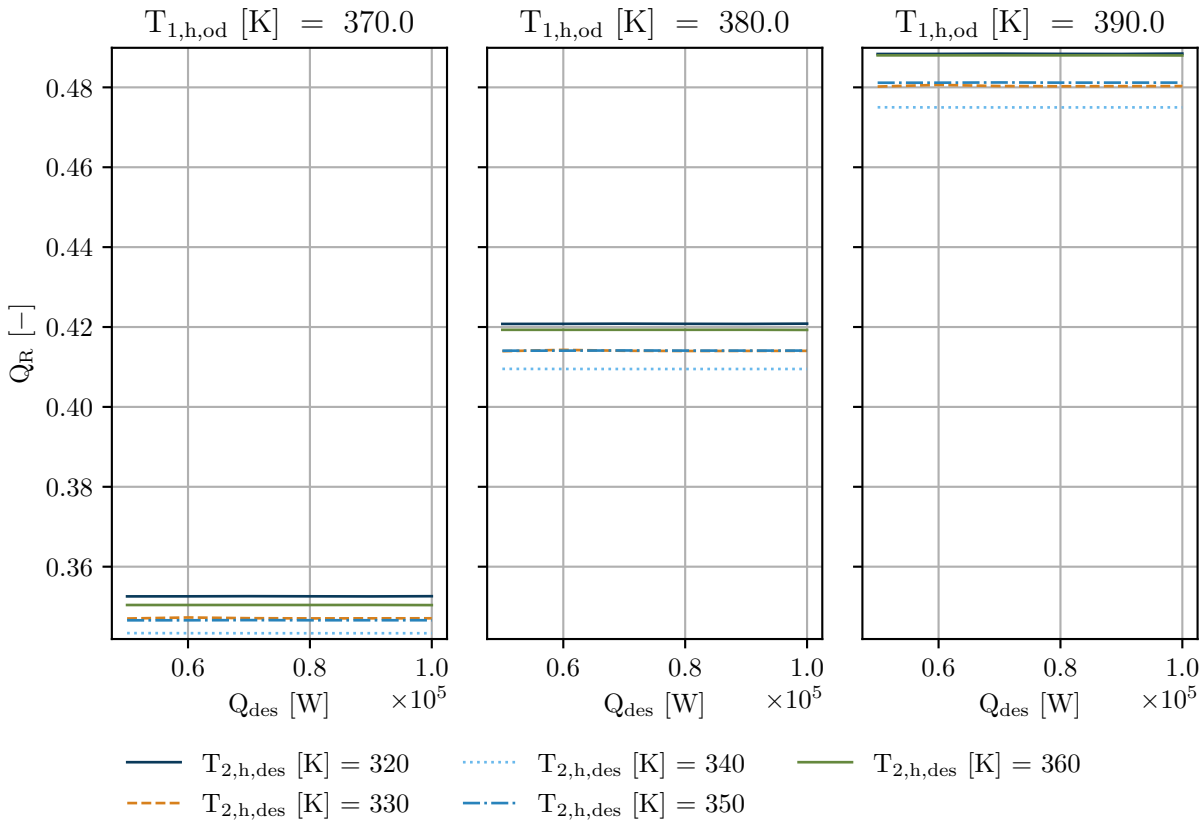

Figure A.5 Off-design performance of the motor TMS with δw_h= 1.025 and Π_{fan}= 1.0

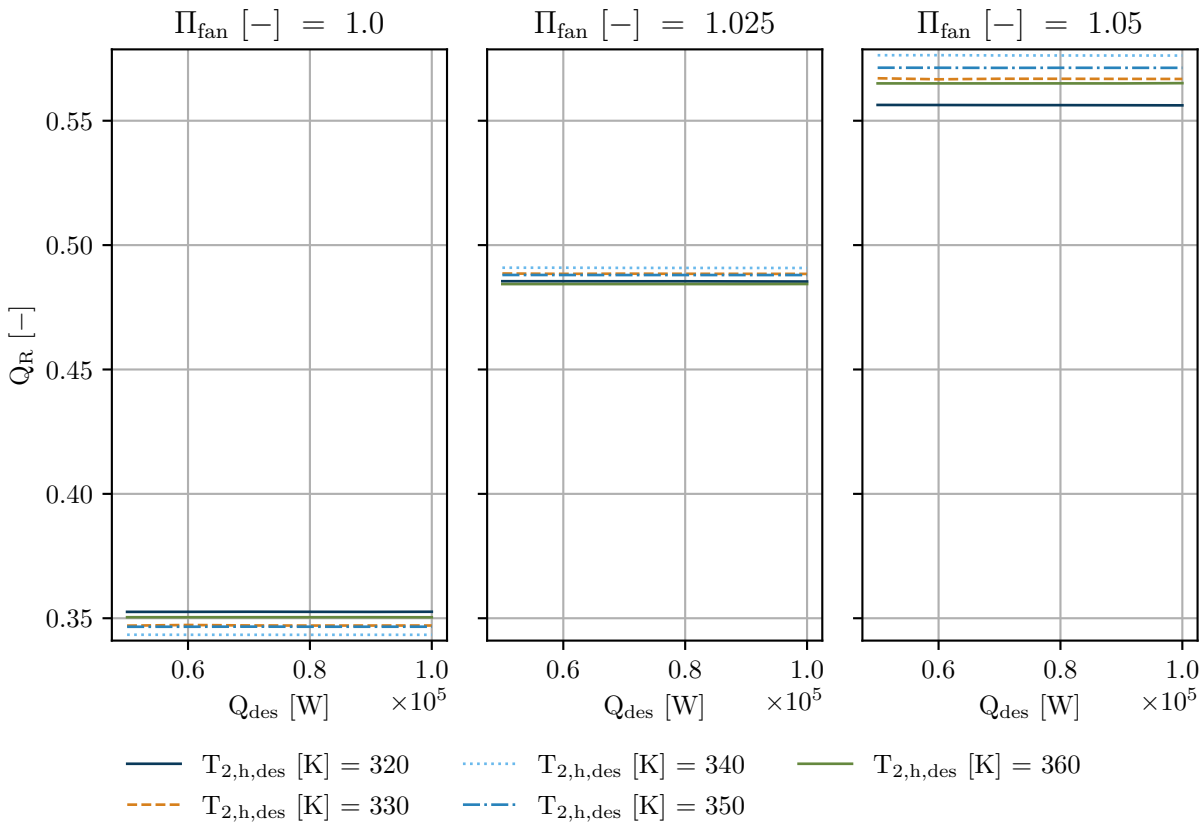

Figure A.6 Off-design performance of the motor TMS with δw_h= 1.025 and $T_{1,h}$ = 370 K

B Additional figures for the wing integrated surface heat exchanger

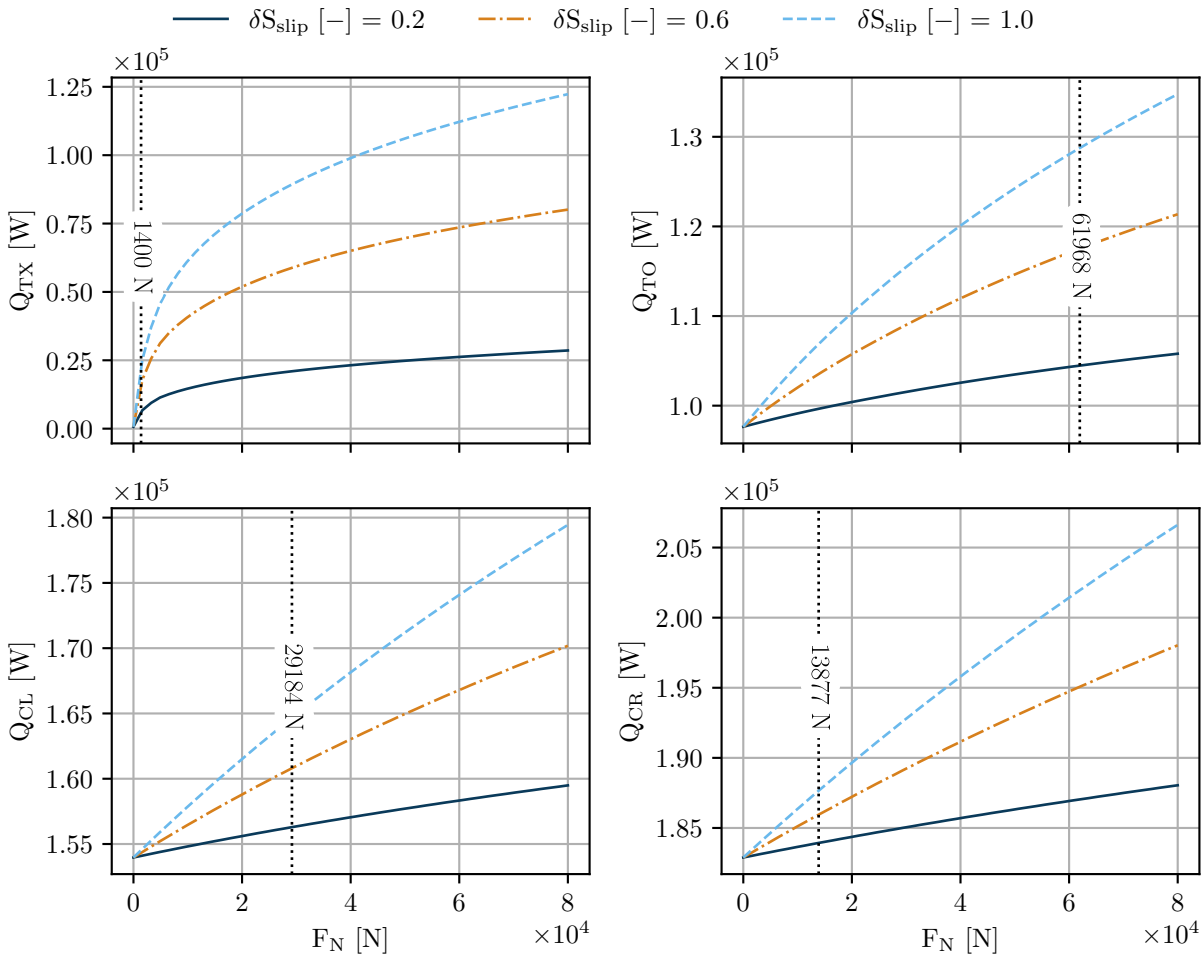

Figure B.1 Influence of relative wing span covered by the propeller slipstream and thrust on the surface cooling potential for the WISH

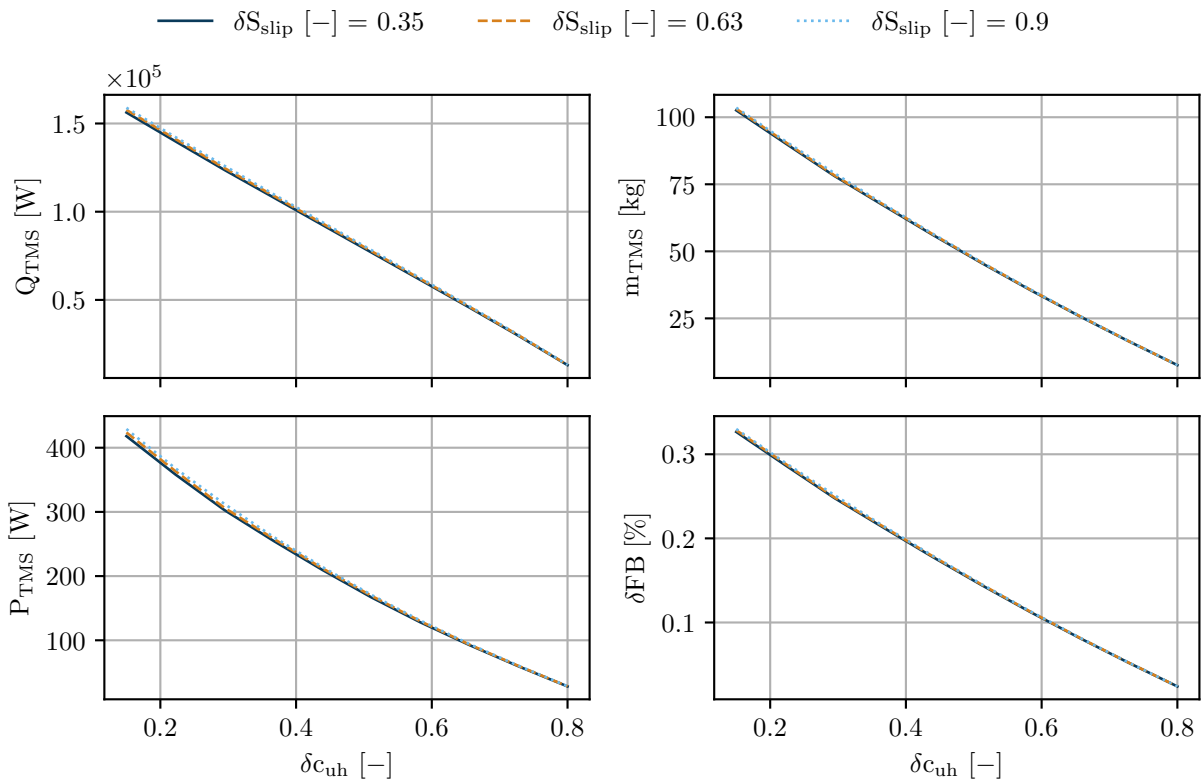

Figure B.2 Influence of relative wing span covered by the propeller slipstream for the main optimization results of the WISH at $T_{1,h}$ = 328 K

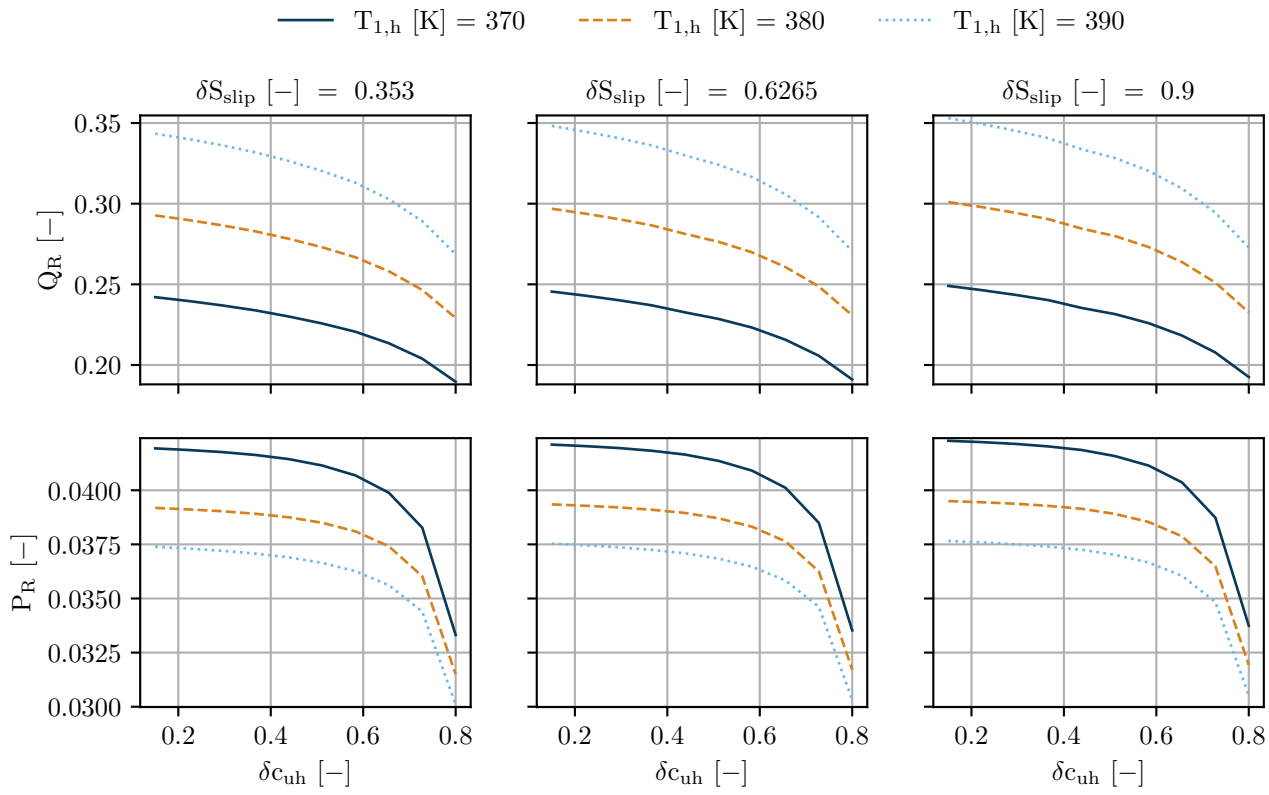

Figure B.3 HDTO results of the motor WISH for δw_h = 0.2

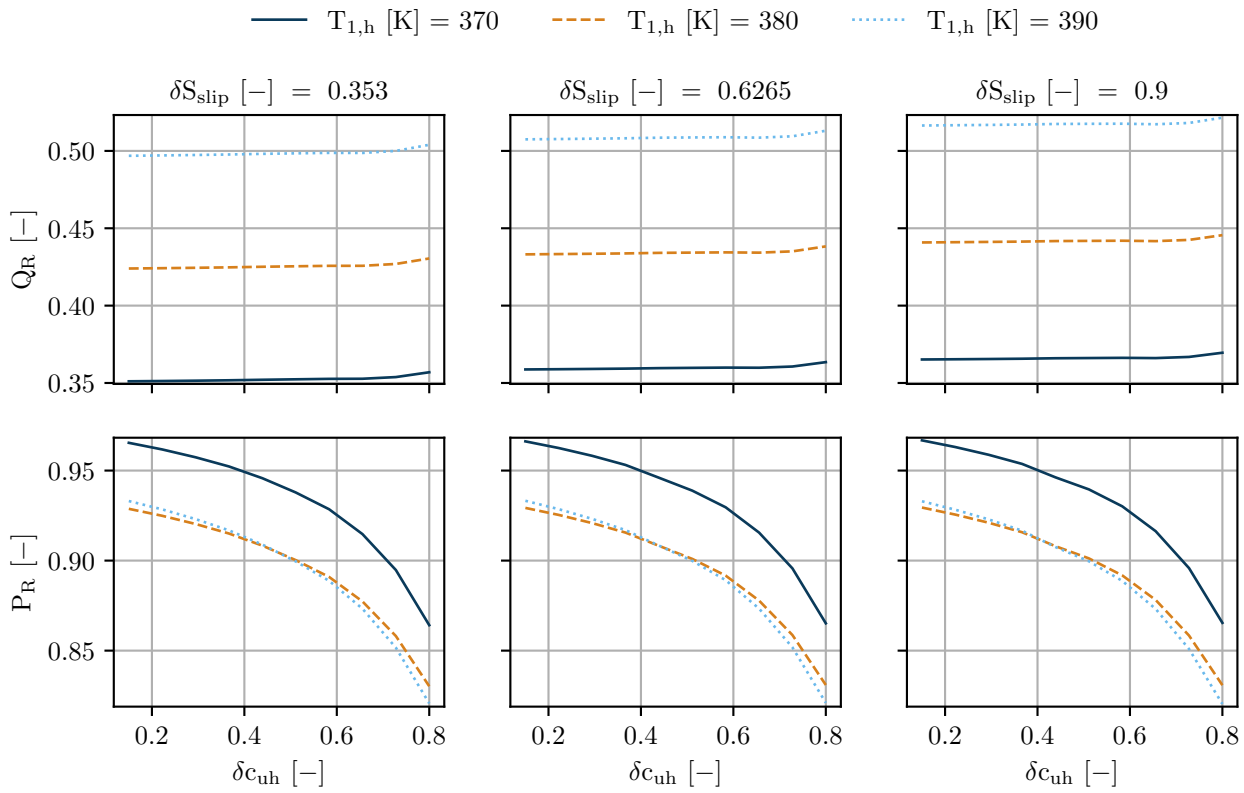

Figure B.4 HDTO results of the motor WISH for $\delta w_h = 1.0$

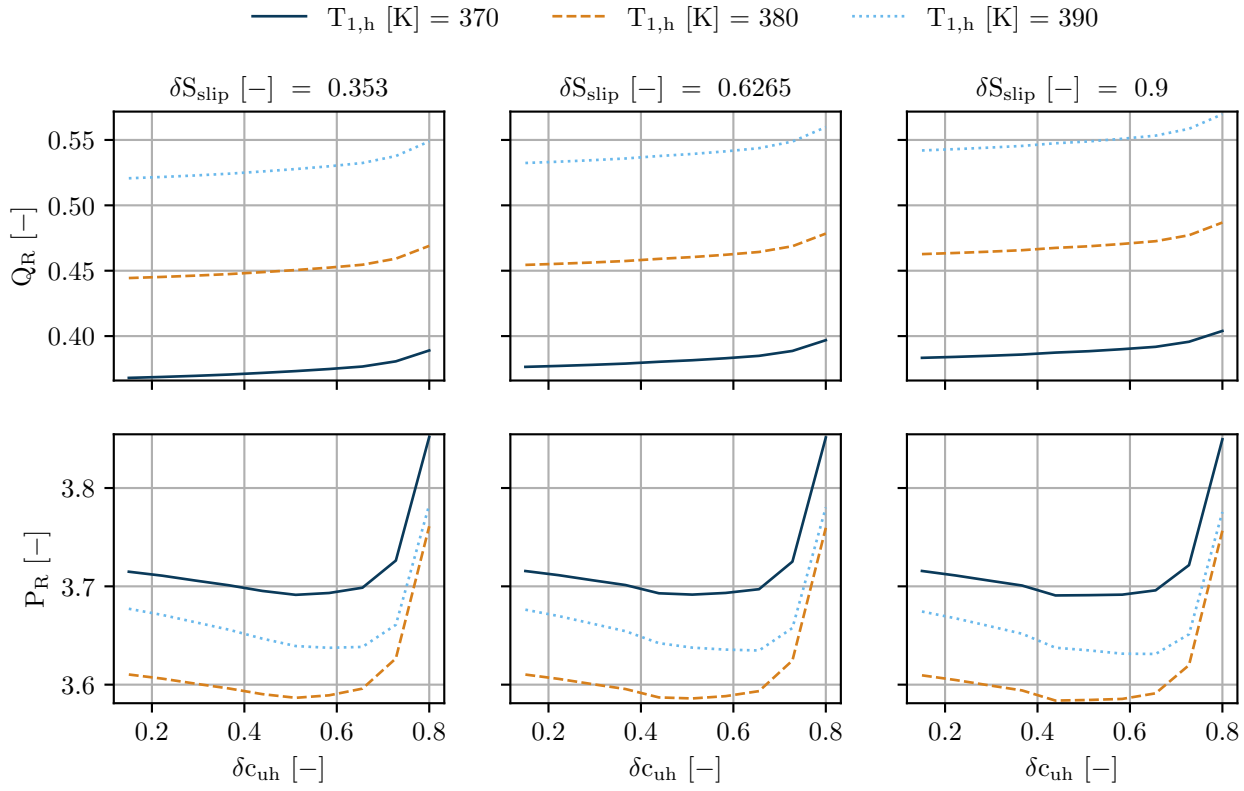

Figure B.5 HDTO results of the motor WISH for $\delta w_h = 2.0$

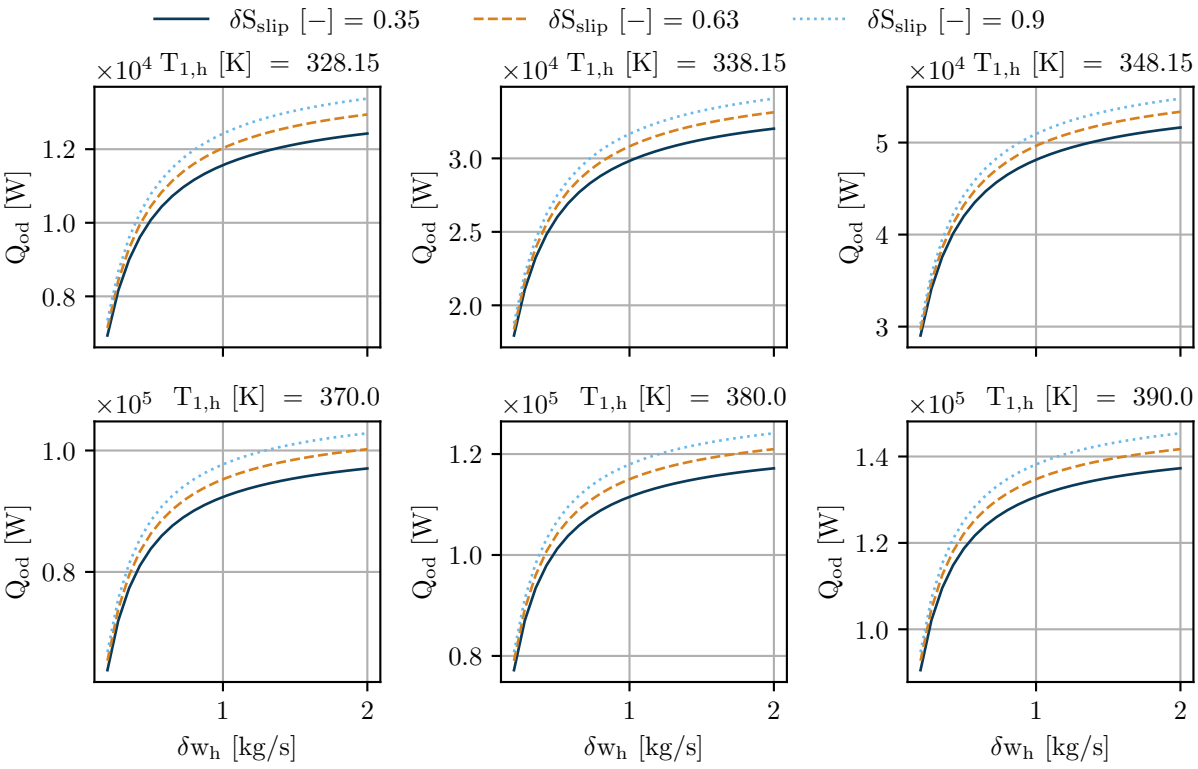

Figure B.6 HDTO absolute heat transfer for the WISH at $\delta c_{\text{uh}} = 0.15$

Bibliography

[1] Kellermann, H., Lüdemann, M., Pohl, M., and Hornung, M., "Design and Optimization of Ram Air–Based Thermal Management Systems for Hybrid-Electric Aircraft," *Aerospace*, Vol. 8, No. 1, 2021, 3. https://doi.org/10.3390/aerospace8010003.

[2] Kellermann, H., Habermann, A. L., and Hornung, M., "Assessment of Aircraft Surface Heat Exchanger Potential," *Aerospace*, Vol. 7, No. 1, 2020, 1. https://doi.org/10.3390/aerospace7010001.

[3] Kellermann, H., Habermann, A.L., Vratny, P.C., and Hornung, M., "Assessment of fuel as alternative heat sink for future aircraft," *Applied Thermal Engineering*, Vol. 170, 2020, 114985. https://doi.org/10.1016/j.applthermaleng.2020.114985, URL http://www.sciencedirect.com/science/article/pii/S135943111931974X.

[4] Kellermann, H., Fuhrmann, S., Shamiyeh, M., and Hornung, M., "Design of a Battery Cooling System for Hybrid Electric Aircraft," *Journal of Propulsion and Power*, Vol. 14, No. 16, 2022, pp. 1–16. https://doi.org/10.2514/1.B38695.

[5] United Nations, "Paris Agreement," , 2015.

[6] ACARE, "Strategic Research & Innovation Agenda: 2017 Update | Volume 1," , 2017.

[7] European Commission, Directorate-General for Mobility, Transport, and Directorate-General for Research and Innovation, *Flightpath 2050 : Europe's vision for aviation : maintaining global leadership and serving society's needs*, Publications Office, 2011. https://doi.org/10.2777/50266.

[8] European Commission, and Directorate-General for Research and Innovation, *Fly the Green Deal : Europe's vision for sustainable aviation*, Publications Office of the European Union, 2022. https://doi.org/10.2777/732726.

[9] Madonna, V., Giangrande, P., and Galea, M., "Electrical Power Generation in Aircraft: Review, Challenges, and Opportunities," *IEEE Transactions on Transportation Electrification*, Vol. 4, No. 3, 2018, pp. 646–659. https://doi.org/10.1109/TTE.2018.2834142.

[10] Sarlioglu, B., and Morris, C. T., "More Electric Aircraft: Review, Challenges, and Opportunities for Commercial Transport Aircraft," *IEEE Transactions on Transportation Electrification*, Vol. 1, No. 1, 2015, pp. 54–64. https://doi.org/10.1109/TTE.2015.2426499.

[11] Rosero, J. A., Ortega, J. A., Aldabas, E., and Romeral, L., "Moving towards a more electric aircraft," *IEEE Aerospace and Electronic Systems Magazine*, Vol. 22, No. 3, 2007, pp. 3–9. https://doi.org/10.1109/MAES.2007.340500.

[12] Rendón, M. A., Sánchez R., C. D., Gallo M., J., and Anzai, A. H., "Aircraft Hybrid-Electric Propulsion: Development Trends, Challenges and Opportunities," *Journal of Control, Automation and Electrical Systems*, Vol. 86, No. 1, 2021, p. 39. https://doi.org/10.1007/s40313-021-00740-x.

[13] Volocopter, "The Roadmap to scalable urban air mobility: White paper 2.0," , 2021.

[14] Joby Aviation, "Joby Aviation," , 2021. URL https://www.jobyaviation.com/.

[15] Airbus, "CityAirbus," , 2021. URL https://www.airbus.com/innovation/zero-emission/urban-air-mobility/cityairbus.html.

[16] Airbus, "Vahana," , 2021. URL https://www.airbus.com/innovation/zero-emission/urban-air-mobility/vahana.html.

[17] Lilium GmbH, "Lilium," , 2021. URL https://lilium.com/.

[18] Pipistrel d.o.o., "Velis Electro," , 2023. URL https://www.pipistrel-aircraft.com/products/general-aviation/velis-electro/.

[19] Eviation, "Alice: Pure Electric," , 2021. URL https://www.eviation.co/.

[20] Zunum Aero, "Zunum Aero," , 2021. URL https://zunum.aero/.

[21] Ampair, "Tailwind," , 2021. URL https://www.ampaire.com/vehicles/.

[22] Graver, B., Zhang, K., and Rutherford, D., "CO2 emissions from commercial aviation, 2018," , 2019.

[23] Bradley, M. K., and Droney, C. K., "Subsonic Ultra Green Aircraft Research: Phase I Final Report," Tech. Rep. NASA/CR–2011-216847, Boeing Research & Technology, 2011.

[24] Bradley, M. K., and Droney, C. K., "Subsonic Ultra Green Aircraft Research: Phase II - Volume II - Hybrid Electric Design Exploration," Tech. Rep. NASA/CR-2015-218704/Volume II, Boeing Research & Technology, Huntington Beach, California, 2015.

[25] Welstead, J., and Felder, J. L., "Conceptual Design of a Single-Aisle Turboelectric Commercial Transport with Fuselage Boundary Layer Ingestion," *54th AIAA Aerospace Sciences Meeting 2016*, Curran Associates Inc, Red Hook, NY, 2016. https://doi.org/10.2514/6.2016-1027.

[26] Peter, F., Habermann, A., Lüdemann, M., Plötner, K., Troeltsch, F., and Seitz, A., "Definition of the CENTRELINE Reference Aircraft and Power Plant Systems," , 2021. https://doi.org/10.25967/530114.

[27] Seitz, A., Habermann, A. L., Peter, F., Troeltsch, F., Castillo Pardo, A., Della Corte, B., van Sluis, M., Goraj, Z., Kowalski, M., Zhao, X., Grönstedt, T., Bijewitz, J., and Wortmann, G., "Proof of Concept Study for Fuselage Boundary Layer Ingesting Propulsion," *Aerospace*, Vol. 8, No. 1, 2021, p. 16. https://doi.org/10.3390/aerospace8010016.

[28] Freeman, J., and Schiltgen, B. T., "ECO-150-300 Design and Performance: A Tube-and-Wing Distributed Electric Propulsion Airliner," *AIAA Scitech 2019 Forum*, American Institute of Aeronautics and Astronautics, Reston, Virginia, 2019. https://doi.org/10.2514/6.2019-1808.

[29] Schiltgen, B. T., and Freeman, J., "Aeropropulsive Interaction and Thermal System Integration within the ECO-150: A Turboelectric Distributed Propulsion Airliner with Conventional Electric Machines," *16th AIAA Aviation Technology, Integration, and Operations Conference*, American Institute of Aeronautics and Astronautics, Reston, Virginia, 2016, p. 154. https://doi.org/10.2514/6.2016-4064.

[30] Singh, R., Freeman, J., Osterkamp, P., Green, M., Gibson, A., and Schiltgen, B., "Challenges and opportunities for electric aircraft thermal management," *Aircraft Engineering and Aerospace Technology*, Vol. 86, No. 6, 2014, pp. 519–524. https://doi.org/10.1108/AEAT-04-2014-0042.

[31] Jacob, F., Rolt, A., Sebastiampillai, J., Sethi, V., Belmonte, M., and Cobas, P., "Performance of a Supercritical CO2 Bottoming Cycle for Aero Applications," *Applied Sciences*, Vol. 7, No. 3, 2017, p. 255. https://doi.org/10.3390/app7030255.

[32] Elsevier, "SCOPUS," , 2022. URL https://www.elsevier.com/solutions/scopus.

[33] von Gersdorff, K., Schubert, H., and Ebert, S., *Flugmotoren und Strahltriebwerke: Entwicklungsgeschichte der deutschen Luftfahrtantriebe von den Anfängen bis zu den internationalen Gemeinschaftsentwicklungen*, 4th ed., Die Deutsche Luftfahrt, Vol. 2, Bernard & Graefe, Bonn, 2007.

[34] Nicks, O. W., "Drag Reduction - Back to Basics," Tech. Rep. 76 11002, NASA, NASA Langley Research Center Hampton, VA, United States, 1975.

[35] Bräunling, W. J. G., *Flugzeugtriebwerke: Grundlagen, Aero-Thermodynamik, ideale und reale Kreisprozesse, thermische Turbomaschinen, Komponenten, Emissionen und Systeme*, 4th ed., VDI-Buch, Springer Vieweg, Berlin, 2015. https://doi.org/10.1007/978-3-642-34539-5.

[36] Soller, S., Kirchberger, C., Kuhn, M., Langener, T., Bouchez, M., and Steelant, J., "Experimental Investigation of Cooling Techniques and Materials for Highspeed Flight Propulsion Systems," *16th AIAA/DLR/DGLR International Space Planes and Hypersonic Systems and Technologies Conference*, American Institute of Aeronautics and Astronautics, Reston, Virigina, 2009. https://doi.org/10.2514/6.2009-7374.

[37] Yellu Kumar, K. R., Qayoum, A., Saleem, S., and Qayoum, F., "Effusion Cooling In Gas Turbine Combustion Chambers - A Comprehensive Review," *IOP Conference Series: Materials Science and Engineering*, Vol. 804, 2020. https://doi.org/10.1088/1757-899X/804/1/012003.

[38] Schwarz, F. M., and Pickford, S., "Geared Turbofan Engine and Cooling Method Thereof," , 2013. European Patent 2 971 664 B1 filed 18.12.2013.

[39] Merzvinskas, M., Bringhenti, C., Tomita, J. T., and de Andrade, C. R., "Air conditioning systems for aeronautical applications: a review," *The Aeronautical Journal*, Vol. 124, No. 1274, 2020, pp. 499–532. https://doi.org/10.1017/aer.2019.159.

[40] Moir, I., *Aircraft Systems: Mechanical, Electrical and Avionics Subsystems Integration*, 3rd ed., Aerospace series, Vol. v.52, John Wiley & Sons Incorporated, New York, 2011. URL https://ebookcentral.proquest.com/lib/kxp/detail.action?docID=470351.

[41] Schiltgen, B., Green, M., Gibson, A., Hall, D., Cummings, D., and Hange, C., "Benefits and Concerns of Hybrid Electric Distributed Propulsion with Conventional Electric Machines," *48th AIAA/ASME/SAE/ASEE Joint Propulsion Conference & Exhibit*, American Institute of Aeronautics and Astronautics, Reston, Virigina, 2012. https://doi.org/10.2514/6.2012-3769.

[42] Brelje, B. J., and Martins, J. R., "Electric, hybrid, and turboelectric fixed-wing aircraft: A review of concepts, models, and design approaches," *Progress in Aerospace Sciences*, Vol. 104, 2019, pp. 1–19. https://doi.org/10.1016/j.paerosci.2018.06.004.

[43] Lents, C. E., Hardin, L. W., Rheaume, J., and Kohlman, L., "Parallel Hybrid Gas-Electric Geared Turbofan Engine Conceptual Design and Benefits Analysis," *52nd AIAA/SAE/ASEE Joint Propulsion Conference*, American Institute of Aeronautics and Astronautics, Salt Lake City, 2016. https://doi.org/10.2514/6.2016-4610.

[44] Rheaume, J., and Lents, C. E., "Design and Simulation of a Commercial Hybrid Electric Aircraft Thermal Management System," *2018 AIAA/IEEE Electric Aircraft Technologies Symposium*, American Institute of Aeronautics and Astronautics, Reston, Virginia, 2018. https://doi.org/10.2514/6.2018-4994.

[45] Rheaume, J. M., MacDonald, M., and Lents, C. E., "Commercial Hybrid Electric Aircraft Thermal Management System Design, Simulation, and Operation Improvements," *2019 AIAA/IEEE Electric Aircraft Technologies*, American Institute of Aeronautics and Astronautics, Indianapolis, 2019. https://doi.org/10.2514/6.2019-4492.

[46] MacDonald, M., Khakpour, Y., and Lents, C. E., "Transient Cooling Approach for a Mhr Class Hybrid Electric Propulsion System Battery Pack," *AIAA Scitech 2020 Forum*, American Institute of Aeronautics and Astronautics, Reston, Virginia, 2020, p. 2019. https://doi.org/10.2514/6.2020-0120.

[47] Rheaume, J. M., and Lents, C. E., "Commercial Hybrid Electric Aircraft Thermal Management Sensitivity Studies," *AIAA Propulsion and Energy 2020 Forum*, American Institute of Aeronautics and Astronautics, Reston, Virginia, 2020. https://doi.org/10.2514/6.2020-3558.

[48] Perullo, C. A., Tai, J., and Mavris, D. N., "A New Sizing and Synthesis Environment for the Design and Assessment of Advanced Hybrid and Electric Aircraft Propulsion Systems," *22nd ISABE Conference*, International Society for Air Breathing Engines, Phoenix, Arizona, 2015.

[49] Gladin, J. C., Perullo, C., Tai, J. C., and Mavris, D. N., "A Parametric Study of Hybrid Electric Gas Turbine Propulsion as a Function of Aircraft Size Class and Technology Level," *55th AIAA Aerospace Sciences Meeting*, American Institute of Aeronautics and Astronautics, Reston, Virginia, 2017. https://doi.org/10.2514/6.2017-0338.

[50] Perullo, C., Trawick, D., Armstrong, M., Tai, J. C., and Mavris, D. N., "Cycle Selection and Sizing of a Single-Aisle Transport with the Electrically Variable Engine(TM) (EVE) for Fleet Level Fuel Optimization," *55th AIAA Aerospace Sciences Meeting*, American Institute of Aeronautics and Astronautics, Reston, Virginia, 2017. https://doi.org/10.2514/6.2017-1923.

[51] Trawick, D., Perullo, C., Armstrong, M., Snyder, D., Tai, J. C., and Mavris, D. N., "Development and Application of GT-HEAT for the Electrically Variable Engine Design," *55th AIAA Aerospace Sciences Meeting*, American Institute of Aeronautics and Astronautics, Reston, Virginia, 2017. https://doi.org/10.2514/6.2017-1922.

[52] Perullo, C., Alahmad, A., Wen, J., D'Arpino, M., Canova, M., Mavris, D. N., and Benzakein, M. J., "Sizing and Performance Analysis of a Turbo-Hybrid-Electric Regional Jet for the NASA ULI Program," *AIAA Propulsion and Energy 2019 Forum*, American Institute of Aeronautics and Astronautics, Reston, Virginia, 2019. https://doi.org/10.2514/6.2019-4490.

[53] Perullo, C., Shi, M., Cinar, G., Alahmad, A., Sanders, M., Mavris, D. N., and Benzakein, M., "An Update on Sizing and Performance Analysis of a Hybrid Turboelectric Regional Jet for the NASA ULI Program," *AIAA Propulsion and Energy 2020 Forum*, American Institute of Aeronautics and Astronautics, Reston, Virginia, 2020. https://doi.org/10.2514/6.2020-3590.

[54] Shi, M., Sanders, M., Alahmad, A., Perullo, C., Cinar, G., and Mavris, D. N., "Design and Analysis of the Thermal Management System of a Hybrid Turboelectric Regional Jet for the NASA ULI Program," *AIAA Propulsion and Energy 2020 Forum*, American Institute of Aeronautics and Astronautics, Reston, Virginia, 2020. https://doi.org/10.2514/6.2020-3572.

[55] Shi, M., Chakraborty, I., Tai, J. C., and Mavris, D. N., "Integrated Gas Turbine and Environmental Control System Pack Sizing and Analysis," *2018 AIAA Aerospace Sciences Meeting*, American Institute of Aeronautics and Astronautics, Reston, Virginia, 2018. https://doi.org/10.2514/6.2018-1748.

[56] Borer, N. K., Patterson, M. D., Viken, J. K., Moore, M. D., Bevirt, J., Stoll, A. M., and Gibson, A. R., "Design and Performance of the NASA SCEPTOR Distributed Electric Propulsion Flight Demonstrator," *16th AIAA Aviation Technology, Integration, and Operations Conference*, American Institute of Aeronautics and Astronautics, Reston, Virginia, 2016. https://doi.org/10.2514/6.2016-3920.

[57] Jansen, R., Bowman, C., and Jankovsky, A., "Sizing Power Components of an Electrically Driven Tail Cone Thruster and a Range Extender," *16th AIAA Aviation Technology, Integration, and Operations Conference*, American Institute of Aeronautics and Astronautics, Reston, Virginia, 2016. https://doi.org/10.2514/6.2016-3766.

[58] Christie, R. J., Dubois, A., and Derlaga, J. M., "Cooling of Electric Motors Used for Propulsion on SCEPTOR," Tech. Rep. NASA/TM—2017-219134, National Aeronautics and Space Adminstration, Cleveland, Ohio, 2017.

[59] Dubois, A., van der Geest, M., Bevirt, J., Christie, R., Borer, N. K., and Clarke, S. C., "Design of an Electric Propulsion System for SCEPTOR's Outboard Nacelle," *16th AIAA Aviation Technology, Integration, and Operations Conference*, American Institute of Aeronautics and Astronautics, Reston, Virginia, 2016. https://doi.org/10.2514/6.2016-3925.

[60] Falck, R. D., Chin, J., Schnulo, S. L., Burt, J. M., and Gray, J. S., "Trajectory Optimization of Electric Aircraft Subject to Subsystem Thermal Constraints," *18th AIAA/ISSMO Multidisciplinary Analysis and Optimization Conference*, American Institute of Aeronautics and Astronautics, Reston, Virginia, 2017. https://doi.org/10.2514/6.2017-4002.

[61] Chin, J., Schnulo, S. L., and Smith, A., "Transient Thermal Analyses of Passive Systems on SCEPTOR X-57," *17th AIAA Aviation Technology, Integration, and Operations Conference*, American Institute of Aeronautics and Astronautics, Reston, Virginia, 2017. https://doi.org/10.2514/6.2017-3784.

[62] Garrett, M., Avanesian, D., Granger, M., Kowalewski, S., Maroli, J., Miller, W. A., Jansen, R., and Kascak, P. E., "Development of an 11 kW lightweight, high efficiency motor controller for NASA X-57 Distributed Electric Propulsion using SiC MOSFET Switches," *AIAA Propulsion and Energy 2019 Forum*, American Institute of Aeronautics and Astronautics, Reston, Virginia, 2019. https://doi.org/10.2514/6.2019-4400.

[63] Anibal, J. L., Mader, C., and Martins, J. R. R. A., "Aerothermal Optimization of X-57 High-Lift Motor Nacelle," *AIAA Scitech 2020 Forum*, American Institute of Aeronautics and Astronautics, Reston, Virginia, 2020. https://doi.org/10.2514/6.2020-2115.

[64] Tallerico, T., Smith, A., Thompson, J. T., Pierson, E. L., Hilliker, C. A., Avanesian, D., Monaghan, K., and Miller, W. A., "Outer Mold Line Cooled Electric Motors for Electric Aircraft," *AIAA Propulsion and Energy 2020 Forum*, American Institute of Aeronautics and Astronautics, Reston, Virginia, 2020. https://doi.org/10.2514/6.2020-3573.

[65] Chapman, J. W., and Schnulo, S. L., "Development of a Thermal Management System for Electrified Aircraft," *AIAA Scitech 2020 Forum*, American Institute of Aeronautics and Astronautics, Reston, Virginia, 2020, p. 2273. https://doi.org/10.2514/6.2020-0545.

[66] Chapman, J. W., Hasseeb, H., and Schnulo, S. L., "Thermal Management System Design for Electrified Aircraft Propulsion Concepts," *AIAA Propulsion and Energy 2020 Forum*, American Institute of Aeronautics and Astronautics, Reston, Virginia, 2020, p. 6. https://doi.org/10.2514/6.2020-3571.

[67] Antcliff, K. R., and Capristan, F. M., "Conceptual Design of the Parallel Electric-Gas Architecture with Synergistic Utilization Scheme (PEGASUS) Concept," *18th AIAA/ISSMO Multidisciplinary Analysis and Optimization Conference*, American Institute of Aeronautics and Astronautics, Reston, Virginia, 2017. https://doi.org/10.2514/6.2017-4001.

[68] More, J. J., Garbow, B. S., and Hillstrom, K. E., "User Guide for MINPACK-1," Tech. Rep. ANL-80-74, Argonne National Laboratory, Argonne, Illinois, 1980.

[69] Kraft, D., "A Software Package for Sequential Quadratic Programming," Tech. Rep. DFVLR-FB 88-28, DLR German Aerospace Center - Insitute for Flight Mechanics, Cologne, 1988.

[70] Glauert, H., "Airplane Propellers," *Aerodynamic Theory*, edited by W. F. Durand, Volume IV, Julius Springer, Berlin, 1935, pp. 169–360.

[71] Novelli, P., "IMOTHEP: towards hybrid propulsion for commercial aviation: Project Overview," , 2021.

[72] ATR, "ATR 42-600 Fact Sheet," , 2022. URL https://www.atr-aircraft.com/wp-content/uploads/2020/07/Factsheets_-_ATR_42-600.pdf, accessed: 11.05.2022.

[73] Habermann, A. L., Kolb, M. G., Maas, P., Kellermann, H., Rischmüller, C., Peter, F., and Seitz, A., "Study of a Regional Turboprop Aircraft with Electrically-Assisted Turboshaft," *Aerospace*, 2023. To be published.

[74] ATR, "ATR 42-500 Flight Crew Operating Manual," , 2010.

[75] ATR, "ATR 42-500 Fact Sheet," , 2022. URL https://www.atr-aircraft.com/wp-content/uploads/2020/07/42-500.pdf, accessed: 11.05.2022.

[76] Bell, I. H., Wronski, J., Quoilin, S., and Lemort, V., "Pure and Pseudo-pure Fluid Thermophysical Property Evaluation and the Open-Source Thermophysical Property Library CoolProp," *Industrial & Engineering Chemistry Research*, Vol. 53, No. 6, 2014, pp. 2498–2508. https://doi.org/10.1021/ie4033999.

[77] Coordinating Research Council, "Handbook of aviation fuel properties," Tech. Rep. CRC Report No. 530, Atlanta, Ga, 1983.